



Montanuniversität Leoben - University of Leoben

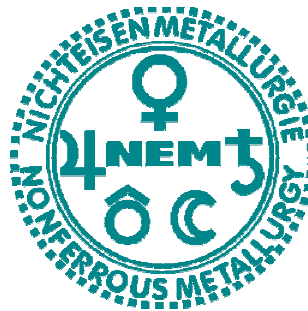
Department Metallurgie - Department of Metallurgy

Nichteisenmetallurgie - Nonferrous Metallurgy



Ph.D. Thesis

Investigation of the Interface Reaction of Al and Binary Al-alloys on Mild Steel Substrates for Al Compound Casting



Author:

Dipl.-Ing. Werner Fragner M.Sc.

Ph.D. thesis to obtain the academic degree of the
Montanuniversität Leoben

Advisors:

Univ.-Prof. Dipl.-Ing. Dr. mont. Helmut Antrekowitsch

Prof. Dipl.-Ing. Dr. Peter J. Uggowitzer

Leoben, May 2012

Eidesstattliche Erklärung

Ich erkläre an Eides statt, dass ich die vorliegende Arbeit selbstständig verfasst, andere als die angegebenen Quellen und Hilfsmittel nicht benutzt und mich auch sonst keiner unerlaubten Hilfsmittel bedient habe.

I declare in lieu of oath, that I wrote this thesis and performed the associated research myself, using only literature cited in this volume.

Werner Fagner

Leoben, May 12th 2012

Acknowledgements

At this point I would like to take this opportunity to thank all the people whose whole-hearted support made this thesis happen.

First of all I think that without the seemingly unbridled patience of my advisors and mentors Univ.-Prof. Dipl.-Ing. Dr. mont. Helmut Antrekowitsch at the Montanuniversität Leoben and Prof. Dipl.-Ing. Dr. Peter J. Uggowitzer at the Eidgenössische Technische Hochschule Zürich these pages would not have come into existence. While sometimes I doubted if I ever finish this work they always had an encouraging word for me to stay on track. Without their support I never would have been able to finish this work. Both handled my matters straightforward and helped me in any way they could. It is hard to imagine to have had other advisors. The word "finally" will cross their minds when reading these pages. Thank you.

Much of the experimental work was done within the ALWS project (Austrian Light Weight Structures). Many thanks to the Austrian National Foundation for establishing this venture.

I also would like to give my thanks to Roman Sonnleitner, a very thoughtful person and a true master of the scanning electron microscope. The best images in this thesis are made by him and the discussions with him helped me to better interpret the results. Gratitude as well deserves his colleague Jaroslav Wosik, who was also involved in the process and deepened my understanding of the modeling process and difficulties of correct phase detection.

At the ETH Zurich Konrad Papis and Bruno Zberg aided me with my experiments. I want to thank them for finding the right experimental setup for our wetting experiments.

A big thank you I would like to express to the LKR team, especially Gottfried Rettenbacher, Maximilian Strini, Anton Hinterberger, Christa Kainhofer and Helmut Kilian for helping me at the industrial scale experiments and their evaluation.

Claudia Sporrer most certainly deserves a big hug for saving my day quite a view times during the writing process by charming away my exasperation, sometimes without even noticing it. Thank you for being there!

Many thanks to Fanny Gaumond and Joël Voyer who were proofreading my work and gave me invaluable advice, while the time frame for them was quite limited.

Thanks to the people of AMAG who supported me at that time: Helmut Suppan, Philip Pucher and Florian Stadler.

Greetings also to the numerous people whom I called and wrote. They gave me valuable information, sometimes more than I had hoped for.

A great deal of assistance to me in the course of writing and before was my "intern" Thomas Stadler, who has finished now himself his master studies. His intelligence and the speed of his work, which besides was always flawless, was scary at times, while he was helpful and amiable at all times. Surely I will never ever get such an intern as him again and he will always be the reference for all others. I dearly hope to keep close contact, since such a person is once in a blue moon.

The one who deserves my deepest gratitude is undoubtedly Priv.-Doz. Dr. Helmut Kaufmann who initiated the topic within the ALWS project and helped me from the moment we meet. The road of this thesis was a curvy one but Helmut Kaufmann was ever so supportive. It is hard to imagine a similar person of integrity and I consider myself blessed not only to have met him but also him staying in touch with me for whatever comes.

I also want to thank my mother, Berta Fragner. Her determination and life in general showed me that there is always way, even when there seems no solution: "You can start whatever you want, but then you have to finish it as well"

Kurzfassung

Die Vorgaben von Politik und auch von den Fahrzeugherstellern für Gewichtsreduktion und Produktionskostenminimierung zukünftiger Transportfahrzeuge werden immer strenger. Aus diesem Grund gewinnt das Konzept des Multi-Material-Mixes immer mehr an Bedeutung. In diesem Kontext sind Aluminium-Stahl-Verbunde, welche durch Verbundguss (Stahl-Insert mit Aluminium umgossen) hergestellt werden, aufgrund ihres hohen Einsparungspotenzials bei gleichzeitiger Funktionsintegration von besonders großem Interesse.

Ein wichtiger und kritischer Aspekt dieser Verbundgussteile ist die Ausbildung intermetallischer Phasen (IMP) an der Grenzfläche vom Stahl zum Aluminium. Sowohl die genaue Ausprägung der möglichen IMPs als auch deren Bildungskinetik ist noch nicht ganz verstanden und verlangt daher nach einer systematischen Untersuchung.

Diese Arbeit beschäftigt sich mit der Bildung der intermetallischen Phasen an der Grenzfläche von Stahl zu Aluminium und Aluminiumlegierungen. Ziel dabei war es, die auftretenden Phasen zu bestimmen, die Bildungskinetik zu charakterisieren und nach Möglichkeit die Phasenbildung in Abhängigkeit der Zeit zu modellieren. Aus diesem Grund wurde nach der Herstellung von definierten Phasen im Labor zur Kalibrierung verschiedene experimentelle Methoden zur Phasenbildung angewendet:

- Schwerkraftkokillenguss mit unterschiedlichen Al-Fe-Massenverhältnissen
- Benetzungsexperimenten in einer sauerstoffarmen Atmosphäre
- Eintauchversuche in Reinaluminium, binären und kommerzielle Legierungen
- Squeeze Casting von Inserts im industrienahen Umfeld

Das System Al-Si, welches im Formgussbereich dominierend ist, besitzen komplexeste Phasenausprägungen mit vielen unterschiedlichen, gleichzeitig auftretenden Phasen im Interface, wie etwa $\text{Fe}_2(\text{Al},\text{Si})_5$ (η), FeAl_4Si (τ_6), $\text{Fe}_2\text{Al}_2\text{Si}$ (τ_1) und $\text{Fe}_3\text{Al}_4\text{Si}_2$ (τ_3). Dies führt unter anderem auch zu einer geringeren Schichtdicke, was sich negativ auf die Anbindung im industriellen Umfeld auswirkt.

Im Rahmen der Arbeiten konnte aber auch gezeigt werden, dass eine chemische Verbindung zusätzlich zu Formschluss und Kraftschluss dem Verbund weitere Festigkeit verleihen kann, je nach Legierungssystem min. 5 MPa (Al-7Si) bis max. 24 MPa (Al-7Zn).

Abschließend werden dem Anwender praxisnahe Tipps und Parameter gegeben, wie im industriellen Umfeld ein stoffschlüssiger Verbund am günstigsten zu erreichen ist.

Abstract

The requirements of politics and manufacturers for weight-saving and low-cost production of prospective of components for future transport vehicles are getting more and more severe. For this reason the concept of multi-material mix is of increasing importance. In this context aluminum-iron compounds produced by means of compound casting (steel insert recast with aluminum) are considered to be of particular importance due to their high potential for cost savings and integration of function.

An essential and critical aspect of such compound castings is the formation of intermetallic phases (IMP) at the Al-Fe interface. Both the nature and the kinetics of potential IMPs are not well understood and require a systematic investigation.

This work deals with the formation of intermetallic phases at the interface of steel to aluminum and aluminum alloys. Aim of this thesis is to determine the emerging phases, characterize the kinetics and model the time dependent phase formation if possible. For this reason several experimental methods of phase formation were applied after producing calibration samples of defined phases in the laboratory:

- Gravity casting with different Al-Fe mass ratios
- Wetting experiments under a controlled atmosphere
- Dipping trials in pure aluminum and binary commercial alloys
- Squeeze Casting of inserts in an industrial environment.

The system Al-Si, which is dominant in shape casting industry, produces the most complex phase morphologies with different, simultaneously emerging phases at the interface such as $\text{Fe}_2(\text{Al},\text{Si})_5$ (η), FeAl_4Si (τ_6), $\text{Fe}_2\text{Al}_2\text{Si}$ (τ_1) and $\text{Fe}_3\text{Al}_4\text{Si}_2$ (τ_3). This leads to a reduced interface thickness among other things, which has a negative influence on the bonding in the industrial environment.

However, it could be also shown that a chemical bonding can add strength to the compound additionally to shape- and force bonding, which range from at least 5 MPa (Al-7Si) to a maximum of 24 MPa (Al-7Zn).

Concluding this thesis are practical tips and parameters for the caster on how to obtain chemical bonding in the industrial environment.

Table of contents

1.	INTRODUCTION	1
1.1	Motivation	1
1.2	Aim of the Thesis.....	2
2.	STATE OF THE ART	4
2.1	Al-Fe Components	5
2.2	Die Soldering.....	7
2.3	The Binary Al-Fe Diagram.....	7
3.	EXPERIMENTS AND PROCEDURES.....	9
3.1	Creating defined binary intermetallic Al-Fe phases.....	9
3.2	Gravity Casting using defined Mass Ratios.....	12
3.3	Wetting Experiments	14
3.4	Dipping Experiments	15
3.5	Real World Castings.....	17
4.	PRACTICAL EXPERIMENTS AND METALLOGRAPHIC EVALUATION.....	21
4.1	Gravity Casting using defined Mass Ratios.....	21
4.2	Gravity Casting using zinc coated steel cubes in 99.7Al.....	36
4.3	Wetting Experiments	38
4.4	Dipping Experiments	46
4.4.1	Evaluation.....	46
4.4.1.1	Dipping experiments in Al-7Cu.....	47
4.4.1.2	Dipping experiments in Al-7Mg	50
4.4.1.3	Dipping experiments in Al-7Zn	52
4.4.1.4	Dipping experiments in Al99.7.....	55
4.4.1.5	Dipping experiments of steel with and without 2 μm Zn-coating in Al-Si alloys.....	57
4.4.1.6	Comparison of the dipping test results	66
4.4.1.7	Dipping experiments in commercial Al-alloys.....	70
4.4.1.8	Influence of zinc coating thickness on interface formation	76
4.5	Real World Castings with the Squeeze Casting Process.....	84
4.5.1	Investigation of area 1: „No chemical bonding“	86

4.5.2	Investigation of area 2: „Chemical bonding“	88
5.	MECHANICAL PROPERTIES OF THE INTERFACE LAYER	92
5.1	Production of the Test Specimen	92
5.2	Tensile Testing of the Test Specimen	93
6.	MODELING OF THE INTERPHASE REACTION	95
6.1	Modeling of the Binary Interface Reaction	95
6.1.1	Solid-state growth of one compound layer	96
6.1.1.1	Reaction diffusion model	97
6.1.1.2	One process in the <i>A-B</i> system	99
6.1.1.3	General case: Reactions 1 and 2 proceed simultaneously	100
6.1.2	The effect of dissolution on the growth of the A_pB_q layer	101
6.1.3	Parabolic Growth	102
6.2	Modeling of multi-component interface reactions	102
6.2.1	Solid State growth of a single compound layer	103
6.2.2	Growth of the <i>ArBs</i> layer at the <i>A/B</i> interface.....	103
6.2.3	Growth of the <i>ArBs</i> layer at the A_pB_q/B interface	105
6.2.4	Growth of the <i>ArBs</i> layer at the A_pB_q/AlB_n interface	106
7.	3D MODELING USING THE EXPERIMENTAL DATA	108
7.1	Experimental techniques for Modeling	108
7.2	Microstructures of Intermetallic Phases.....	109
7.3	Imaging analysis of microstructures	111
7.4	Growth mechanism of Intermetallic Phases	112
8.	SUMMARY AND OUTLOOK	118
9.	REFERENCES	I
10.	LIST OF FIGURES.....	XI
11.	LIST OF TABLES	XIX
12.	APPENDIX	XX
	Publications in the course of this Thesis.....	XX

1. Introduction

1.1 Motivation

The desire to reduce CO₂ emissions is omnipresent at the moment (2012) as it is also legally enforced.^[1] Especially the transportation industry and particularly the automotive industry as a means of individual transport wish to reduce this impact in greenhouse gas emissions.^[2]

There are several ways to achieve the goal of CO₂ emission reduction, one is by making the engines and the components for the power-train more efficient, developing new technologies like start-stop automatic and hybrid concepts^[3] including energy recovery (micro-, mild- and full-hybrids)^[4] or engine downsizing just to name a few. Weight saving is a key issue^[5] as fuel consumption is directly proportional to weight.^[6] Therefore less weight means less CO₂ emissions and thus "greener" cars.^[7] Furthermore decreasing gas consumption also means cost savings, an increasingly important buying decision for many customers. Weight saving becomes even more necessary with hybrid electric cars as the load of electric components and the battery adds up comparing to similar cars that run solely with a combustion engine. Heavy necessities such as safety and convenience features further increase the vehicle mass and therefore demand light-weight components, both in material and design, in order to keep the final car weight at a moderate level.^[8]

Weight saving can be accomplished by various ways which include thoughtful construction from the beginning.^[9] A frequently used approach is to lighten the car body, also named body in white, in the beginning of the production process. Besides the engine motor components and power-train applications can contribute significantly to mass reduction without the customer noticing it. Lightweight design and construction is here a key factor. However, most replacements of components with weight-saving potential consist of one material type due to difficulties in making joint material parts. Additionally to ever present chemical issues (i.e. corrosion) between two different materials with different electrochemical potentials such as aluminum and steel, components consisting of two materials always demand a joining technique, which renders the part more expensive than a one material solution, even though the demands could be better met when using different materials.

A representative material combination for composite parts is joining aluminum to steel: Steel is strong, ductile and cheap (leaving specialty steels such as TRIP or TWIP steels aside) as a construction material. Yet, there is a limited capability to integrate several design functions

in one part in comparison to cast structures that can be accomplished via the casting route. This is where aluminum and aluminum (high pressure die) casting is a proven and efficient method in part production. Highly evolved casting processes allow for large parts with complex geometry, that lead to a high function integration, as component castings and lately even as structural parts. The cost saving potential via the casting route is huge due to manufacturing a single part that integrates several other parts and functions from previous designs. These were usually made up of semi-finished products which included multiple operations like stamping and joining to finish the assembly. Hence, if the demanded properties can be achieved, casting is becoming the preferred way of part production. But, since the strength of aluminum castings is limited, a combination of these materials is desirable. The joining aluminum and steel using a casting process is therefore a key issue in further reducing vehicle weight or in finding other industrial applications.^[4, 5]

The resulting bond between these two materials can have three characteristics, which can occur all at the same time, but not necessarily.

- a. Force-bonding: Aluminum shrinks onto the steel substrate and therefore applies a force on it which results in a physical bonding.
- b. Shape-bonding: Through micro- and macro-gearing the two parts hold together
- c. Chemical bonding: Aluminum and steel react upon contact diffuse into each other and/or form an intermetallic phase which results in a chemical bond.

1.2 Aim of the Thesis

This work deals solely with chemical bonding of aluminum and steel and thus investigates the possibility of joining aluminum and steel using a casting process (gravity and pressure assisted) via chemical bonding. In this procedure the solid insert consists of a mild steel component (such as DX 54 D according to EN 10346)^[10, 11] and the aluminum is cast in its liquid state around this insert.

Goal of the thesis is to investigate and characterize the formation of the Al-Fe interface depending on different aluminum alloys. In the literature several authors discuss the interaction of pure molten aluminum and iron substrates.^[12-26] For industrial applications however, cast alloys such as Al-7Si are used and here the literature is sparse.^[27, 28] As a consequence, this thesis deals also with the influence of mayor alloying elements of cast Al-alloys on the bonding behavior and its quality. The focus however lies in the observation of the Al-Si-Fe system, since most of the casting alloys used in the automotive industry lie

within the aluminum-silicon alloy family. The iron counterpart is set to a mild steel substrate as mentioned before and was not varied.

In order to put the Al-Fe-Si system into the right perspective, not only the binary Al-7Si alloy is investigated, but also the Al-7Cu, Al-7Mg and Al-7Zn alloys. Reason for this is that there are some cast alloys that have similar composition as Al-Si alloys, although they are less often used.

It is important not to forget to gain practical knowledge in order to provide advice to component designers and the foundryman on which parameters suit best for optimal chemical bonding. Chemical bonding is generally welcomed primarily with moving parts. With parts that are solely force bonded a crack could open up between the joined partners upon load and an electrolyte (salt-water from winter services) facilitates contact corrosion in an area that does not dry up quickly by the reason of capillary moisture. A chemical bonding could avoid such a crack.

The thesis is divided in two parts. The first part deals with the characterization of the interface formation, the second with the modeling of the interface formation based on the findings of the characterization. At the end, practical advice to the industry should be made. This is crucial due to the fact that while the chemical bonding certainly adds to the total strength of the composite material, intermetallic phases that form in the interface are known to be brittle^[11] and therefore reduce the ductility to an extent where the bonding is no longer acceptable for industrial applications. Hence, a balance must be found between chemical bonding that adds to the strength and an interface thin enough not to weaken the bond by its brittleness. For this, two methods of casting need to be investigated: Gravity casting and pressure assisted casting like squeeze (high pressure casting). These casting procedures differ in the cooling rate of the aluminum within the process after the cavity is filled.

2. State of the Art

Compound materials are being already applied to commercial applications in numerous ways including Al-Fe composite casting, which has been in use since decades and even increased in recent years owing to the weight saving efforts of the industry. In composite casting, a cast part is joined with one or more inserts via the casting process which means this is a process where one partner is solid (Fe) and the other liquid (Al) which embeds the insert. Classical joining operations like welding, soldering, riveting and clinching can be saved. This method can be used for different material combinations. The aluminum melt usually has a temperature of 700°C to 740°C when cast and the steel insert temperature ranges from room temperature to 300°C at insertion. The insert must be completely dry and not moist, therefore most inserts are preheated. As noted earlier, the joint in composite casting can have three characteristics which are force-bonding, shape-bonding and chemical-bonding which can occur all at the same time, but not necessarily.^[29]

For force-bonding^[29], aluminum shrinks onto the steel substrate and the combination of friction and internal stresses due to the different coefficients of thermal expansion apply a strong force on the insert which results in a good physical bonding. Nevertheless stress relaxation can reduce the bonding force in the course of the lifetime of the composite. Additionally, movements can lead to small openings in the bond and via capillary forces corrosion can occur in the joint.

Shape-bonding describes a process where the bonding of the individual parts is accomplished via their geometrical shape and is also a robust form of joining. The large degree of freedom for shape casting is very beneficial for this kind of attachment. Even so the same restrictions apply as with force-bonding.

Chemical-bonding is a connection of the two parts on an atomic level. For the composite casting of aluminum to steel, several intermetallic phases can emerge at the interface which, as long as they stay intact during the cooling process, can ensure a high-strength bond. To achieve this, the steel surface has to be removed from any oxides and a re-oxidation has to be prevented. It is known that intermetallic phases are brittle at room temperature^[30] which means that cracks can easily propagate in the thin layer of the interface. Therefore a purely chemical-bonding is thought to be less than ideal for strong compound castings and is always backed up by either force- or shape-bonding or both. In the composite casting process, force-bonding happens naturally as the insert is generally completely enclosed by the liquid aluminum.

2.1 Al-Fe Components

Today the industry already produces and uses components consisting of an aluminum and a steel part. But these are mostly joined by welding. In general cast structures use force- and shape-bonding, but not chemical-bonding. Additionally, most of the compound castings that are in series production serve in the premium segment of the automotive industry.

An example is a brake disk from Brembo (Figure 1), where two different inserts (one ceramic and one pre-cast iron) are recast into the final component. This helps not only to reduce weight, but also to reduce the residual deformation at the end of the brake. Another usage of casting aluminum to steel are bush bearing (Figure 2).



Figure 1: Brembo brake disk consisting of a ceramic and precast iron inlay

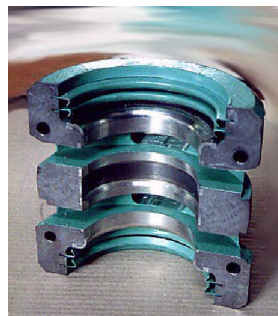


Figure 2: Bush bearing of steel with aluminum insert

For a long time already the so called Alfin Process exists. This technique is used mainly for high performance diesel pistons (Figure 3). The Piston has three contact rings to the cylinder wall, of which the first ring bears most of the load. Thus this ring is usually made of austenitic cast iron. The process works by immersing the cast iron ring in a melt made of a specific Al-Si based-alloy with the purpose of forming an intermetallic bonding layer, then removing the ring from the immersion bath, placing it into a mould and then directly afterwards recast it with the piston alloy. Sometimes this is performed using argon as a cover gas, however the process is still not well understood concerning the reaction and diffusion kinetics.



Figure 3: Example of an aluminum piston with a steel insert

High pressure die casting process also use the VarioStruct process (Figure 4), which incorporates aluminum fins in a steel u-profile to increase rigidity. The process was developed by the team of Univ.-Prof. Dr.-Ing. A. Bührig-Polaczek and Imperia GmbH was created to promote parts made by this process.



Figure 4: VarioStruct part produced via high pressure die casting

While VarioStruct can produce chemical bonding with certain Al-Fe combinations under particular process parameters, intermetallics of aluminum and steel can be found more readily by Al-Fe welding applications.^[31-35] The best known process here is the cold metal transfer process (CMT) which evolved from the continuous adaptation of the metal inert gas (MIG) and metal active gas (MAG) welding process. However, CMT is designed to minimize any intermetallic formation in order to reduce the brittleness of the welding seam as can be seen in Figure 5.

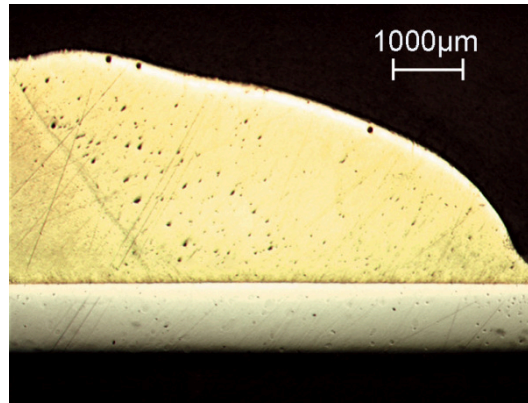


Figure 5: Micrograph of a CMT produced welding seam of Aluminum to a steel sheet

Several automotive companies are testing prototypes to implement Al-Fe castings into series production but little is published so far.

2.2 Die Soldering

In die casting steel, dies and molds are used to form the shape of the casting. Here, an undesired phenomenon can occur which is called "die soldering" which describes the sticking of the cast part in the metallic die, generally happening in the high pressure die casting process. This method is based on the formation of intermetallic phases of Al and Fe (mainly Al_3Fe_2) that have a lower melting point than the die material itself. This topic has been investigated and several papers have been published on this subject and how to avoid die soldering.^[36]

This work now uses the findings in the opposite direction and while in usual part casting this phenomenon is sought to be prevented, efforts are being made for better understanding it and eventually using it for composite casting.

2.3 The Binary Al-Fe Diagram

In the phase diagram of Al-Fe (Figure 6) shows that several intermetallic phases are expected in an intermetallic layer between the two bonding partners when going from Fe to Al, such as FeAl_2 , Fe_2Al_5 and FeAl_3 . However, since the Al melting temperatures in technical processes are normally below 800 °C - mostly about $730\text{ °C} \pm 20\text{ °C}$ - formation kinetics might favor a specific phase.^[37] Pure Aluminum is supposed to wet steel at these temperatures decently, so intermetallic phases can be expected. Additionally, diffusion between the

bonding partners is expected, especially from iron into aluminum, since in liquids, diffusivities are at least several orders of magnitude higher than in solids.

If binary Al-alloys are used, the situation concerning possible intermetallic phases (IMP's) gets even more complex, both regarding their type and their formation kinetics. In a first step, besides pure Al, three different binary test-alloys were selected for the investigation: Al-Si, Al-Cu and Al-Zn, each with 7 weight percent (± 0.1 wt%) of major alloying content.

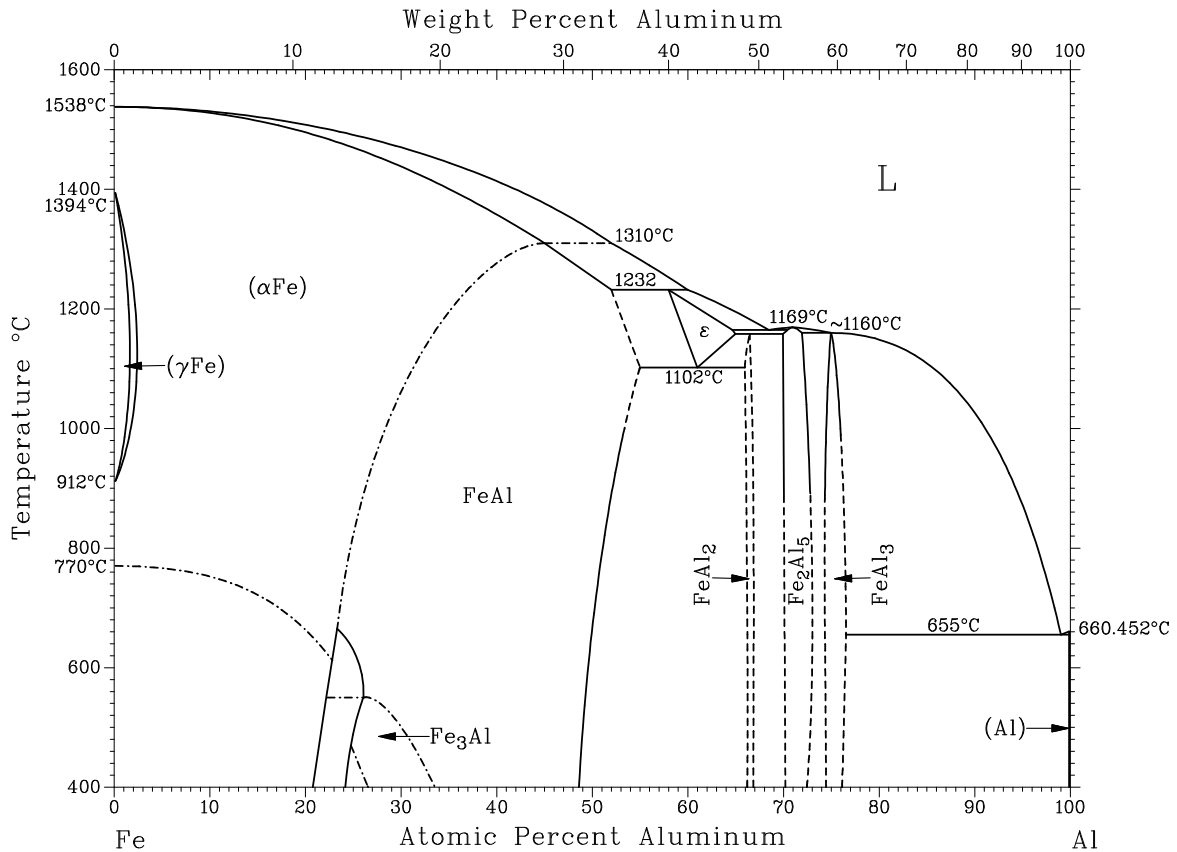


Figure 6: Al-Fe phase diagram (bottom atomic-, top weight percent)^[38]

3. Experiments and Procedures

To understand the mechanisms of the interface formation of the binary Al-Fe system (solid steel insert recast with molten aluminum) and the ternary systems with additional copper, magnesium, silicon, and zinc experiments were conducted.

3.1 Creating defined binary intermetallic Al-Fe phases

Calibration samples were produced to create a batch of reference phases. The aluminum (and aluminum alloys respectively) and steel samples were fixed in their composition and came from one batch to evaluate and characterize the according Al-Fe phases and their properties. The material was created using an electric arc furnace in a protective atmosphere (99.9999% Ar). To create the phases according to the following mass ratios were used: 90 Al-10 Fe, 80 Al-20 Fe, 70 Al-30 Fe, 23 Al-77 Fe, 27 Al-73 Fe and 17 Al-83 Fe.^[39]

For the production of the calibration phases, ingots with a purity of 99.999 wt% Al and 99.98 wt% Fe were employed. The metals were molten together in the electric arc furnace, then wrapped in a molybdenum foil and stored in evacuated quartz ampoules. They were tempered in a resistance furnace for 170 hours at 850 °C and then quenched in distilled water at room temperature.

Characterization was carried out via XRD (Philips MPD diffractometer and Image-Plate-Guinier-camera) to examine the lattice structure and parameters. The chemical compositions of the intermetallic phases were investigated via scanning electron microscope SEM and energy dispersive X-ray analysis (EDX, Philips XL 30 FEG ESEM and EDAX Phoenix System with correction factors).

It was discovered that individual Al-Fe phases of Al-Fe compound castings were sometimes very thin (1 μm or less). Since the analyzed area activated by the 20 kV accelerated electron beam (and thus the source of the X-ray quanta) is sometimes larger in the extent of several μm , than the phase itself, the X-ray spectrum produced originates from the area surrounding phase as well and lead to a tampered and biased quantitative result.

Analyses carried out at a lower acceleration voltage of the electrons (for instance 5 kV) have a lower penetration depth and therefore, the amount of the spectrum that comes from the surrounding area is smaller. The disadvantage of such a low acceleration voltage is that X-ray quanta with energy of less than 5 kV may not be sufficient for some elements to be

detected properly, and for that reason the resulting signal is sometimes not completely distinct.

Fe and Al deliver well separable peaks in this energy band which can be used for quantification which is not the case in ternary systems with elements such as copper, magnesium, silicon and zinc.^[40]

Though the EDAX analyzing software delivers a different result via integrated correction factors at 5 kV than a quantification at 20 kV, the reproducibility of the analysis is excellent and can be used for the designation of individual phases as Table 1 illustrates.

Table 1: Averages and Standard deviations of EDX analysis of 71Al 29Fe (Fe_5Al_2) and 75,5Al 24,5Fe ($\text{Fe}_{13}\text{Al}_4$ or more commonly named Fe_3Al)

	Average				Standard deviation			
	Al wt%	Al at%	Fe wt%	Fe at%	Al wt%	Al at%	Fe wt%	Fe at%
71Al 29Fe @ 20 kV	55.2	71.8	44.8	28.2	0.17	0.12	0.17	0.12
71Al 29Fe @ 5 kV	47.8	65.5	52.2	34.8	0.38	0.35	0.38	0.35
75,5Al 24,5Fe @ 20 kV	61.7	77.0	38.3	23.0	0.12	0.09	0.12	0.09
75,5Al 24,5Fe @ 5 kV	54.9	71.6	45.1	28.4	0.52	0.43	0.52	0.43

After all possible Al-Fe phases were produced and characterized, the system Al-Fe-Si was examined. The following phases were made and identified using the same procedure as described above: T4 ($\text{Fe}_{15}\text{Al}_{58}\text{Si}_{27}$), T5 ($\text{Fe}_2\text{Al}_7\text{Si}$) and T6 (FeAl_4Si).

The phases T4-T6 were evaluated via EDX and the data used as standards for the phase characterization of intermetallic phases that develop in the "real" life interface, that is the Al-Fe bonding in casting experiments between the aluminum alloy and the steel insert.

Another important mechanical property of materials is their hardness. Especially for composite materials, different hardness values of the bonding partners play a crucial role for the final product. A relatively soft aluminum is cast around harder steel to form even harder intermetallic phases.^[41] Therefore, the micro-hardness of the most frequently emerging aluminum-iron phases (Al_3Fe , more correctly $\text{Fe}_{13}\text{Al}_4$, and Al_5Fe_2) was investigated.

While high micro-hardness values could be confirmed, the intermetallics phases were very brittle. This can be seen in the typical cracks^[42] at the pyramid edges of the micro-hardness indentations on Figure 7.

Sampling Parameters: Load (F): 100 Newton
 Load time: 10 seconds

Vickers hardness values:

Al_5Fe_2 : $935 \pm 8 \text{ HV } 0,1$
 Al_3Fe : $765 \pm 11 \text{ HV } 0,1$

The results obtained correspond well with values from the literature.^[43]

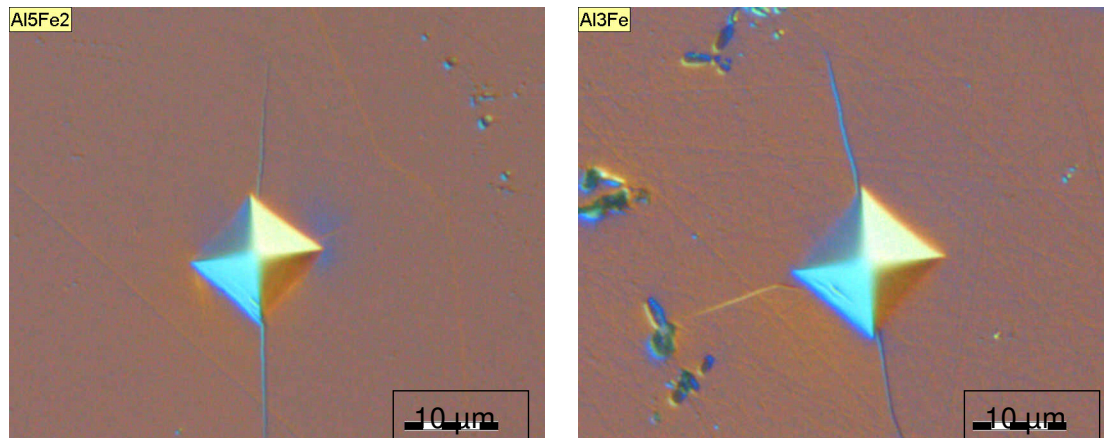


Figure 7: Measurement of micro-hardness: a) Al_5Fe_2 and b) Al_3Fe

3.2 Gravity Casting using defined Mass Ratios

Using form industrial gravity casting conditions, the experiments should show until which mass ratio of liquid pure aluminum and solid low alloyed steel (material number 1.0226) intermetallic phases. For this purpose, steel cubes were recast with aluminum.

Aim of these trials is to find out at which mass ratio between aluminum and steel an interface formation happens and what kind of intermetallics form. Due to the relatively low heat conductivity of steel compared to aluminum, a higher surface temperature of the smaller steel cubes compared to the larger one is expected. Furthermore less heat is absorbed by smaller steel cubes. These factors should lead to a wider intermetallic phase zone (IMPZ) at the Al-Fe interface.

For the trial aluminum with a purity of 99,97 % was melted and kept at a temperature of 700°C. The steel cubes were lowered into the die via a 0,5 mm thick iron wire so they were hanging freely in the middle of the die, which was itself a hollow steel cube with an open top having 100 mm edge length (volume of 1 l). The steel cube was hanging in the middle at a height of 50 mm – half of the side length and could be recast on all faces. A schematic of the experimental setup is depicted in Figure 8.

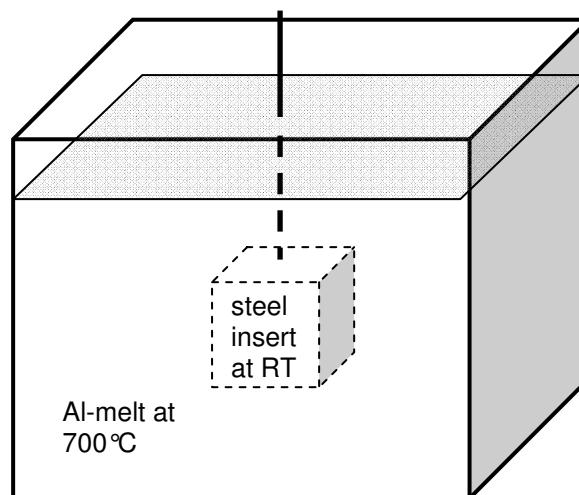


Figure 8: Schematic of setup for recasting of steel with aluminum at different mass ratios

Two of the cubes had thermocouples installed as well to record the cooling curve. These cubes were the one with Fe-Al mass ratio 1:1 and 1:50. Seven different mass ratios were cast as shown in Table 2.

Table 2: Mass ratio of steel to aluminum

mass ratio	side length steel cube mm	weight steel g	weight aluminum g
1:1	62.7	1921.7	1921.7
1:2	52.0	1095.9	2191.7
1:5	39.4	478.7	2393.5
1:10	31.6	246.9	2469.3
1:15	27.7	166.4	2495.6
1:25	23.5	100.7	2517.1
1:50	18.7	50.7	2533.4

At the beginning of the experiment, the steel cube had a temperature of 25°C, the aluminum 700°C and the die temperature was between 250°C and 300°C. After cooling, the composite was cut in four parts. In every quarter, a steel part was embedded as it can be seen in Figure 9.

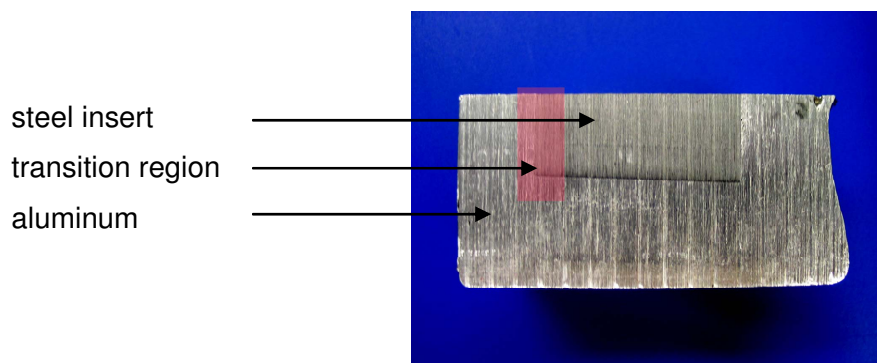


Figure 9: Quarter of a sample of steel recast with aluminum

Figure 10 shows the cooling curve and rate during the cooling of the smallest (18,7 mm, blue line, mass ratio Fe-Al 1:50) and the largest steel cube (62.7 mm, red line, mass ratio Fe-Al 1:1). It can be noticed that the small cube maintains a high temperature (which is 660°C, the melting temperature of pure aluminum) for a longer time (3 min) than the large cube which absorbs so much heat out of the aluminum that the system cools down rapidly. The two lines (light blue and orange) indicate the cooling rate (at the secondary y-axis) in °C/s. A maximum cooling rate can be observed, which is much larger with the big mass of the large steel cube. Once the temperature of the melt equalizes in the die, the cooling rate evens out at a low level.

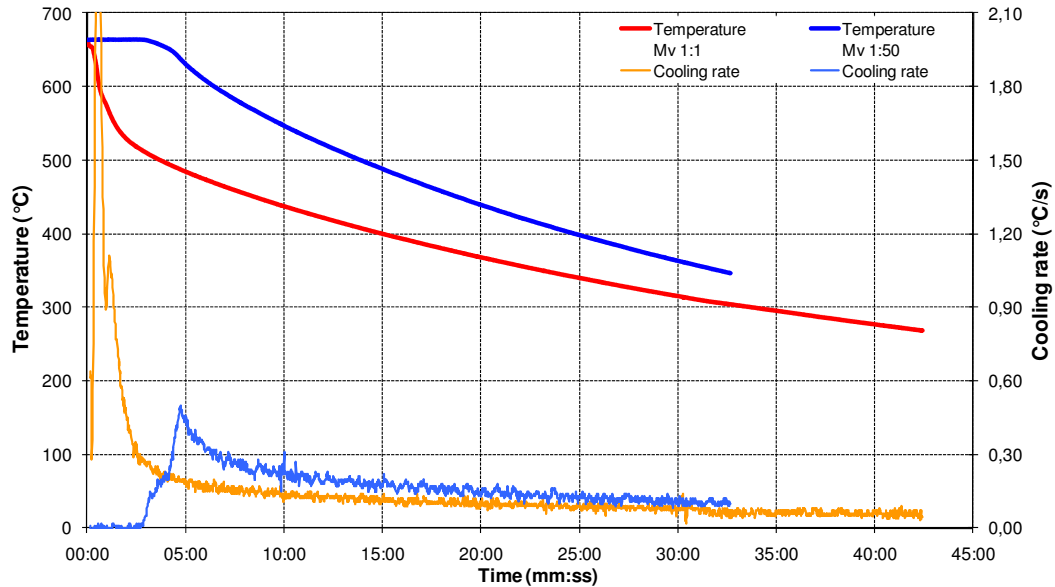


Figure 10: Cooling curve and cooling rates of steel cubes recast with aluminum

3.3 Wetting Experiments

The wetting experiments were conducted using an experimental setup depicted in Figure 11. The system is gas tight and runs under different atmospheres as well as under vacuum. In a horizontal furnace (Lindberg Blue M) a quartz glass cylinder was inserted. A mild steel plate of size 30 mm x 15 mm x 2 mm (material number 1.0226) was placed inside and serves as the substrate. Small amounts (about 2 g) of aluminum or its binary alloys were placed inside a quartz glass syringe. The system was heated to 600°C and then kept for two minutes to allow any volatile substances to disappear. Then the arrangement was heated to 700°C and kept additional 5 minutes for the Al-alloy to melt. After this procedure, part of the liquid Al (about 1 g) was pushed out of the syringe using the steel rod manipulator. In doing so, any oxide of the aluminum was stripped off. When the Al-alloy had contact with the steel plate for 10 seconds at the desired temperature, which was 700°C for the first series of experiments, the system was air cooled to room temperature.

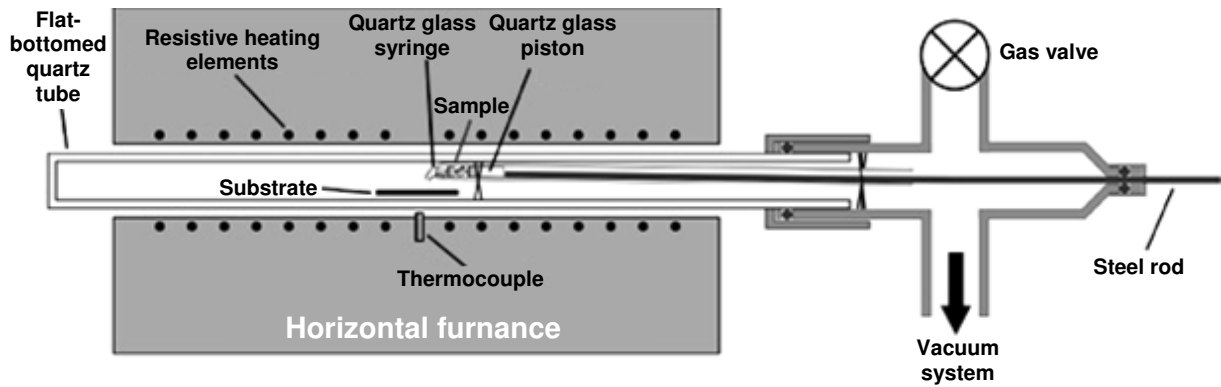


Figure 11: Experimental setup for wetting experiments

At first, inert gas (Argon 5.6 and 6.0, and Ar with 7 % H₂) was used. But since oxidation of the steel plate could still be observed and the wetting mechanism of Al was reduced, the wetting procedure was finally performed under high vacuum ($5 \cdot 10^{-3}$ Pa) using an ABB turbo vacuum pump. The heating curve and the experimental procedure are shown in Figure 12.

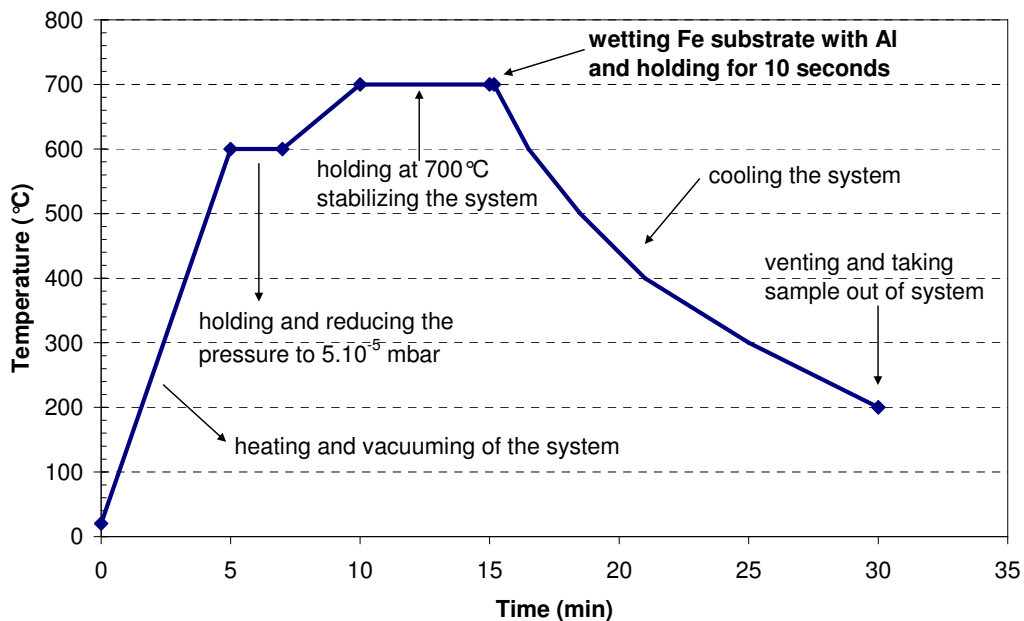


Figure 12: Temperature profile and experimental procedure of the wetting experiment

3.4 Dipping Experiments

For characterizing and modeling the reaction and diffusion kinetics an experiment had to be designed to understand the speed of the interface formation. Furthermore the tests should be easily conducted in order to start and stop the reaction within a second and be very reproducible to get proper results to work with.

A good way to achieve these goals where dipping experiments: Aim of these experiments is the metallographic assessment of intermetallic phases (IMP) and the intermetallic phase zone (IMPZ) at the interface between the mild steel insert and aluminum and aluminum binary alloys respectively as a function of the exposure time in the melt.

When producing aluminum-steel compounds by means of casting, several different parameters influence the formation of intermetallic phases at the interface^[44, 45], like the surface texture of the steel, the preheating temperature of the insert and the die, the temperature gradient of the interface during casting and the cooling rate of the compound itself. To reduce this large array of parameters that would lead to an unmanageable trial matrix the dipping experiments were always conducted at a constant temperature of 700 °C (isothermal) with the steel strip inserts being always alike. Solely the dipping time and the composition of the aluminum melt were varied.

For the dipping experiments 300 μm thick steel strips with electrolytic polished surface structure and a 2-3 μm zinc coating for oxidation protection (zinc coated electrodes from the company Kocour) were used. The usage of such thin steel plates ensures immediate heating to the surrounding temperature (Al-melt with 700 °C, measured with a type K thermocouple as outlined in Figure 13a and displayed in Figure 13b) and consequently a quantitative examination of the steel plate thickness reduction as well as the growth of the IMPZ by analyzing the cross-sectional area.

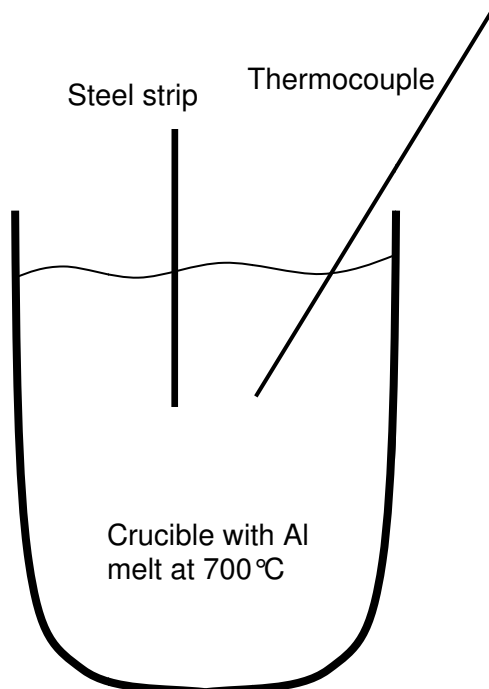


Figure 13: Schematic (a) and real (b) world test setup of dipping experiment with steel strips (ambient temperature) into liquid aluminum at 700 °C

The 100 mm long steel strips with a width of 20 mm were dipped into the melt and after withdrawal cooled in the air at room temperature. For tracking the growth of the IMPZ with time for each time a new strip was dipped. The following dip times were used: 2, 5, 10, 15, 30, 60 und 120 seconds. For Al-Si alloys additional dip times where 1, 20, 45, 90, 180, 240 and 300 seconds as seen in Figure 14. These supplementary dip times completed the picture, since they where necessary for accounting for the slower interface formation rate.



Figure 14: Steel strips dipped into a binary Al-Si7 alloy with dipping times ranging from 1 s (left) to 300 s (5 min, right)

Since first trials with small, zinc coated steel plates showed encouraging results with regard to reproducible results of the growth of intermetallic phases at the interface, the trials were made not only with pure Al99.7, but also with Al-7Mg, Al-7Zn, Al-7Cu as well as Al-7Si, Al-12Si, Al-17Si and even the commercial alloys AlSi7Mg0.3 and AlMg5Si2Mn.

3.5 Real World Castings

To transfer the findings to the industrial environment squeeze casting (SQC) was applied. This process is similar to high pressure die casting (HPDC)^[46, 47] with two differences: a) the plunger speed is slower (about 0,5 m/s compared to 4 m/s using HPDC) and b) the shot sleeve is vertical, allowing for laminar melt flow from bottom to top. This process is generally used for high performance castings^[48] with little to no air entrapment and therefore well suited for the experiments.

The machine, an UBE HVSC (horizontal die movement, vertical shot sleeve) with 350 t clamping force, is depicted in Figure 15.



Figure 15: UBE HVSC 350 t squeeze casting (SCQ) machine with dosing robot

As a die a so called step die with decreasing wall thickness was employed. The resulting cast part with its dimensions is outlined in Figure 16 (here without insert). For compound casting low alloyed steel inserts were placed in the middle of the 14 mm step as depicted in Figure 17. At the first batch the steel inserts were pickled in 10 % HCl for 1 min and then immediately inserted and recast. The second test batch was Zn-coated (galvanic coating with a thickness of 5 μm).

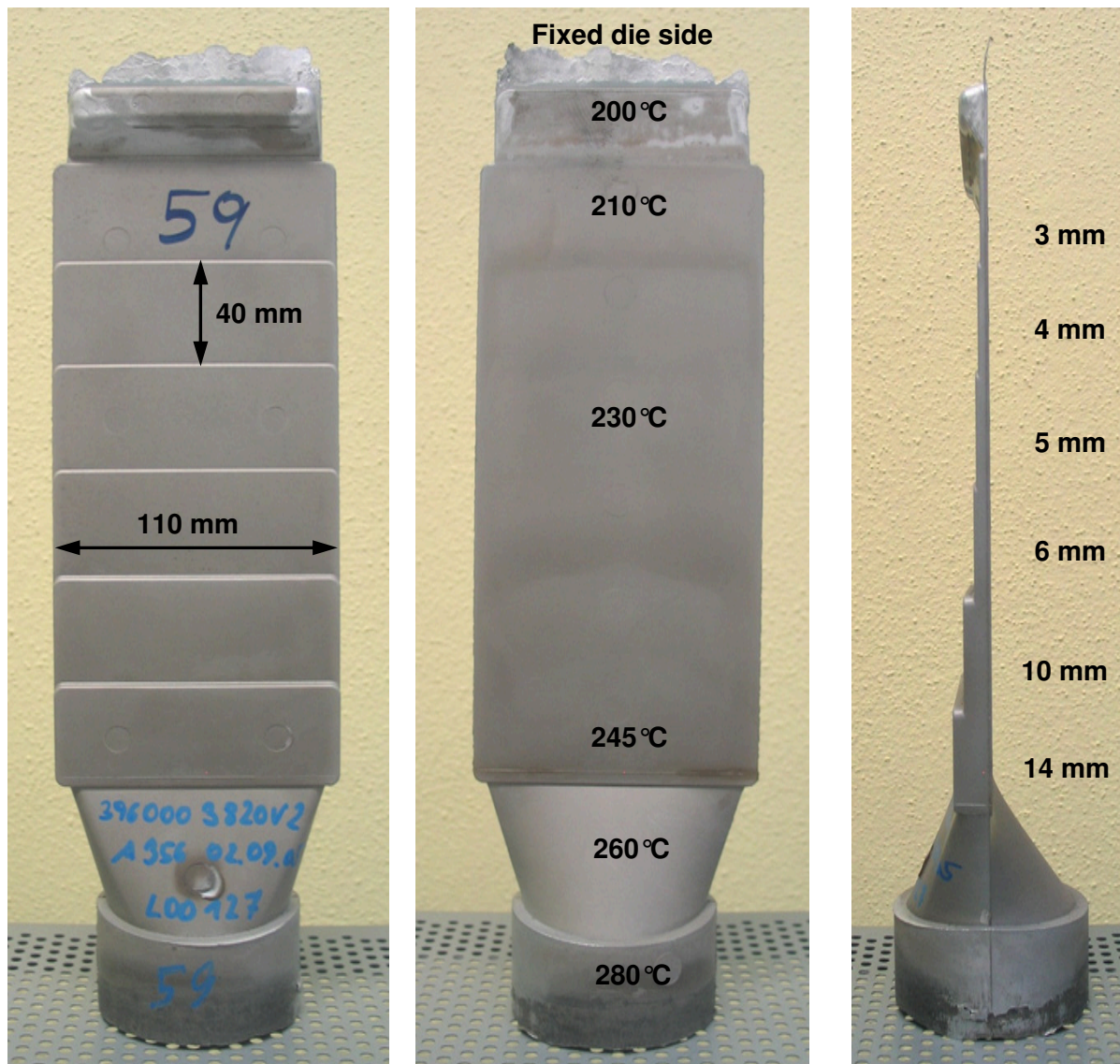


Figure 16: Dimensions of step die casting (without insert)

Aim of these trials was the characterization of the aluminum-iron interface and the identification of emerging faces in an industrial environment. Besides pure 99.7Al the following binary alloys were tested: Al-7Si, Al-7Mg, Al-7Zn and Al-7Cu.

The melt temperature for the casting was set to $700^{\circ}\text{C} \pm 7^{\circ}\text{C}$ and the steel insert was dry and at room temperature, but heated up quickly to die temperature (which was 245°C as described in Figure 16). The time from inserting the steel part to the casting procedure itself is approximately 8-10 seconds (die closing, shot sleeve swinging into place and docking, casting).

For each material combination five parts were cast. As can be seen in Figure 17, the low mass ratio of aluminum to the insert is not favorable for a good joint (less than 1:1). Furthermore the steel oxidized immediately upon inserting it in the die (like blue annealing)^[49] which additionally contradicted any chemical bonding. This proved to be true for the non-

coated steel inserts as 99.7Al-Fe was the only combination that exhibited an intermetallic layer at the interface. The other samples had no chemical bonding at all and separated during the casting procedure.

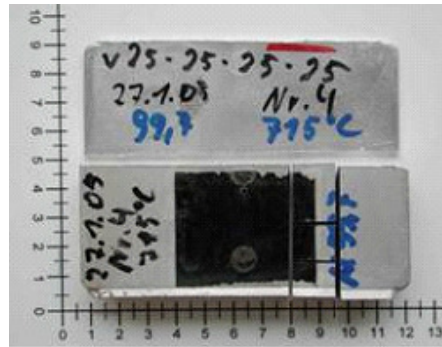


Figure 17: Position of the steel insert at the 14 mm thick step

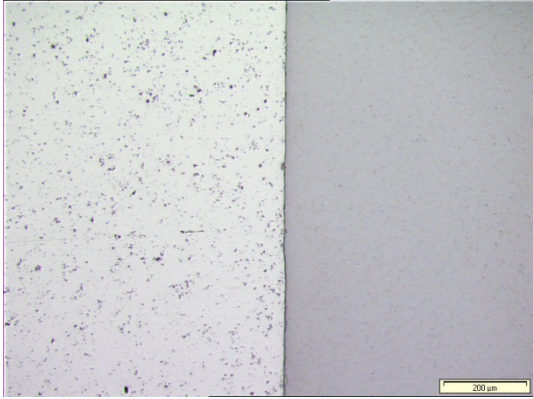
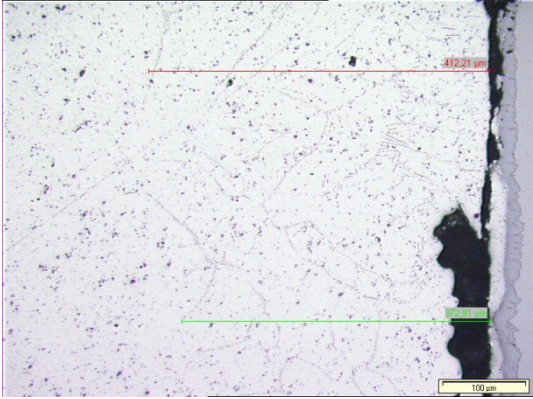
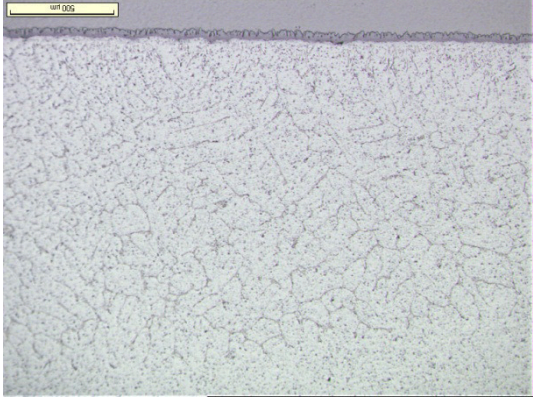
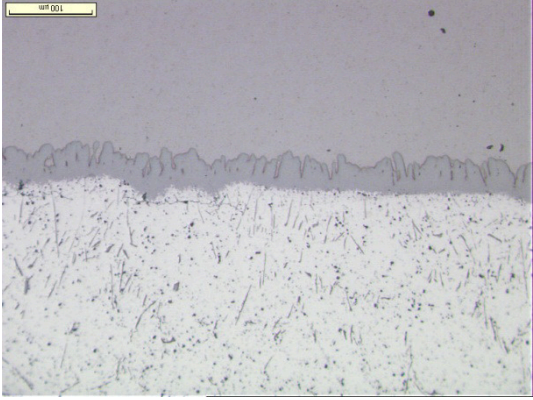
4. Practical Experiments and Metallographic Evaluation

The results of the experiments were investigated using either conventional polishing procedures and light microscopy^[50] or, most of the time, ionic pickling and scanning electron microscopy (SEM) with energy dispersive X-ray analysis (EDX).

4.1 Gravity Casting using defined Mass Ratios

First a light microscopical investigation of the gravity castings was performed to make a first evaluation of the interface. As can be seen in Table 3 there was in general a chemical bonding, at least for the high mass ratios (Fe-Al better than 1:10) However, the intermetallics at the interface are very brittle as they broke during the cutting process.

Table 3: Cube experiments: the metallographic comparison of Fe-Al ratios 1:50 and 1:15 show that with increasing steel mass compared to aluminum melt the chemical bonding of the interface decreases (Trial 1), whereas with high mass ratios there is a continuous intermetallic layer.

Trial Nr.	Ratio	Zoom	Zone	Trial Nr.	Ratio	Zoom	Zone
1	1:50	100x	Diffusion layer	1	1:50	200x	Diffusion layer
							
4	1:15	50x	Diffusion layer	4	1:15	200x	Diffusion layer
							

To analyze the influence of the Al-Fe mass ratio on the formation of the intermetallic phase zone at the interface layer between aluminum and steel, cross-section polishes were made and afterwards etched via focused ion beam (FIB), firstly to remove any polishing artifacts from the section, secondly to better show the pattern of the microstructure in the steel as well as in the intermetallic phases.^[51, 52]

As it turned out, all samples with a mass ratio of Al to Fe < 10:1 had a very low connection within the compound casting and most of them even separated during the cutting procedure. Just the composite casting with smaller steel cubes (Al to Fe ratio > 10:1) had an intermetallic connection that was strong enough to withstand the polishing procedure. Figure 18 to Figure 25 represent the results of the SEM investigations of the Al-Fe interface of these samples.

At first the experiments with a mass ratio of Fe-Al 1:50 were investigated. As can be seen below a good intermetallic connection could be obtained.

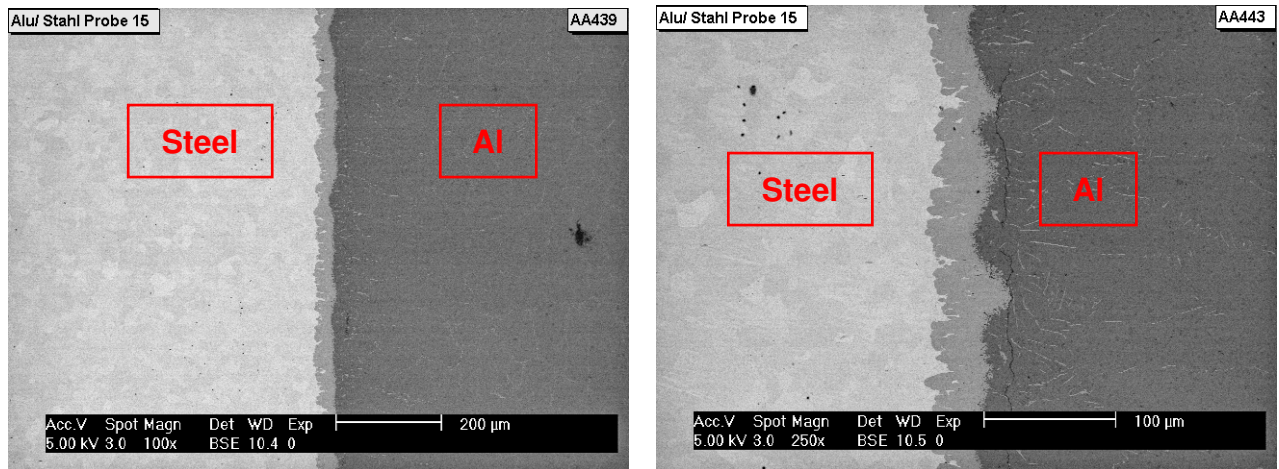


Figure 18: Mass ratio Fe-Al 1:50: Al-Fe phase over the whole profile, vermicular Al-Fe phase visible in the aluminum

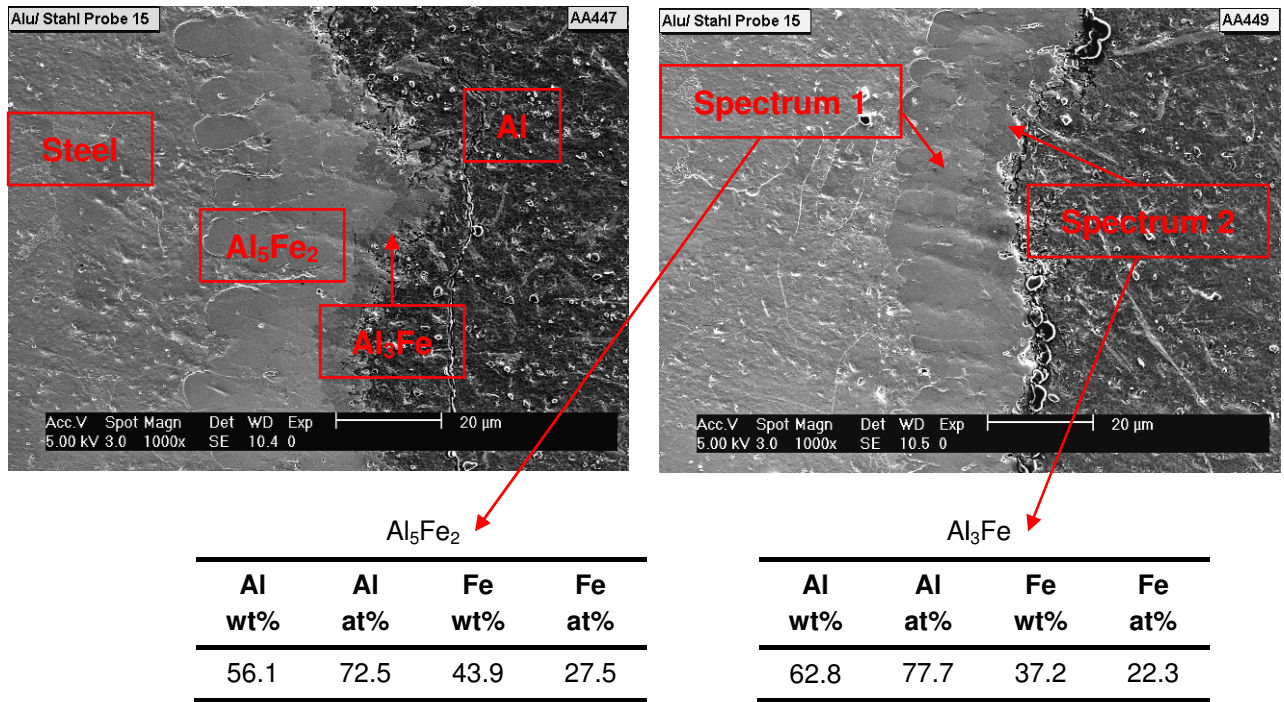


Figure 19: Mass ratio Fe-Al 1:50: Boundary layer steel/aluminum, EDX analyses from the intermetallic phase agrees with the results of the standards; The phase turned towards the aluminum could be identified as Al_3Fe , the phase turned towards the steel as Al_5Fe_2 (EDX analyses at 20 kV)

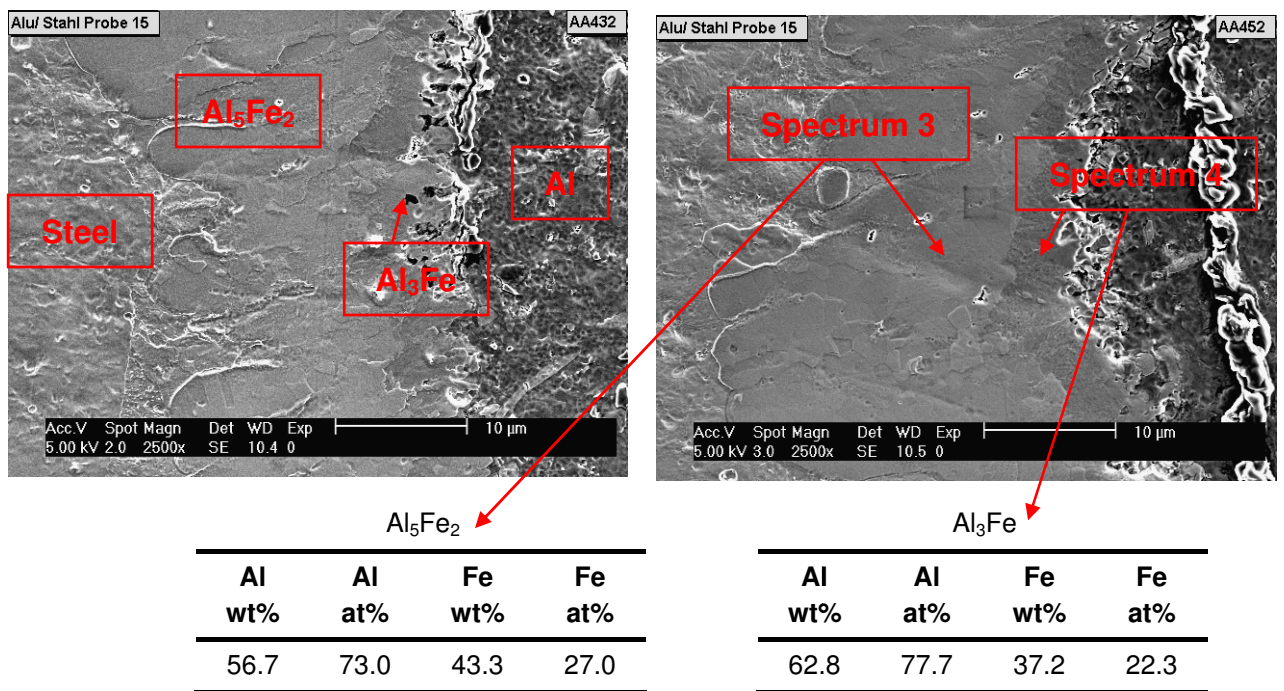


Figure 20: Mass ratio Fe-Al 1:50: Boundary layer steel/aluminum, EDX analyses from the intermetallic phase agrees with the results of the standards (EDX analyses at 20 kV)

The experiments with a mass ratio of Fe-Al 1:25 show a similar behavior as can be seen in Figures 21 to 25. However, a good intermetallic connection could not always be obtained.

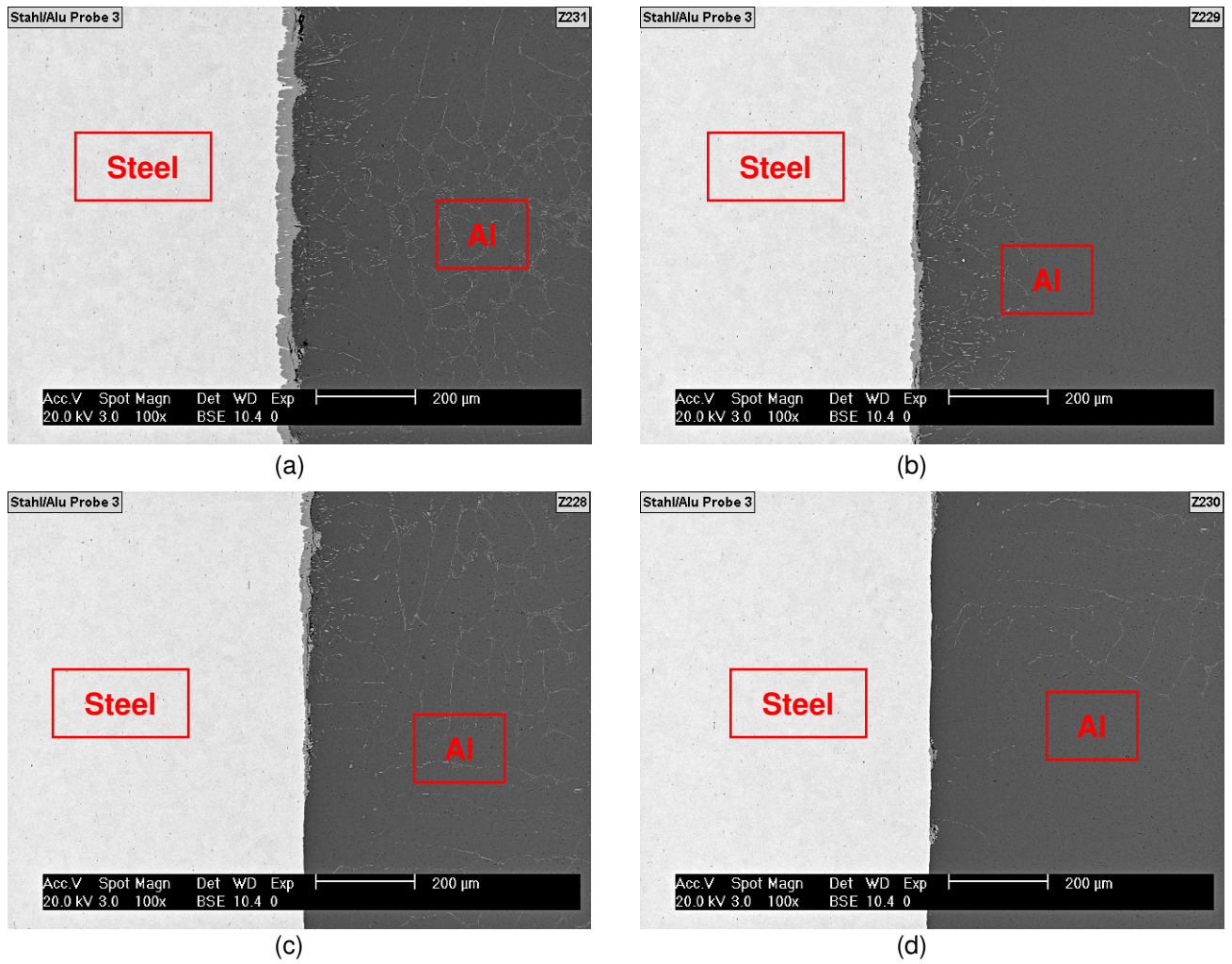


Figure 21: Mass ratio Fe-Al 1:25: Overview boundary layer Steel/Al, different thick developed intermetallic phases, in some areas are no intermetallic phases at the boundary layer (thickness of the intermetallic phase decrease from (a) to (d))

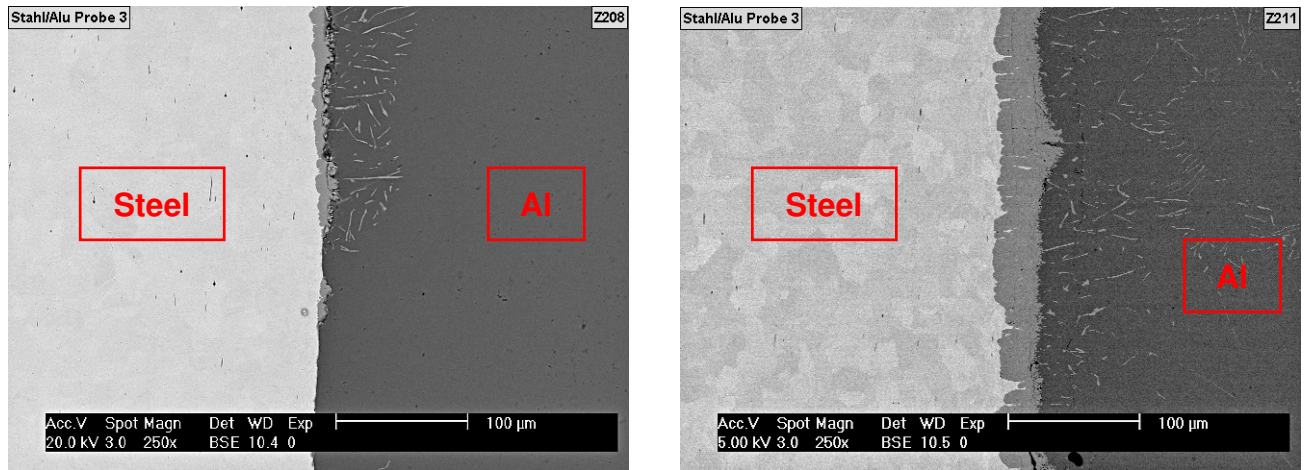


Figure 22: Mass ratio Fe-Al 1:25: Overview boundary layer Steel/Al, different thick developed intermetallic phases; In the area at the boundary layer developed intermetallic phase, the phase extend bacillary into the Al-matrix.

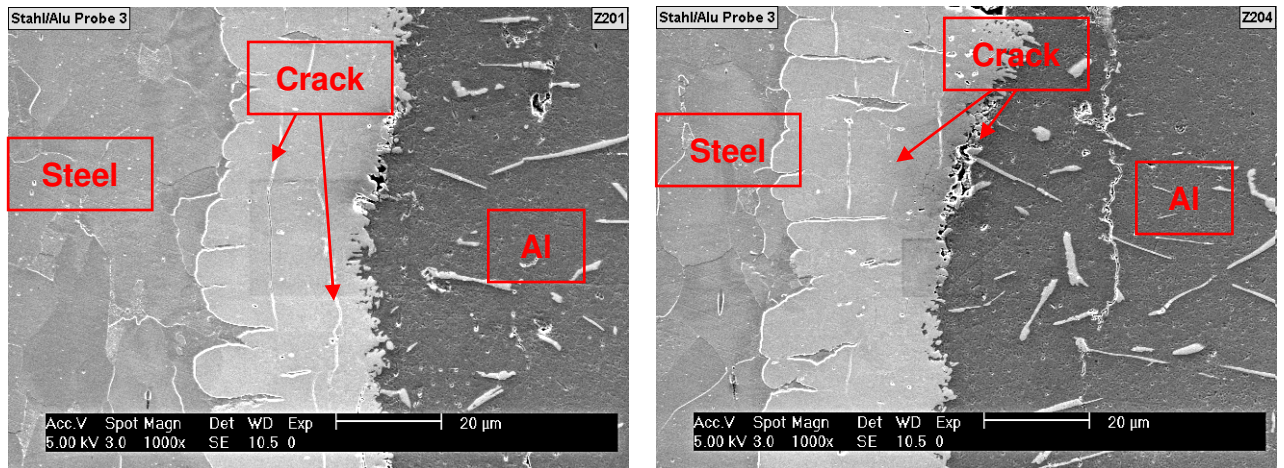


Figure 23: Mass ratio Fe-Al 1:25: Detectable cracks in the intermetallic phase

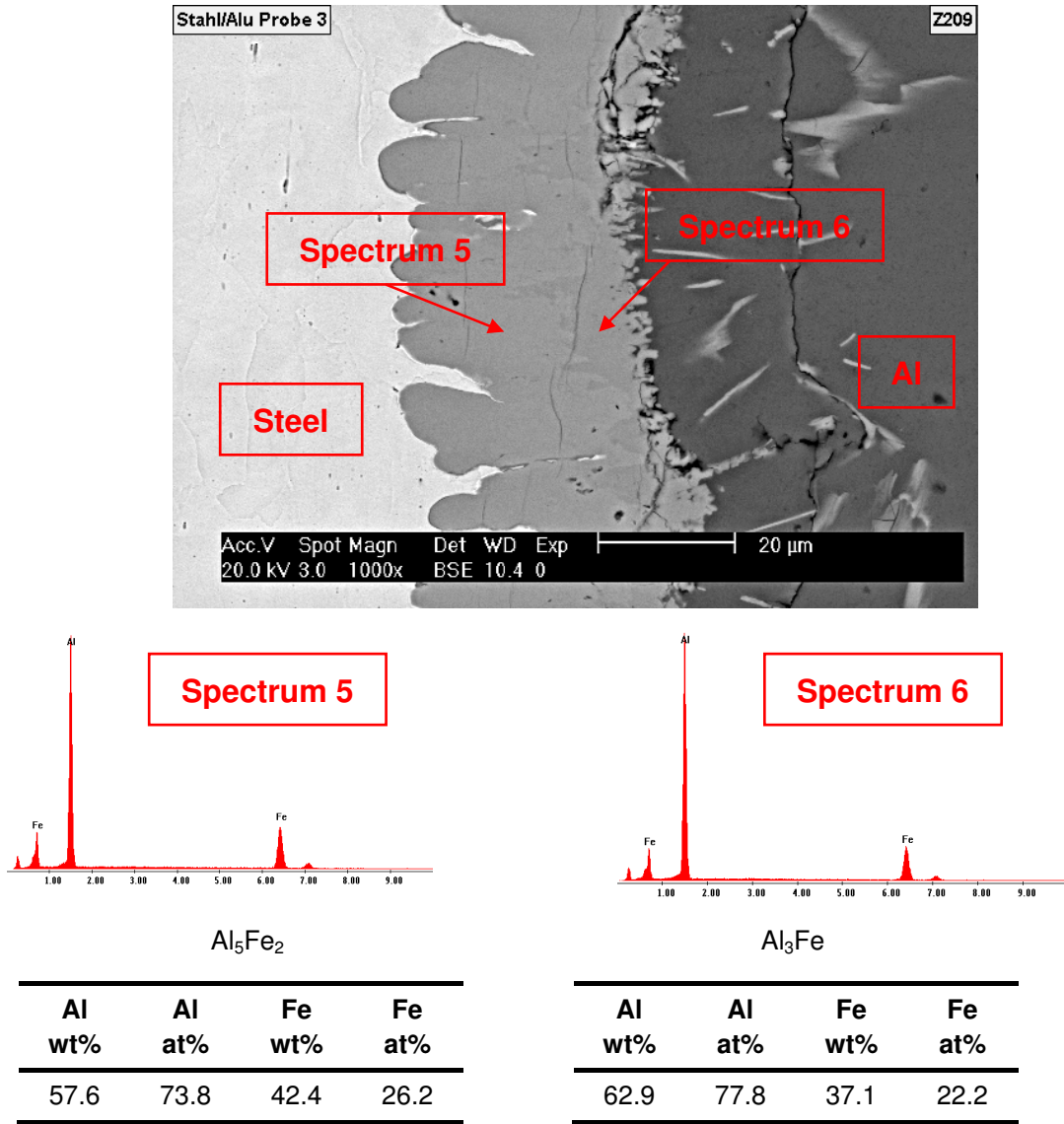


Figure 24: Mass ratio Fe-Al 1:25: At the boundary layer steel/Al two intermetallic phases form (Al_5Fe_2 towards steel, Al_3Fe towards Al); These two phases have different contrasts in the BSE-Picture (the phase with more aluminum is a little bit darker); EDX analyses at 20 kV

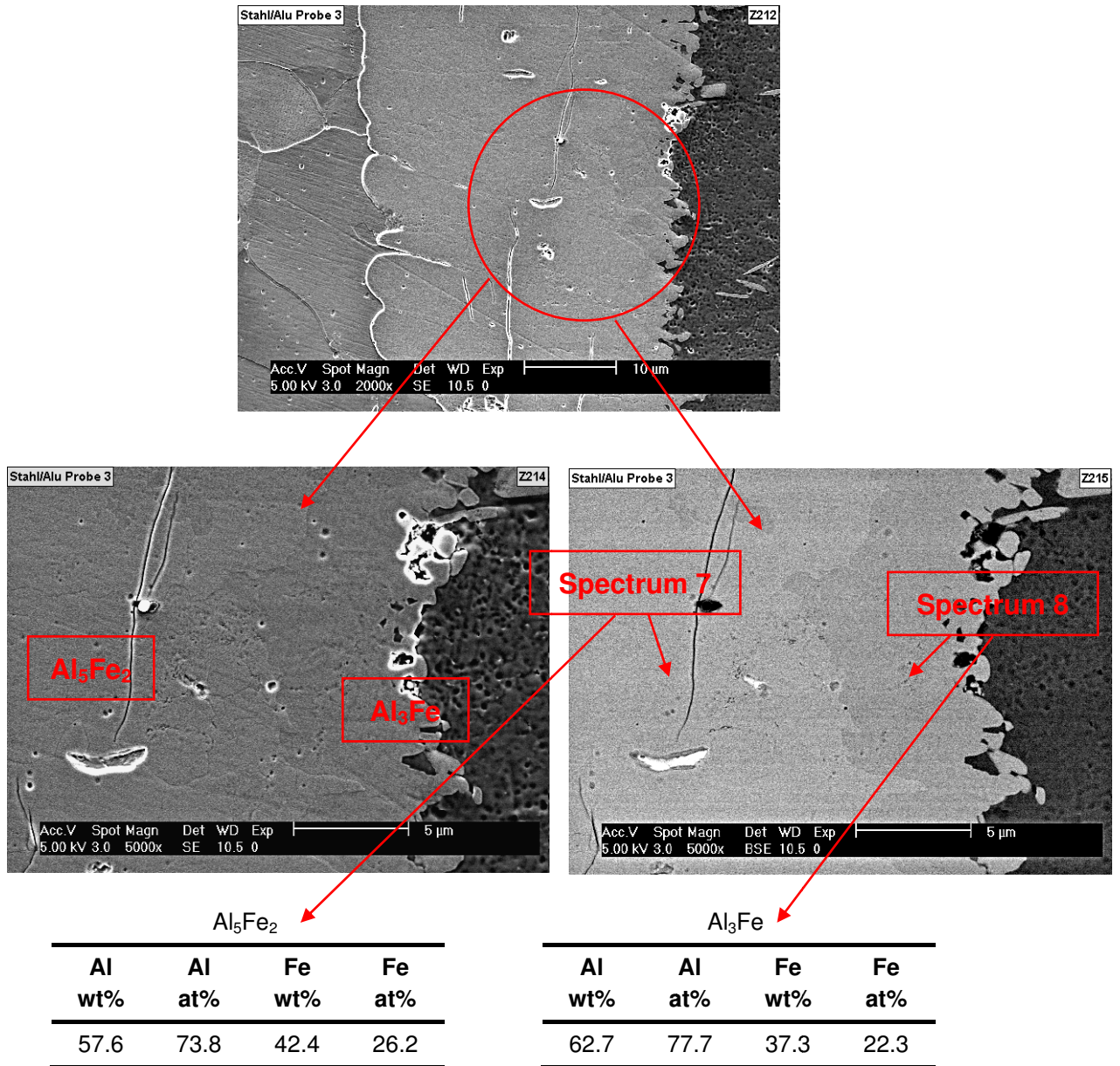


Figure 25: Mass ratio Fe-Al 1:25: Analyses of the boundary layer

At the Al-Fe interface two different intermetallic phases can be observed: Al₅Fe₂ at the boundary to the steel insert and Al₃Fe at the boundary of the recast aluminum. While Al₃Fe at the edge to Al appears "unraveled", Al₅Fe₂ at the edge to the steel insert looks "smoother".

For Figure 26 to Figure 31 below on the left SE-electrons were detected, for the image below on the right back scattered electrons were used to increase contrast (elementary contrast, the aluminum rich phase appears darker). The EDX-analysis was performed with 20 kV.

The experiments with a mass ratio of Fe-Al 1:15 show a similar behavior than the experiments with a mass ratio of Fe-Al 1:25 as Figures 26 to 31 depict.

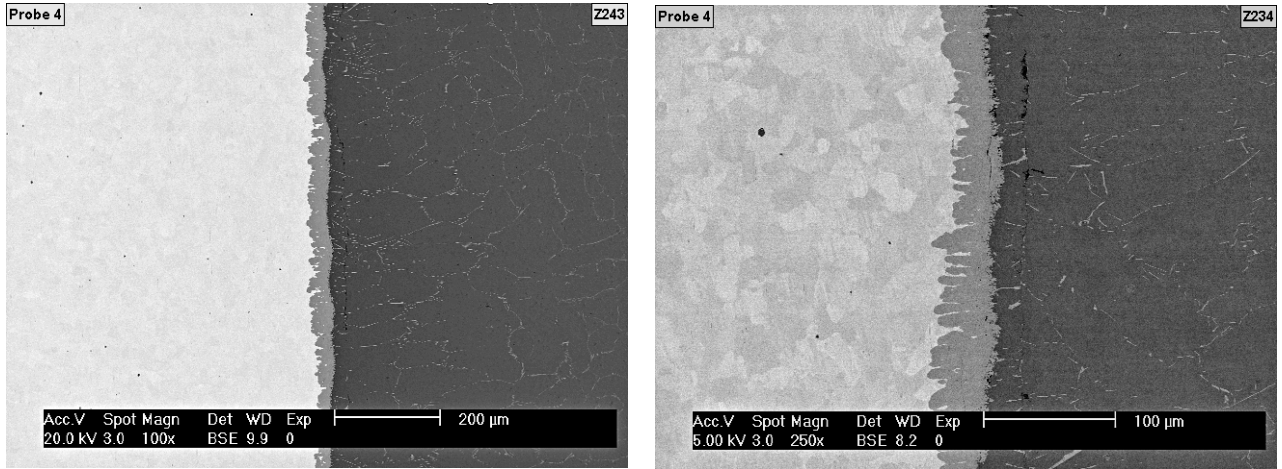


Figure 26: Mass ratio Fe-Al 1:15: Overview, bacillary Al-Fe intermetallics in Al-melt

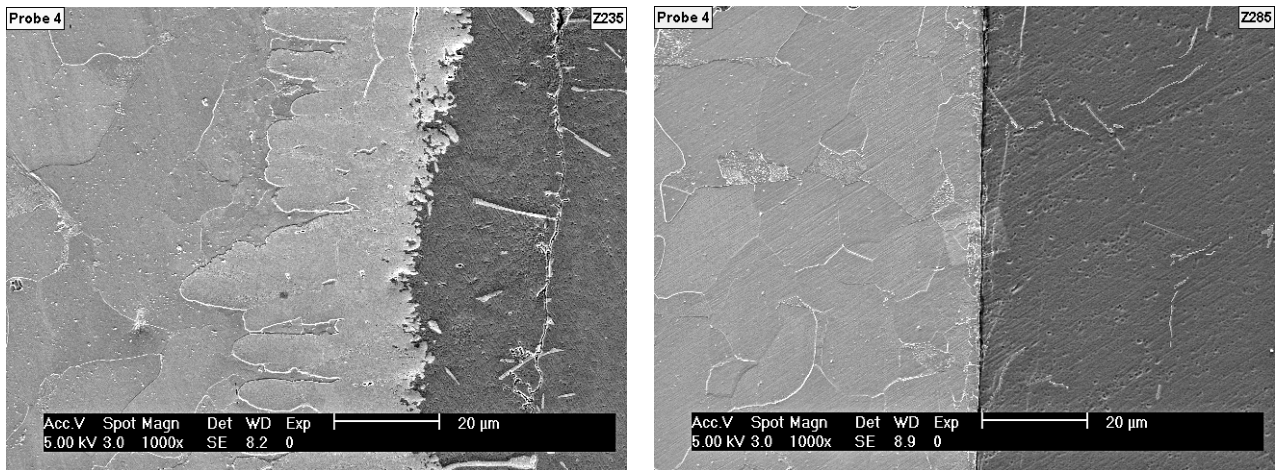
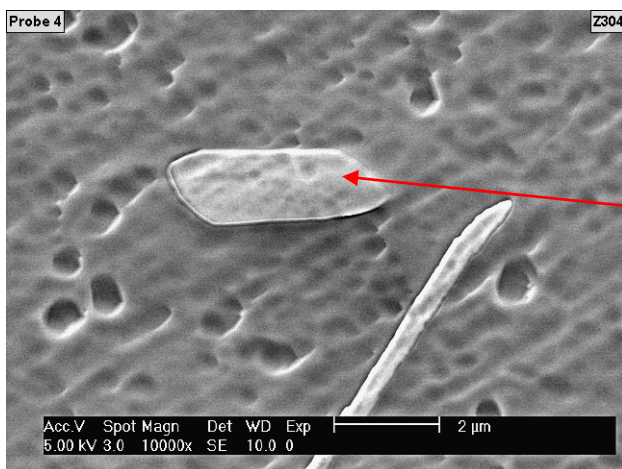


Figure 27: Mass ratio Fe-Al 1:15: Intermetallic phases not developed over the whole profile (no phase in the right picture)



Al ₃ Fe			
Al wt%	Al at%	Fe wt%	Fe at%
55,2	71,8	44,8	28,2

Figure 28: Mass ratio Fe-Al 1:15: Al-Fe-particle in Al-matrix + EDX analysis (at 5 kV) shows Al₃Fe

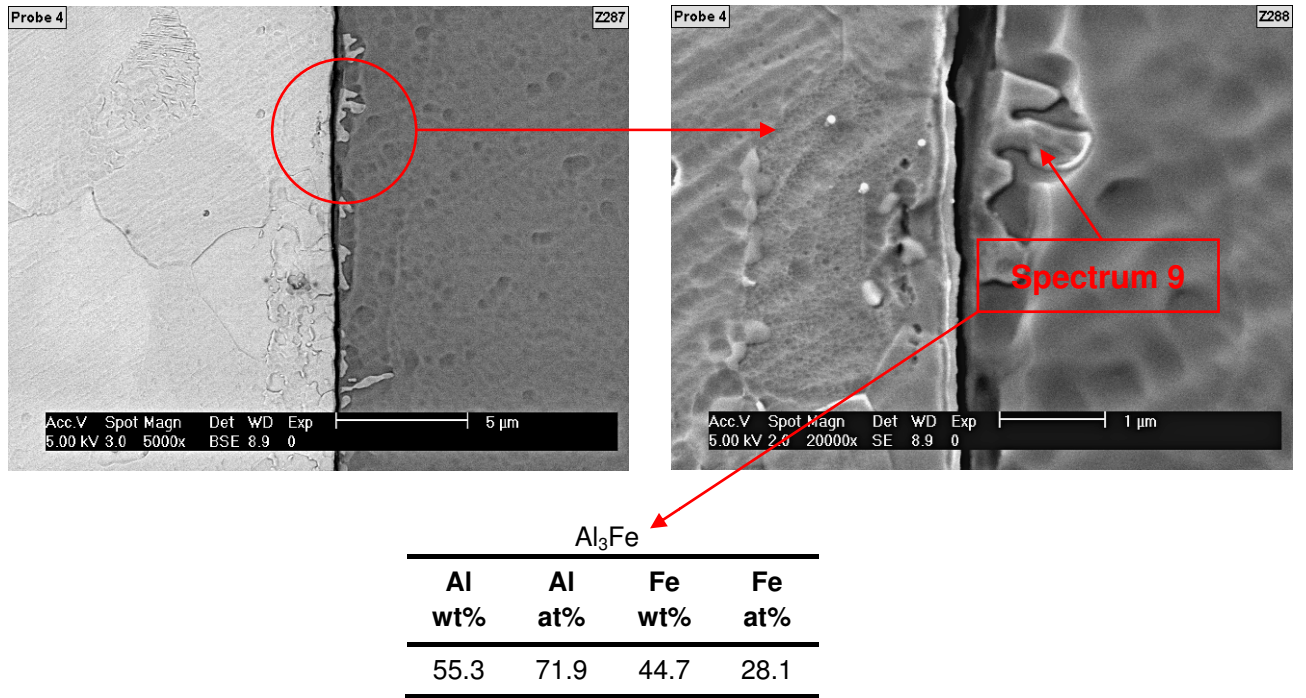
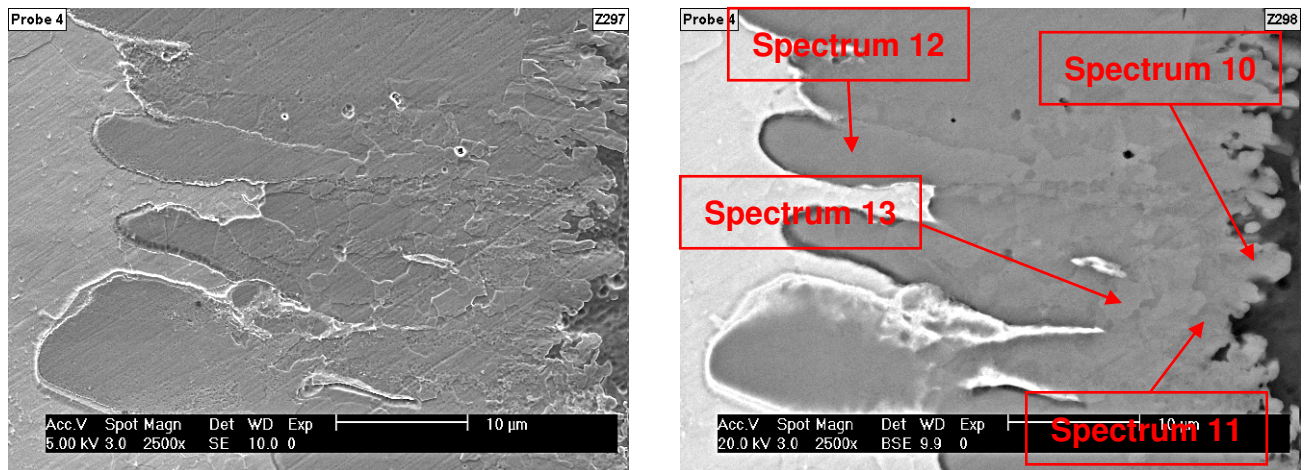


Figure 29: Mass ratio Fe-Al 1:15: In some areas at the boundary layer Steel/Al the Al_3Fe begins to develop (EDX analysis at 5 kV)



Al_5Fe_2 (Spectrum 12)

Al wt%	Al at%	Fe wt%	Fe at%
51.1	68.4	48.9	31.6

Al_5Fe_2 (Spectrum 13)

Al wt%	Al at%	Fe wt%	Fe at%
50.2	67.6	49.8	32.4

Al_3Fe (Spectrum 10)

Al wt%	Al at%	Fe wt%	Fe at%
54.8	71.5	45.2	28.5

Al_3Fe (Spectrum 11)

Al wt%	Al at%	Fe wt%	Fe at%
54.6	71.3	45.4	28.7

Figure 30: Mass ratio Fe-Al 1:15: Visible grain structure in the intermetallic phase: Fine grained structure from Al_3Fe , relative large grain from Al_5Fe_2 ; EDX analysis at 5 kV shows the existence of two phases (Al_5Fe_2 , Al_3Fe)

In the transition region of the steel insert to the intermetallic phase it can be observed, that in some grains the intermetallic phase has not formed completely yet (Figure 31, right image grab using back scattered shows a bright seam at the border of the intermetallic grain). The EDX-analyses were performed with 5 kV (lower penetration depth) and show that in the dark areas of the grain Al_5Fe_2 has formed already, but in the bright seam the Fe-content is still high.

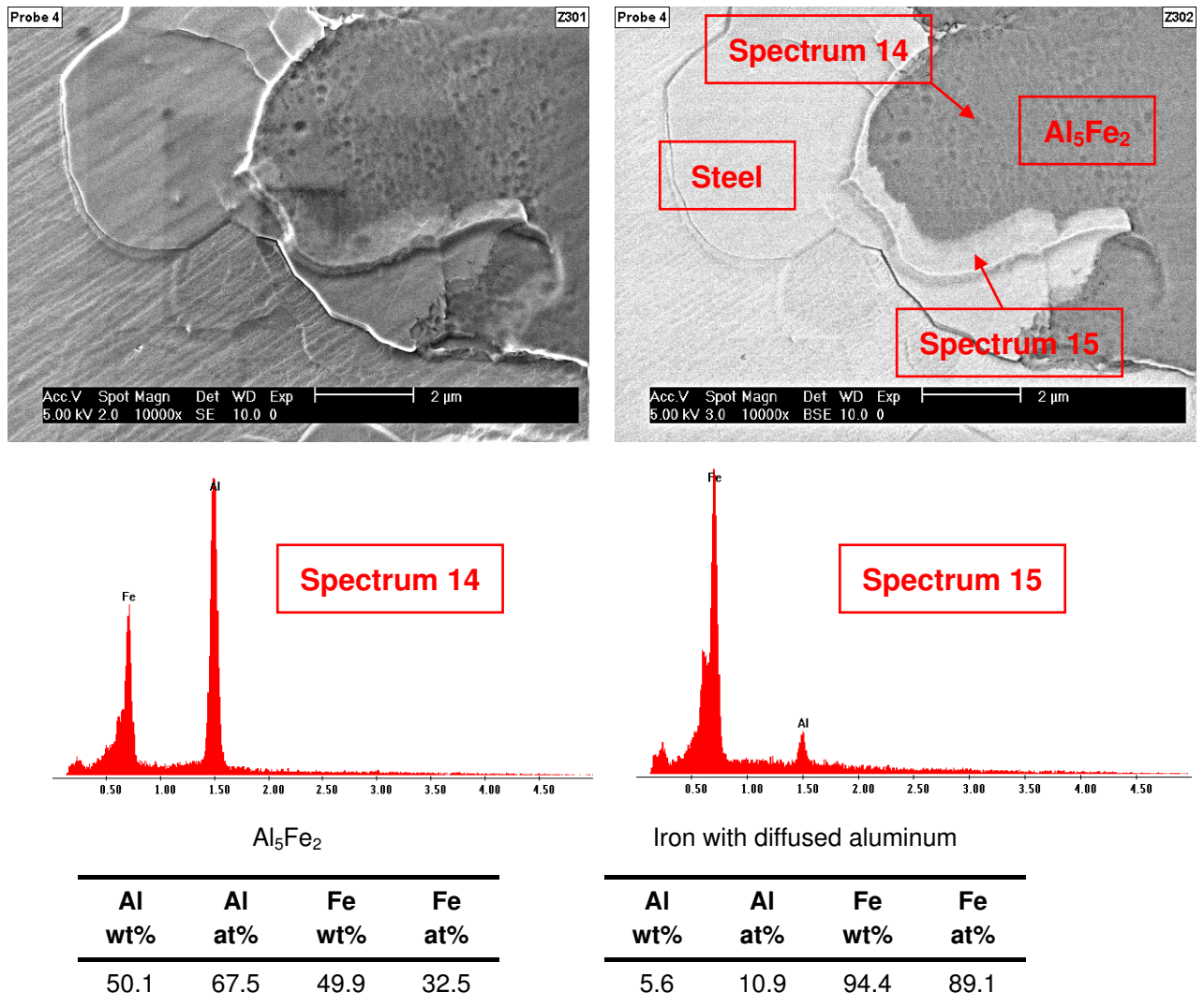


Figure 31: Mass ratio Fe-Al 1:15: Transition region of Fe to Al (intermetallic in grain)

The Fe-Al mass ratio of 1:10 seems to be the border case for chemical bonding with this test as Figures 32 to 34 clearly illustrate. Literally no interface formation can be found along the surface of the insert, but at the edges (where there is more Al surrounding the steel) different contrast at varying acceleration voltage and individual detectors can be observed. The element contrast is more pronounced at IMPZ at 20 kV (Figure 32, lower right image) than with 5 kV (lower left image), however the signal comes from a higher depth which results in a soft border of the grains. SE electrons are better suited for imaging finer details, especially at 5 kV (upper left image).

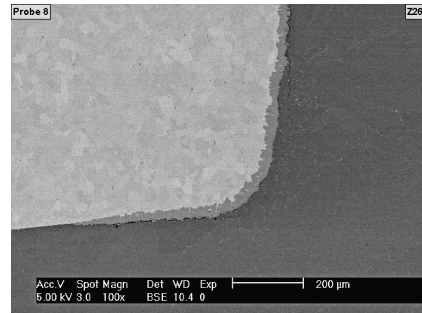


Figure 32: Mass ratio Fe-Al 1:10: Overview, Development of intermetallic phases at the flanges

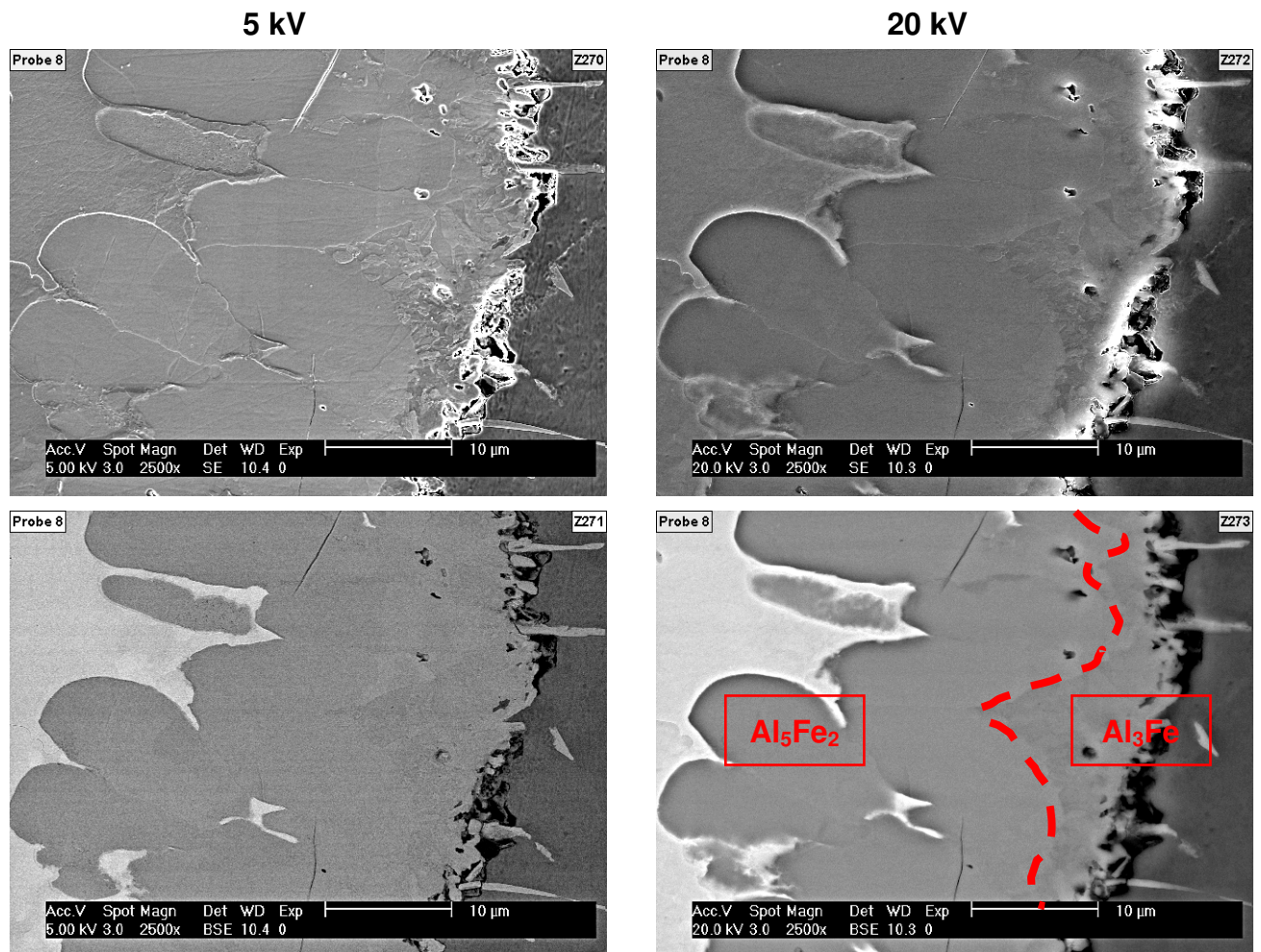
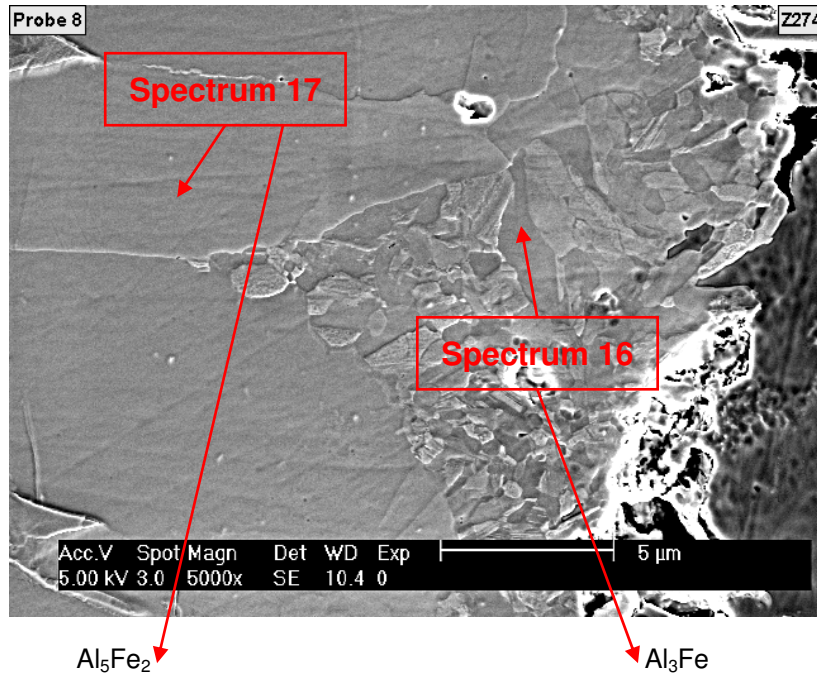


Figure 33: Mass ratio Fe-Al 1:10: Element contrast



Al_5Fe_2

Al wt%	Al at%	Fe wt%	Fe at%
52.0	69.2	48.0	30.8

Al_3Fe

Al wt%	Al at%	Fe wt%	Fe at%
56.2	72.7	43.8	27.3

Figure 34: Mass ratio Fe-Al 1:10: The phase with more aluminum (Al_3Fe) is much finer grained than the phase with less aluminum (Al_5Fe_2)

As has been stated before, at an even lower mass ratio of Fe-Al 1:5 it is similar to Fe-Al 1:10 which confirms that no chemical bonding could be observed with Fe-Al ratios lower than 1:10. The reason for this is the fast cooling rate of the aluminum melt that surrounds to a point, where formation of intermetallic phases is not possible any more. Figures 39 and 40 show the evaluation of the steel insert and it can be seen, that no chemical reaction between the steel insert and the aluminum melt has happened. Some oxides have been found as well, but too few to be the reason for the non-bonding.

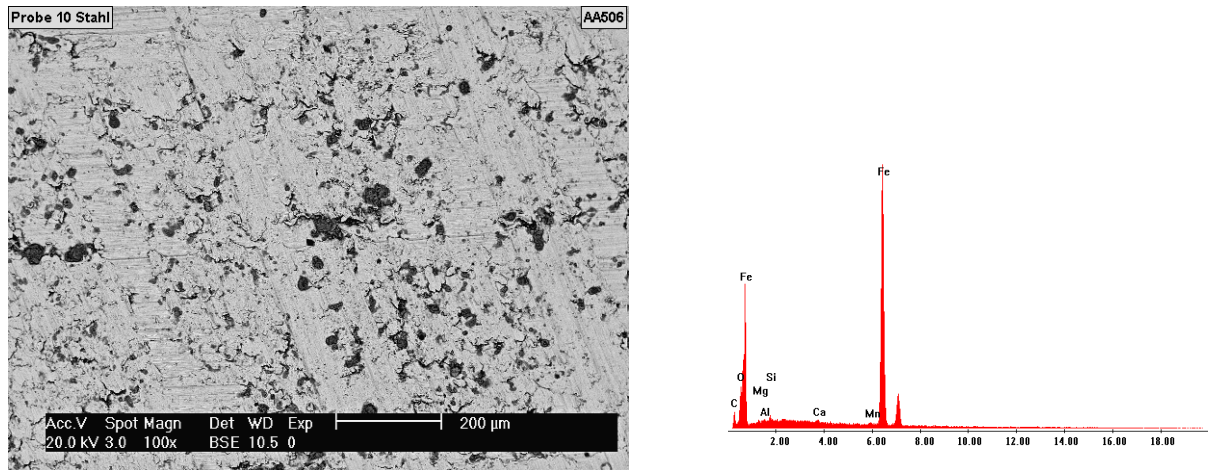


Figure 35: Mass ratio Fe-Al 1:5: BSE picture from the steel surface near the crack + EDX analysis of the whole in the picture displayed area: Hardly any Al detectable.

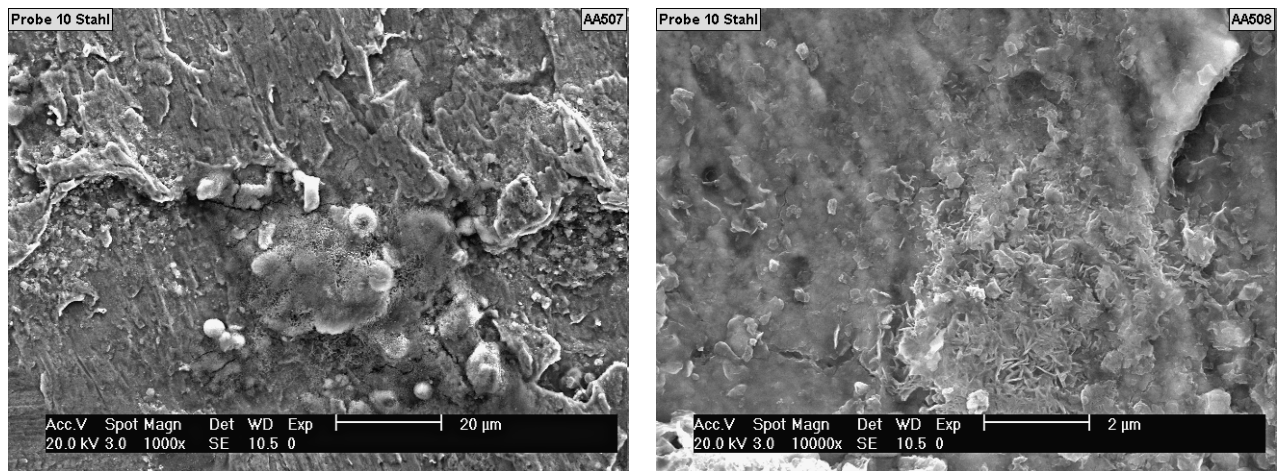


Figure 36: Mass ratio Fe-Al 1:5: SE picture from the steel surface with middle (left) and high (right) magnification; Oxide can be spotted on the surface.

With an even higher Fe-Al ratio of 1:1, no chemical-bonding could be found. This time in addition to the steel insert (Figures 37 and 38), also the recast Al was investigated (Figures 39 and 40) but again, no trace of the other bonding partner (here Fe) could be found.

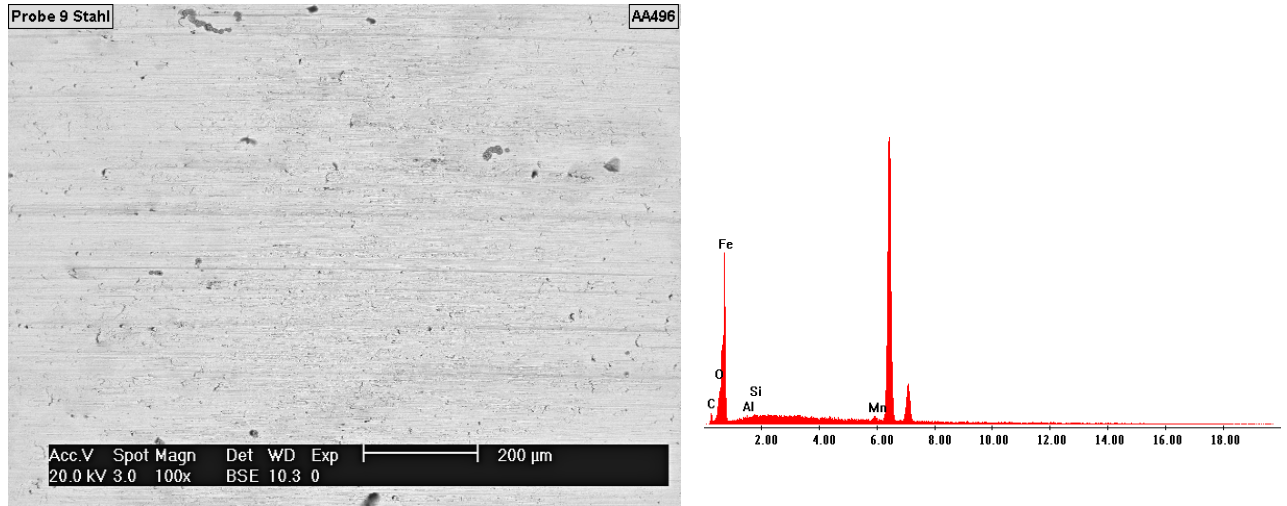


Figure 37: Mass ratio Fe-Al 1:1: BSE picture from the steel surface near the crack + EDX analysis of the whole in the picture displayed area: Hardly Al detectable

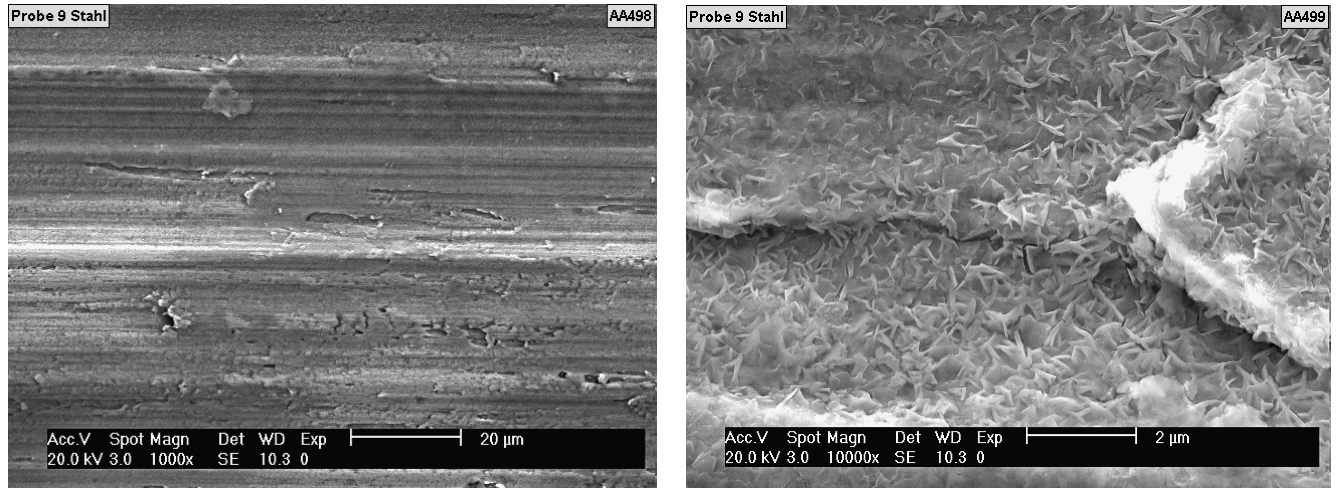


Figure 38: Mass ratio Fe-Al 1:1: SE picture from the steel surface with middle (left) and high (right) magnification

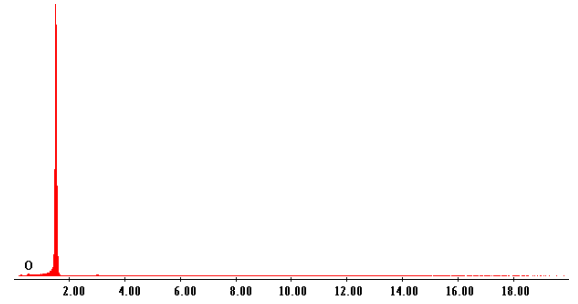
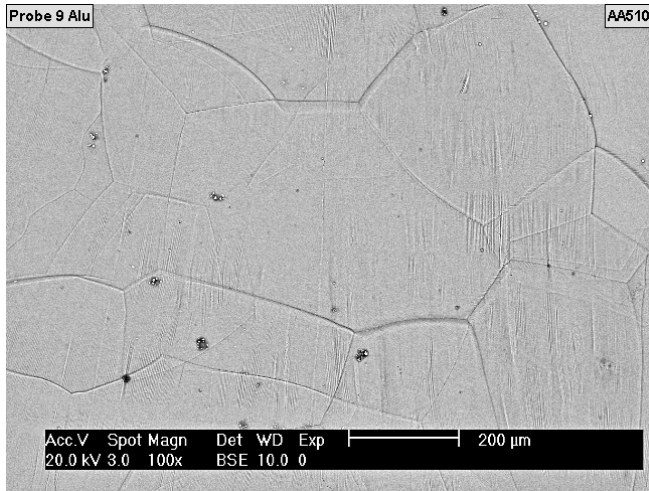


Figure 39: Mass ratio Fe-Al 1:1: BSE picture from the aluminum surface near the crack + EDX analysis of the whole in the picture displayed area: No Fe detectable, just O; Grain boundaries clearly visible

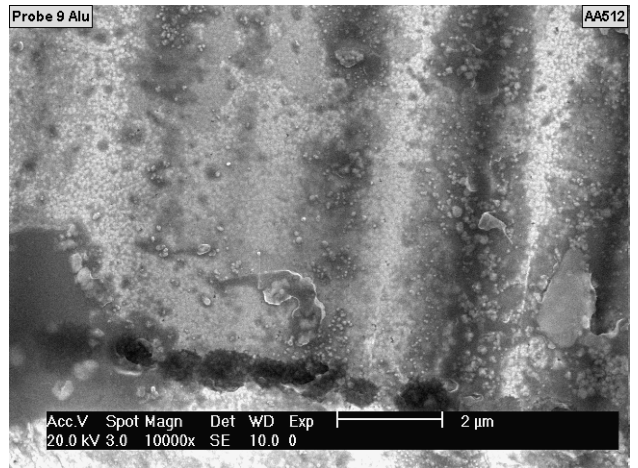
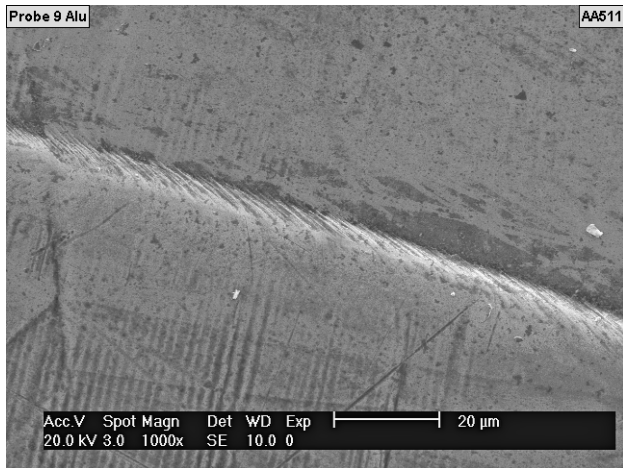


Figure 40: Mass ratio Fe-Al 1:1: SE pictures from the aluminum surface with different magnifications

4.2 Gravity Casting using zinc coated steel cubes in 99.7Al

To find out the difference of interface formation between non-coated and zinc coated steel inserts, last mentioned galvanically Zn-coated (2 μm coating thickness) cubes were used for compound casting with Al-Fe ratios of 1:25, 1:15 and 1:10. To estimate a possible temperature influence of the steel insert on the evolution of the intermetallic phase zone (IMPZ), some samples were pre-heated to 100°C, the others were at room temperature when recast with aluminum, adding up to six pieces.

Again the samples were cast as before and characterized via metallography. The results can be summarized as follows:

- Aluminum steel inserts had a continuous intermetallic interface layer, regardless of the preheating temperature as can be observed in Figure 41.
- The area of the IMPZ correlates to dipping times with zinc-coated steel strips in 99.7Al of around 20 to 30 seconds, independently of the mass ratio or the preheating temperature.
- With careful pretreatment of the inserts (meaning correct pickling and Zn-coating) the influence of the mass ratio Al-Fe is negligible.
- Identification of the phases in the IMPZ showed Al_5Fe_2 at the border to steel and Al_3Fe at the border to aluminum. Compared with the dipping experiments the iron content in the phases is slightly higher (Figure 41).

Room temperature

100 °C

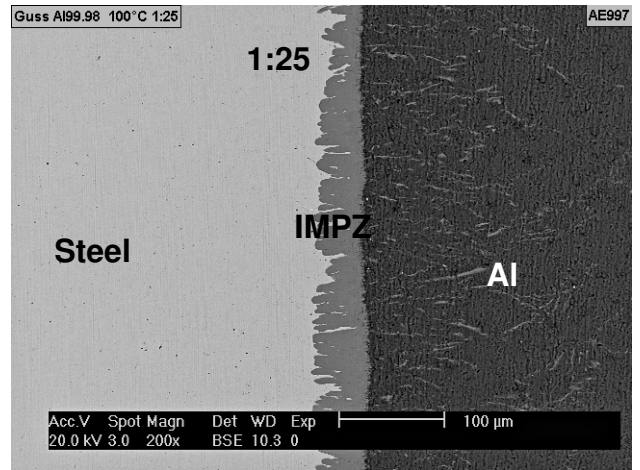
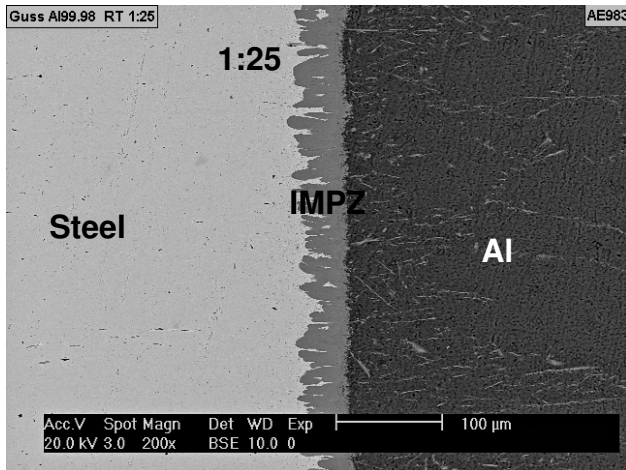
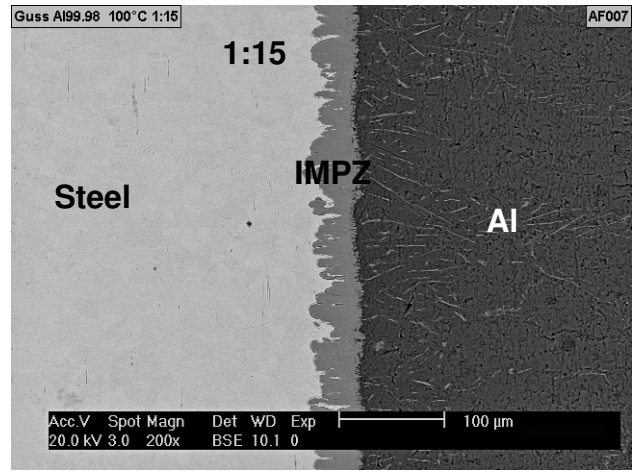
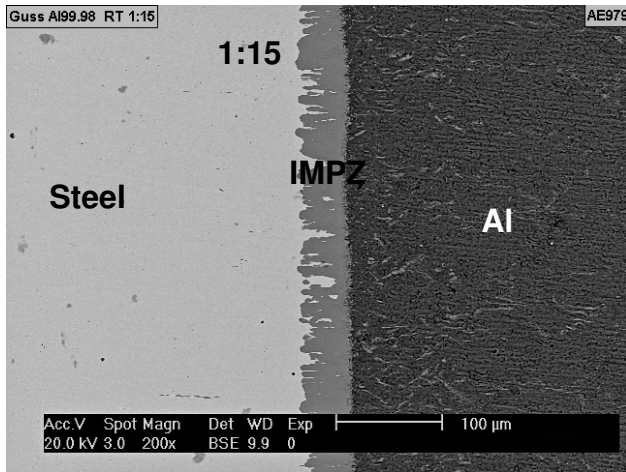
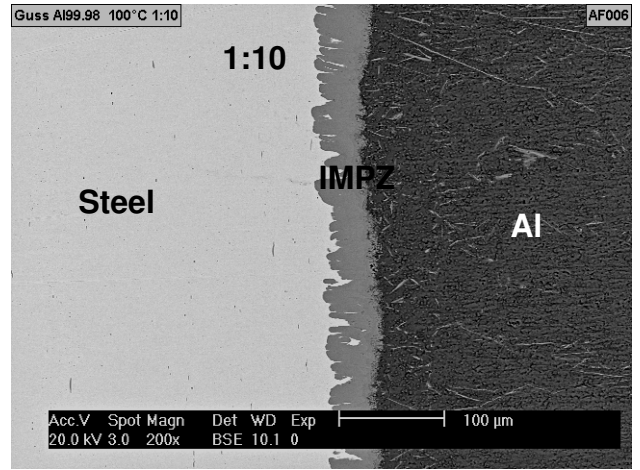
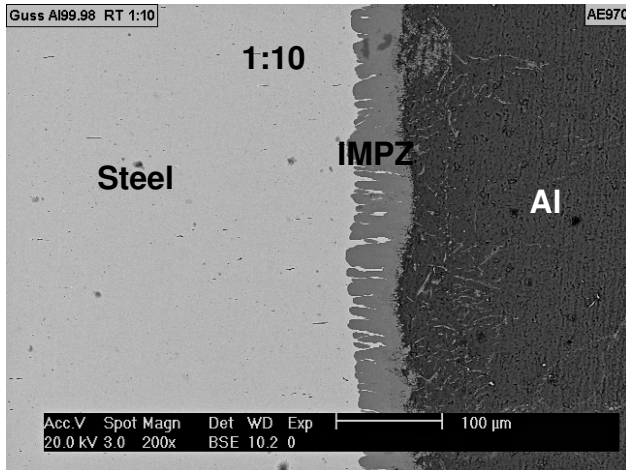
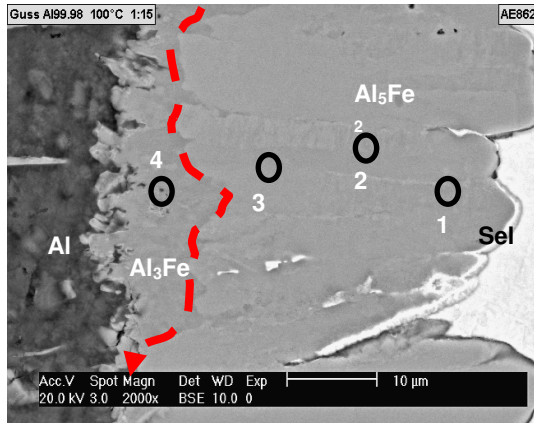


Figure 41: REM/BSE pictures from cast samples steel in Al99.7 show the transition zone Steel/IMPZ/Aluminum: Constant development of the IMPZ independent from the mass ratio steel/aluminum and the preheating temperature of the steel cubes.



Analysis	Phase	Al at%	Fe at%
1	Al_5Fe_2	71.0	29.0
2	Al_5Fe_2	71.2	28.8
3	Al_5Fe_2	71.4	28.6
4	Al_3Fe	75.0	25.0

Figure 42: REM/BSE pictures of the IMPZ with a preheating temperature of 100°C (steel cube, mass ratio Fe-Al 1:15) and quantitative tabulation from the EDX analysis at the marked points: Identification of phase Al_5Fe_2 at the border to steel and phase Al_3Fe at the border.

4.3 Wetting Experiments

In Figure 43 and Figure 44 samples as they came out of the experimental setup can be seen. The images show the polished iron plate from above with the drop on it. As can be clearly seen from Figure 45 and Figure 46, the wetting angle Θ (as depicted in Figure 47) is changed considerably when changing from Al99.98 to Al-7Si. Unlike Si and Mg, Zn and Cu do not seem to have a significant impact on the wetting angle of Al to Fe as Table 4 suggests. As for Mg a reaction has been observed at the melt containing glass syringe: an exchange of Mg and Si from the SiO_2 could have happened, since in the Al-7Mg sample also Si could be detected by EDX. This has to be investigated further.

Additionally adding of Si to the aluminum altered the morphology of the intermetallic layer compared to the pure material.^[53-55] The structure has a blocky appearance and is much less tongue shaped, furthermore does the intermetallic layer contain Al-Fe-Si phases (detected by EDX) on the iron side. Moreover a significant decrease of the intermetallic layer between Al and Fe can be observed.

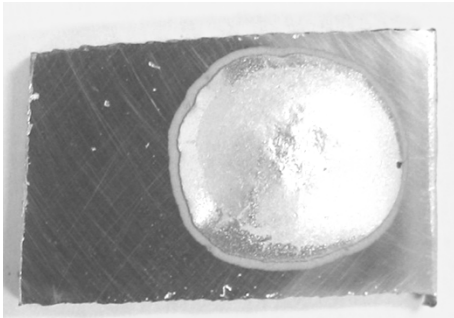


Figure 43: Sample Al/Fe

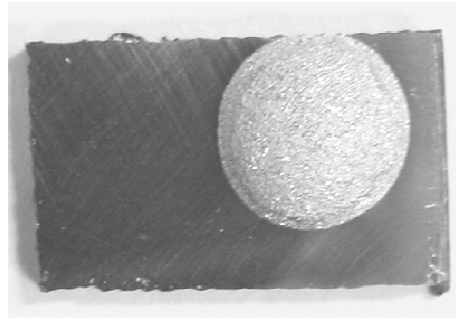


Figure 44: Sample Al-7Si/Fe

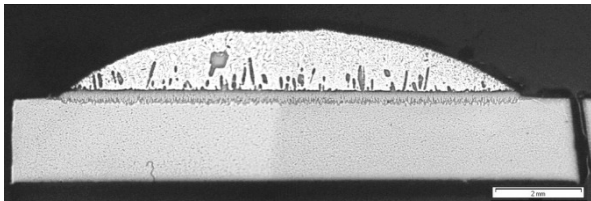


Figure 45: Al/Fe (12,5x)

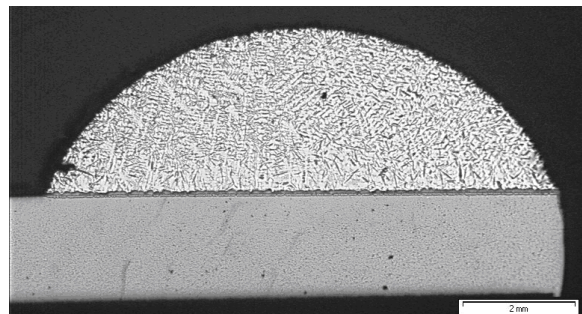


Figure 46: Al-7Si/Fe (12,5x)

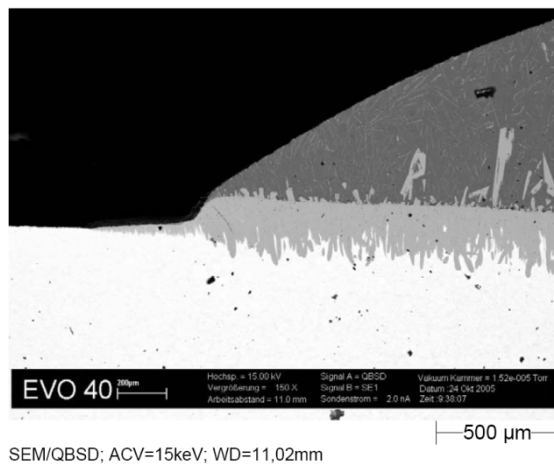


Figure 47: Interface of Al_{99.98}/Fe couple on the edge. The different wetting angle of aluminum and the intermetallic layer on the iron substrate can be seen

An additional influence of the alloying elements can be observed for the interface thickness. The Fe/Al_{99.98} couple has an average thickness of 260 µm, alloying elements decrease the thickness, with Cu and Zn having a less significant influence than Mg and Si. However Fe/Al-7Si couple has the thinnest section, as Table 4 shows and is considerable thinner than all others.

Table 4: Wetting angles of Al and Al-alloys on Fe as an average of 12 measurements each with standard deviation as well as the maximum width of the intermetallic layer

Alloy used	Average wetting angle (°)	Standard deviation (°)	Max. Interface width (μm)
Al99.98	37	4	260
Al-7Cu	33	3	190
Al-7Si	49	4	100
Al-7Zn	35	3	220

All samples were with the same procedure prepared: Cut in the middle, polished, edged and analyzed via optical and electronic microscopy.

Additionally adding of Si to the aluminum altered the morphology of the intermetallic layer compared to the pure material as Figure 48 and Figure 49 show. The structure is blockier and less tongue shaped. Moreover a significant decrease of the intermetallic layer between Al and Fe can be observed.

Compared with the Al99.98/Fe interface (Figure 48) the morphology of the intermetallic layers of Al-7Cu/Fe (Figure 50) and Al-7Zn/Fe (Figure 51) couples do not change significantly as that of Al-7Si/Fe (Figure 49). Both exhibit the tongue like shape of the interface growing into the iron substrate. Also Al-Fe phase in needle like shape can be observed in the aluminum.

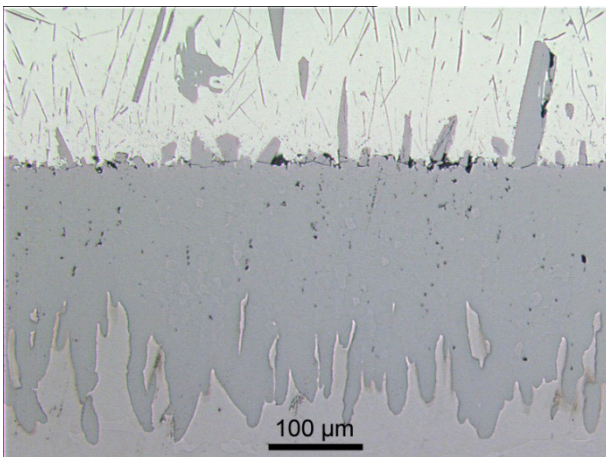


Figure 48: Intermetallic layer interface of Al99.98/Fe couple

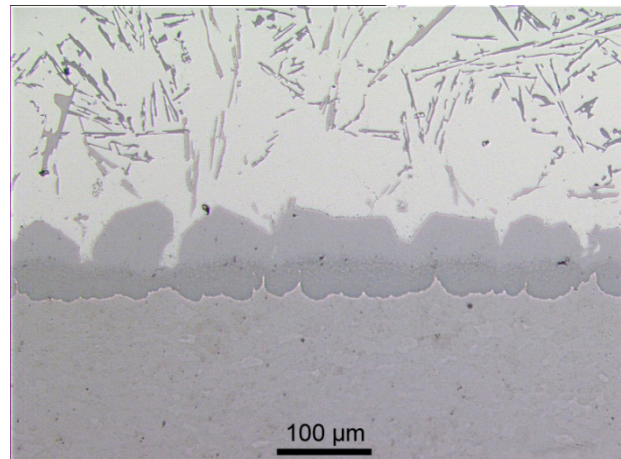


Figure 49: Intermetallic layer interface Al-7Si/Fe couple

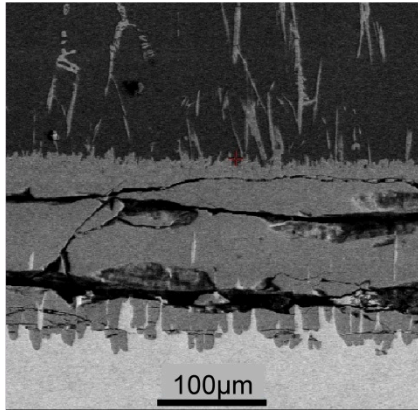


Figure 50: Intermetallic layer interface of Al-7Cu/Fe couple

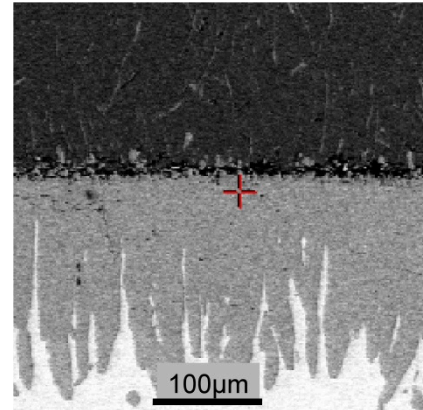
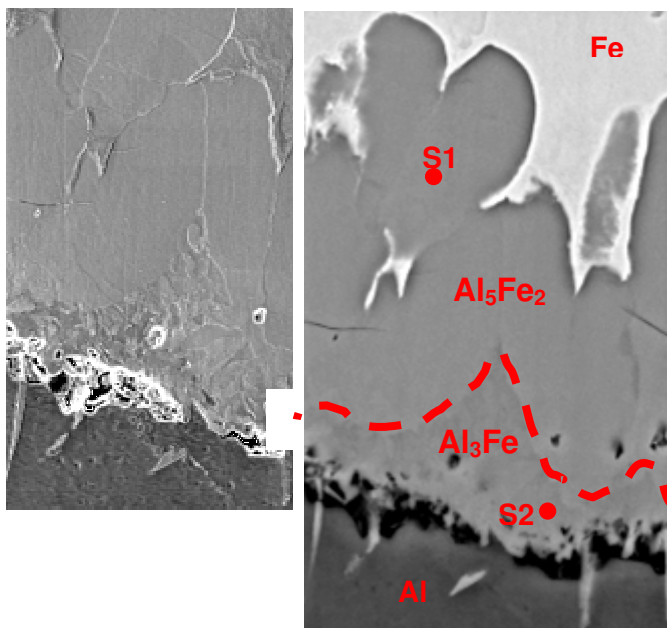


Figure 51: Intermetallic layer interface of Al-7Zn/Fe couple

In literature the statement can be found that the Al-Fe interface consists of Al_3Fe phases or Al_5Fe_2 phases. Additional investigation of the interface employing ionic pickling revealed that the interface can be clearly divided in a two phase material as Figure 52 shows. The tables contain also the values of the reference material at 20 kV (annealed at 850°C for 168 hours, then water quenched) that have been made for this investigation. Surprisingly, this distinction could not be made by means of conventional polishing, neither using optical microscopy, nor electronic microscopy. The two phases were identified as Al_5Fe_2 and Al_3Fe on the iron and aluminum side, respectively. The measurements are an average of 10 readings each, with pure intermetallic phases as a reference.



S1 = Al_5Fe_2

Al wt%	Al at%	Fe wt%	Fe at%
56.1	72.5	43.9	27.5
Reference Material			
55.2	71.8	44.8	28.2

S2 = Al_3Fe

Al wt%	Al at%	Fe wt%	Fe at%
62.8	77.7	37.2	22.3
Reference Material			
61.7	77.0	38.3	23.0

Figure 52: Al 99.98/Fe interface using an electronic microscope and phase identification of Points S1 and S2

Afterwards Fe/Al-7Si couples were investigated in more detail. Contrary to the pure Al-Fe sample the interface here is more complex. The shape of the interface changed from the tongue like appearance (see Figure 52) to a more blocky structure as depicted in Figure 53. EDX measurements were carried out in two areas to check the composition, shown in Figure 54. Since zinc has such a good solubility in both Al and Fe, not a lot of intermetallic phases are expected, as shown in Table 5. Similar to copper, but the intermetallic copper phases are very brittle, so this could explain the cracks of the prepared sample in the interface.

The EDX measurements (Figure 55 to Figure 58) revealed several phases that were not present in the Fe/Al99.98 interface, due to the absence of Silicon. Among them η , τ_1 , τ_3 , τ_5 , τ_6 clearly could be identified. The θ phase (FeAl_3) could not be found, instead of the τ_6 phase the FeAl_4Si phase exists. From ternary diagrams it is believed that additional phases can be found at the interface (Table 6).

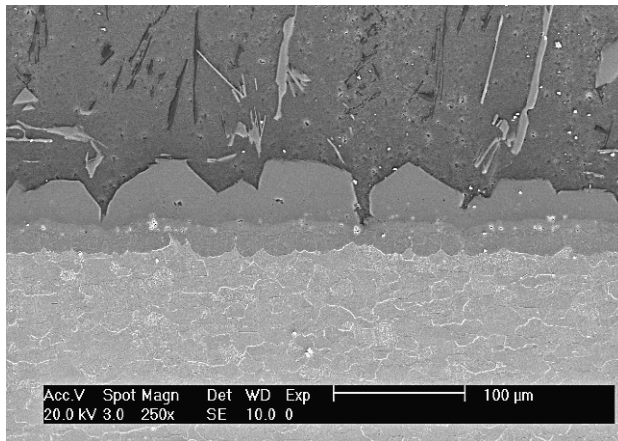


Figure 53: Fe/Al-7Si interface (Al-7Si Top, Fe bottom)

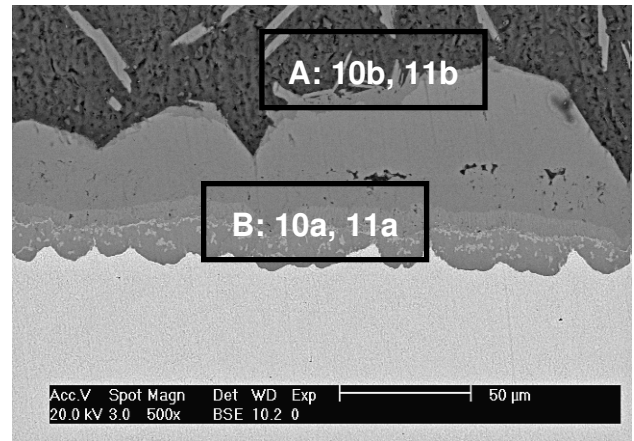


Figure 54: Fe/Al-7Si interface (500x) and approximate areas from where EDX spectrums were taken

Table 5: Expected/possible IMP's formed at the Fe/Al interface.

System	Expected intermetallic phases	Source
Fe/Al99.98	Fe_2Al_5 , FeAl_3	ASM ^[38]
Fe/Al-7Si	$\text{Fe}_2(\text{Al,Si})_5$, $\text{Fe}(\text{Al,Si})_3$, $\text{Fe}_2\text{Al}_7\text{Si}$, $\text{Fe}_2\text{Al}_5\text{Si}_2$, $\text{Fe}_2\text{Al}_2\text{Si}$, FeAl_4Si	Gupta ^[56, 57]
Fe/Al-7Cu	$\text{Fe}_2(\text{Al,Cu})_5$, $\text{Fe}(\text{Al,Cu})_3$, $\text{Fe}_2\text{Al}_7\text{Si}$	ASM ^[38] , Zhang ^[58]
Fe/Al-7Zn	$\text{Fe}_2(\text{Al,Zn})_5$, $\text{Fe}(\text{Al,Zn})_3$	ASM ^[38]

For wetting experiments high vacuum proved most stable. Any gas (inert or reducing) did not prevent oxidation of the iron substrate during heating and therefore will not be considered in the next such experiments. Silicon clearly has the most impact on the interface (thickness and morphology).

When looking at the phase diagram it is clear that not only Al_5Fe_3 and Al_3Fe develop at the interface, but also FeAl_2 on the iron side. Even with ionic pickling this phase could not be observed yet so that it is likely that kinetics do not favor this face.

The interfaces of the Fe/Al-7Cu and the Fe/Al-7Zn couple did not show several distinct different intermetallic phases. The ternary phase diagram of Al-Fe-Zn shows a high solubility of Zn, so that no distinct Zn-containing phases could be found in the interface. This might also be the reason why the morphology of this intermetallic layer is very similar to that of pure aluminum. Furthermore, as with FeAl_2 growth kinetics could play an important role in the formation of intermetallics.

With 7 wt% Cu the Al-Fe interface reduces in thickness, but it also seems that the formation of intermetallic phases leads to a more brittle sample, that either broke during cooling due to different CTE of the materials or at the sample preparation. It has to be said that the sample preparation was equal to all samples.

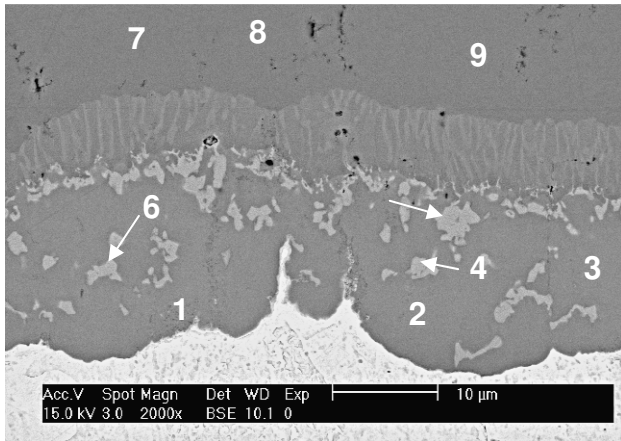


Figure 55: Sample 1, Area A: EDX points

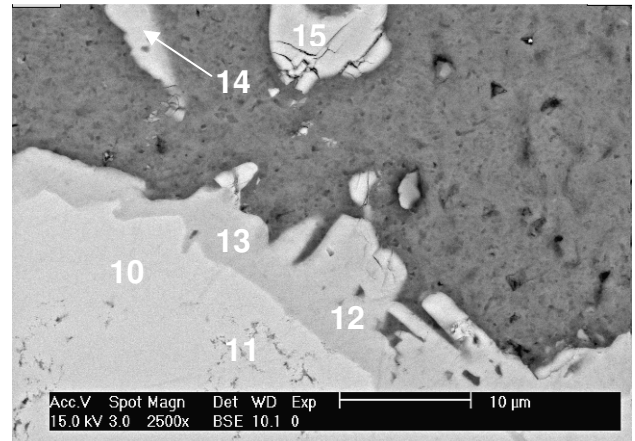


Figure 56: Sample 1, Area B: EDX points

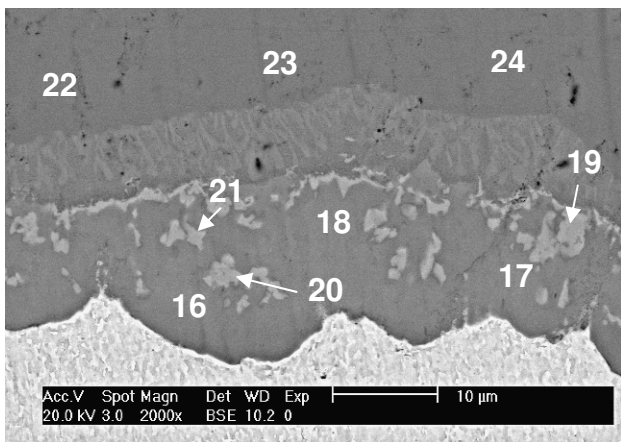


Figure 57: Sample 2, Area A: EDX points

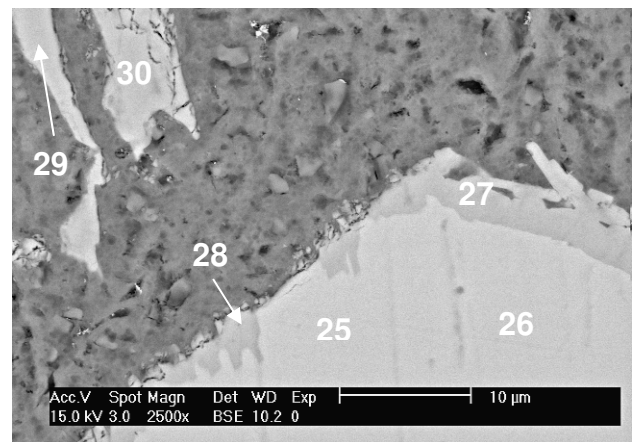


Figure 58: Sample 2, Area B: EDX points

Table 6: EDX measurements from Figure 55 to Figure 58, the intermetallic compounds detected and their phase names

Spectrum Nr.	Al at%	Si at%	Fe at%	Compound	Phase Name
1	72.3	0.9	26.8	Fe ₂ (Al,Si) ₅	η
2	72.3	1.1	26.6	Fe ₂ (Al,Si) ₅	η
3	72.1	1.1	26.8	Fe ₂ (Al,Si) ₅	η
4	44.5	20.9	36.6	Fe ₂ Al ₂ Si	τ ₁
5	41.2	23.6	35.2	Fe ₂ Al ₂ Si	τ ₁
6	38.5	26.1	35.4	Fe ₂ Al ₂ Si	τ ₁
7	71.1	9.9	19.0	Fe ₂ Al ₇ Si	τ ₅
8	70.9	9.9	19.2	Fe ₂ Al ₇ Si	τ ₅
9	70.6	10.3	19.1	Fe ₂ Al ₇ Si	τ ₅
10	70.6	10.4	19.0	Fe ₂ Al ₇ Si	τ ₅
11	70.9	10.4	18.7	Fe ₂ Al ₇ Si	τ ₅
12	67.5	17.5	15.0	FeAl ₄ Si	τ ₆
13	68.3	17.3	14.3	FeAl ₄ Si	τ ₆
14	67.5	17.3	15.3	FeAl ₄ Si	τ ₆
15	69.9	16.5	13.7	FeAl ₄ Si	τ ₆
16	71.6	1.3	27.1	Fe ₂ (Al,Si) ₅	η
17	72.2	1.0	26.8	Fe ₂ (Al,Si) ₅	η
18	72.6	0.8	26.7	Fe ₂ (Al,Si) ₅	η
19	46.1	21.1	32.7	Fe ₃ Al ₄ Si ₂	τ ₃
20	48.9	17.8	33.3	Fe ₃ Al ₄ Si ₂	τ ₃
21	46.0	20.3	33.7	Fe ₃ Al ₄ Si ₂	τ ₃
22	71.3	9.6	19.1	Fe ₂ Al ₇ Si	τ ₅
23	71.0	9.9	19.1	Fe ₂ Al ₇ Si	τ ₅
24	71.2	10.0	18.8	Fe ₂ Al ₇ Si	τ ₅
25	70.4	10.4	19.2	Fe ₂ Al ₇ Si	τ ₅
26	70.2	10.2	19.6	Fe ₂ Al ₇ Si	τ ₅
27	67.5	16.4	16.1	FeAl ₄ Si	τ ₆
28	70.9	15.0	14.2	FeAl ₄ Si	τ ₆
29	68.2	16.8	15.0	FeAl ₄ Si	τ ₆
30	70.2	15.6	14.2	FeAl ₄ Si	τ ₆

4.4 Dipping Experiments

The analysis of the individual phases was performed by scanning electron microscopy (SEM) via energy dispersive X-ray analysis (EDX) after the according sample preparation. Highly important for identifying individual phases is the correct sample preparation. Here focused ion beam pickling (FIB) proved invaluable: Not only it allows the analysis of large sample areas (in the range of several cm²) but also shows a high contrast of the grain structures in the occurring phases and the substrate material.

While the reaction zone at the interface of the Al-Fe compound is called intermetallic phase zone (IMPZ) within this zone several intermetallic phases (IMP) can emerge. ^[52, 59-67]

4.4.1 Evaluation

Figure 59 illustrates the process of evaluation in determining quantitatively the amount of the intermetallic phase zone, the residual steel and the thickness of the complete composite (which can be thinner or thicker than the original 300 μm thick steel strip). Reason for choosing this method is because of the finger shape like formation of the IMPZ, which does not allow positively optical thickness interpretation. The length of the evaluated area in every image is 405 μm which also implies that all images were taken at the same magnification (200x). This means that always the same area was compared among each another. The original area of the non-dipped steel strip is therefore constantly 121.500 μm^2 .

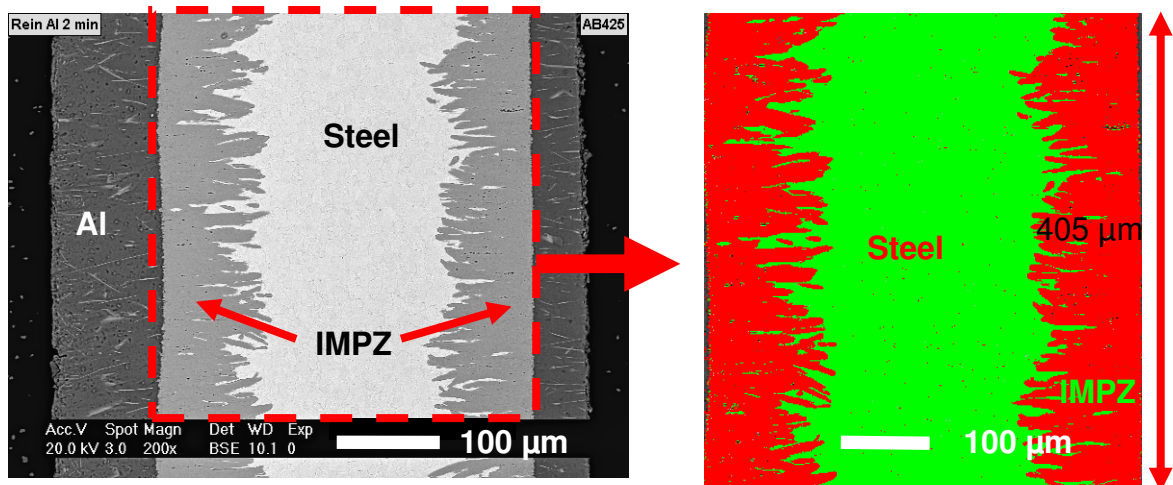


Figure 59: Score of the area ratio IMPZ/Steel by setting color levels: Red for IMPZ and green for Steel

4.4.1.1 Dipping experiments in Al-7Cu

Figure 60 shows the evolution of the intermetallic phase zone and the concurrent reduction of the steel strip width over time. The IMPZ clearly emerged already after 2 s dipping time (left part of the image) and continuously increases in thickness with time. In nearly every micrograph at beginning of the dipping process some detached, “wave-like” material from the intermetallic phase zone can be noticed.^[53, 58] This phenomenon ceases after 15 s. Steel strips with dipping times of 30 s or more do not exhibit these detached intermetallics anymore. The cause of this could be movements of the melt at the beginning of the interface formation which causes some material that is momentarily just loosely attached to move away from the interface.

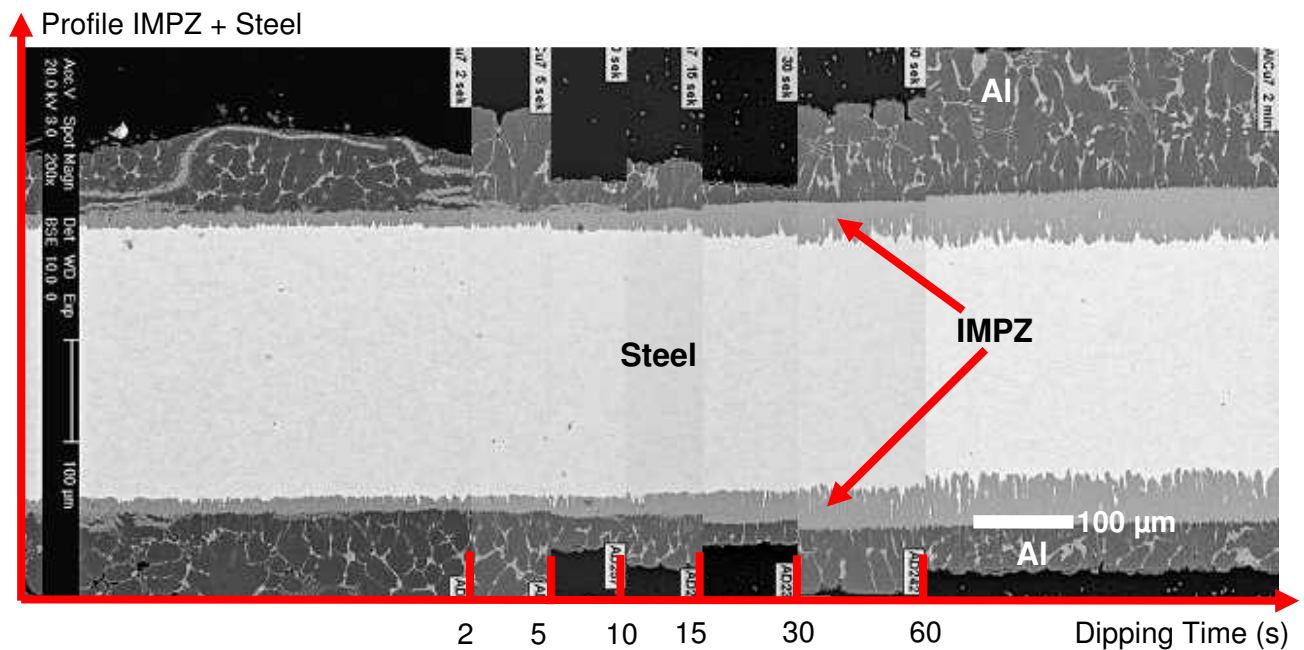


Figure 60: Dip experiments Al-7Cu: Sequence of SEM pictures from the ion beam etched profile of Steel/Al-7Cu with different dipping times: Decrease of steel profile and growth of IMPZ with increasing dipping time

The evaluation of the IMPZ progression and the reduction of the steel strip width are illustrated in Figure 61. While the cross-section of the steel decreases linearly except for the first 5 seconds, the increase of the IMPZ reduces after 60 s, which means that in the first minute the formation is controlled by the reaction kinetics, while afterwards diffusion through the IMPZ^[30] to form further intermetallic compounds is the limiting element. The overall area of IMPZ and steel thereby stays relatively constant.

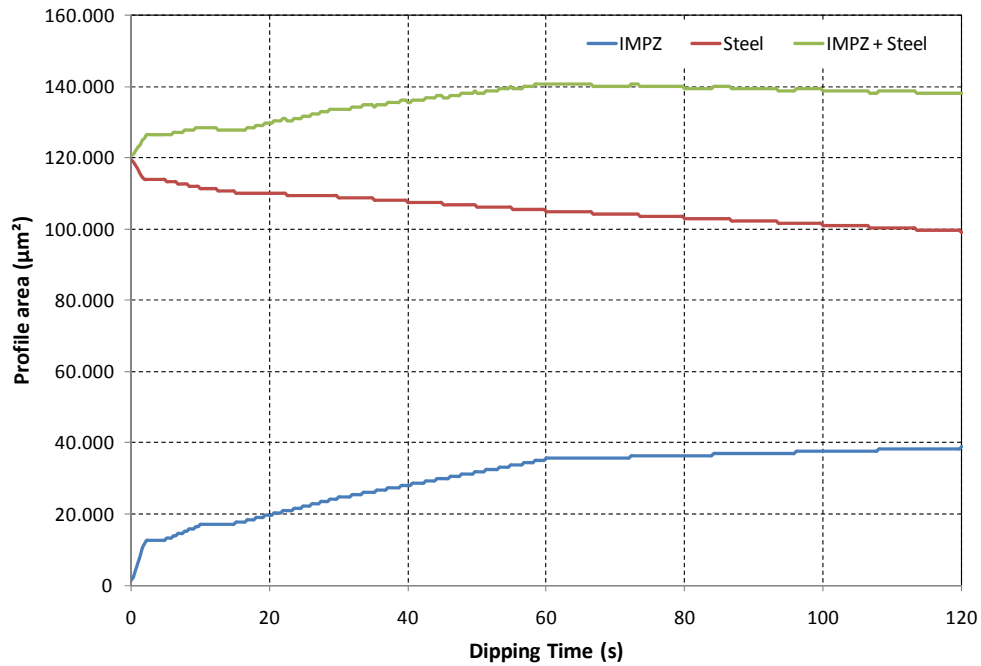


Figure 61: Dip experiments Al-7Cu: Growth of the IMPZ with increasing dipping time and decreasing steel profile, the overall thickness (Steel + IMPZ) persist constant from 60 seconds dipping time

Via quantitative analysis of EDX measurements of the IMPZ the following phases could be identified: Al_5Fe_2 at the border to the steel strip and Al_3Fe at the border to aluminum. The Cu-content within the individual intermetallic phases is low and varies from 0.5 to 1 at% (Figure 62 and Table 7).

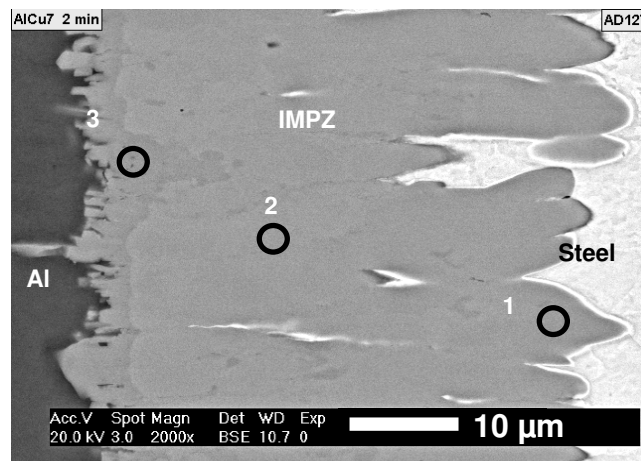


Figure 62: Dip experiments Al-7Cu: REM picture of an ion beam etched profile from a compound sample Steel/Al-7Cu after 120 seconds dipping time: The different phases in the IMPZ are well specifiable

Table 7: Dip experiments Al-7Cu: EDX analysis from the in Figure 62 marked points: The composition conform the phases Al_5Fe_2 and Al_3Fe with little percentage of Cu

Analysis	Phase	Al at%	Fe at%	Cu at%
1	$(Al_{1-x}Cu_x)_5Fe_2$	70.2	28.8	1.0
2	$(Al_{1-x}Cu_x)_5Fe_2$	71.0	28.5	0.5
3	$(Al_{1-x}Cu_x)_3Fe$	76.2	22.8	1.0

In the IMPZ at the interface of steel and aluminum Al-Fe phases with a low Cu content could be detected. The corresponding Al-Fe-Cu phases though were found in the Al-matrix as shown in Figure 63.

The left image of Figure 63 shows finger shaped growth of the IMPZ in the steel and a relatively straight change of the IMPZ to the aluminum alloy. At the right picture a precipitate in the Al-7Cu alloy can be seen which consists of two different Al-Fe-Cu phases (see EDX-analysis at the two points and Table 8). Flaky, plane particles with relative high concentration of Fe and bone-formed branched dispersions with high concentration of Cu could be found in the Al-melt.

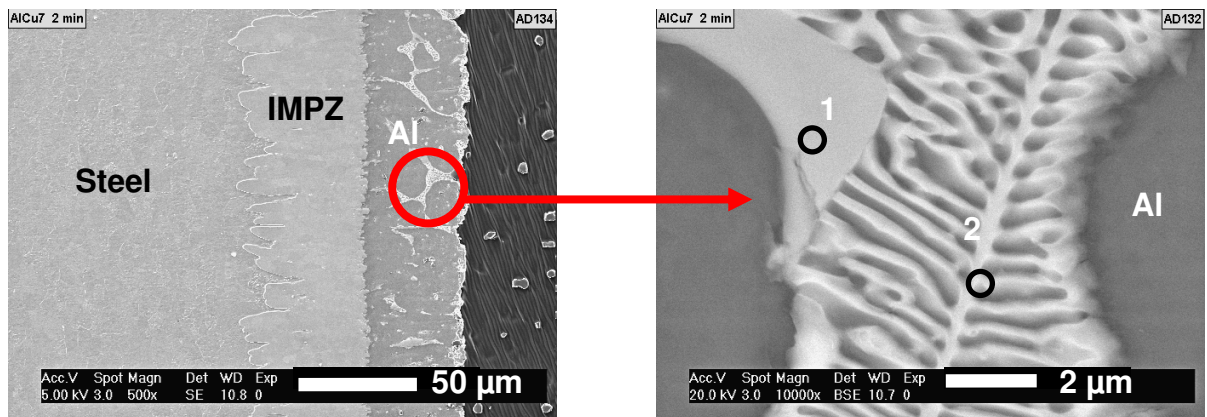


Figure 63: Dip experiments Al-7Cu: SEM picture (left: Secondary electrons (SEM-SE), right: Backscattered electrons (SEM-BE)) of an ion beam etched profile from a compound sample Steel-Al-7Cu after 120 seconds dipping time: Finger-shaped growth of the IMPZ into the steel and detail picture of an dispersion in Al

Table 8: Dip experiments Al-7Cu: EDX analysis from the in Figure 63 marked points at the dispersions in the Al-Matrix

Analysis	Al at%	Fe at%	Cu at%
1	77.6	16.4	6.0
2	81.4	0.5	18.1

4.4.1.2 Dipping experiments in Al-7Mg

Analog to the Al-7Cu dipping results interface formation with the alloy Al-7Mg leads to a reduction in the cross-sectional area of the steel strip and an increase in the IMPZ thickness as well. Accordingly the interface shows finger shaped growth at the steel border. Nonetheless there are two distinct differences when comparing these results to the ones with the Al-7Cu alloy:

1. The cross-sectional area of the steel strip decreases much faster
2. There is a difference in the IMPZ formation: While the IMPZ of the Al-7Cu dipping trials stabilized within the first 15 s, with Al-7Mg the wave like formations stay up to 120 s dipping time and it seems that the IMPZ cannot consolidate as it broadens. The layer is dense just at the border to steel. The boundary to the aluminum material is less dense and intermetallic and alloy alternate.

Figure 64 illustrates this phenomenon quite clearly

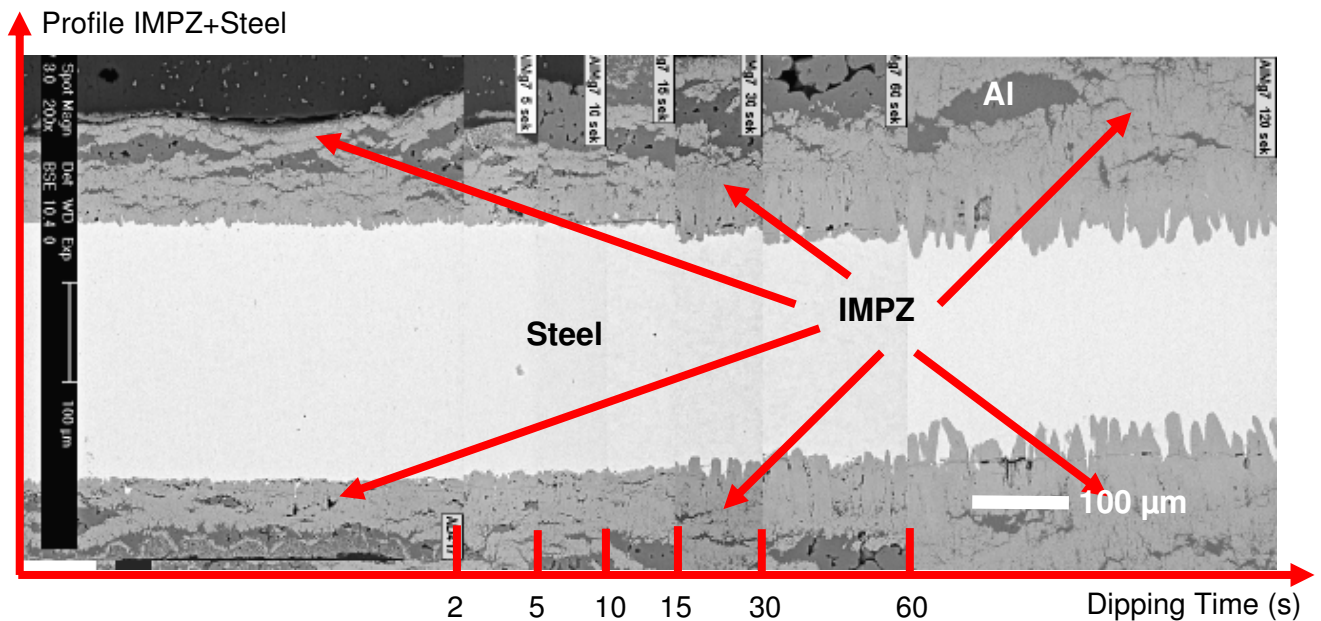


Figure 64: Dip experiments Al-7Mg: Sequence of SEM pictures from the ion beam etched profile of Steel/Al-7Mg with different dipping times: Decrease of steel profile and growth of IMPZ with increasing dipping time.

The evaluation of the IMPZ progression and the reduction of the steel strip width are illustrated in Figure 65. It can be observed that the IMPZ formation speed reduces somewhat with time. The growth does not stop, probably due to the above mentioned effect. Additionally it can be stated that the interface width is much thicker than compared to Al-7Cu. The steel profile decreases linear except the first 5 seconds (comparable with Al-7Cu), the gradient of IMPZ slim down from about 30 seconds dipping time

In the IMPZ at the interface of steel and aluminum Al-Fe phases with a low Mg content could be detected. The images of Figure 66 show an IMPZ that is less dense than the Al-7Cu interface layer. The IMPZ is broken (cracks parallel to the boundary layer), and is not compact at the boundary to Al-7Mg (aluminum islands in the IMPZ). The EDX-analysis at the three points is shown in Table 9.

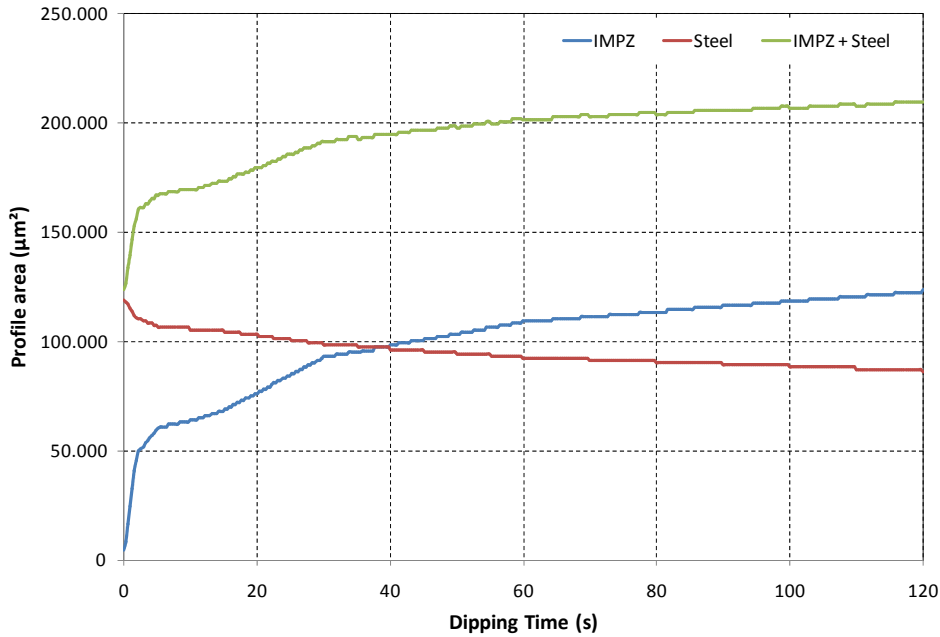


Figure 65: Dip experiments Al-7Mg: Growth of the IMPZ with increasing dipping time and decreasing steel profile, intense growth of the overall thickness (Steel + IMPZ)

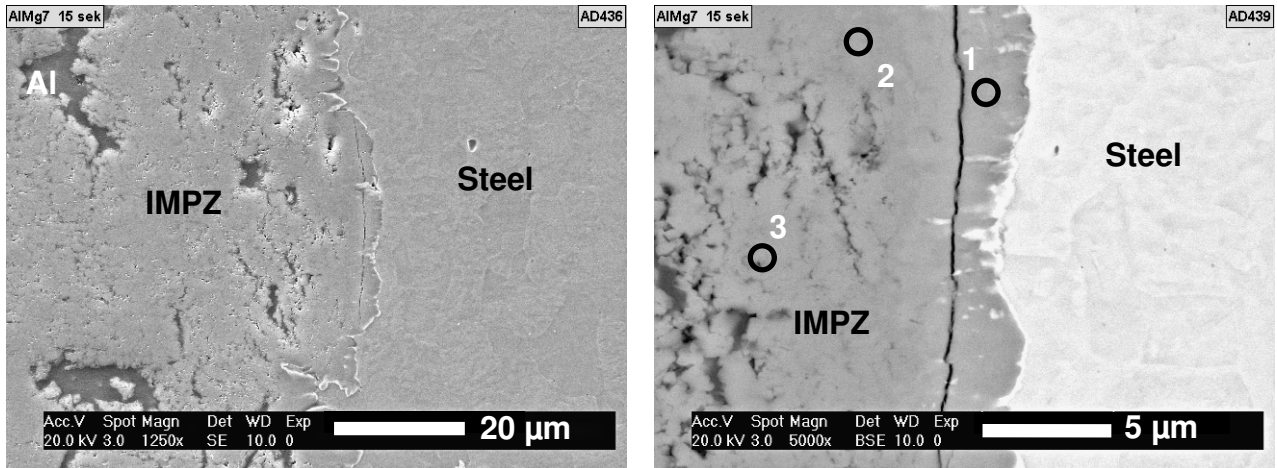


Figure 66: Dip experiments Al-7Mg: SEM picture (left: Secondary electrons (SEM-SE), right: Backscattered electrons (SEM-BE)) of an ion beam etched profile from a compound sample Steel/Al-7Mg after 15 seconds dipping time

Table 9: Dip experiments Al-7Mg: EDX analysis from the in Figure 66 marked points: The composition conforms the phases Al_5Fe_2 and Al_3Fe , compared to Al-7Cu the concentration of Mg in the IMPZ is higher

Analysis	Phase	Al at%	Fe at%	Mg at%	Zn at%
1	$(Al_{1-x}Mg_x)_5Fe_2$	71.1	26.1	1.4	1.4
2	$(Al_{1-x}Mg_x)_3Fe$	73.5	23.0	2.5	1.0
3	$(Al_{1-x}Mg_x)_3Fe$	74.0	22.1	3.3	0.6

4.4.1.3 Dipping experiments in Al-7Zn

Compared to the dipping experiments with the binary alloys Al-7Cu and Al-7Mg the dissolution of the steel strip is much faster in Al-7Zn.^[27] After 30 s the thickness of the steel insert is already considerably reduced. Samples with a longer dipping time could not be analyzed, since after 60 s just small residuals of the original steel strip were remaining which did not allow for a correct analysis of the phase formation. The IMPZ formed at the interface detaches in wave like structures and moves into the aluminum melt and does not stabilize with time as in the case of Al-7Mg (Figure 67). Overall however the total thickness of IMPZ and the steel insert stays constant with time (Figure 68).

The extreme fast dissolution of the steel is not homogenous along the cross section, but begins in certain areas and continues there at an accelerated rate as Figure 69 depicts. The left part of the image shows the beginning of the fast dissolution in a specific area after 5 s, whereas another area, not far away has a much slower IMPZ formation, see table 10. The right image shows the situation after 30 s, where 50 % of the original steel material has already been dissolved. Despite ongoing work and further examination the process of the localized attack and its reason cannot yet be explained.

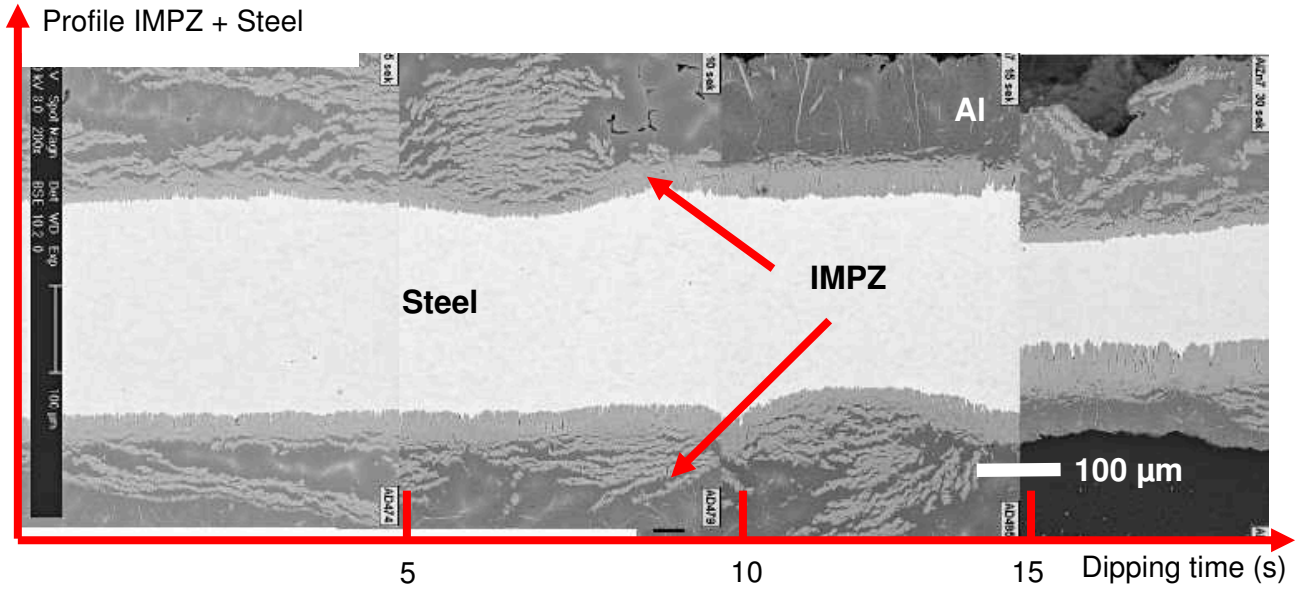


Figure 67: Dip experiments Al-7Zn: Sequence of SEM pictures from the ion beam etched profile of Steel/Al-7Zn with different dipping times: Decrease of steel profile and growth of IMPZ with increasing dipping time

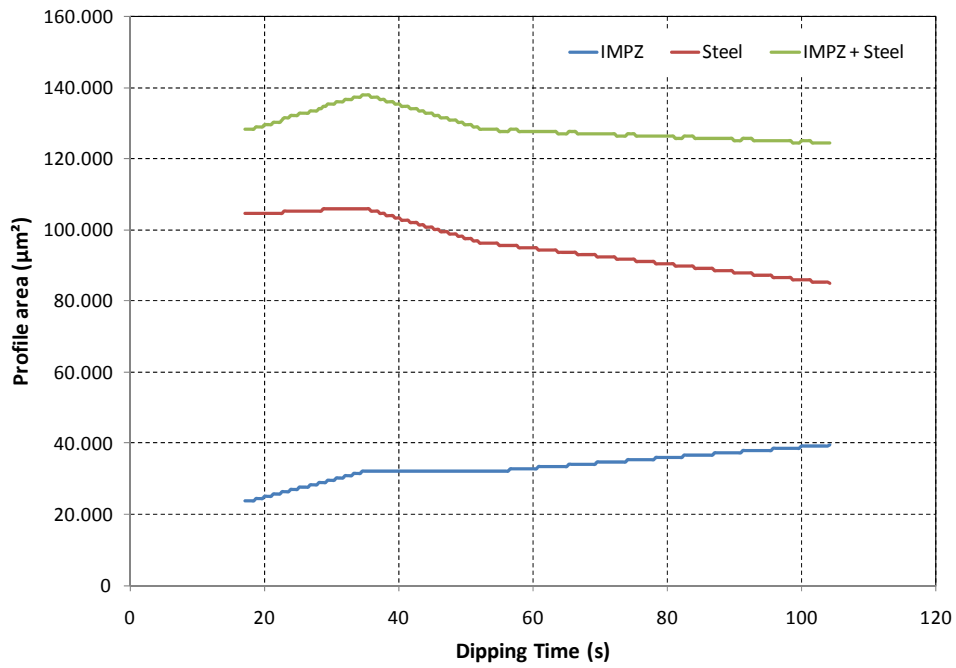


Figure 68: Dip experiments Al-7Zn: Growth of the IMPZ with increasing dipping time and highly decreasing steel profile

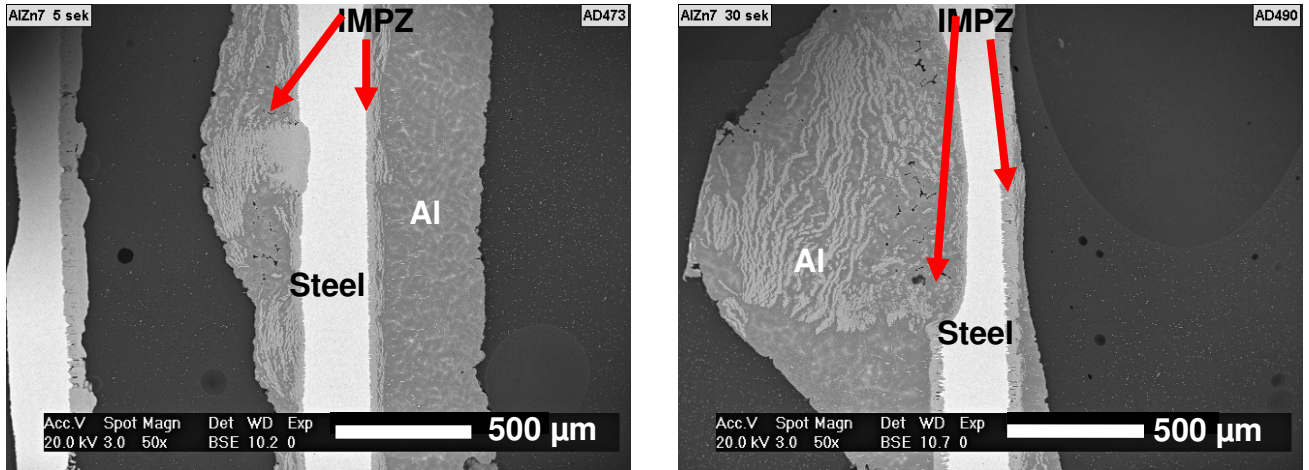


Figure 69: Dip experiments Al-7Zn: SEM picture of an ion beam etched profile from a compound sample Steel/Al-7Zn after 5 seconds dipping time (left) and 30 seconds dipping time (right): Unbalanced dissolution of the steel

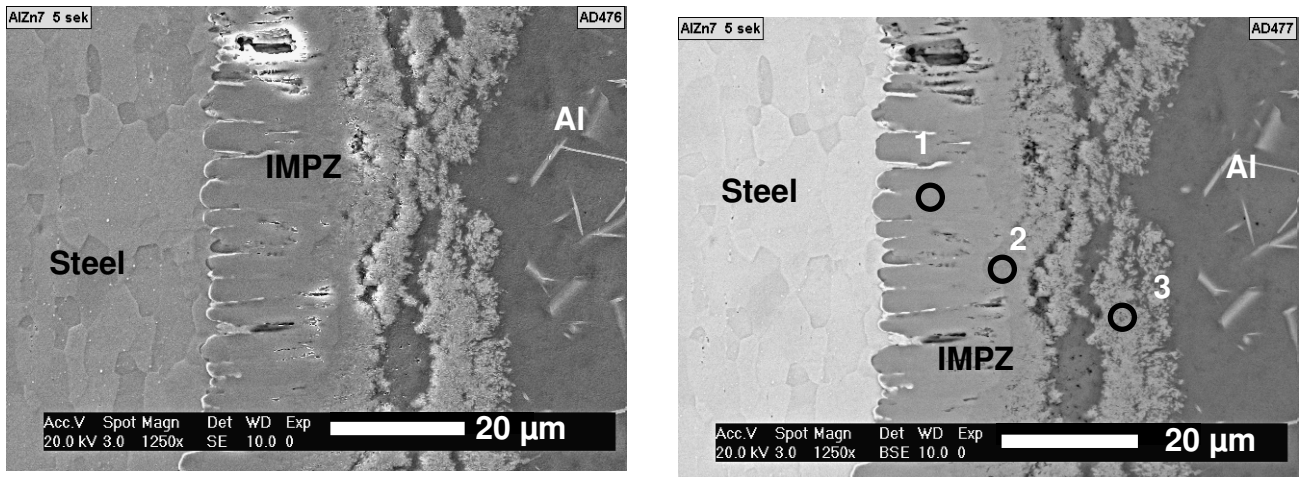


Figure 70: Dip experiments Al-7Zn: SEM picture (left: Secondary electrons (SEM-SE), right: Backscattered electrons (SEM-BE)) of an ion beam etched profile from a compound sample Steel/Al-7Zn after 5 seconds dipping time: Finger-shaped growth of the IMPZ into the steel, no correlation between grain structure of steel and the IMPZ

Table 10: Dip experiments Al-7Zn: EDX analysis from the in Figure 70 marked points: the composition conform the phases Al_5Fe_2 and Al_3Fe , the concentration of Zn inside the IMPZ is marginal (ca. 1 at %)

Analysis	Phase	Al at%	Fe at%	Zn at%
1	Al_5Fe_2	71.8	27.2	1.0
2	Al_3Fe	76.2	22.8	1.0
3	Al_3Fe	78.1	20.9	1.0

4.4.1.4 Dipping experiments in Al99.7

Figure 71 illustrates the reduction of the cross-sectional area of the steel insert for the dipping experiments in Al99.7 and the increase of the IMPZ. Again the detachment of the wave like intermetallic phases from the interface at the beginning of the dipping process could be observed. This detachment, that with time gradually becomes less severe, can be observed up to a dip time of 15 s and then stops. Shape and morphology of the IMPZ look very similar to those of the dipping trials in Al-7Cu as Figure 72 shows. The EDX measurements listed in Table 11 show a thick Al_5Fe_2 layer at the steel side and a thin Al_3Fe layer at the aluminum side. Nevertheless both the IMPZ thickness growth and the reduction of the cross-section of the steel are lower in the Al99.7 samples compared to the ones dipped in Al-7Cu (see Figure 72). The steel profile decreases linear except the first 5 seconds (comparable with Al-7Cu), the gradient of IMPZ slim down from about 30 seconds dipping time.

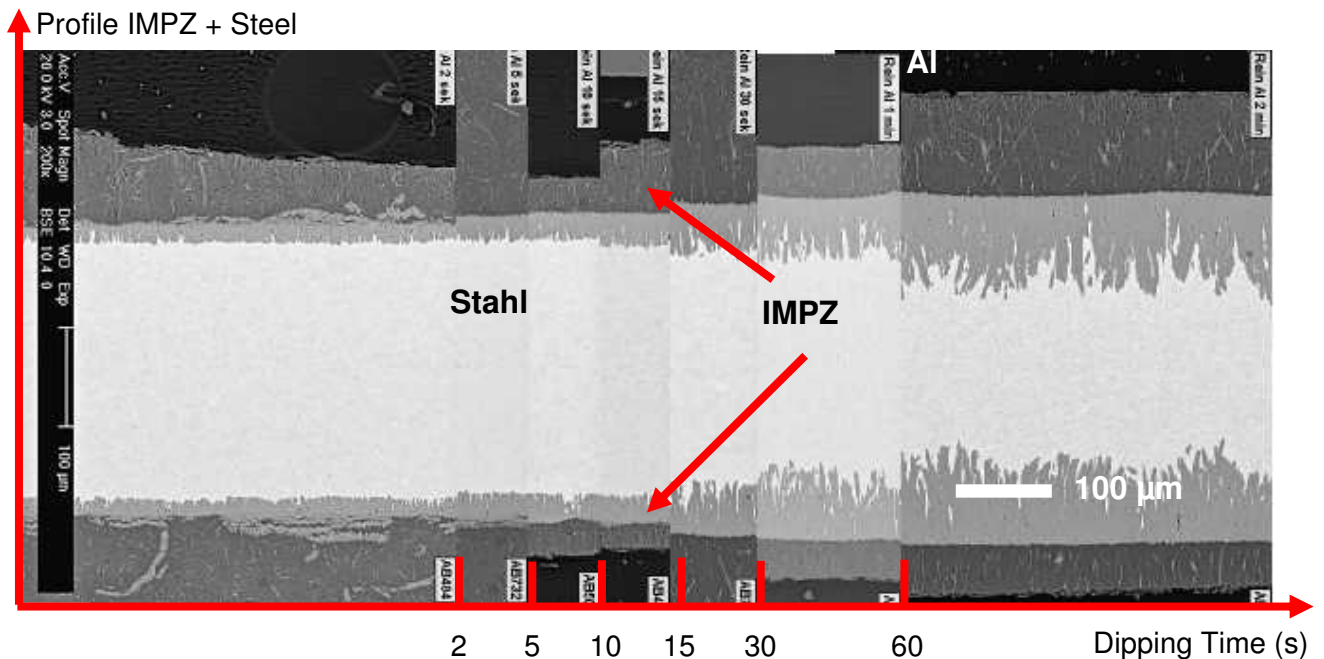


Figure 71: Dip experiments Al99.7 + 2 μm Zinc: Sequence of SEM pictures from the ion beam etched profile of Steel/Al99.7 with different dipping times: Decrease of steel profile and growth of IMPZ with increasing dipping time

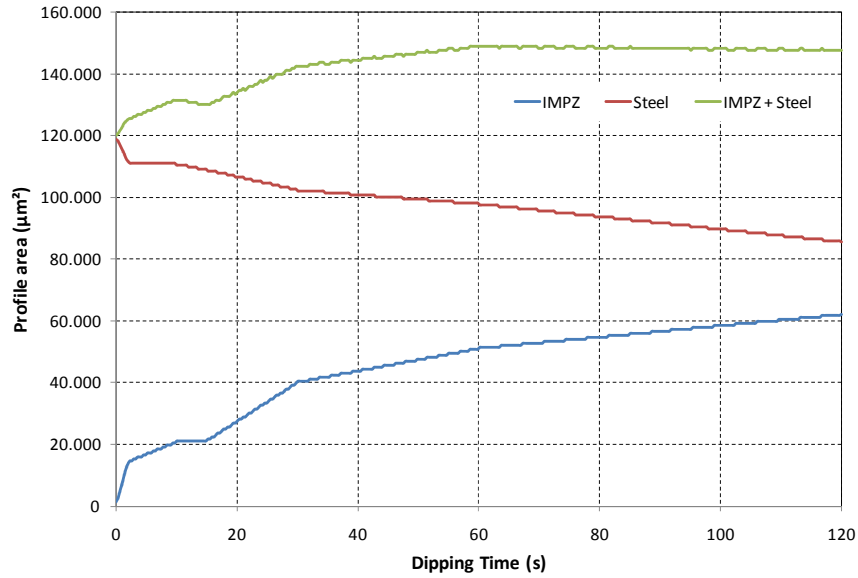


Figure 72: Dip experiments Al99.7 + 2 µm Zinc: Growth of the IMPZ with increasing dipping time and decreasing steel profile, the overall thickness (Steel + IMPZ) is constant after about 60 seconds dipping time

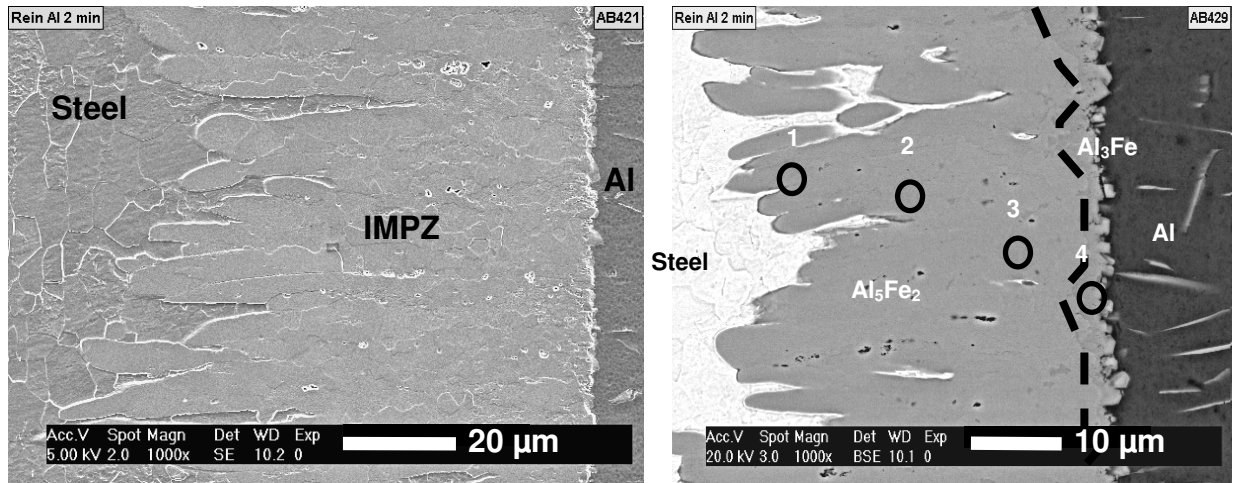


Figure 73: Dip experiments Al99.7: SEM picture (left: Secondary electrons (SEM-SE), right: Backscattered electrons (SEM-BE)) of an ion beam etched profile from a compound sample Steel-Al99.7 after 120 seconds dipping time: No correlation between grain structure of steel and the IMPZ

Table 11: Dip experiments Al99.7: EDX analysis from the in Figure 73 marked points: The composition of 1, 2, and 3 conform the phase Al_5Fe_2 with little decrease of the Fe concentration towards aluminum. The composition of 4 conforms to Al_3Fe phase

Analysis	Phase	Al at%	Fe at%
1	Al_5Fe_2	73.5	26.5
2	Al_5Fe_2	73.9	26.1
3	Al_5Fe_2	74.2	25.8
4	Al_3Fe	77.6	22.4

4.4.1.5 Dipping experiments of steel with and without 2 μm Zn-coating in Al-Si alloys

So far dipping experiments were described using the binary alloys Al-7Cu, Al-7Mg, Al-7Zn und Al99.7. Since the Al-Si system is of great importance for the casting industry, not only the hypo-eutectic composition Al-7Si was tested, but also the eutectic Al-12Si and the hyper-eutectic Al-17Si, both representing a large array of alloy families in the aluminum casting industry.

These trials showed that the Zn-coating has an influence of the IMPZ formation for hyper-eutectic alloys. For this reason experiments steel strips that where etched in 10 % HCl solution immediately before dipping into the aluminum melt were conducted. A time of less than 10 s from drying the insert with a clean cloth to dipping into the melt ensured a steel surface that was virtually oxide free.

4.4.1.5.1 Dipping experiments of a steel strip with 2 μm Zn-coating in Al-7Si

Contrary to the dipping trials with the binary alloys Al-7Cu, Al-7Mg, Al-7Zn und Al99.7 the emerging interface had a considerable different morphology. The width of the interface is even after 120 s dipping time much smaller than any of the interfaces of the dipping trials described until now. Additionally the dissolution of the steel into the melt is much slower than in the other alloy systems.

After 10 s dipping time of the Zn-coated steel strips into the melt at 700 °C a thin intermetallic phase zone (IMPZ) can be observed, shown in Figure 74. The dimension of the IMPZ does not change much with time, but the combined thickness of the steel strip and the IMPZ reduces somewhat (Figure 75). With time the steel profile decreases. There is a continuous formation of IMPZ on both sides not before 10 seconds dipping time - the width of IMPZ however is irregular and there is no growth of the IMPZ with increasing dipping time.

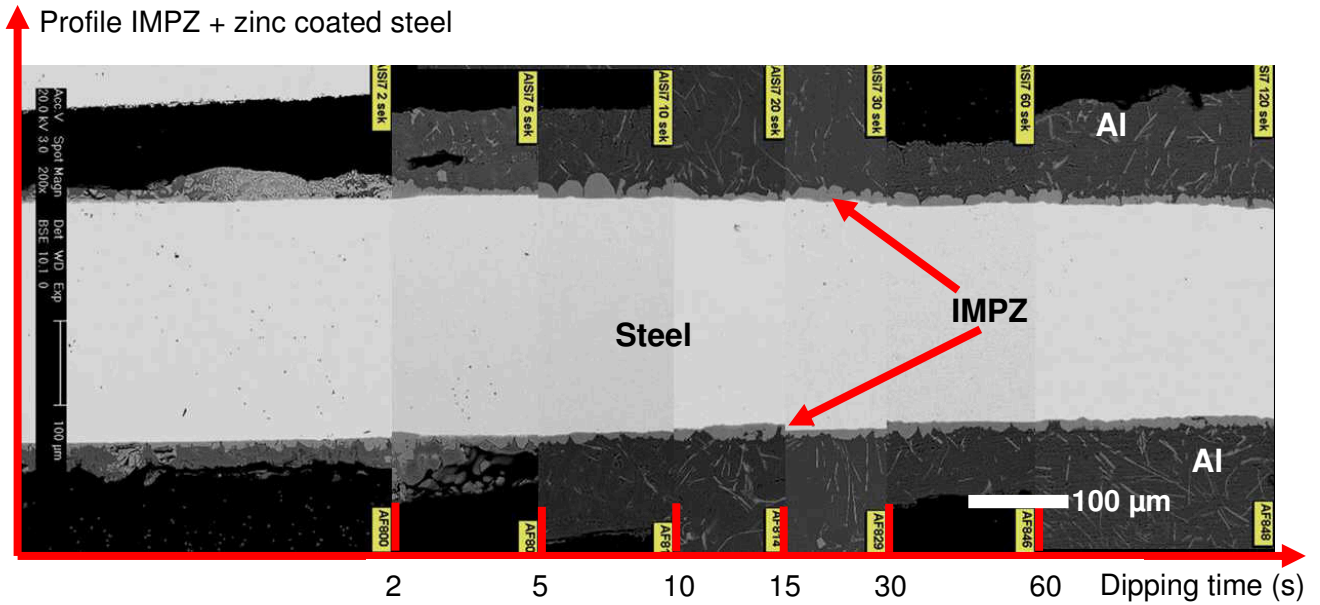


Figure 74: Dip experiments Al-7Si + 2 μm Zinc: Sequence of SEM pictures from the ion beam etched profile of zinc coated steel and Al-7Si with different dipping times

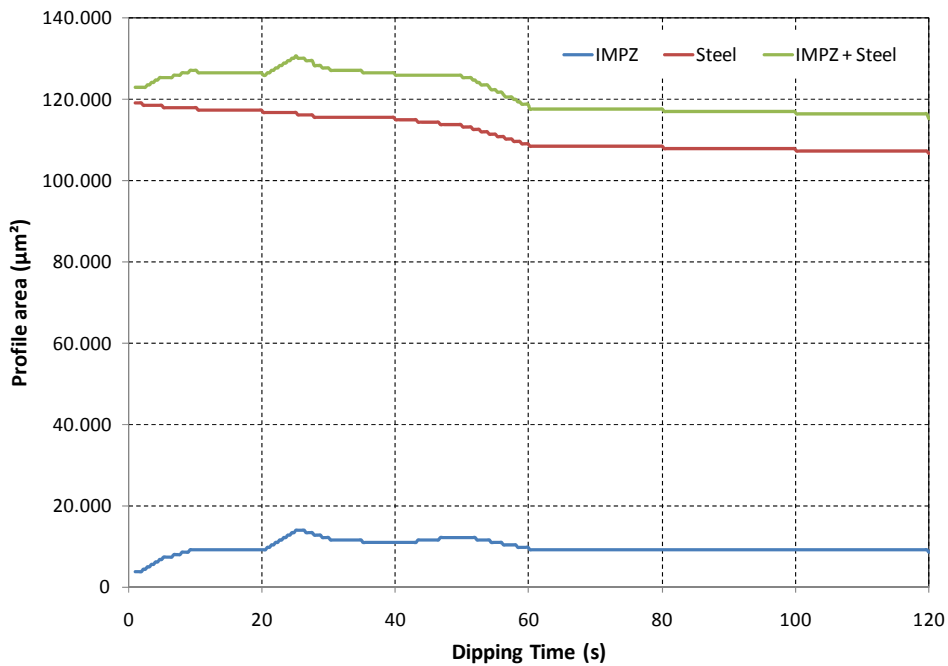


Figure 75: Dip experiments Al-7Si + 2 μm Zinc: Little decrease of the steel profile with increasing dipping time; Growing of the IMPZ stops after 10 seconds, thus results in a decreasing of the overall thickness Steel + IMPZ

To identify the emerging phases of the Al-7Si-Fe system, they were analyzed via EDX at single, largely formed recognizable phases (Figure 76). Table 12 shows the EDX-results of the intermetallic phases after 5 s (left image) and 120 s dipping time (right image).

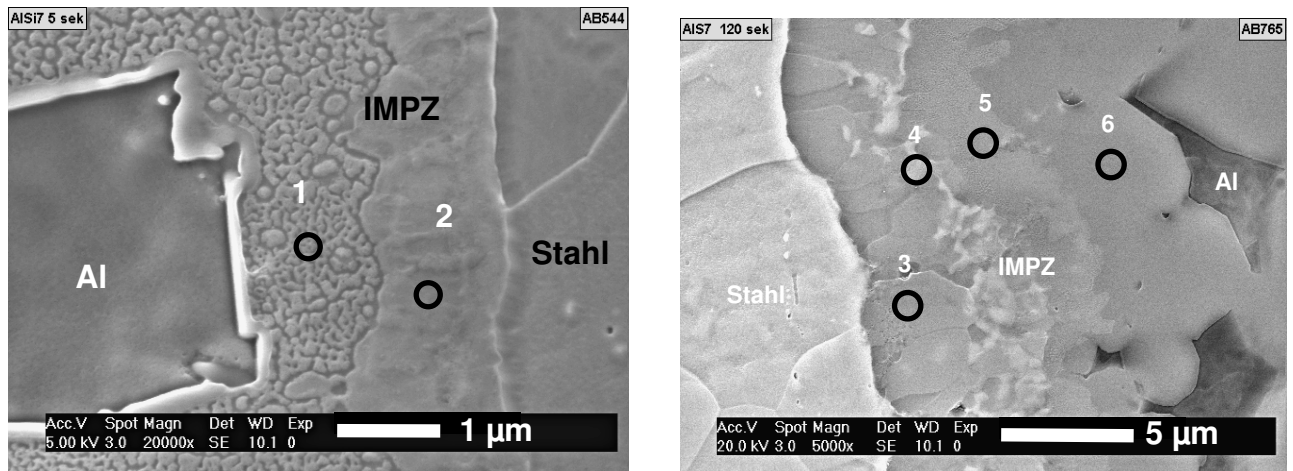


Figure 76: S Dip experiments Al-7Si: EM picture (secondary electrons (SEM-SE)) of an ion beam etched profile from Steel-Al-7Si after 5 seconds (left) and 120 seconds (right) dipping time: τ_5 and Al_5Fe_2 could already be identified after 5 seconds dipping time.

Table 12: Dip experiments Al-7Si: EDX analysis from the six in Figure 76 marked points conform to the phases $(\text{Al}_{1-x}\text{Si}_x)_5\text{Fe}_2$, $\text{Fe}_{25}\text{Al}_{60}\text{Si}_{15}$, $(\text{Al}_{1-x}\text{Si}_x)_3\text{Fe}$ and $\text{Fe}_2\text{Al}_7\text{Si}$ (τ_5).

Analysis	Phase	Al at%	Fe at%	Si at%	Zn at%
1	$\text{Fe}_2\text{Al}_7\text{Si}$ (τ_5)	70.2	20.6	9.1	-
2	$(\text{Al}_{1-x}\text{Si}_x)_5\text{Fe}_2$	66.5	5.0	28.5	-
3	$(\text{Al}_{1-x}\text{Si}_x)_5\text{Fe}_2$	70.2	27.5	2.2	0.7
4	$\text{Fe}_{25}\text{Al}_{60}\text{Si}_{15}$	55.5	29.1	15.5	-
5	$(\text{Al}_{1-x}\text{Si}_x)_3\text{Fe}$	72.8	22.7	4.3	-
6	$\text{Fe}_2\text{Al}_7\text{Si}$ (τ_5)	71.9	18.9	9.3	-

Analysis of the chemical composition of these phases that formed during the dipping tests shows a complex menagerie of phases. Most of the time four different phases have been identified:

- $\text{Fe}_2\text{Al}_7\text{Si}$ (τ_5)
- $(\text{Al}_{1-x}\text{Si}_x)_5\text{Fe}_2$
- $\text{Fe}_{25}\text{Al}_{60}\text{Si}_{15}$
- $(\text{Al}_{1-x}\text{Si}_x)_3\text{Fe}$

4.4.1.5.2 Dipping experiments of an etched steel strip in Al-7Si

Figure 77 shows the evolution of the steel strip thickness over time. The IMPZ is present already at the beginning of the dipping (1 s, seen on the left hand side) and stays at a constant width from 5 s on as Figure 78 depicts.

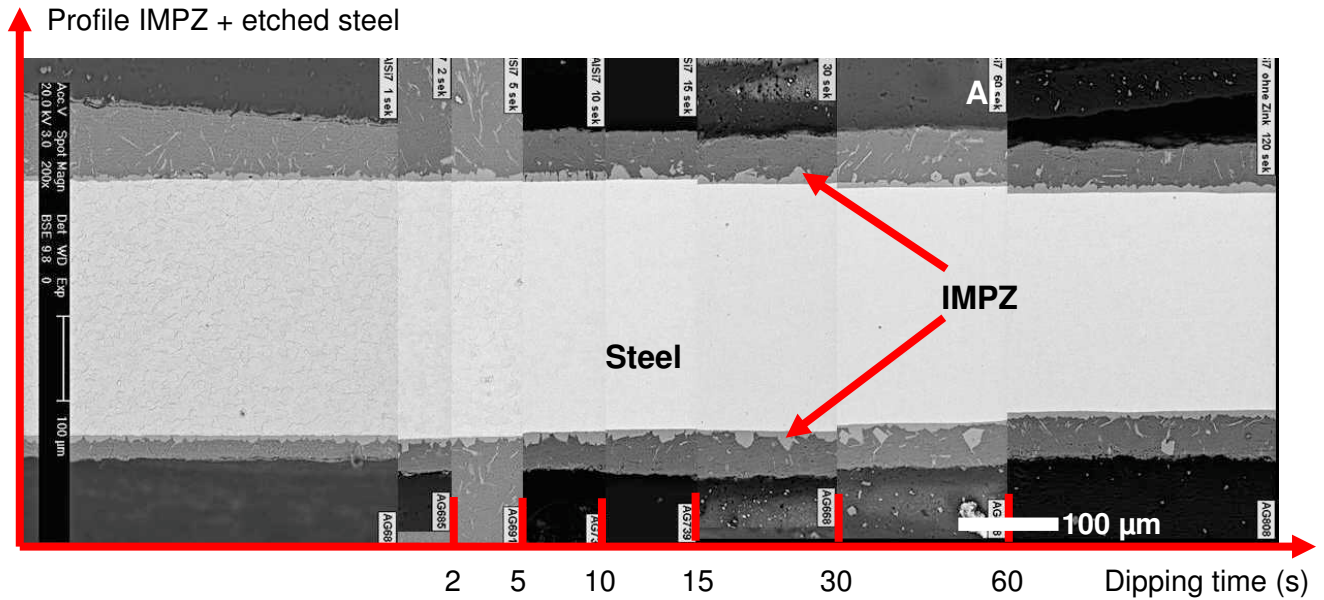


Figure 77: Dip experiments Al-7Si: Sequence of SEM pictures from the ion beam etched profile of pickled steel and Al-7Si with different dipping times: Light decrease of steel profile; Continuous formation of IMPZ on both sides after 1 seconds dipping time; No growth of the IMPZ after 5 seconds

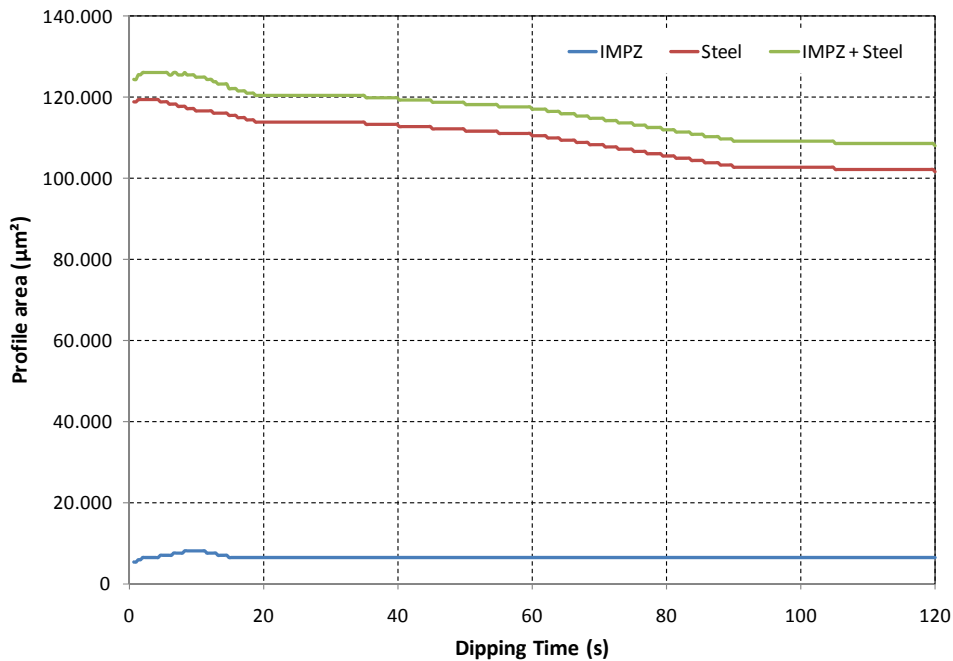


Figure 78: Dip experiments Al-7Si + pickled: Both steel profile as well as overall thickness (steel + IMPZ) decreases during the 120 seconds dipping time. The width of the IMPZ does not change after the first 5 seconds

The IMPZ formation after already one second is the biggest difference between the etched steel strip and the Zn-coated steel strip where the interface emerges only after 5 to 10 s on both sides.

4.4.1.5.3 Dipping experiments of a steel strip with 2 μm Zn-coating in Al-12Si

The formation of the IMPZ as well as the cross-sectional reduction of the Zn-coated steel strip upon dipping into the Al-12Si melt show at the beginning a similar behavior than in the Al-7Si melt. Not until a dipping time of 10 s and more the IMPZ emerges on both sides of the insert. Additionally the reduction of the cross-sectional area of the steel strip is again much slower compared to the experiments with the binary alloys of Al-7Cu, Al-7Mg or Al99.97.

The main difference to the Al-7Si melt is the development of very long ($> 100 \mu\text{m}$) skewers into the Al-matrix after long dipping times as illustrated at the right edge of Figure 79. Even the morphology of the IMPZ is somewhat skewed at the interface.

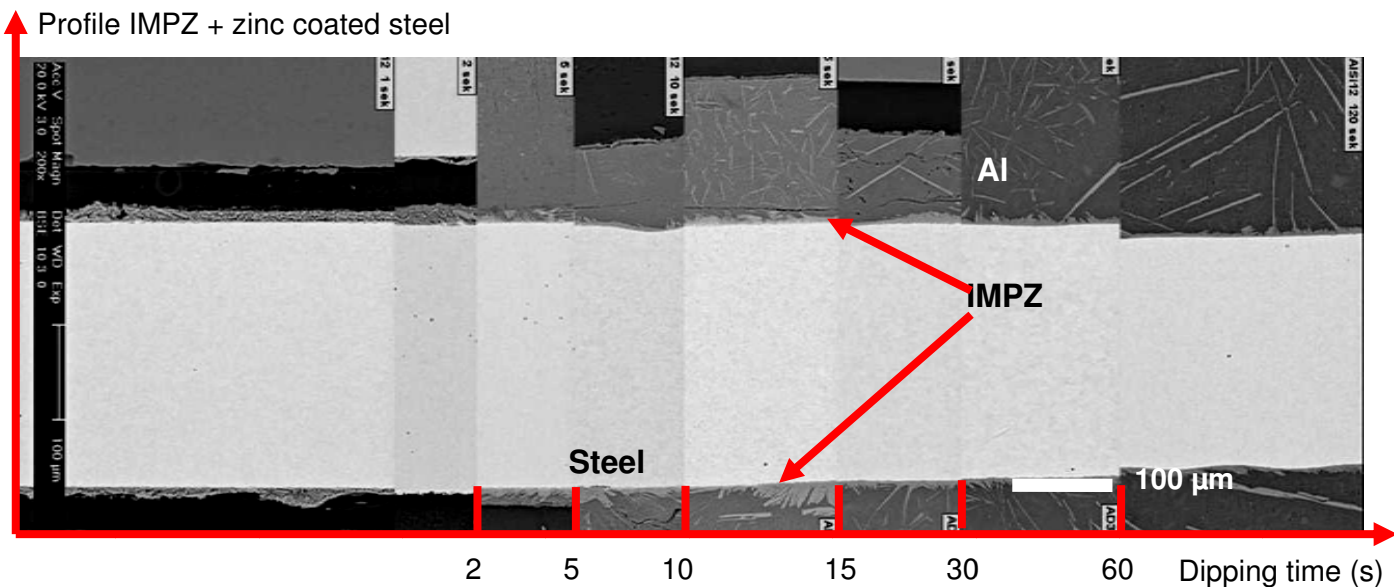


Figure 79: Dip experiments Al-12Si + 2 μm Zinc: Sequence of SEM pictures from the ion beam etched profile of steel and Al-12Si with different dipping times: Decrease of steel profile with increasing dipping time and double sided growing of IMPZ not before 5-10 seconds; Very long, bar-shaped dispersion into the Al-Matrix, which grow with increasing dipping time.

In Figure 80 the very slow reduction of the steel with is depicted. The Figure also shows that the IMPZ is formed after about 5 s and stays constant afterwards.

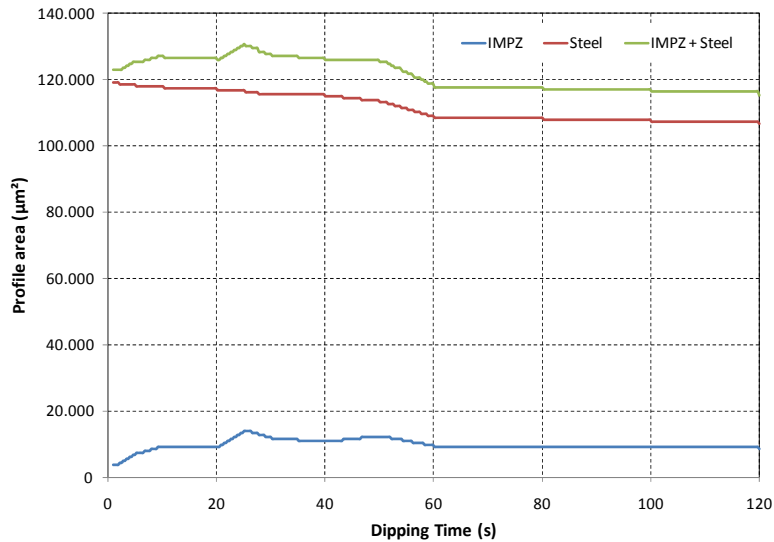


Figure 80: Dip experiments Al-12Si + 2 µm Zinc: Growing of the IMPZ until 5 seconds dipping time, following the width of IMPZ is constant; The steel profile and the overall thickness (steel + IMPZ) decrease with increasing dipping time.

4.4.1.5.4 Dipping experiments of an etched steel strip in Al-12Si

The formation of the IMPZ as well as the cross-sectional reduction of the etched steel strip upon dipping into the Al-12Si melt shows a similar behavior like a Zn-coated steel strip. Again the IMPZ is formed after about 5 s and stays constant afterwards as Figure 82 depicts.

However there are differences of the etched steel strips compared to the Zn-coated ones as can be clearly seen in Figure 81 an even formation of the IMPZ on both sides is already present after 1 second as well as a good connection to the aluminum, and the long skewer like phases in the Al-matrix are present even after 5 s.

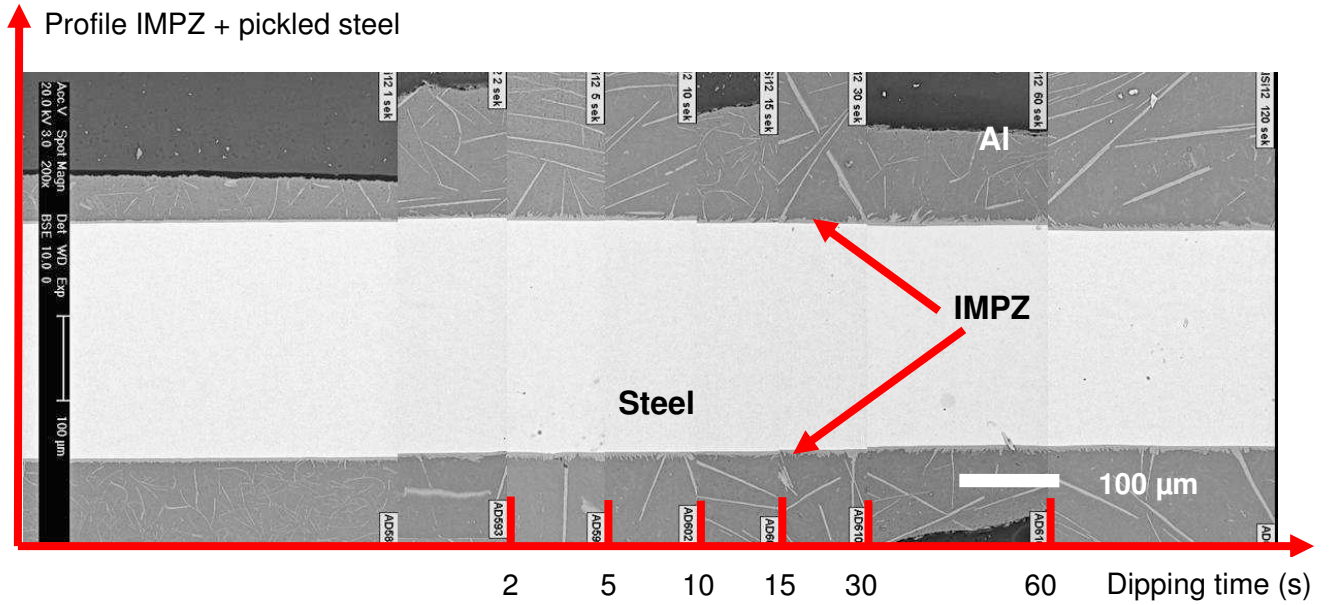


Figure 81: Dip experiments Al-12Si + pickled: Sequence of SEM pictures from the ion beam etched profile of pickled steel and Al-12Si with different dipping times: Smooth growing of the IMPZ already after 1 second dipping time; Good connection to the Al-Matrix.

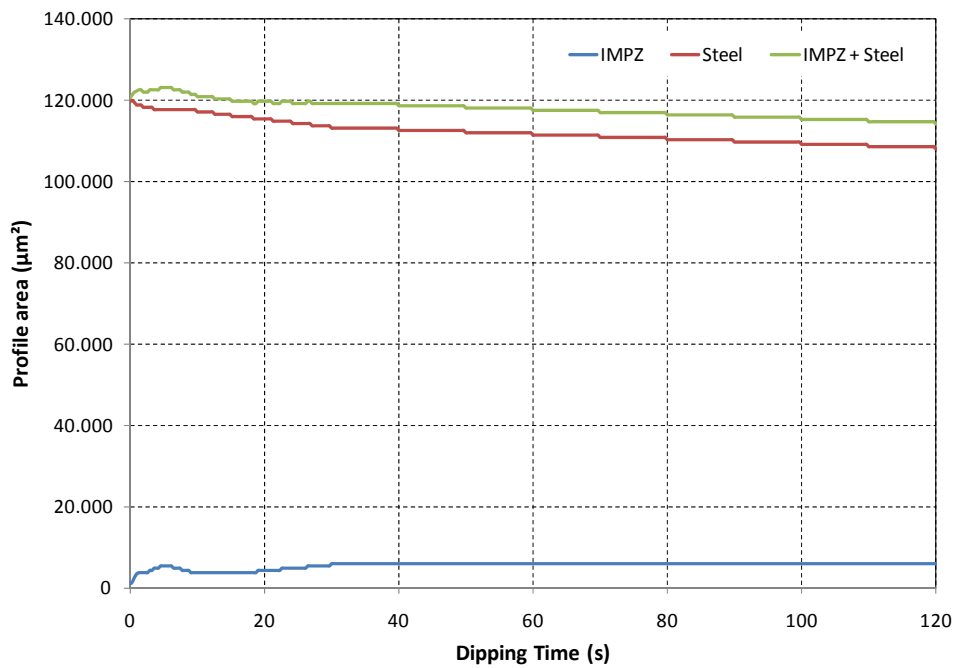


Figure 82: Dip experiments Al-12Si + pickled: Trend of the thickness of IMPZ and steel profile: The very thin IMPZ is constant after 5 seconds dipping time. Slow decrease of steel profile with increasing dipping time.

4.4.1.5.5 Dipping experiments of a steel strip with 2 μm Zn-coating in Al-17Si

Comparable with the dipping trials of the Zn-coated steel strips in Al-7Si and Al-12Si there are issues during the IMPZ formation in the beginning 5-10 s and therefore a good Al-Fe connection exist only afterwards. Since this binary alloy is hyper-eutectic, primary Si precipitates can be observed near the steel surface (shown in Figure 83).

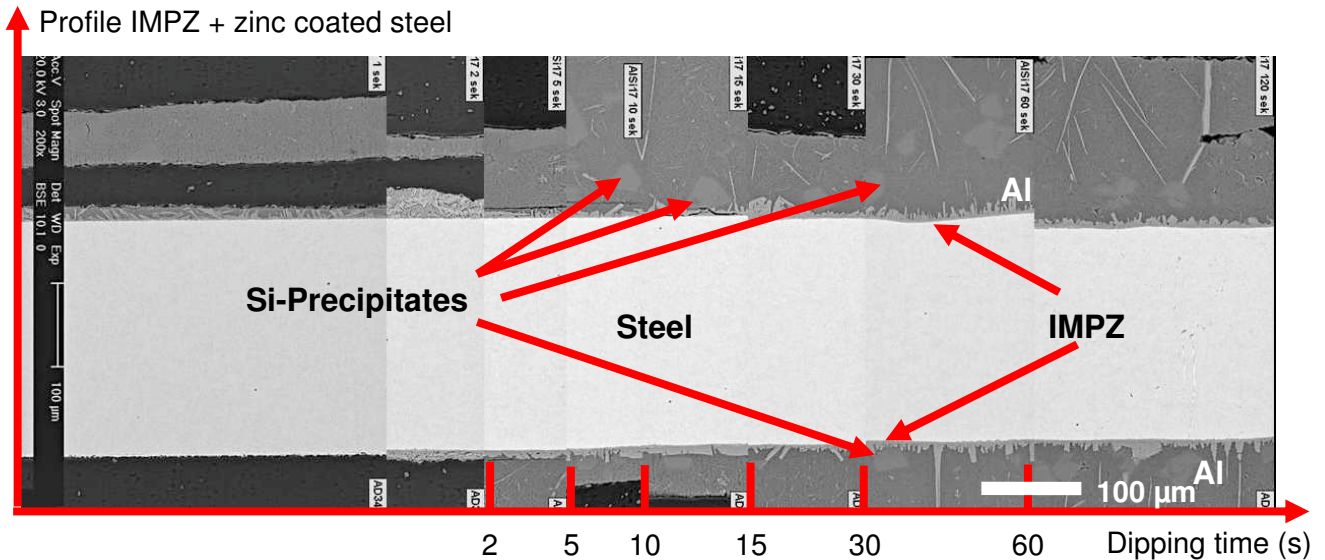


Figure 83: Dip experiments Al-17Si: Sequence of SEM pictures from the ion beam etched profile of steel and Al-17Si with different dipping times: Both-sided growing of the IMPZ and connection to the Al-Matrix not before 5-10 seconds. Primary Si dispersions (bright gray areas) at the border to steel.

Again, the formation of the IMPZ is unsteady. Figure 84 shows that the IMPZ stays constant after about 5 to 10 s while the steel gradually dissolves into the melt.

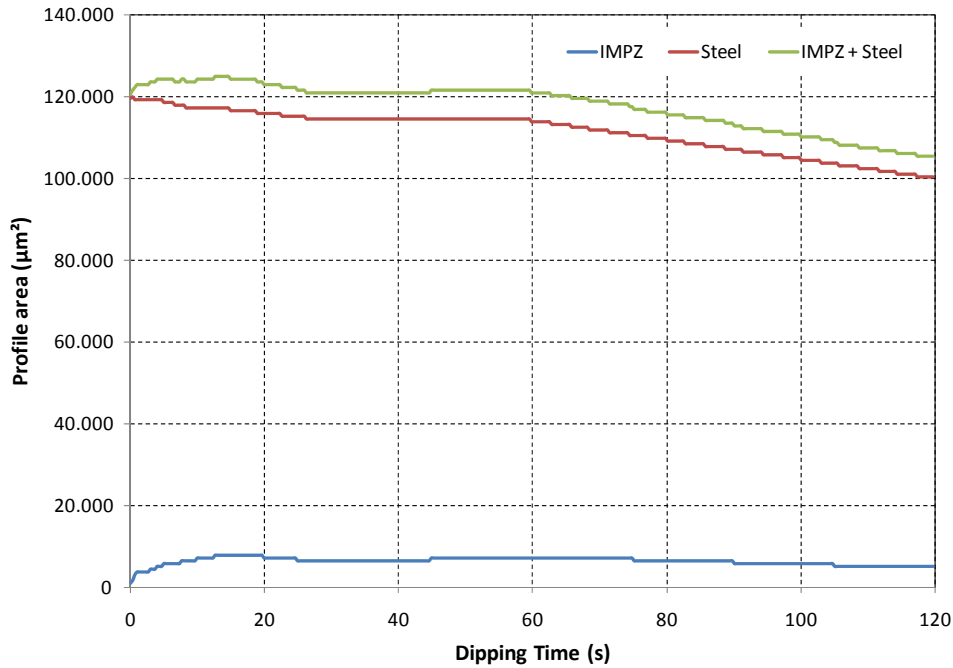


Figure 84: Dip experiments Al-17Si + 2 µm Zinc: Trend of the thickness of IMPZ and steel profile: The IMPZ is constant after 5 seconds dipping time. Slow decrease of steel profile with increasing dipping time.

4.4.1.5.6 Dipping experiments of an etched steel strip in Al-17Si

An even formation of the IMPZ on both sides is already present after 1 second similar to the results of the experiments with the alloys Al-7Si and Al-12Si with an etched steel strip. It has to be noted though, that the formation is not as regular as with Al-12Si. An increase of the width of the IMPZ with ongoing dipping time cannot be observed (Figure 85). The cross-sectional area of the steel strip decreases as the steel gradually dissolves into the melt.

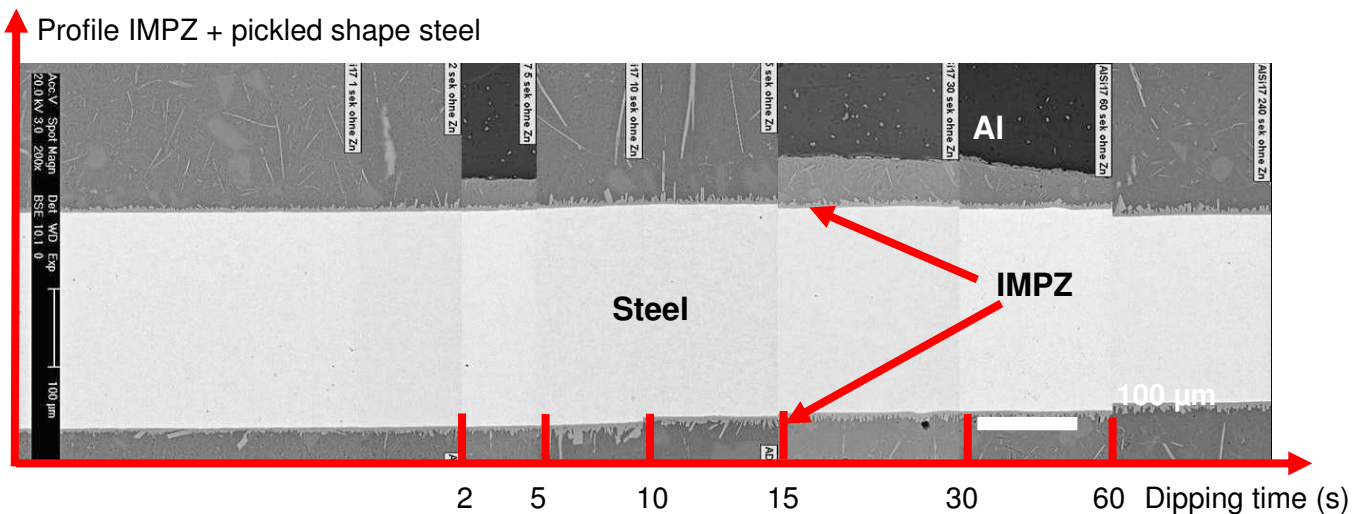


Figure 85: Dip experiments Al-17Si + pickled: Sequence of SEM pictures from the ion beam etched profile of pickled steel and Al-17Si with different dipping times: Decrease of the steel profile; Connection to the Al-17Si Matrix already after 1 second dipping time.

Figure 86 shows the familiar development of the steel strip thickness and the constant width of the IMPZ after a dipping time of 5 to 10 s.

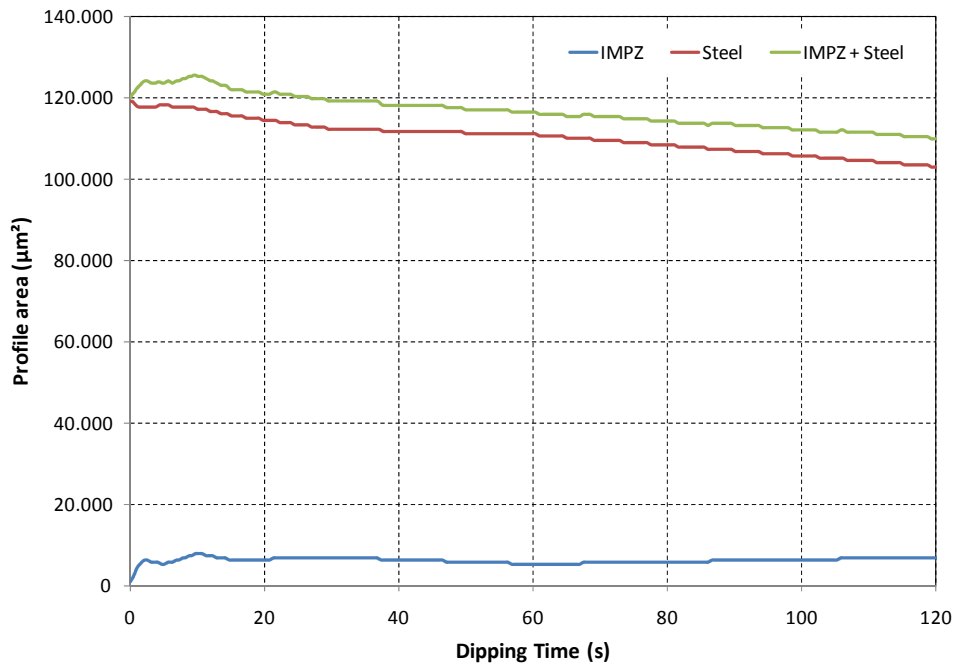


Figure 86: Dip experiments Al-17Si + pickled: Trend of the thickness of IMPZ and steel profile: The IMPZ is constant after 5 seconds dipping time. Slow decrease of steel profile with increasing dipping time.

4.4.1.6 Comparison of the dipping test results

In the following diagrams the development of the cross-sectional area of the steel strip (Figure 87) and the area increase of the intermetallic phase zone (Figure 88) are shown for the dipping trials in molten Al99.7 and the binary alloys Al-7Cu, Al-7Mg, Al-7Zn and Al-7Si.

As can be seen the dissolution of steel into the melt is fastest in the binary alloy Al-7Zn and the slowest dissolution rate happens in Al-7Si. Cu in the alloy reduced the reduction of the cross-sectional area of the steel strip as well, while Magnesium has relatively little influence when talking Al99.7 as reference.

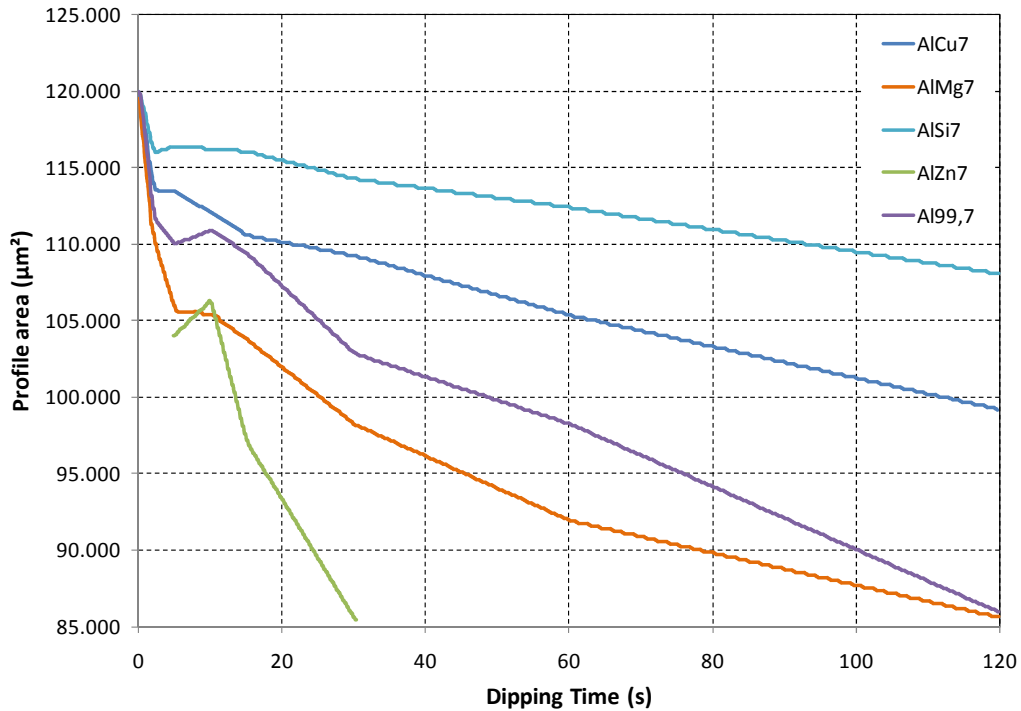


Figure 87: Decrease of the steel profile area during dipping into Al-7Cu, Al-7Mg, Al-7Si, Al-7Zn and Al99.7

The growth of the IMPZ is lowest with the binary alloy Al-7Si followed by Al7-Cu. Interestingly the IMPZ formation speed of Al-7Zn is similar to the one in pure aluminum Al99.7 even though steel dissolves much quicker in the Zn containing melt.

Contrary to this the IMPZ of the binary alloy Al-7Mg on the Al-Fe interface grows exceptionally fast while the steel dissolution is comparable to the one in pure aluminum Al99.7.

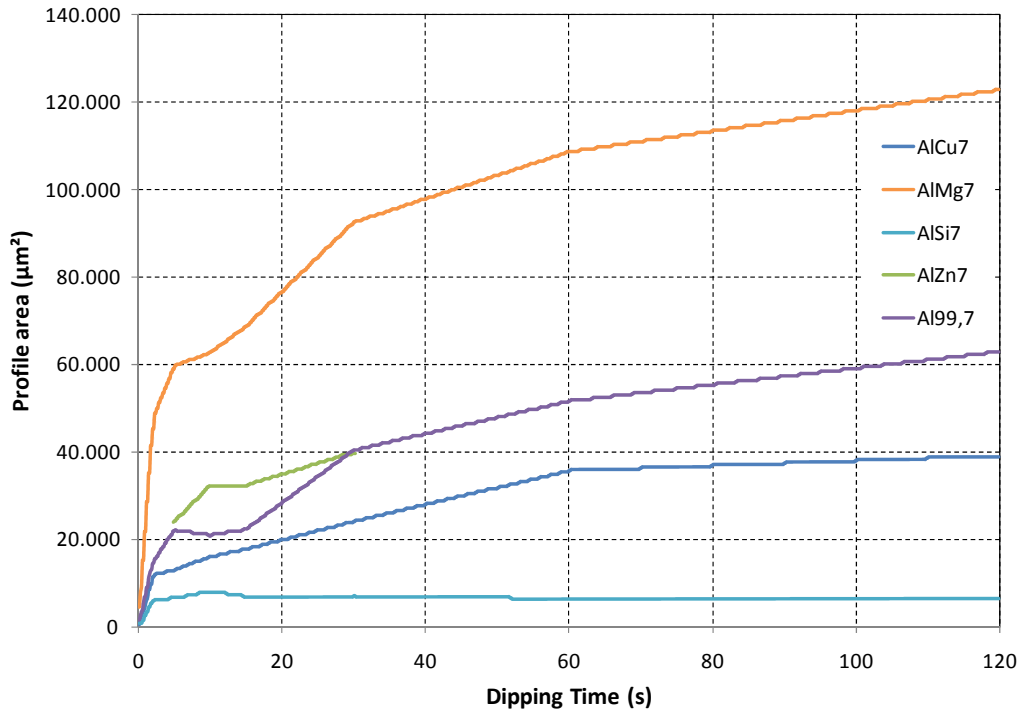


Figure 88: Increase of the IMPZ area during dipping into Al-7Cu, Al-7Mg, Al-7Si, Al-7Zn and Al99.7.

Summing up it can be stated that the thinnest IMPZ emerge with Al-7Si. In general intermetallic phases a brittle (especially Al-Fe phases as measured in this thesis) and therefore not wanted as a thick layer. This result of a thin intermetallic reaction zone encourages for producing Al-Fe composite castings in an industrial environment. However the irregular formation of the IMPZ and consequently the bonding between the partners after short contact (dipping) times has to be improved.

One possibility to generate a good bonding between a steel insert and an Al-Si alloy could be the usage of etched and oxide free steel surfaces. The comparison between etched and Zn-coated steel strips in otherwise constant experimental parameters is shown in Figure 89 and Figure 90. This allows the conclusion that a Zn-coating generally enhances a thicker IMPZ with time up to an eutectic Al-Si melt.

A further observation is that the development of the intermetallic phase zone is independent of the surface treatment of the steel surface (it has to be noted however, that the galvanic zinc coating is just 2 µm thick). The cross-sectional area of the steel strip is diminishing with increased dipping time in the melt, while at the same time the area of the IMPZ stays constant after 5 to 10 s at a low level.

These experiments have shown the crucial role of a third element in the liquid partner of a compound casting in the Al-Fe system. Via simultaneous formation of several different

phases in the system Al-Si-Fe during dipping in the melt, those phases interfere with each other and therefore grow at a slower rate as elements that form no or few additional phases compared to the pure Al-Fe system. Therefore the total thickness of the IMPZ in the Al-Si-Fe system is lower.

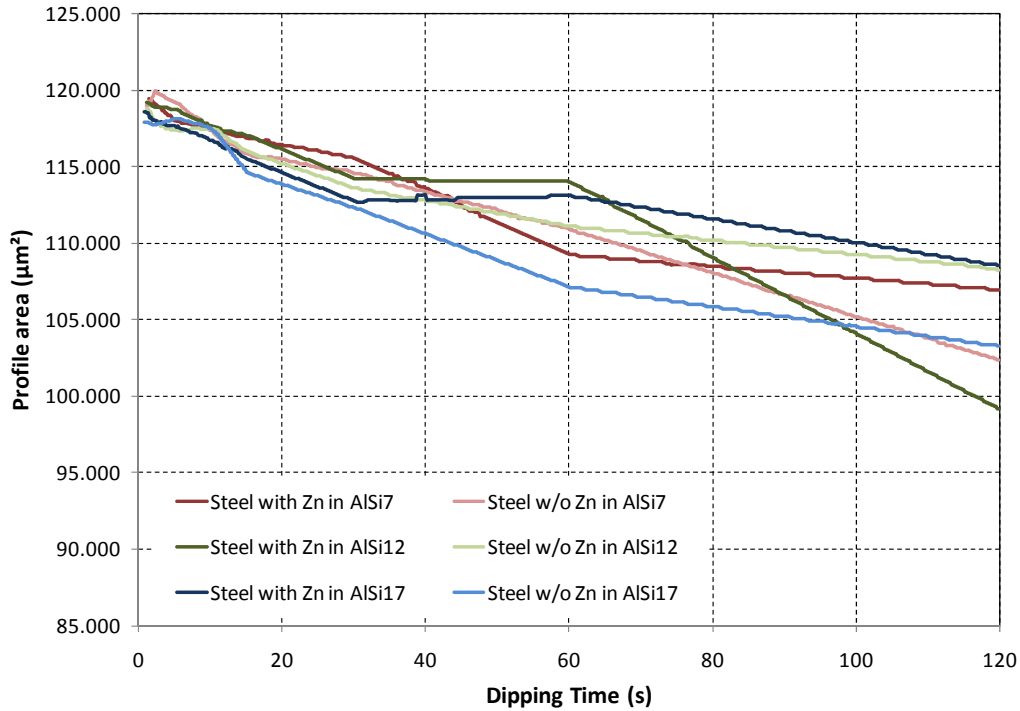


Figure 89: Comparison of steel profile transformation while dipping in Al-7Si, Al-12Si and Al-17Si (steel profile each zinc coated/not coated).

By varying the silicon content of the binary alloy from 7 to 12 to 17 (hypo-eutectic, eutectic and hyper-eutectic) the main difference is in the even formation of the IMPZ after a short dipping time with different surface treatment of the steel strip: With a Zn-coated steel surface an even IMPZ emerges after 5 to 10 s while etched steel strip produce an IMPZ after already 1 s exposure time in the corresponding melt as can be seen in Figure 90.

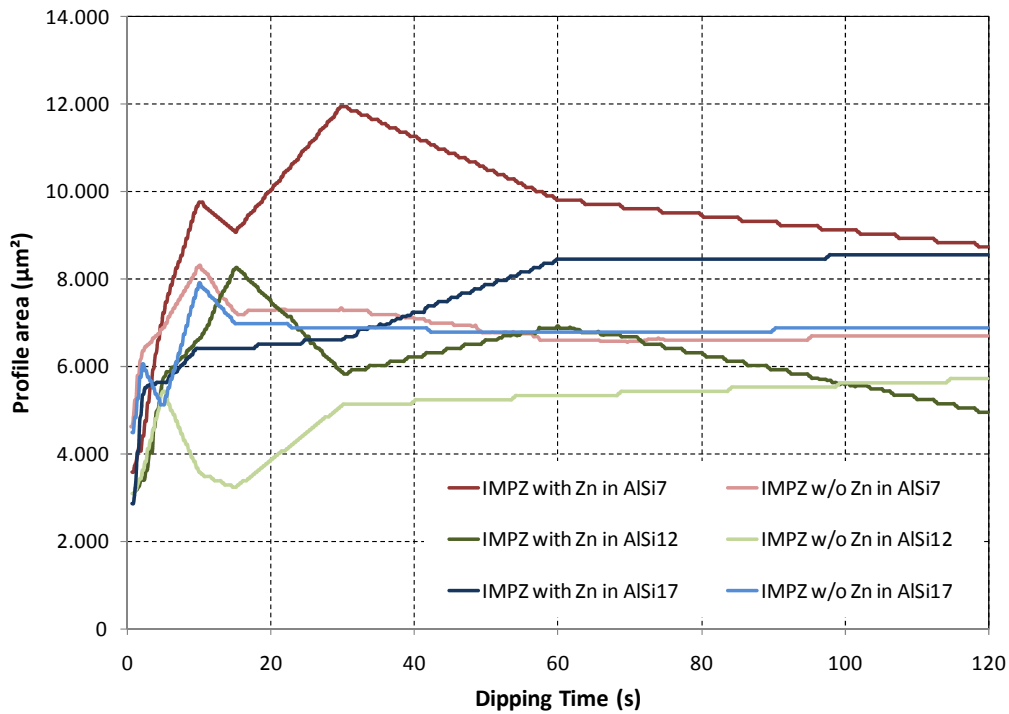


Figure 90: Trend of the steel profile and the dispersion and transformation of the IMPZ with different preprocessed steel surfaces and different Al-Si alloys

For production of Al-Fe composite castings etching the Zn-coating away from the steel insert is not favorable if oxidation until the recasting cannot be eliminated. However if the steel insert does not see a high temperature before casting, an etched insert could possibly have an advantage for interface formation. Another advice would be to make the Zn-coating as thin as possible.

4.4.1.7 Dipping experiments in commercial Al-alloys

After these promising results of the dipping tests in binary alloys two commercial Al-X systems were tried out. These were the technical alloys AlSi7Mg0.3 and AlMg5Si2Mn, which means that now the system is not ternary any more but quaternary. [68-70]

4.4.1.7.1 Dipping experiments in AlSi7Mg0.3 (A356)

Figure 91 shows the development of the cross-section of the dipping tests in a commercial AlSi7Mg0.3 alloy: With time the thickness of the steel strip reduces while the IMPZ stays constant after already 2 s. However it can be observed that the IMPZ is not present everywhere in the examined area - there are spots where no intermetallics are formed (left image border). It can be stated that whereas the IMPZ stays constant over time, the growth of it is inhomogeneous.

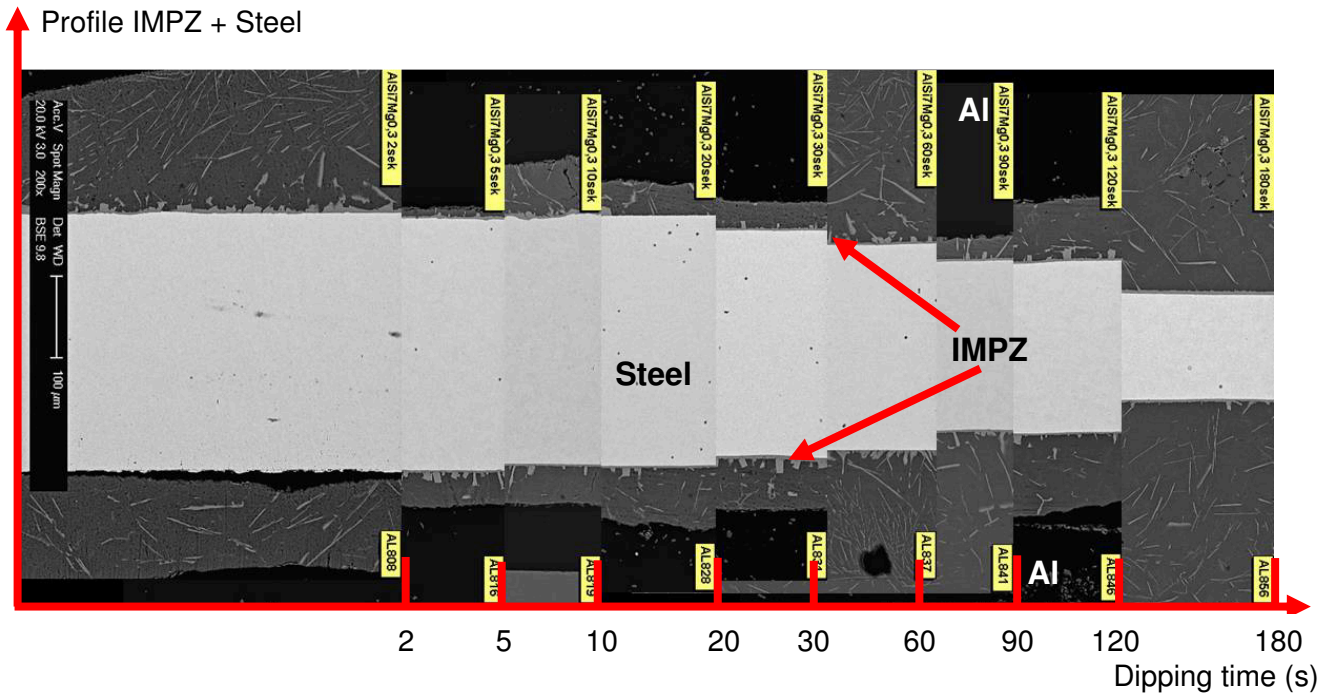


Figure 91: Dip experiments AISi7Mg0.3: Sequence of SEM pictures from the ion beam etched profile of steel and AISi7Mg0.3 with different dipping times: Decrease of the steel profile and constant thickness of IMPZ with increasing dipping time.

The overview of the width of the steel strip and the IMPZ are illustrated in Figure 92. While the steel thickness reduces linearly with time after 5 s insertion into the AISi7Mg0.3 melt, the thickness of the IMPZ stays at a very low level along the whole dipping time.

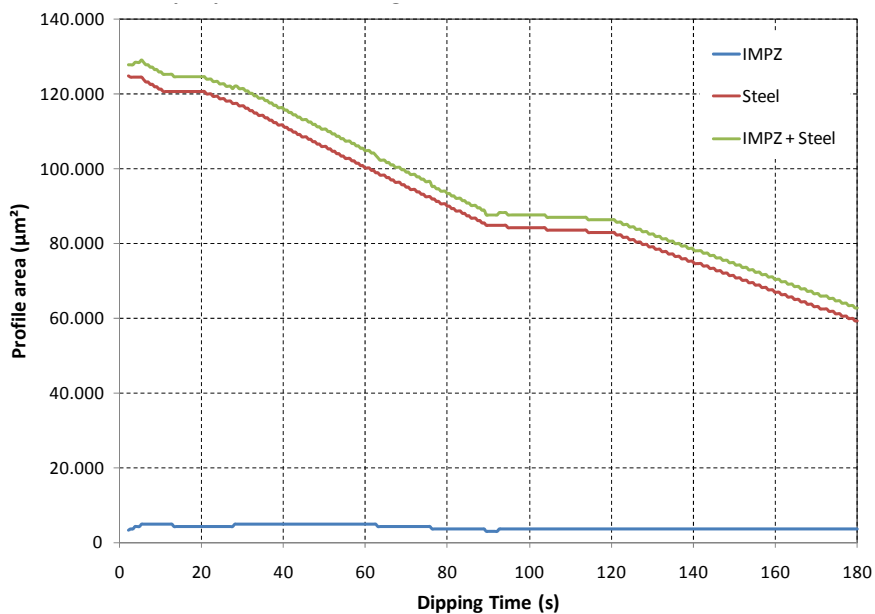


Figure 92: Dip experiments AISi7Mg0.3: Constant thickness of IMPZ and decreasing thickness of steel profile with increasing dipping time. The overall thickness (steel + IMPZ) decreases. The steel profile decreases linearly.

4.4.1.7.2 Dipping experiments in AlMg5Si2Mn (Magsimal59)

The so called Magsimal59 (common trade name), or better AlMg5Si2Mn is a cold hardening aluminum high pressure die casting alloy with very good mechanical properties without any heat treatment (casting condition F) for safety critical parts (even for dynamic loading).

The formation of the IMPZ during the dipping experiments is similar to the AlSi7Mg0.3. Nonetheless there are some differences: The IMPZ is more uniform and a bit thicker as can be seen in Figure 93 and Figure 94.

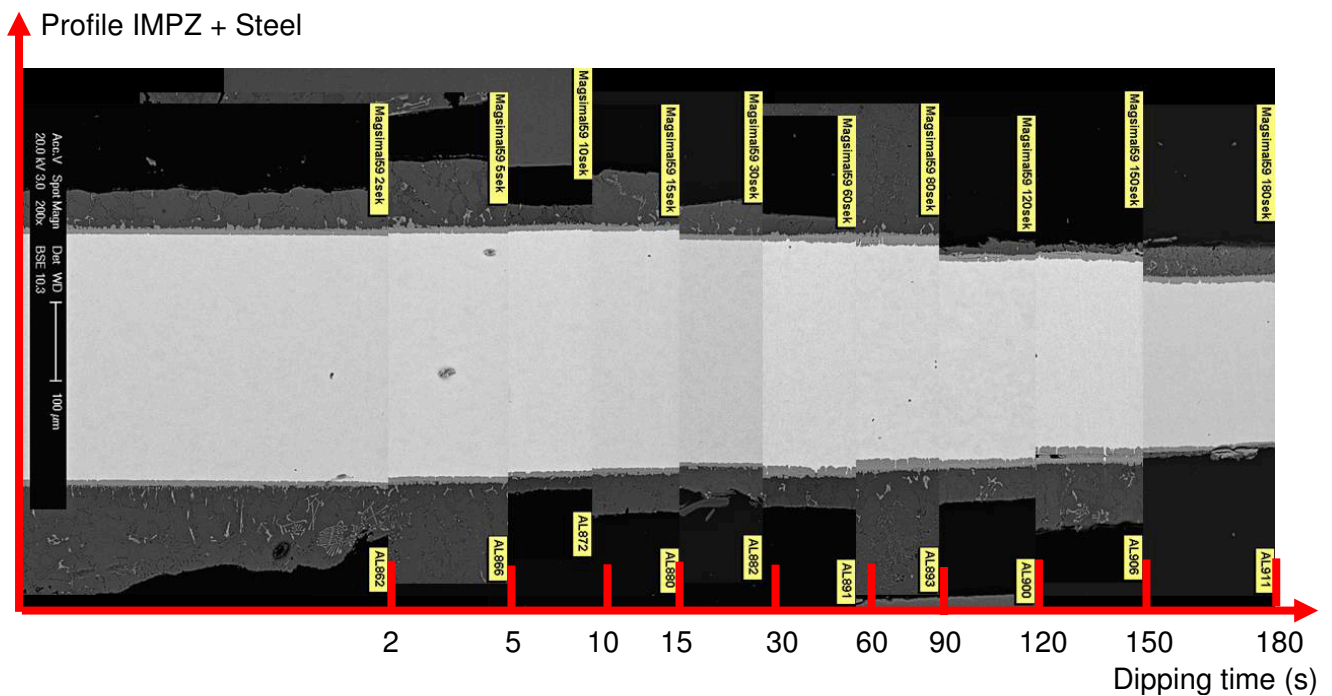


Figure 93: Dip experiments AlMg5Si2Mn: Sequence of SEM pictures from the ion beam etched profile of steel and Magsimal59 with different dipping times: Light respectively no growing of the IMPZ and decrease of the steel profile with increasing dipping time.

Looking at Figures 91 to 95 reveals that the combination of silicon and magnesium being simultaneously present in the melt make the Al-Fe system much more complex for compound casting: While a little amount (0.3 %) of Mg in the AlSi7Mg system reduce the homogeneity and thickness of the intermetallic layer compared to the trials made with the binary alloy Al-7Si, a magnesium content of 5 % in the presence of 2 % silicon resembles much more the Al-7Si alloy dipping results than the ones from the system Al-7Mg with iron. This proves that even small amounts of an additional element can change the game for compound casting significantly when one seeks to get a chemical bonding between the binding partners. Unfortunately this means that from these results no deduction to other alloy systems (such as the commonly used alloy AlSi9Cu3Fe, where additionally Mg and Zn are present) can be made.

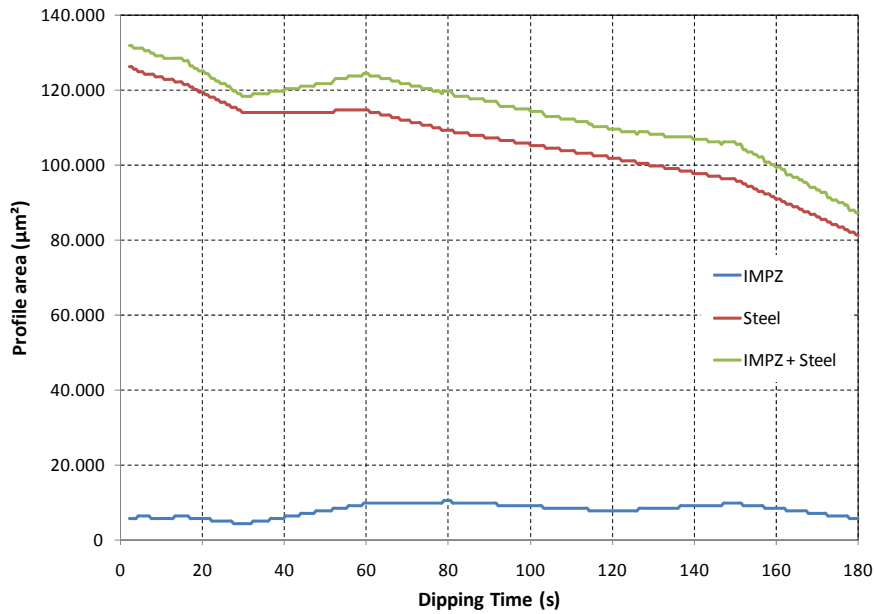


Figure 94: Dipping results of AlMg5Si2Mn (Magsimal59): Light respectively no growing of the IMPZ and decrease of the steel profile with increasing dipping time. The overall thickness (Stahl + IMPZ) decreases during the dipping time.

Below Figure 95 depicts the difference of the steel dissolution between the two commercial alloys AlSi7Mg0.3 and AlMg5Si2Mn. While at first 30 seconds (during the interface layer buildup) the dissolution of steel is equal, the Magsimal59 alloy forms a more dense IMPZ that reduces diffusion speed of the Fe atoms into the melt compared to the A356 alloy.

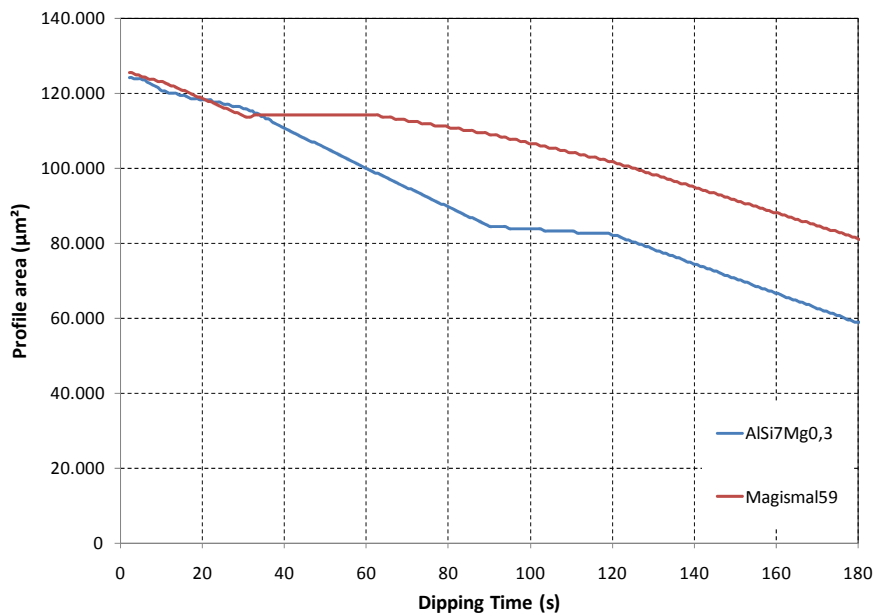


Figure 95: Thickness changing of the steel strip during the dipping tests. The profile decreases faster while dipping in AlSi7Mg0.3 than in Magsimal59.

Comparing the nature of the IMPZ of Magsimal59 (AlMg5Si2Mn) with the binary alloys Al-7Mg and Al-7Si during dipping some differences can be observed. With the Magsimal59 alloy the IMPZ thickness stays constant which is similar to the behavior of the alloy Al-7Si.

However with the Al-7Si alloy the thickness of the steel strip reduces at a higher rate. The commercial alloy AISi7Mg0.3 shows similar IMPZ kinetics, but here the steel thickness decreases even faster than with the alloy Magsimal59.

During the SEM investigations it was discovered, that the emerging IMPZ phases got cracks and whole fragments were flaking off the interface layer (see Figure 96 right). After 180 s the thickness of the IMPZ is less than after a dipping time of 150 s. It is therefore very likely that the IMPZ that is formed with a commercial alloy is very brittle. After reaching a certain thickness, complete areas of the interface peel off. This cycle is repeating with ongoing dipping time.

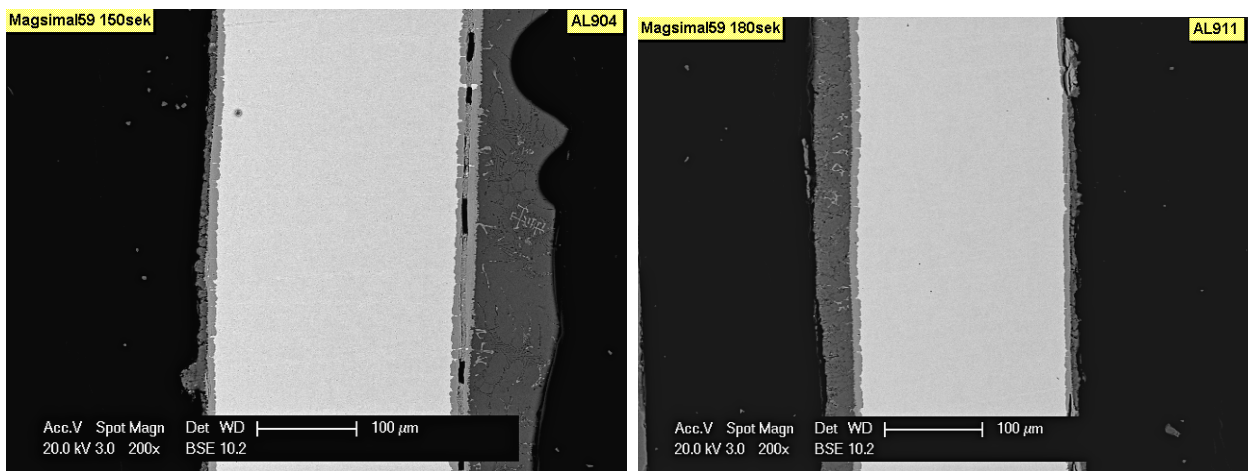


Figure 96: SEM pictures of the ion beam etched profile of steel and AISi7Mg0.3 after 150 seconds (left) and 180 seconds (right) dipping time.

After a closer look to the IMPZ between Magsimal59 and the steel strip cracks can be identified already after 10 s dipping time. These thereby separated areas show differences in the chemical composition as Figure 97 reveals. The intermetallic near the steel insert contains considerably more iron while the layer closer to the aluminum melt contains more aluminum as table 13 clearly shows. Some manganese is incorporated in this layer as well. It is conceivable that stresses between these different intermetallic layers lead to the separation.^[71-73]

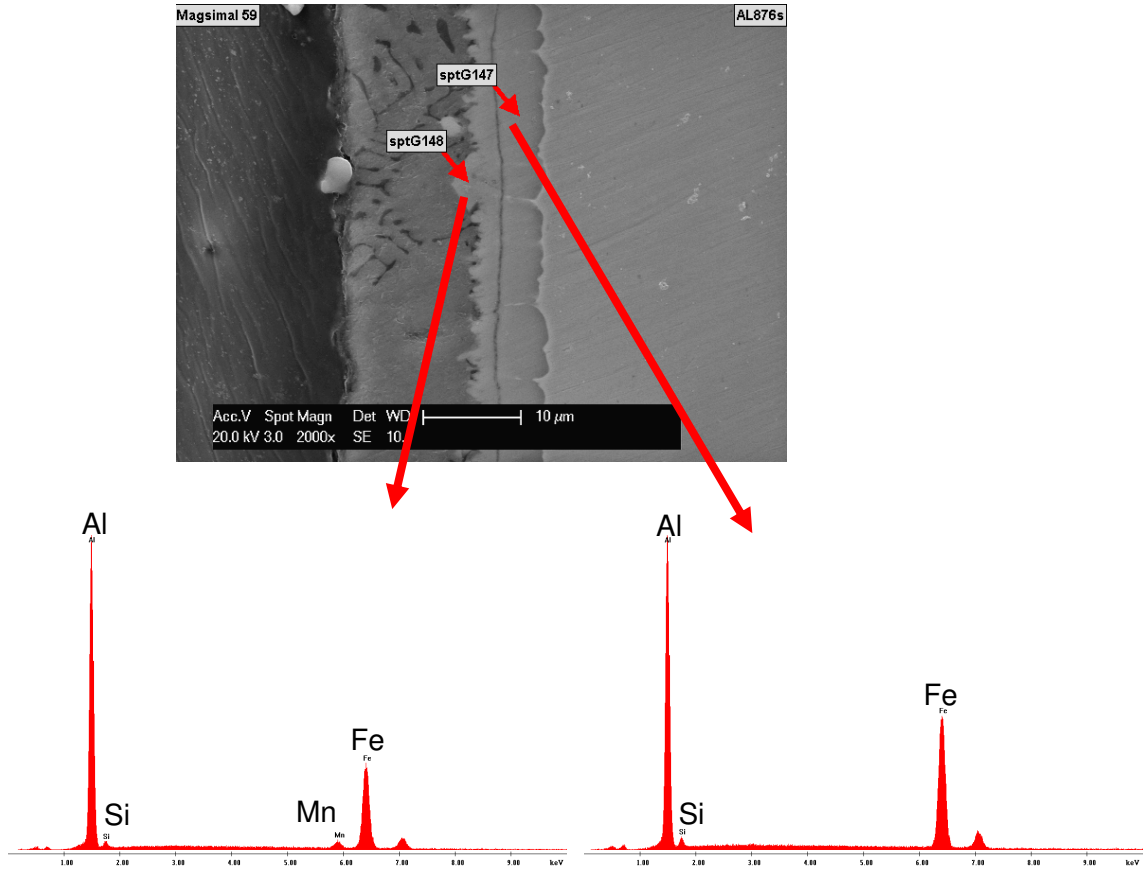


Figure 97: SEM pictures of the ion beam etched profile of steel and AlSi7Mg0.3 after 10 seconds dipping time and related EDX spectrum.

Table 13: EDX analysis of the marked points in Figure 97

Analysis	Al at%	Fe at%	Si at%	Mn at%
sptG147	59.6	38.5	2.0	-
sptG148	66.5	29.7	1.8	2.2

4.4.1.8 Influence of zinc coating thickness on interface formation

In this thesis the change in the bonding mechanism between Zn-coated and etched steel inserts were investigated. From this a further question arises: Is there an effect of different Zn-coating thickness on the IMPZ formation between steel and Al-7Si alloys?

To clarify this matter the steel strips were electro polished and galvanized with Zn. The thickness of the coatings were 5 μm , 10 μm , 15 μm , 20 μm and 25 μm . Dipping times were 1, 2, 5 and 10 seconds. The best result from an early optical examination seemed to be the steel strips with a Zn-coating of 15 μm thickness. Figure 98 shows the development of the IMPZ up to a dipping time of 10 s. Due to the relatively large amount of zinc (nearly 10 % of the total thickness of the immersed steel strip for 15 μm Zn-coating) the IMPZ formation is selectively accelerated as was described in the Al-7Zn/Fe system in this work. Looking more closely at the interface of these areas in which the steel dissolves rather quickly, an enrichment of Zn can be at the interface detected. This is again an indication the presence of Zn considerably enhances the dissolution of the steel into the aluminum melt.

Figures 99 and 100 show the difference of the interface reaction between two areas after a dip time of one second with corresponding EDX mappings. While Figure 99 shows an area where there is strong but unsteady interface reaction and heavy steel dissolution into the melt, in Figure 100 a desired reaction where an even and dense IMPZ is formed can be seen. As stated before, the mechanism for this behavior could not yet be pointed out and thus the reaction cannot be steered into the desired direction. Figure 101 shows the compound after a dip time of 10 seconds where Zn still can be found at the interface (last EDX mapping image on the right)

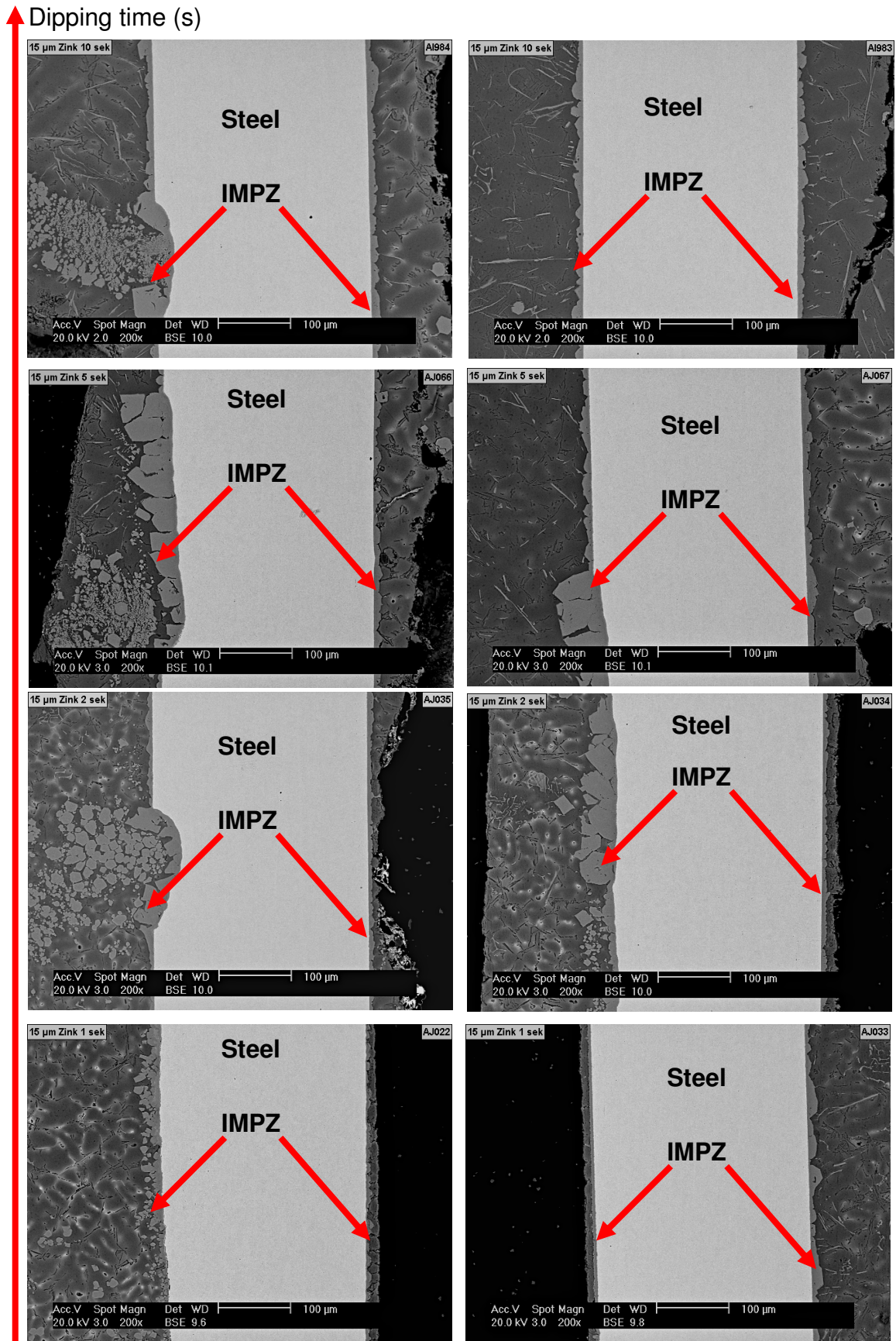


Figure 98: SEM/BSE pictures from the 15 μm zinc coated steel profile in Al-7Si up to 10 seconds dipping time: Unbalanced growing of IMPZ; Zn accelerate the fast dissolution in the steel profile.

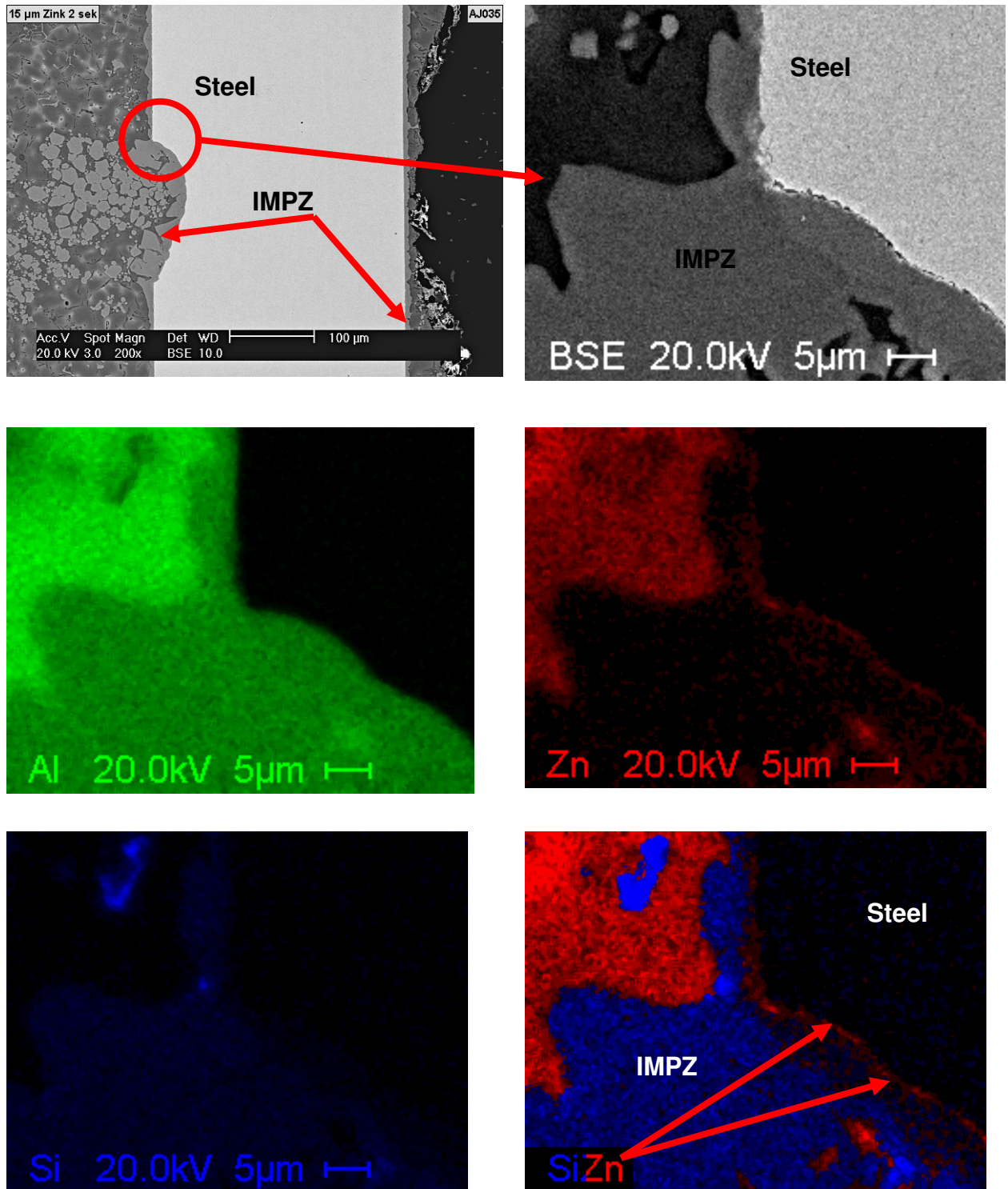


Figure 99: SEM/BSE pictures + EDX-Mappings of the elements Al, Zn and Si from the 15 µm Zinc coated steel profile in Al-7Si with 1 second dipping time: Especially in areas with heavy dissumption of steel there is no Zn at the boundary layer between steel and IMPZ (picture right bottom).

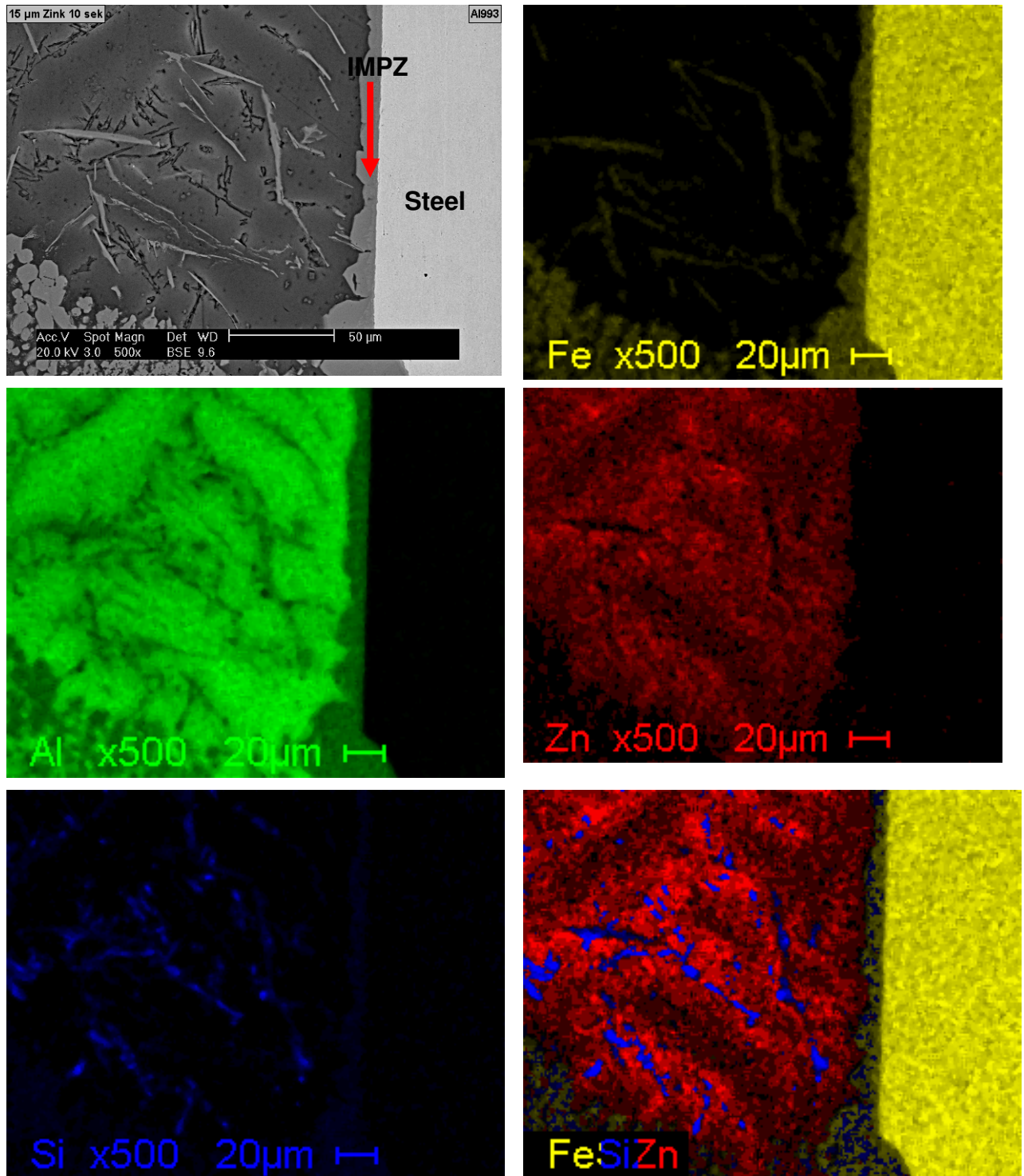


Figure 100: SEM/BSE pictures + EDX-Mappings of the elements Fe, Al, Zn and Si from the 15 µm Zinc coated steel profile in Al-7Si with 1 second dipping time: High concentration of Zn in the Al-Si alloy near the IMPZ. No Zn at the boundary layer steel/IMPZ is detectable.

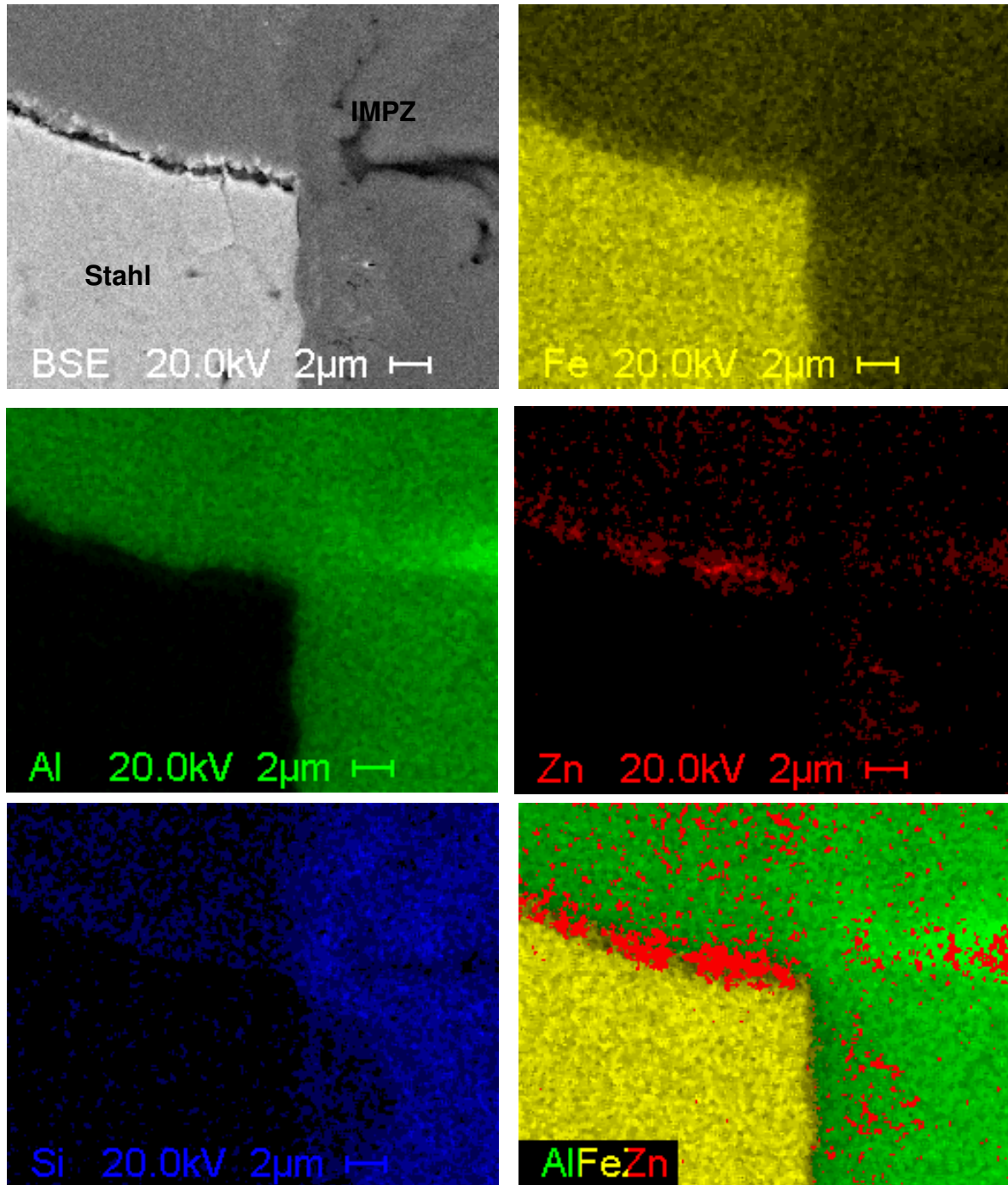


Figure 101: SEM/BSE pictures + EDX-Mappings of the elements Fe, Al, Zn and Si from the 15 μm Zinc coated steel profile in Al-7Si with 10 second dipping time: As seen in the 1 second dipped steel part also after 10 seconds dipping time Zn is detectable on the boundary layer steel/IMPZ where the steel profile dissipate very fast.

Figure 102 shows the development of the steel strip thickness and the formation of the IMPZ over time for the first 10 s for 5 μm thick Zn-coated steel strips dipped into Al-7Si. As can be observed, a continuous IMPZ emerges just after 10 s. Still, the width of the IMPZ is very irregular.

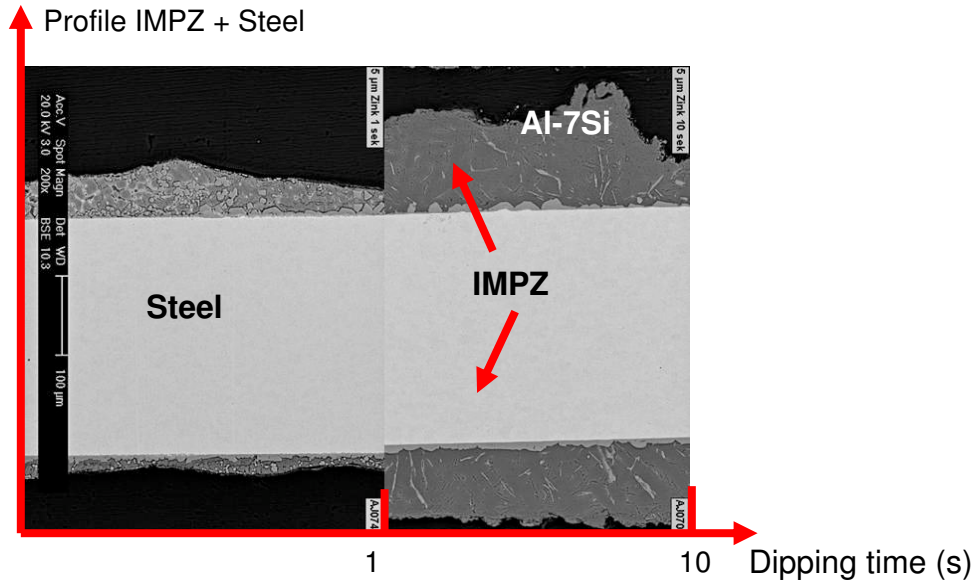


Figure 102: Sequence of SEM pictures from the ion beam etched profile of steel and Al-7Si with different dipping times: Steel with 5 μm zinc coat; Formation of IMPZ and decrease of the steel profile depending on the dipping time.

Figure 103 shows the development of the steel strip thickness and the formation of the IMPZ over time for the first 10 s for 15 μm thick Zn-coated steel strips dipped into Al-7Si. Again, the IMPZ width is inconsistent, but additionally in places an accelerated dissolution of the steel and therefore a reduction in the strip thickness could be recognized. These irregularities can be explained by the severe presence of Zn at the very beginning of the dipping experiment.

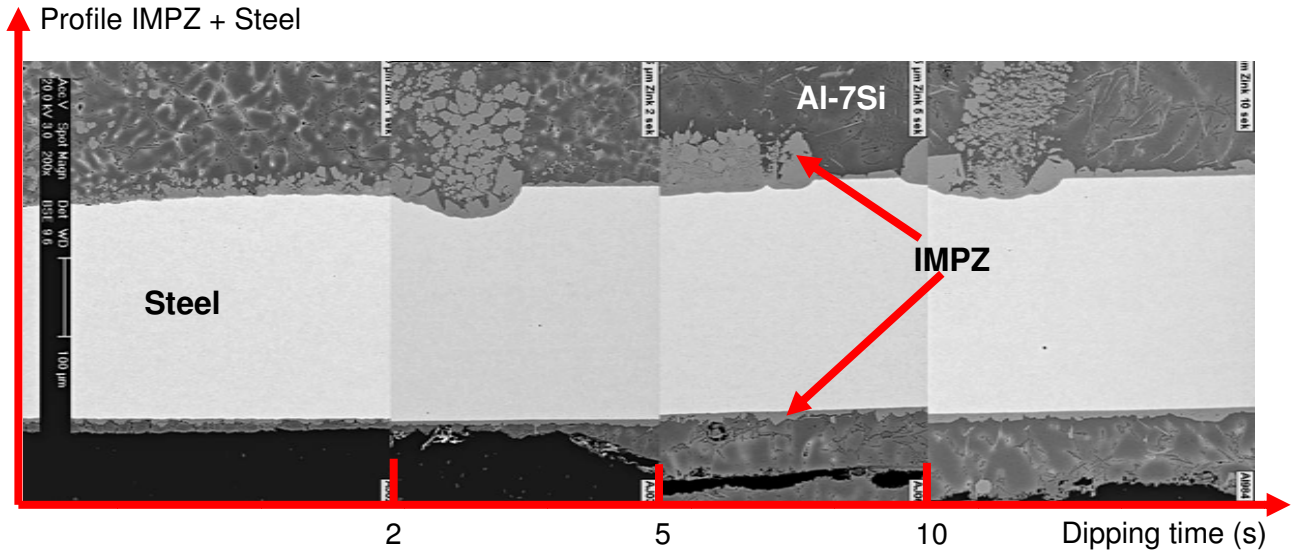


Figure 103: Sequence of SEM pictures from the ion beam etched profile of steel and Al-7Si with different dipping times: Steel with 15µm zinc coat; Formation of IMPZ and decrease of the steel profile depending on the dipping time.

The IMPZ which emerges after 1 second after dipping the 15 µm Zn-coated steel strip into the binary Al-7Si alloy is shown in Figure 104. Within the IMPZ two distinct areas can be clearly distinguished (left light gray, right dark gray). EDX analyses were performed to determine the chemical composition of these two phase regions. The results of these spot measurements (sptF, marked in Figure 104) are shown in Table 14: The lighter area is the $(Al_{1-x}Si_x)_5Fe_2$ phase which is additionally enriched with zinc. The darker region consists of Fe_2Al_7Si (T_5) and is enriched in Zn as well. It can be safely stated that with even shorter dipping times higher Zn contents would be found in the steel-IMPZ interface.

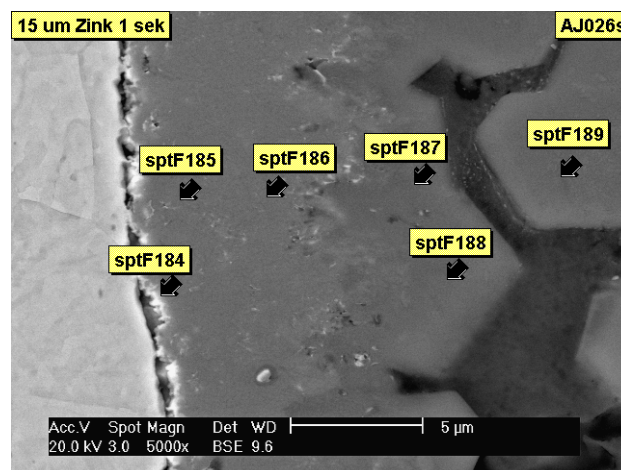


Figure 104: IMPZ, between steel and Al-7Si after 1 second dipping time. Chemical analysis were made on the marked points.

Table 14: Chemical composition of IMPZ at the points shown in Figure 104

Analysis	Al at%	Fe at%	Zn at%	Si at%	Phases
SptF184	52.9	37.7	7.0	2.5	$\text{Fe}_2\text{Al}_7\text{Si}$ (T_5)
SptF185	69.9	23.6	3.3	2.6	$\text{Fe}_2\text{Al}_7\text{Si}$ (T_5)
SptF186	70.9	23.4	2.2	3.6	$(\text{Al}_{1-x}\text{Si}_x)_5\text{Fe}_2$
SptF187	70.2	19.1	0.9	9.7	$(\text{Al}_{1-x}\text{Si}_x)_5\text{Fe}_2$
SptF188	69.1	19.7	1.0	10.2	$\text{Fe}_2\text{Al}_7\text{Si}$ (T_5)
SptF189	72.0	17.4	1.1	9.6	$(\text{Al}_{1-x}\text{Si}_x)_5\text{Fe}_2$

To put this result into relation Figure 105 depicts the IMPZ of steel and Al-7Si after 10 seconds of dipping time. Again the areas of the EDX spots are marked. Table 15 shows the results: In the IMPZ the following phases can be determined: $(\text{Al}_{1-x}\text{Si}_x)_5\text{Fe}_2$ and $\text{Fe}_2\text{Al}_7\text{Si}$ (T_5). Near the steel-IMPZ interface Zn enrichment up to 3 % can still be observed after 10 s. Still, the amount of Zn is lower that the results from the 1 s dipping specimen.

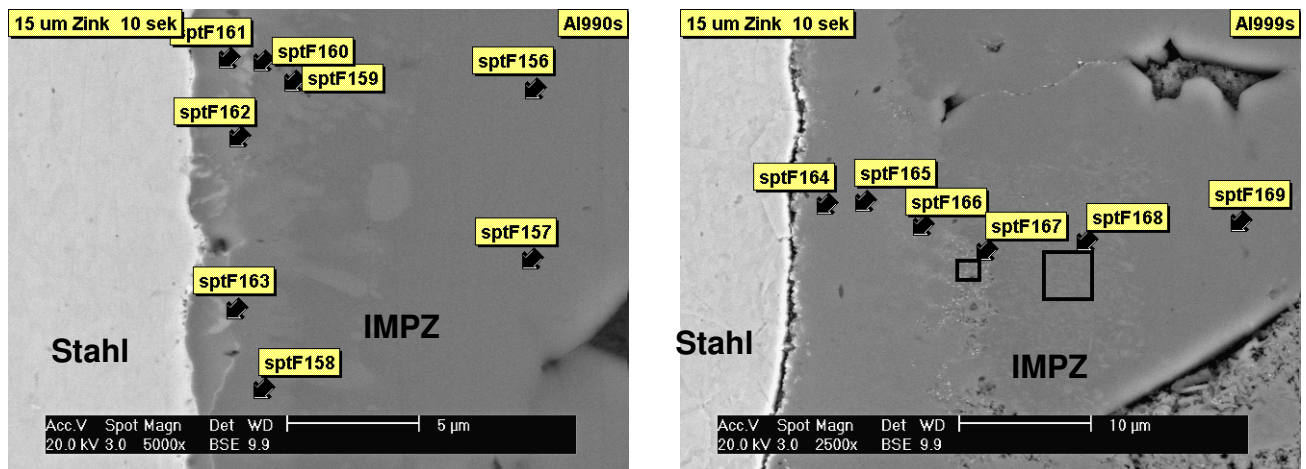


Figure 105: IMPZ, between steel and Al-7Si after 10 second dipping time. Chemical analysis were made on the marked points.

Table 15: Chemical composition of IMPZ at the points shown in Figure 105

Analysis	Al at%	Fe at%	Zn at%	Si at%	Phases
SptF156	69.5	21.4	-	9.0	Fe ₂ Al ₇ Si (T ₅)
SptF157	69.6	21.3	-	9.1	Fe ₂ Al ₇ Si (T ₅)
SptF158	70.4	26.7	-	2.9	(Al _{1-x} Si _x) ₅ Fe ₂
SptF159	70.4	25.5	1.0	3.2	(Al _{1-x} Si _x) ₅ Fe ₂
SptF160	59.7	29.5	1.1	9.8	Fe ₂ Al ₇ Si (T ₅)
SptF161	63.3	32.4	2.1	2.2	(Al _{1-x} Si _x) ₅ Fe ₂
SptF162	63.8	31.6	2.1	2.4	(Al _{1-x} Si _x) ₅ Fe ₂
SptF163	59.1	30.9	1.4	8.6	Fe ₂ Al ₇ Si (T ₅)
SptF164	70.1	26.5	1.6	1.8	(Al _{1-x} Si _x) ₅ Fe ₂
SptF165	70.7	25.7	1.7	1.9	(Al _{1-x} Si _x) ₅ Fe ₂
SptF166	69.8	25.2	2.7	2.3	(Al _{1-x} Si _x) ₅ Fe ₂
SptF167	70.4	24.1	2.9	2.6	(Al _{1-x} Si _x) ₅ Fe ₂
SptF168	68.7	22.7	1.5	7.1	Fe ₂ Al ₇ Si (T ₅)
SptF169	68.4	21.5	0.8	9.3	Fe ₂ Al ₇ Si (T ₅)

4.5 Real World Castings with the Squeeze Casting Process

For providing the reader of this work with practical advice, industrial castings were performed in a near industrial environment but with controlled conditions. The most obvious trend for composite Al-Fe castings are structural parts, therefore the preferred method of sample production was pressure assisted casting (squeeze casting) that is similar to the common high pressure die casting process with the advantage, that in general the casting quality is better due to the nature of the process (laminar flow from bottom to top with little to no air entrapment).

The castings were performed with electro polished and galvanically Zn-coated steel blocks measuring 20 mm x 20 mm. The sample preparation was the same as for the gravity cast test pieces. The casting alloy was the binary alloy Al-7Si to have comparable results to the dipping experiments.

Figure 106 illustrates a schematic drawing of the sampling. It could be observed that no chemical bonding had taken place as the component casting separated during the cutting

and polishing procedures, especially in area 1, where the aluminum melt directly contacted the sample head-on. In area 2, where the melt was flowing adjacent to the sample during casting (and the initial heat loss was less dramatic), chemical bonding could be established.

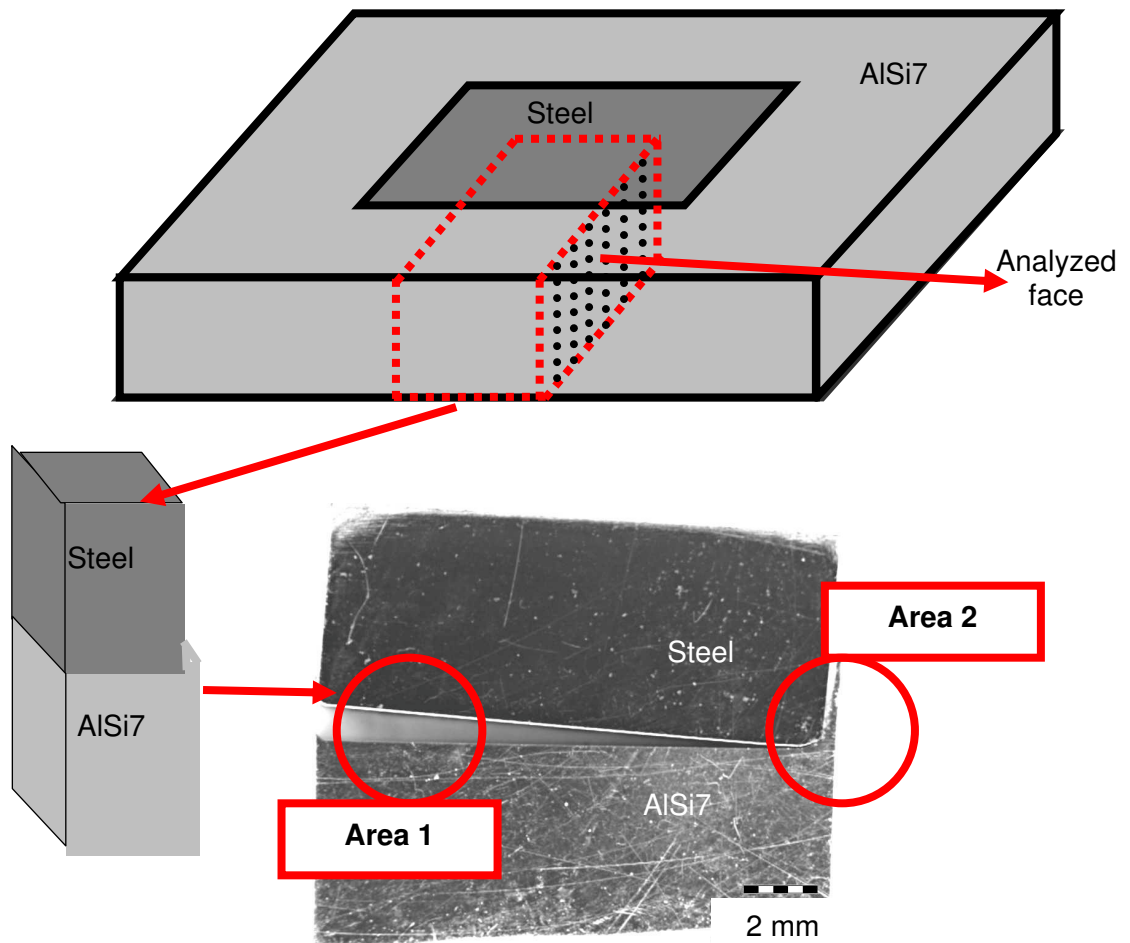


Figure 106: Schematic view of sampling after „Squeeze Cast“ experiments: Metallic continuity only in the boundary area of the casting part (area 2).

4.5.1 Investigation of area 1: „No chemical bonding“

The top REM/BSE image of Figure 107 shows that the Zn-coating started to separate from the steel insert during the casting process and begins to melt into the aluminum. Those areas are encircled with the red dotted line. EDX-analyses of the Al-Fe interface in this area reveal two different phases in the separated part (spectrum 2 and spectrum 3) as well as the formation of a very thin (< 1 μm) Fe-Al-Zn-Si phase at the steel surface (spectrum 1), meaning that the time for interface development was too short until the Al solidified in the die.

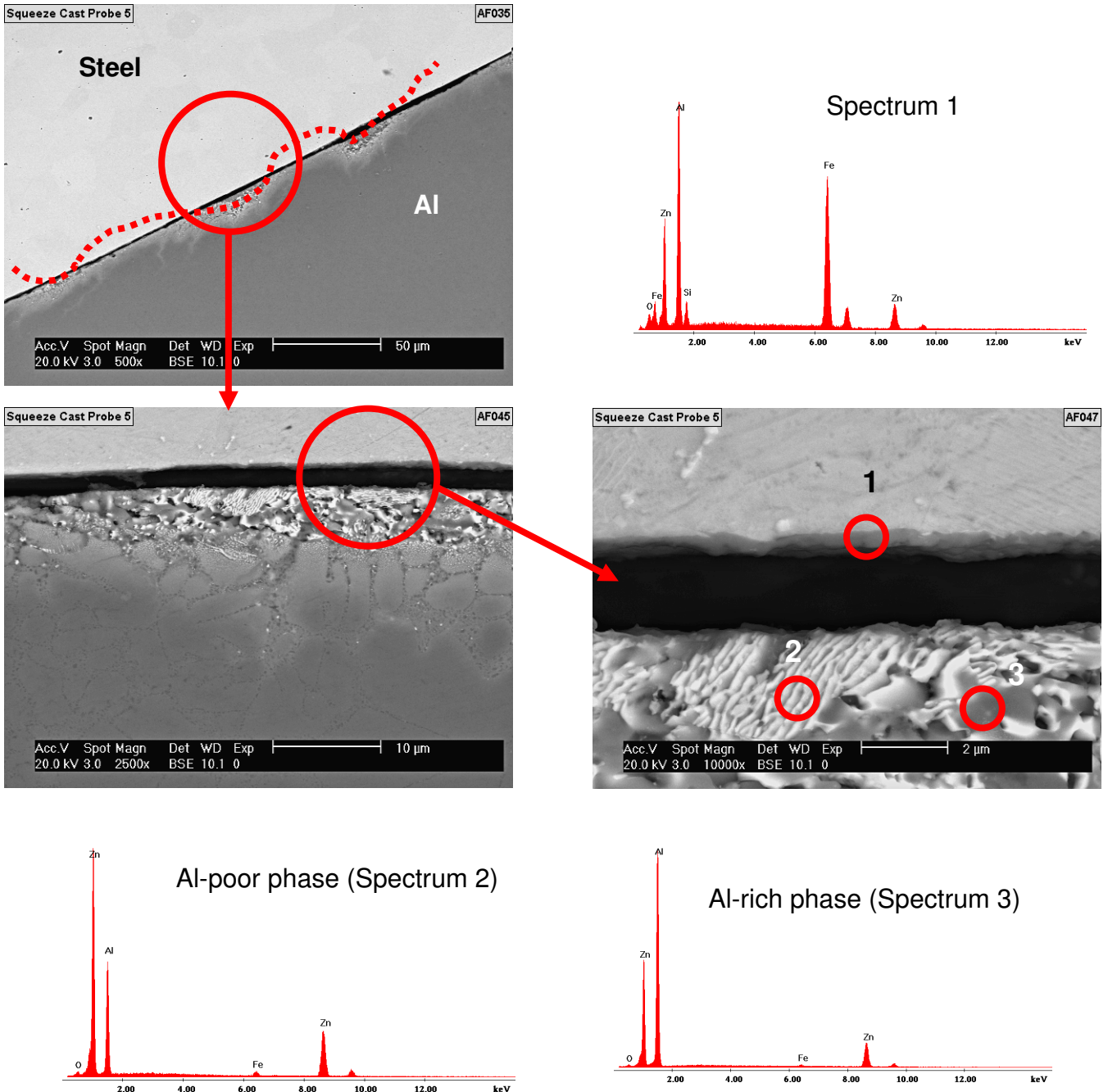


Figure 107: SEM/BSE pictures of the boundary layer steel/aluminum and EDX analysis on the marked points: No connection, very thin IMPZ at the steel surface, Zn goes into the aluminum melt.

Cracks could be detected that were going right through in the casting process freshly formed IMPZ, which consists of Zn enriched aluminum melt as Figure 108 illustrates. The top REM/BSE image of Figure 108 shows clearly the Zn-rich area in the aluminum via the bright contrast of Zn (marked with a red dotted line). The lower left image illustrates, that Zn exists in the shape of finest particles in these light gray area. Element analysis of the encircled areas of the lower right image shows the formation of Al-Fe-Si-Zn-containing particles (spectrum 1) at the interface to the steel insert. In the areas 2 and 3 (spectrum 2 and 3) Al-Zn- as well as Al-Fe-Zn-Si-containing particles could be detected.

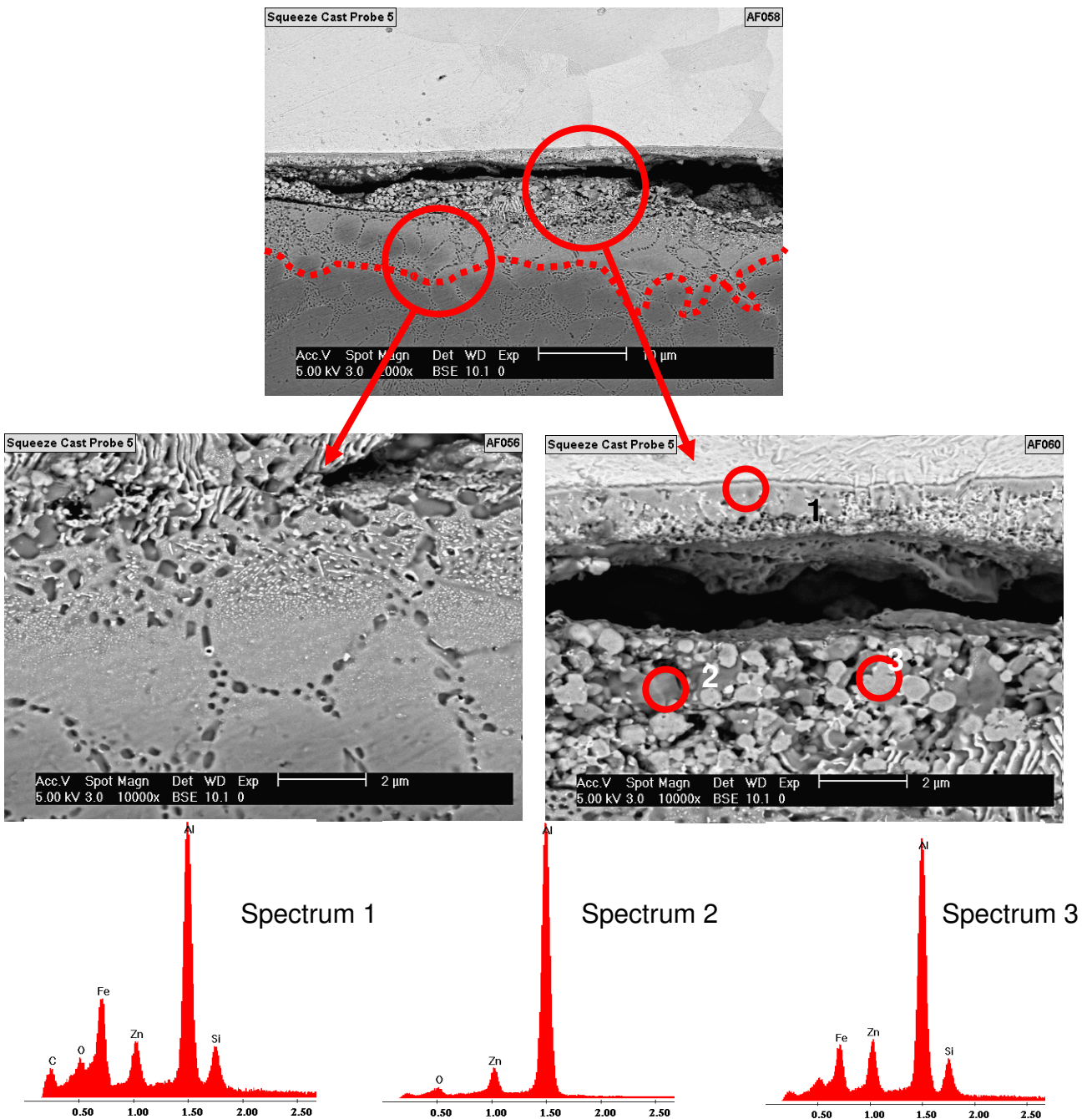


Figure 108: SEM/BSE pictures at the boundary layer steel/aluminum: Construction of Al-Fe-Zn-Si-particles in boundary area, no bonding in this area.

4.5.2 Investigation of area 2: „Chemical bonding“

Figure 106 showed the beginning of the chemical bonding in area 2 where the aluminum melt directly contacted the sample head-on so the cooling time was too fast and the interface development time was too short to form a consistent intermetallic layer. However, in area 2, where the melt was flowing adjacent to the sample during casting and the initial heat loss was less dramatic (the insert had time at this surface to heat up), chemical bonding could be established as shown in Figure 109.

Interestingly, the formation of an intermetallic phase at the border to the steel insert could not be observed as the right image of Figure 109 illustrates. The bright, very small particles at the right side of Figure 109 mainly contain Zn and the structure of this reaction zone seems porous.

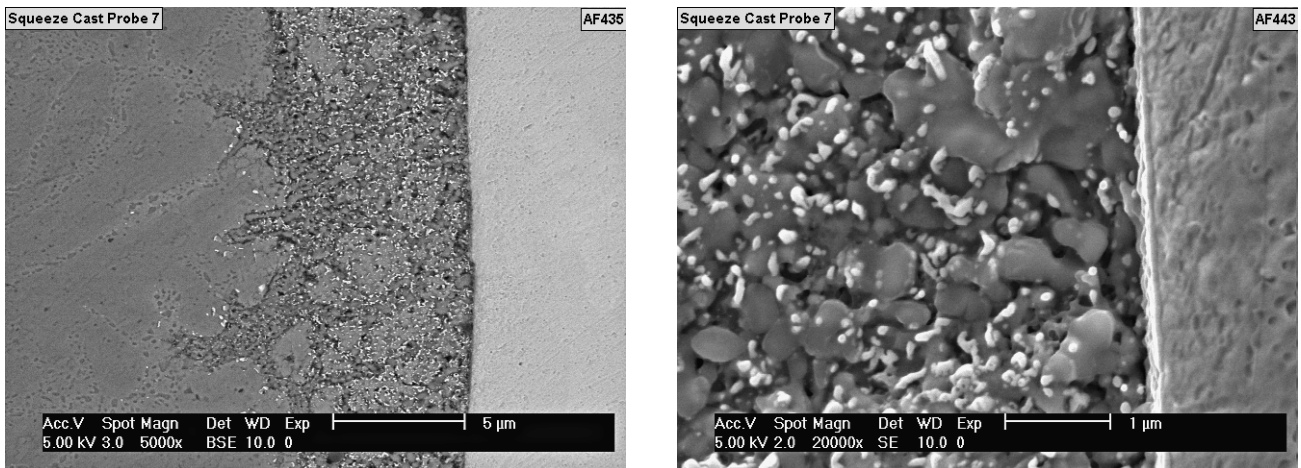


Figure 109: SEM/BSE pictures: Porous structure in the zone between steel and aluminum.

This reaction zone between steel and aluminum contains Al, Zn, Si, and O. It can be shown that the composition of these elements changes with respect to the distance of the steel insert: With increasing distance from the steel the content of Si, Zn, and O reduces, as can be seen clearly in the graphically superimposed EDX-analyses in Figure 110. At the interface border to steel Si, Zn, and O accumulate.

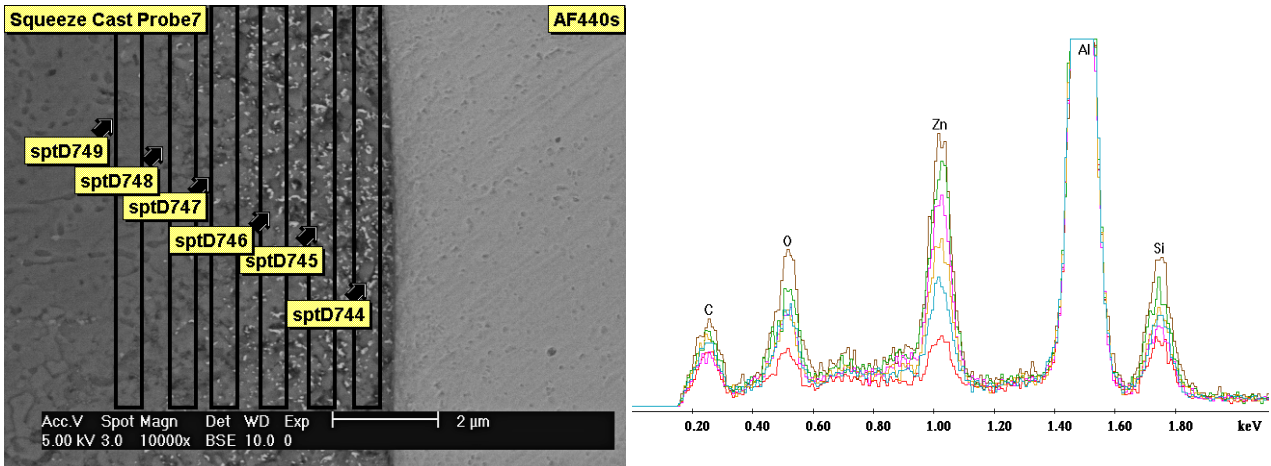
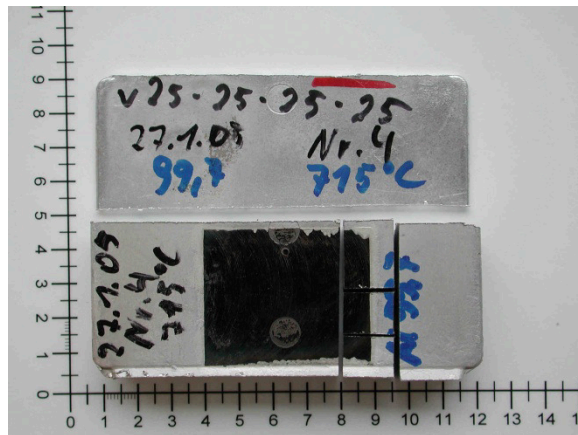


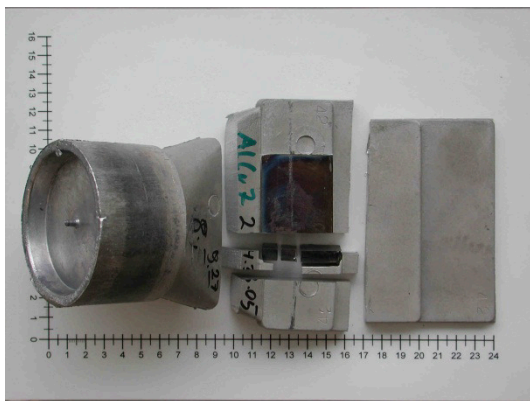
Figure 110: SEM/BSE pictures from the transition zone steel/aluminum and EDX analysis at the marked areas: At the border to steel an accumulation of Si, Zn, and O was detected.

To complete the study in castings in an industrial environment, different insert shapes were recast with pure aluminum and the binary alloys Al-7Cu, Al-7Mg, Al-7Si, and Al-7Zn. To evaluate the possibility to dispense with the Zn-coating for castings, where inserts touch the hot (245 °C) die, these insert were not coated. The sample preparation can be seen in Figure 112.

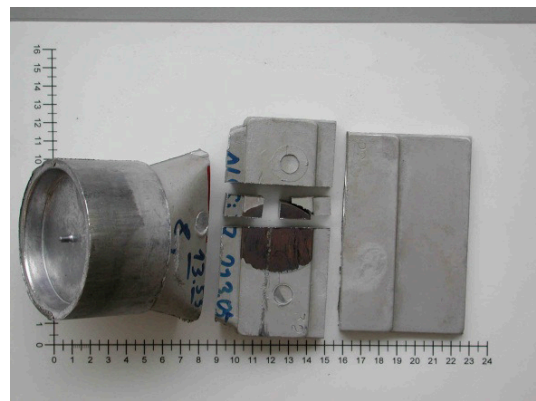
Again a cross-sectional polish was performed at the interface. Ionic pickling was applied here as well to reveal the microstructure of the aluminum and the steel at once, something that cannot accomplished with normal etching. As expected there was neither a reaction at the Al-Fe interface (Figure 112, images), nor any diffusion happening between aluminum and iron as the graphs of Figure 112 below show: Neither intermetallic phases or diffusion of steel into aluminum or reverse can be detected, also there is no increased oxygen concentration at the boundary layer of steel and aluminum. The oxidation during the 8-10 s before the recasting, where the insert heated up to the die temperature was too severe to form any chemical bonding.



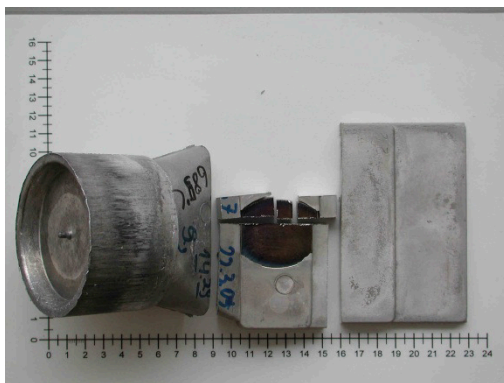
Pure Aluminum/Steel



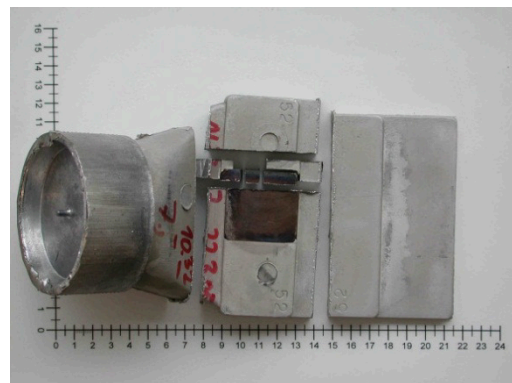
Al-7Cu/Steel



Al-7Si/Steel



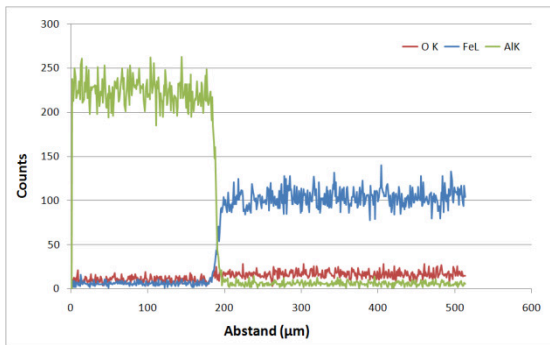
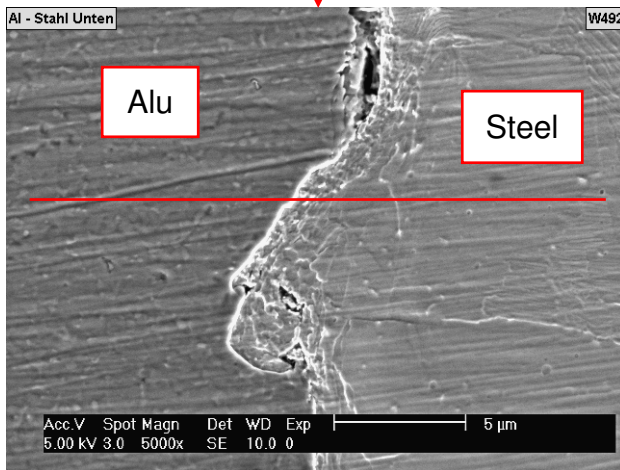
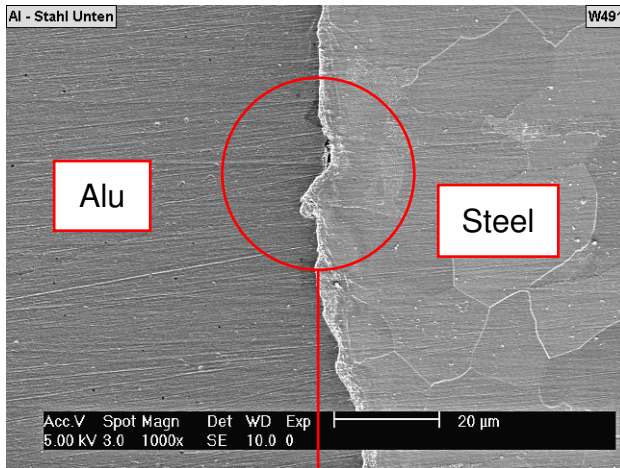
Al-7Mg/Steel



Al-7Zn/Steel

Figure 111: Aluminum/Steel compound castings after mechanical trench: Connection Al-alloy/steel is very bad.

Bottom Area



Middle Area

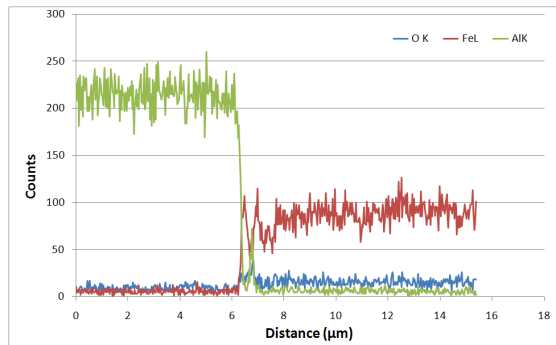
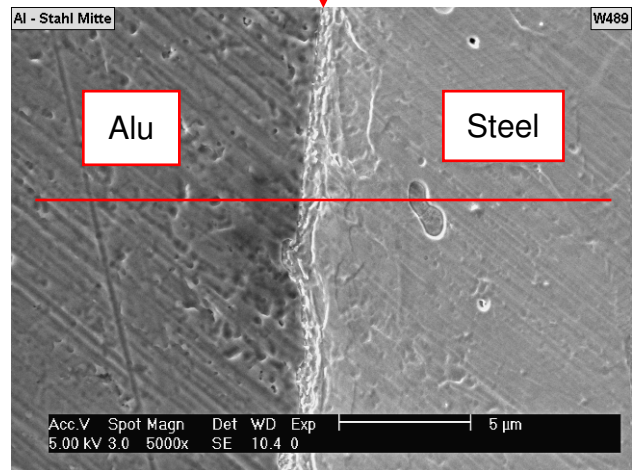
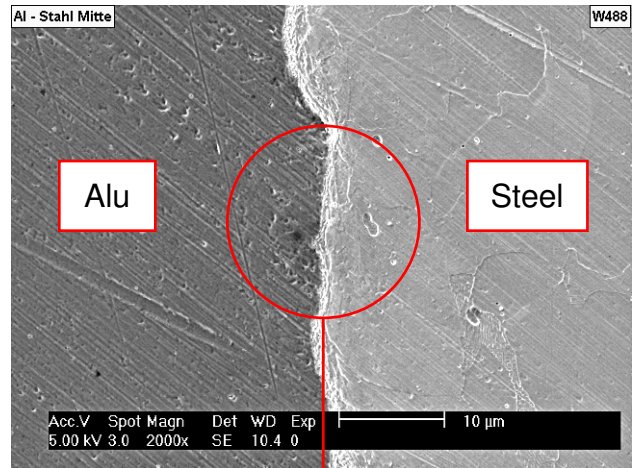


Figure 112: Profile pure aluminum/steel in the middle and bottom area from the cast composite; The raw structures at the boundary layer arise from different etching behavior. The graphics below shows the elements dispersal along the red line drawn in the SEM picture.

5. Mechanical Properties of the Interface Layer

No literature could be obtained that solely measured the bonding strength of the interface alone, since most geometries implicate force- and shape-bonding, too. Hence the aim of this thesis was to develop and employ a test method to measure the amount of strength that is added to the composite casting when a chemical bonding via an intermetallic phase zone is formed.

The dipping tests proved to be a reliable way to create an IMPZ with desired properties (thickness, chemical characteristics etc.). As a consequence this method of creating a chemical- bonding between an aluminum alloy and steel was used to measure quantitatively the mechanical properties of the interface formed.

5.1 Production of the Test Specimen

A very interesting question arises when trying to characterize a compound casting especially in terms of mechanical properties: What is the strength of the interface alone, without force- or shape-bonding? Is it worth the entire struggle or is it so brittle that it is better to avoid chemical bonding of the compound partners?

In order to find an answer to this question a special die was designed as depicted in Figure 113. The die itself is made of Monalite®, a homogeneous, finely-pored, insulating calcium silicon material for non-ferrous metallurgy – non-wetting and inert to corrosion when in direct contact with a number of non-ferrous metals/alloys such as aluminum. The die with a size 150 mm x 150 mm x 30 mm is symmetrical in one direction. On each side a block (40 mm x 30 mm x 20 mm) was cut out that could either host a copper or a Monalite insert and therefore control the temperature flow and the cooling rate. In the center of the die the familiar steel strip (100 mm x 20 mm x 0.3 mm) is clamped. Then aluminum is cast from above in both compartments. After solidification the compound casting is taken out.

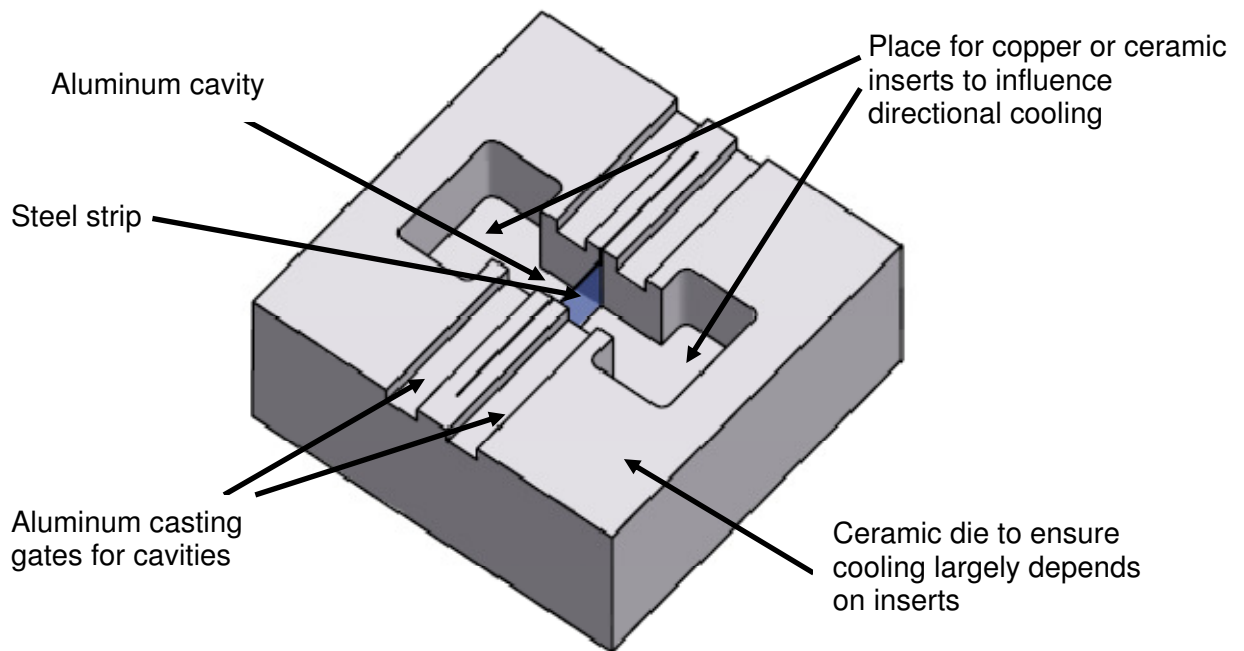


Figure 113: Assembly for evaluating interface strength in cast compound structures with tensile test specimen

The symmetrical Al-Fe compound casting (with two interfaces, one on each side of the strip) is then machined to a size of 10 mm x 10 mm x 100 mm as depicted in Figure 114.

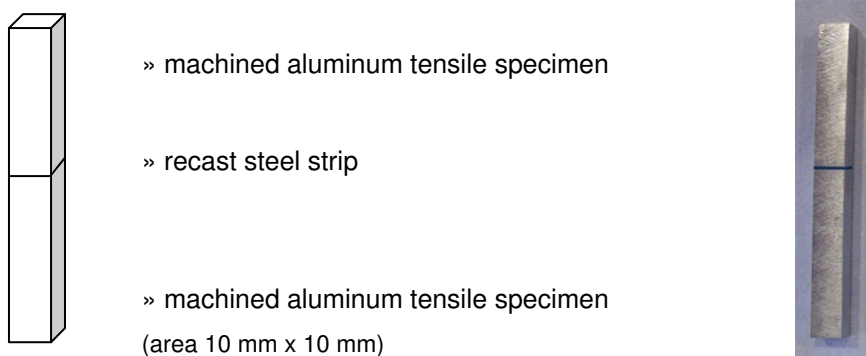


Figure 114: Schematic and image of Al-Fe compound cast specimen from Monalite die

5.2 Tensile Testing of the Test Specimen

The tensile specimens are then tested. It has to be noted that the assessment of the interface strength is simultaneously examined on both sides of the casting, so the specimen will always fail at the weaker interface. This leads to a slightly inferior performance as if the

average would have been taken from samples with just one interface. However, this test geometry has been proven best to create relatively reproducible results.

These results are shown in Figure 115 below. Besides different alloys there are values for the inserts made of ceramic (Monalite, with slow cooling and therefore thicker intermetallic layer) and copper (high cooling and therefore thinner intermetallic layer).

Interestingly the results show that fast cooling leads to better values, as predicted: While a thin interface creates a bonding between the partners, the interface is still the weakest link. The only exception is Al-7Si. This can be explained with the slow interface development (several competing phases during formation) and so more time is needed to create a stable bond.

The measured strengths range from 5 MPa (lower value of Al-7Si with ceramic insert) to 24 MPa (Al-7Zn with ceramic insert) proving that the interface bonding is best when no intermetallic phases are present.

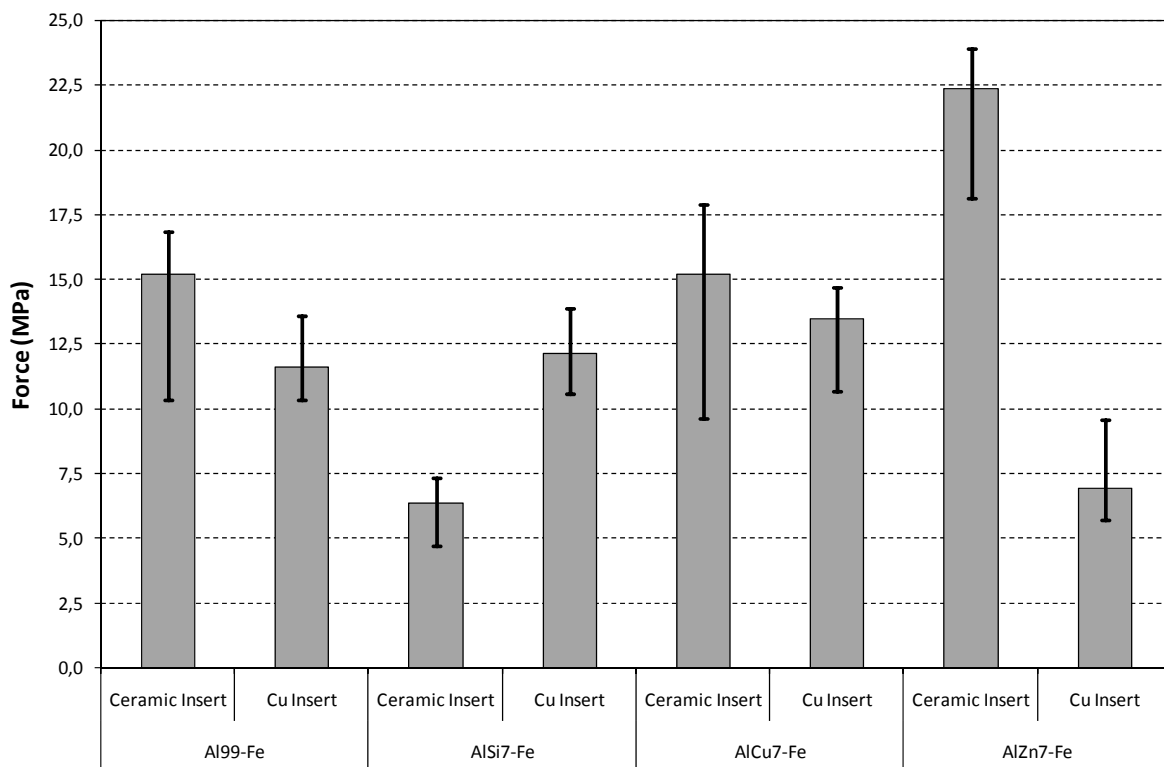


Figure 115: Results of tensile tests for strength of formed interface

6. Modeling of the Interphase Reaction

With all this data generated of the interface formation with time for different binary and commercial alloys, the next logical step would be the modeling of the reaction in order to evaluate the possibility and amount of the chemical-bonding when recasting a steel insert with aluminum. For this a literature research was done for binary and multicomponent interface reactions and then a time dependent model was developed based on the data generated within this thesis.

6.1 Modeling of the Binary Interface Reaction

In spite of theoretical interest and obvious practical importance the kinetics of interface reactions of aluminum to steel have so far received comparatively little attention.^[74, 75] If a continuous, coherent layer of solid product separates the reactants from one another the rate of diffusional transport of the reacting species through the layer becomes the dominant factor determining the overall reaction rate. In such a case the layer growth usually follows the parabolic law which was first established experimentally by Tammann and was then obtained theoretically by Wagner.^[76, 77]

Theories developed by Wagner^[78], Kidson^[79] and other investigators are based upon Fick's laws (mainly upon Fick's first law) and take no account of the rate of chemical reactions which, as could be observed in the experiments, dominate the beginning of the growth of the IMPZ and therefore seem to be debatable in the case of a chemical compound layer built by a solid compound (steel) and a melt (aluminum). Dybkov^[83, 84] states a number of discrepancies between the existing "diffusional" theory and the experimental data available in the literature as published in his papers. The main ones he describes as following:

1. From a "diffusional" point of view, there is no restriction on the number of compound layers growing simultaneously in a given couple. All the layers are expected to occur and grow simultaneously. This is contrary to the observations made via the dipping tests, especially in the Al-Si-Fe system where several different phase formations can happen depending on the process parameters. No reports of the simultaneous growth of a large quantity of compound layers could be found.

2. The layer growth seldom parabolic in multi-phase systems, especially in those cases where two or more compound layers grow simultaneously such as the above mentioned Al-Si-Fe system. In the initial stage the process can be observed as non-parabolic, the layer thickness-time relationship seems following more a linear manner.^[77, 85]
3. From diffusional considerations it follows that the formed layer cannot then disappear because the smaller the thickness the greater is the layer growth rate, that being inversely proportional to the existing layer thickness.^[74, 76, 77] However different experiences have been made. It has been shown that even intermetallic phases which are thermodynamically stable at a given temperature can disappear in favor of other phases.^[86]

Neglecting the chemical reaction step in the beginning of the interface formation appears to be the main source of discrepancies between the theory and experiment. An equation taking into account the relative influence of physical and chemical phenomena on the rate of growth of a chemical compound layer was first proposed by Evans in 1924.^[87] Evans' equation provides a suitable basis for understanding the nature of the processes taking place in multiphase binary systems.

Dybkov attempts in his work to affirm the role of diffusion and that of chemical reactions in determining the compound layer-growth kinetics, and to develop a physicochemical theory of heterogeneous kinetics in binary systems based on Evans' equation and Arkharov's concept of the reaction diffusion.^[88]

6.1.1 Solid-state growth of one compound layer

The first and easiest case is a single intermetallic layer A_pB_q , that emerges between the binding partners consisting of the elements A and B , as shown in Figure 116.

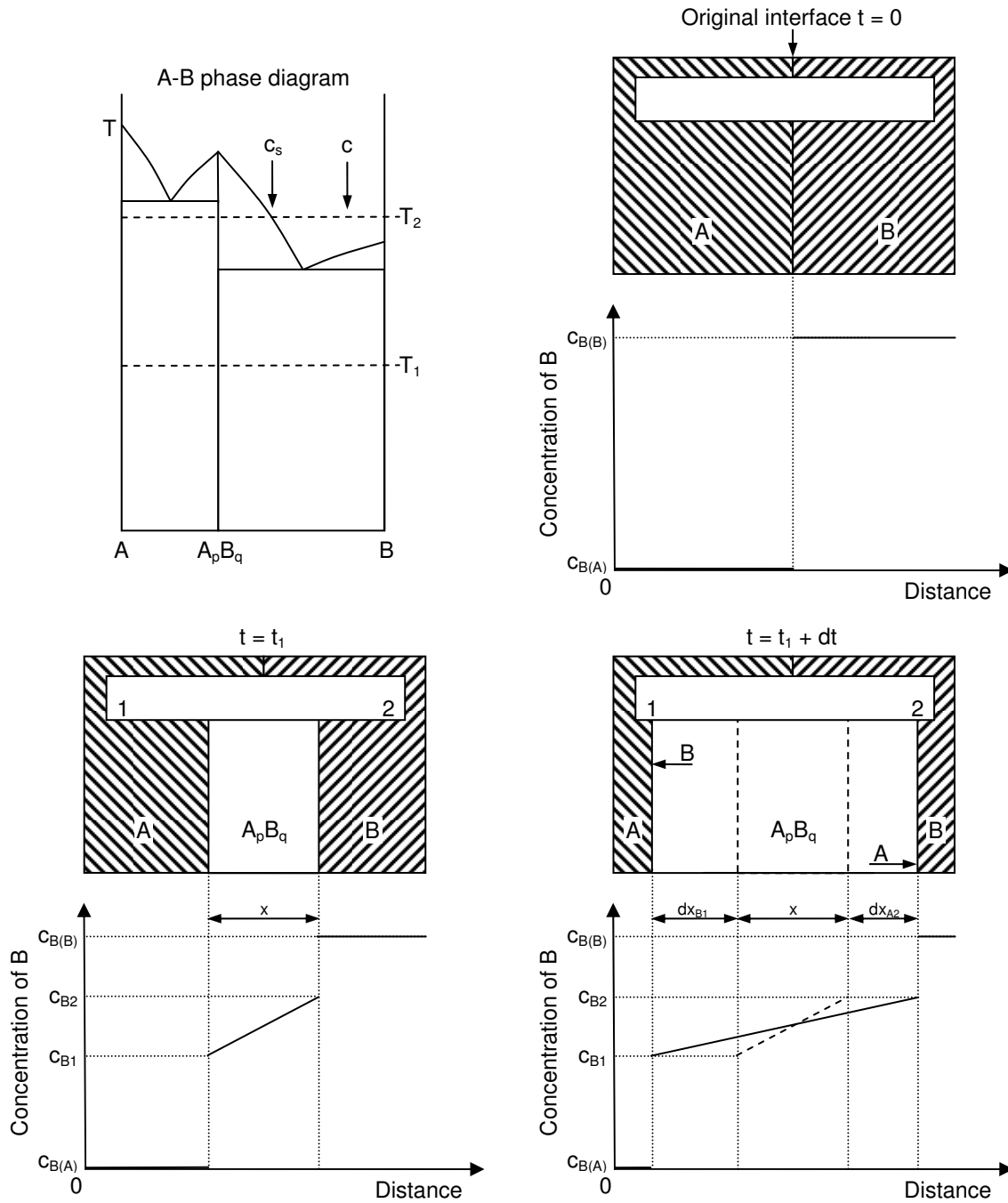


Figure 116: Schematic diagram to illustrate the growth of the $A_p B_q$ layer between the elements A and B according to Dybkov^[80]

6.1.1.1 Reaction diffusion model

The solid-state growth of the $A_p B_q$ layer between the two mutually insoluble ($c_{B(A)} = 0 = 0$ and $c_{A(B)} = 0$) elementary substances A and B , at a given temperature T_1 is due to two parallel processes each of which proceeds in two succeeding steps:

1. B atoms diffuse across the A_pB_q layer and then react at the A/A_pB_q interface (interface 1) with the surface A atoms
2. A atoms diffuse across the layer in the opposite direction and react at the A_pB_q/B interface (interface 2) with the surface B atoms

From the kinetics point of view, reactions 1 and 2 are, in general, different, while the reacting substances are the same. This is because the reactants A and B enter these reactions either as diffusing or as surface atoms. Both processes involve two consecutive steps:^[88]

- a) diffusion of atoms through the layer
- b) chemical reaction with the participation of these atoms taking place at the interface between the layer and either A or B

The processes involving these two steps are usually called the reaction or chemical diffusion.^[88]

Dybkov makes now the following assumptions:^[84]

1. the concentrations of components A and B in the layer at boundaries 1 and 2 are equal to the limits of the A_pB_q homogeneity range
2. a change in concentration with distance within the A_pB_q layer is linear (see Figure 1);
3. during growth, both the boundary concentrations and a linear concentration distribution remain almost unchanged, which is of course a simplification but works well for these kinds of systems (there might be a concentration gradient due to reaction partner depletion at the interface).

It should be noted that these assumptions are usually made to treat the growth kinetics of compound layers.^[78, 87]

Taking these assumptions into account, a condition of a quasi-stationary concentration distribution arises when the concentrations of A and B within the A_pB_q layer depend only on position and are independent of time.^[76] It is obvious that this condition is undoubtedly satisfied in the case of stoichiometric compounds having no ranges of homogeneity. This approximation can be justified in the case of chemical compounds with narrow ranges of homogeneity.

6.1.1.2 One process in the A - B system

Reaction 1 is the only reaction in the A - B system when the diffusion of A within the A_pB_q layer is negligible compared to that of B . In an initial stage of the interaction, the A_pB_q layer thickness is small and therefore the diffusional path is short. Hence, a number of B atoms are able to reach the A/A_pB_q interface. Thus the overall rate of reaction 1 is only limited by the reactivity of the A surface. In such a case, the layer-growth rate is constant. This reaction regime of growth of the A_pB_q layer is one of the two limiting cases. Another extreme is the diffusional regime of its growth when the rate of reaction 1 is limited only by the rate of diffusional transport of B atoms across the layer, the further chemical reaction with the participation of these atoms being quick. This is the case if the A_pB_q layer is thick. This "diffusional" case can easily be treated using Fick's first law^[80]

$$j_B = -D_B \frac{\partial c_B}{\partial x} \quad (1)$$

Where j_B is the flux of the diffusing B atoms across the A_pB_q layer towards interface 1 (mol m⁻² sec⁻¹); D_B the diffusion coefficient of B into the A_pB_q lattice (m² sec⁻¹); c_B the concentration of component B within the compound layer (mol m⁻³).

If the chemical reaction is spontaneous then all the B atoms passing across the layer per unit time are reacting with the surface A atoms into the A_pB_q compound at interface 1. This results in an increase in thickness of the layer. Dybkov^[80, 81, 82] therefore draws the conclusion that

$$k_{1B1} = \frac{D_B(c_{B2} - c_{B1})}{c_{B1}} \quad (2)$$

is the rate constant of the layer growth under conditions of diffusional control (physical constant, m²sec⁻¹). In the subscript 1B1 the preceding 1 ahead of $B1$ indicates the diffusional regime of the layer growth and the other indexes have the former meaning.

In general, the growth rate of the A_pB_q layer depends on both the rate of diffusion and the rate of chemical reaction since each of these two processes always proceeds at a finite rate. The general relationship for the reaction can be stated as

$$\left(\frac{dx}{dt}\right) = \frac{k_{0B1}}{1+(k_{0B1} x/k_{1B1})} \quad (3)$$

Integration of equation 3 at the initial condition $x = 0$ at $t = 0$ yields

$$t = \frac{x^2}{2k_{1B1}} + \frac{x}{k_{0B1}} \quad (4)$$

The equations of this type were first obtained by Evans.^[87]

It has to be noted that the reactivity of the A surface towards B atoms remains constant, the substance A being uniform from a macroscopic view-point, whereas the flux of these atoms through the A_pB_q layer gradually decreases as the layer thickens. Accordingly there exists a condition of the layer thickness at which these quantities are equal.

If the rate of reaction at the A surface is less than the flux of B atoms through the A_pB_q layer and therefore there is an "excess" of these atoms which can be used by the layers of other chemical compounds (enriched in component A compared to A_pB_q). On the other hand if there is a deficit of B atoms because the rate of reaction at the A surface is greater than the flux of B atoms through the layer. On reaching interface 1, each B atom will therefore be combined into compound. Hence, no B atom is available for the growth of other layers enriched in component A .^[81, 82]

6.1.1.3 General case: Reactions 1 and 2 proceed simultaneously

In general, reactions 1 and 2 take place simultaneously. The growth of the A_pB_q layer to the left from the original A - B interface is according to reaction 1 while its growth to the right is due to reaction 2. Dybkov states for this

$$dt = \left(\frac{x}{k_{1B1}} + \frac{1}{k_{0B1}}\right) dx_{B1} \quad (5)$$

and

$$dt = \left(\frac{x}{k_{1A2}} + \frac{1}{k_{0A2}}\right) dx_{A2} \quad (6)$$

where k_{0A2} is a chemical constant and k_{1A2} is a physical (diffusional) constant.^[81, 82]

Reactions 1 and 2 are considered to be independent of one another for the two following reasons:

- a) They are separated in space
- b) The fluxes, j_A and j_B , of components A and B across the growing A_pB_q layer appear to be independent of each other

This is due to the fact that in the lattice of a chemical compound each component forms its own sublattice.^[76] In this sublattice all atoms as well as all sites are structurally equivalent. Again, the vacancies are continuously created in the sublattices as reactions 1 and 2 proceed, namely, the vacancies in the B sublattice according to reaction 1 appear at boundary 1 whereas the appearance of vacancies in the A sublattice at boundary 2 is due to reaction 2. The vacancies formed are filled by the atom-by-atom movements. Thus the B atoms are transferred from interface 2 to interface 1 while the A atoms are transferred in the opposite direction. The most essential point is that each kind of atoms moves in its own sublattice, thus not hindering the movement of another kind of atoms.

There exists another critical value at which the reactivity of the B surface towards A atoms and the flux of A atoms through the A_pB_q layer are equal. The existence of the critical thicknesses, $x_{1/2}^{(A)}$ and $x_{1/2}^{(B)}$, provides a basis for the theoretical definitions of the reaction and diffusional regimes of growth of the A_pB_q layer. That is the regime of growth of the layer is reaction controlled with regard to component B if $x < x_{1/2}^{(B)}$ and is diffusional with regard to this component if $x > x_{1/2}^{(B)}$. Dybkov shows that therefore an initial portion of the thickness-time relationship is always a straight line and the long-time portion of the $x-t$ relationship is parabolic.^[81-83]

6.1.2 The effect of dissolution on the growth of the A_pB_q layer

If A is a solid and B a liquid, and the liquid is undersaturated with A then the dissolution of the layer occurs simultaneously with its growth. The overall change in thickness of the layer is therefore the difference between the rate of growth of the layer and the rate of its dissolution, which results in a steady state condition (similar to the dipping experiment results of Al-7Cu to steel)

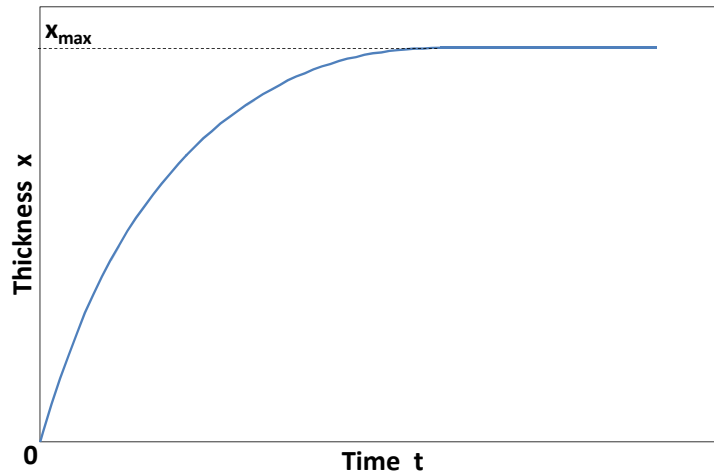


Figure 117: Growth of the A_pB_q layer under conditions of its simultaneous dissolution into the liquid at a constant rate.^[80]

6.1.3 Parabolic Growth

The conclusion of the previous chapter so far is that a reaction-diffusion model ends up in an parabolic growth, that eventually stops as the dissolution of the intermetallic layer happens at the same speed as new intermetallic phase forms (in a state of equilibrium). However, in real world casting the aluminum melt will be solidified before this happens.

1. Growth of the A_pB_q compound layer between the elements A and B is due to two simultaneous processes.
2. Each of these two processes occurs in two consecutive (alternate) steps: (a) Diffusion of atoms; (b) Chemical reactions with the participation of these atoms.
3. In general, an initial portion of the layer thickness-time relationship is linear but there is then a gradual transition from a straight line to a parabola.

6.2 Modeling of multi-component interface reactions

When modeling multi-component interface reactions, the situation gets a bit more complex.^[89] Depending on the involved elements a single compound layer or a multi compound layer can be formed. For analytical purposes the former will be explained here.

6.2.1 Solid State growth of a single compound layer

Considering the case where three chemical compounds A_pB_q , A_rB_s and A_lB_n exist in the A - B system (Figure 118), the homogeneity ranges of these compounds except for A_pB_q are considered to be very narrow compared to the average contents of components A and B . Consider first the case where a single layer of the chemical compound A_rB_s grows at the A/B interface (Figure 119).^[89]

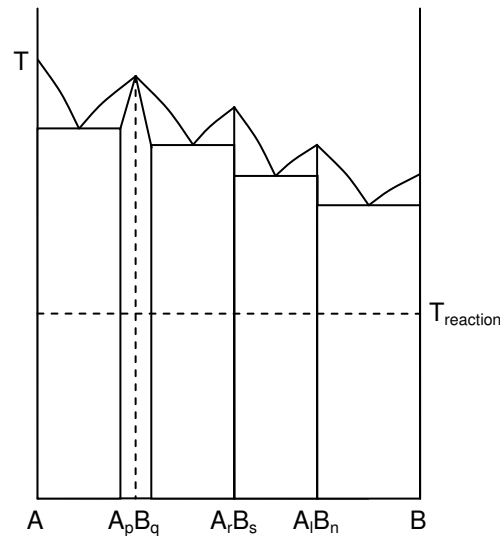
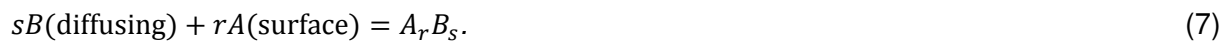


Figure 118: Schematic phase diagram of a binary system with three chemical compounds^[83]

6.2.2 Growth of the A_rB_s layer at the A/B interface

The solid state growth of the A_rB_s layer at the interface between the two mutually insoluble substances A and B is according to two simultaneous processes. Firstly, the B atoms diffuse across the A_rB_s layer and then react at the A/A_rB_s interface (interface 1, Figure 119) with the surface A atoms:



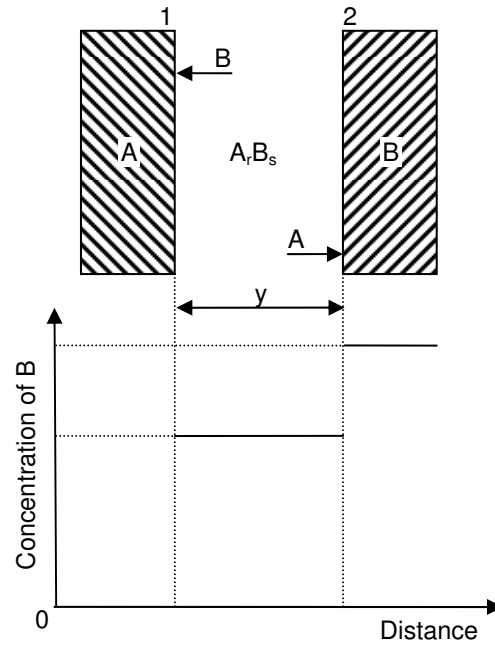


Figure 119: Schematic diagram to illustrate the growth of the $A_r B_s$ layer between the mutually insoluble elements A and B ^[89]

Secondly, the A atoms diffuse across the layer in the opposite direction and react at the $A_r B_s/B$ interface (interface 2) with the surface B atoms:



From the view-point of kinetics, reactions (7) and (8) are, in general, different. Both reactions involve two consecutive steps:

1. Diffusion of atoms through the layer.
2. Chemical transformations with the participation of these atoms taking place at the interface between the layer and either A or B .

The process involving these two steps is usually called reaction or chemical diffusion. The time required for the $A_r B_s$ layer to thicken at the $A/A_r B_s$ interface is the sum of the time of diffusion of B atoms to this interface and the time of further chemical reaction with the participation of these atoms. The time of diffusion is directly proportional to both the existing $A_r B_s$ layer thickness and the increase of its thickness whereas the time of reaction is directly proportional to the increase in the $A_r B_s$ layer thickness and is independent of its total thickness.^[84]

The reactions are considered to be independent of one another. Therefore, the total increase in thickness of the $A_r B_s$ layer is the sum of both. The parabolic law of the growth was first established experimentally by Tammann and was then obtained theoretically by Wagner^[78]

and further developed by Dybkov.^[80-83, 89] As only relatively thick compound layers are observable with the help of the usual experimental techniques, parabolic law kinetics is observed more often than linear law kinetics.^[83, 89]

6.2.3 Growth of the A_rB_s layer at the A_pB_q/B interface

A schematic diagram to illustrate the solid state growth of the A_rB_s layer between A_pB_q and B is shown in Figure 120. Consider the case where the content of A in A_pB_q is equal to the lower limit of the A_pB_q homogeneity range. The A_rB_s layer grows as the B atoms diffuse across its bulk and react with A_pB_q at interface 1 to form A_rB_s .

This layer also grows as the A atoms diffuse from interface 1 to interface 2 and react with B . The reactions at interface 2 are clearly the same in the $A-A_rB_s-B$ and $A_pB_q-A_rB_s-B$ systems.

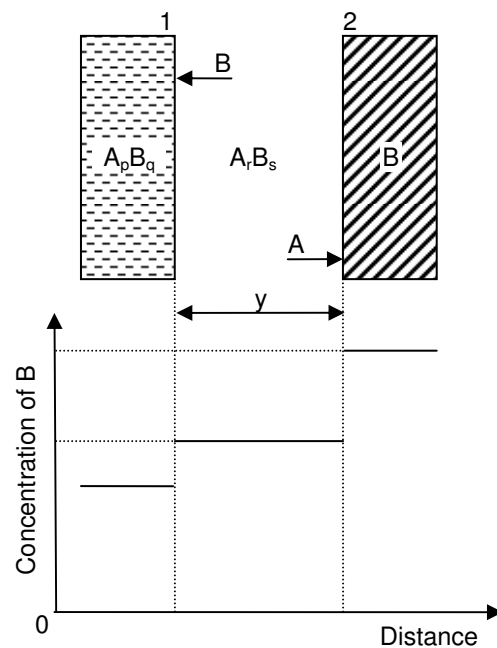


Figure 120: Schematic diagram to illustrate the growth of the A_rB_s layer between the A_pB_q and B phases.^[93]

Another situation arises, however, at interface 1. Firstly, the reactions at this interface are different in those systems. Secondly, in the latter system the layer of A_pB_q acts as a source of A atoms for reaction (2). Since the content of component A in the A_pB_q compound cannot be less than the lower limit of its homogeneity range, the A_pB_q phase becomes unstable as reaction (2) proceeds and therefore it must partly transform into another phase. It is clear that the amount of this transformation is directly proportional to the extent of reaction (2).^[93]

Overall there are three interfaced velocities:

1. The movement of interface 1 to the left (see Figure 120) as reaction (10) proceeds
2. The movement of interface 2 to the right as reaction (2) proceeds
3. The movement of interface 1 to the left as a result of a phase transformation

Dybkov analytically examines additionally growth of the A_rB_s layer at the expense of component A , and the growth of the layer at the expense of both components, which will not be discussed here in detail.^[93, 96-99]

6.2.4 Growth of the A_rB_s layer at the A_pB_q/A_lB_n interface

The A_lB_n phase is a source of B atoms for this reaction. However, if the content of component B in A_lB_n is equal to the lower limit of the A_lB_n homogeneity range, then the A_lB_n phase becomes unstable and partly transforms into A_rB_s .^[93]

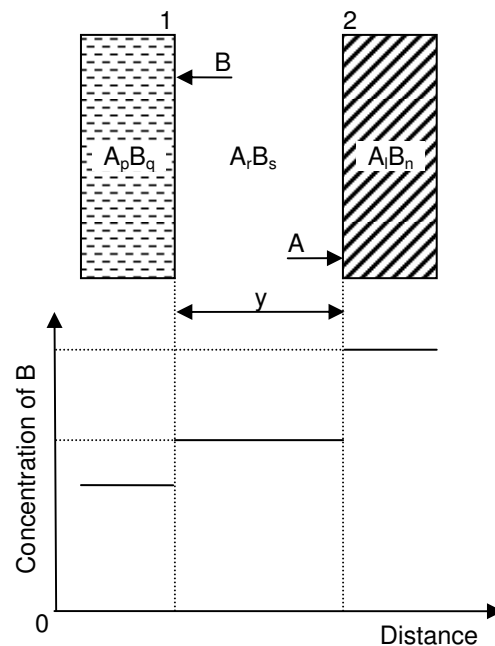


Figure 121: Schematic diagram to illustrate the growth of the A_rB_s layer between the A_pB_q and A_lB_n compounds.^[93]

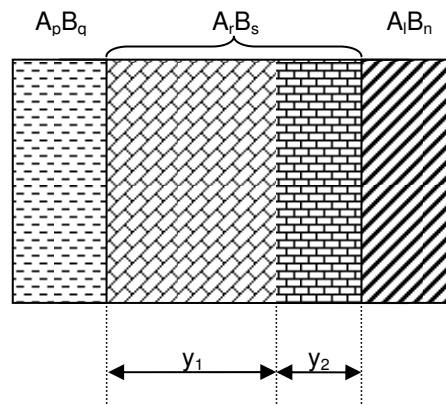


Figure 122: Representation of a duplex structure of the $A_r B_s$ layer in the $A_p B_q - A_r B_s - B$ system.^[93]

It should be emphasized that a comparison of growth rates is correct only if the $A_r B_s$ layer is a single one in all the reaction couples, the layers of other compounds of a given binary system being absent.

7. 3D Modeling using the experimental data^[118]

The growth of intermetallics phases of the dipping experiments between molten aluminum and solid steel was investigated via the imaging analysis of the scanning electron microstructures.^[90] Results from focused ion beam analysis revealed the isotropic growth of intermetallics phases on the plane parallel to interface between steel and Al. Diffusive controlling mechanism was confirmed during the growth of intermetallics phases and a 3D model was derived to find that the growth of the intermetallics phases (IMP) was dependent on $t^{0.15}$ of dipping time.^[108]

The microstructure of IMPs shows interesting and intriguing morphology. Some researchers report the observation of tongue like morphology of the IMPs between solid iron and molten aluminum^[11, 37, 91, 92] which is explained as the anisotropic inter-diffusion along different crystallographic directions during the growth of IMPs^[41] after the reaction controlled the beginning of the formation.

Up to now, investigations on the growth dynamics of IMPs are mostly based on the relationship between the thickness of the IMPs and the reaction time. Among those investigations, the thickness of IMPs is measured via maximal/minimal thickness^[92], or mean thickness calculated as the ratio between the total area and the total length of IMPs^[67]; Fractal analysis^[42] and width of half height are also applied as well.^[54] Due to the mostly complicated pattern of IMPs, obviously the method on the treatment of the IMPs has to be standardized or generalized to minimize the uncertainty and enhance the comparability of the results between different researchers.

Here, the growth of IMPs between molten aluminum and solid steel was investigated via an imaging analysis method. Aim is to correlate the growth of the volume of IMPs with the reaction time for the construction of a standardized method for the 3D investigation on chemical reactions at solid-liquid interface, especially the reactive diffusion controlled process.

7.1 Experimental techniques for Modeling

The results were obtained via the test specimen of the dipping trials. The microstructures of the cross-section of samples are observed with a scanning electron microscopy (Model: FEI XL30 ESEM-FEG) equipped with EDAX. To investigate the three-dimensional morphology of

IMPs, a focused ion beam (FIB) instrument (mode: FEI, Quanta 200D) is applied to etch the sample at the interface between steel and aluminum towards the inner part of sample, which then opens the microstructures of IMPs in the direction perpendicular to the interface between solid steel and liquid aluminum.

7.2 Microstructures of Intermetallic Phases

Figure 123 (a) shows a back scattering electron (BSE) image of a cross-section view of the interfacial microstructure between steel and Al. Heavy elements with high atomic number show bright signals due to a high intensity on BSE operational modus in SEM^[2]. Thus Figure 123 (a) can be divided into three areas with different brightness, the bright area at the right side is steel, the dark one at the left side is Al, and the grey one with tongue like pattern located in between is iron aluminides. The EDAX analysis at different positions at the IMPs zone is concluded in Table 16, which shows that the major part of IMPs is Fe₂Al₅ phase, and a thin part in contact with Al is FeAl₃ phase. Figure 123 (b) displays the growth behavior of IMPs with dipping time. For comparison, a 90° rotation according to Figure 123 (a) is adopted for each image and only a slim part of image is selected. As shown in Figure 123 (b), IMPs firstly grow steadily with dipping time from the both interfaces, then fast after 15 s, the separative distance between neighboring tongue increases with time, implying that the heterogeneous growth of IMPs becomes more apparent. The length and width of IMPs tongue both increase with dipping time. Figure 123 (c) shows a 3D view of a sample fabricated with FIB etching, which is dipped in molten aluminum for 10 s same as the sample in Figure 123 (a). It is found that IMPs display a similar tongue like pattern in the direction perpendicular to the observing plane in Figure 123 (a), which indicates that the growth of IMPs is isotropic on the plane parallel to the interface between steel and Al. The results in Figure 123 have revealed the complexity of the growth of IMPs between solid steel and molten aluminum, and cannot be simplified with a single value representing the 1D growth of IMPs. Therefore it requires the modification to the previously adopted methods or new ones for the analysis of the growth of IMPs.

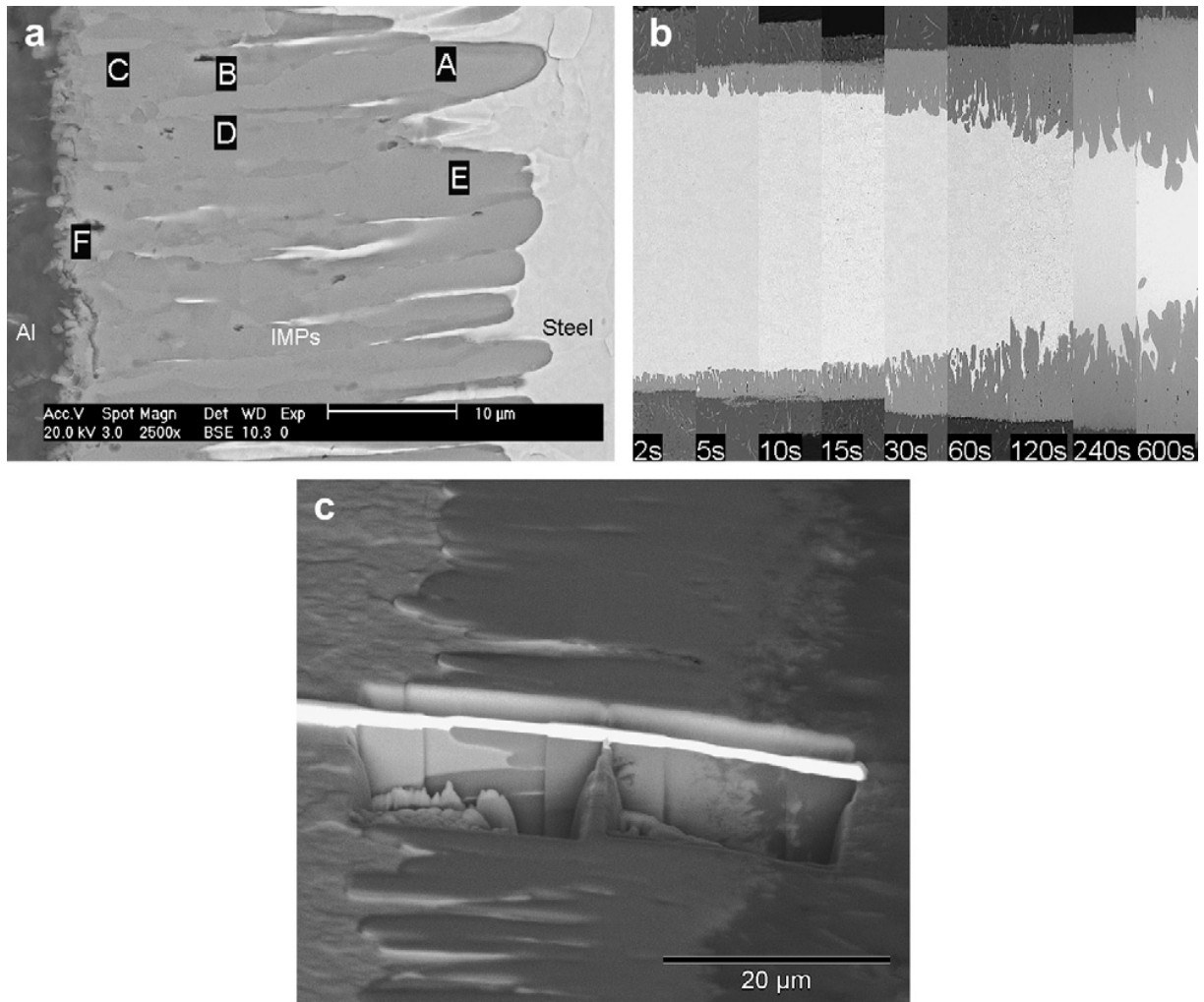


Figure 123: (a) Microstructures of the IMPs dipping time 10 s; (b) Collection of BSE maps, the geometry of each strip is 445.90 μm x 60.53 μm; (c) FIB cross-section (dipping time: 10 s).

Table 16: EDAX results from Figure 123 (a)

	Fe at%	Al at%	Phase
A	28.00	72.00	Fe_2Al_5
B	27.86	72.14	Fe_2Al_5
C	27.80	72.20	Fe_2Al_5
D	28.04	71.96	Fe_2Al_5
E	28.37	71.63	Fe_2Al_5
F	25.74	74.26	FeAl_3

7.3 Imaging analysis of microstructures

To overcome the difficulties of irregular phase shapes in the intermetallic phase zone (tongue like, blocky, islands forming etc.), the image analysis software AnalySIS (Soft-Imaging system GmbH) was adopted for the analysis of the SEM images: Phase coding analysis based on the contrasts of steel, IMPs and aluminum phases in the BSE images. Figure 124 explains how a BSE image is coded with different phases, where the bright, grey and dark phases in a BSE image are clarified into green, red and black ones respectively according to their contrast value recognized by the software, the areas of different phases are then calculated automatically by the software. Since the clarification of different phases is dependent on their contrast acquired from BSE image, it is strictly required to set comparable contrast and brightness parameters during the recording of BSE images. Because the mentioned software calculates the area of phase with irregular shapes or patterns, and returns the results of area with an integrated method, it is believed that a high accuracy with high reliability can be assured. This method is especially suitable for the analysis of patterns with highly disordered or irregular shapes, and can be developed into a standardized method.

For the actual imaging analysis, a general frame with geometry of $406\ \mu\text{m} \times 355\ \mu\text{m}$ from the BSE image is selected. For each sample, four to five frames from different BSE images observed at different positions on the sample are analyzed, and the results of the area of IMPs and steel are compared in Table 17.

Table 17 shows that the standard errors for the measured areas of the IMPs and steel are small, the highest error for the acquired area of IMPs is less than $\pm 5\%$; And the standard error for steel is even below $\pm 1.0\%$ in all cases. The results confirm the uniform growth of IMPs throughout the steel strip.

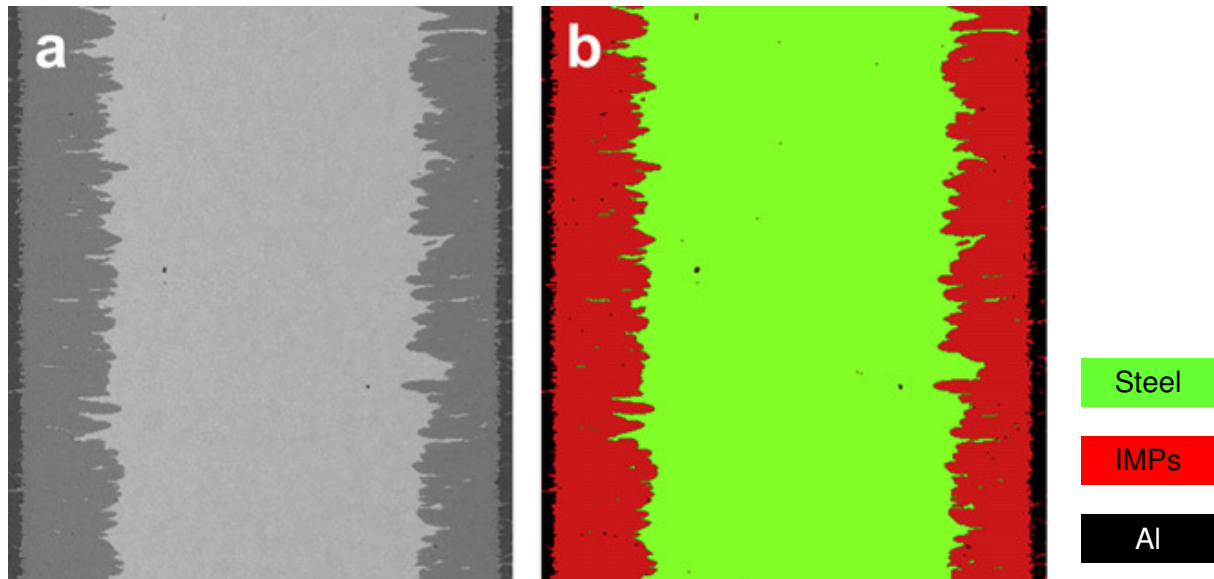


Figure 124: Image analysis via phase coding method, (a) original image; (b) phase coded image.

Table 17: Area of IMPs and steel

Dipping time (s)	Area of IMPs (μm^2)	Standard error (\pm %)	Area of steel (μm^2)	Standard error (\pm %)
2	18 622.0	2.6	111 183.8	0.2
5	26 952.2	2.0	109 952.5	0.4
10	23 034.8	4.9	111 106.0	0.2
15	24 212.0	3.8	109 412.2	0.2
30	40 544.2	1.0	102 863.0	0.2
60	52 015.1	1.0	98 760.5	0.3
120	63 727.6	1.0	85 300.7	0.8
240	77 042.2	2.9	76 552.9	1.1
600	109 988.9	0.8	60 970.2	1.0

7.4 Growth mechanism of Intermetallic Phases

There have been lots of investigations on the growth mechanisms of IMPs between molten Al and solid steel, or more widely between solid and liquid, chemical reaction and the diffusion of reactive reactants are widely accepted mechanisms. Those conclusions are mainly derived from the results on the 1D treatment of the growth of IMPs, for the modeling on the growth of IMPs a 3D treatment was carried out.

It is reported that FeAl_3 phase does not change too much with the increase of reaction time^[92], the growth of IMPs between liquid aluminum and solid steel is mainly due to the growth of the Fe_2Al_5 phase. Since the growth of IMPs starts from the interface towards steel bulks, the diffusion of Fe atom towards molten aluminum is not considered here. Therefore, the formation of Fe_2Al_5 can be described to the reaction between Fe and diffusive Al atoms as shown in equations (1) and (2):^[93]



or



Supposing that the growth of Fe_2Al_5 is controlled by the chemical reaction (9) or (10), the growth rate of Fe_2Al_5 phase should have the following relationship with the decreasing rate of Fe at any specified time t :

$$\frac{d(M_{\text{Fe}_2\text{Al}_5})/dt}{d(M_{\text{Fe}})/dt} = C \quad (11)$$

where, $M_{\text{Fe}_2\text{Al}_5}$ and M_{Fe} are the masses of increased Fe_2Al_5 phase and decreased steel respectively, and C is constant. The integration of equation (11) has the following relationship:

$$\int \frac{M_{\text{Fe}_2\text{Al}_5}}{dt} \cdot dt = C \int \frac{M_{\text{Fe}}}{dt} \cdot dt \quad (12)$$

Then,

$$V_{\text{Fe}_2\text{Al}_5} \cdot \rho_{\text{Fe}_2\text{Al}_5} = C \cdot V_{\text{Fe}} \cdot \rho_{\text{Fe}} \quad (13)$$

where, $V_{\text{Fe}_2\text{Al}_5}$ is the increased volume of Fe_2Al_5 phase, V_{Fe} is the decreased volume of steel; $\rho_{\text{Fe}_2\text{Al}_5}$ ($4.1 \times 10^3 \text{ kg/m}^3$) and ρ_{Fe} ($7.8 \times 10^3 \text{ kg/m}^3$) are the density of Fe_2Al_5 and Fe phases respectively.^[108]

Two parameters $A_{\text{Fe}_2\text{Al}_5}$ and A_{Fe} are now introduced as the areas of cross-section of the increased IMPs and decreased steel respectively. $A_{\text{Fe}_2\text{Al}_5}$ is directly from Table 17, A_{Fe} can be calculated simply from Table 17 by subtracting the value of original area with the value of a specified time which leads to the following approximation:

$$\frac{V_{\text{Fe}_2\text{Al}_5}}{V_{\text{Fe}}} \approx \left(\frac{A_{\text{Fe}_2\text{Al}_5}}{A_{\text{Fe}}} \right)^{\frac{3}{2}} \quad (14)$$

Correlating equations (13) and (14) generates:

$$\frac{M_{\text{Fe}_2\text{Al}_5}}{M_{\text{Fe}}} = \left(\frac{A_{\text{Fe}_2\text{Al}_5}}{A_{\text{Fe}}} \right)^{\frac{3}{2}} \cdot \frac{\rho_{\text{Fe}_2\text{Al}_5}}{\rho_{\text{Fe}}} = C \quad (15)$$

Figure 125 plots A_{IMPs} as a function of A_{Steel} . Two distinct regions can be clarified in Figure 125: The first region before dipping time of 15 s corresponds to the beginning stage, where A_{IMPs} increases fast with A_{Steel} ; And the second region starts from the dipping time of 30 s, where A_{IMPs} increases linearly with A_{Steel} . Since the growth of Fe_2Al_5 phase is the overwhelming step in the growth of IMPs at prolonged dipping time, A_{IMPs} and A_{Steel} can be replaced with $A_{\text{Fe}_2\text{Al}_5}$ and A_{Fe} respectively. In the following part, only $A_{\text{Fe}_2\text{Al}_5}$ and A_{Fe} is used. A linear fitting of this region is achieved with a coefficient of 1.55255, then C is calculated to be about 1.0 according to equation (15), which implies that the growth of IMPs is not controlled by the chemical reaction for the formation of Fe_2Al_5 phase. Therefore, the growth of IMPs is believed to be controlled by the diffusion of reactants (mainly Al through solid steel in this case).

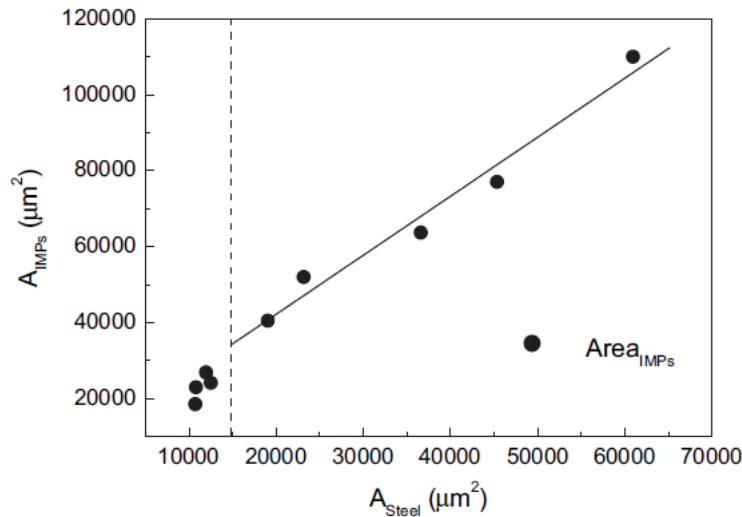


Figure 125: Relationship between A_{IMPs} and steel

For the growth of the IMPs, it's assumed that it can be described as the three-dimensional integration of three different distribution functions:

$$V = \iiint f(x, t)g(y, t)h(z, t)dx dy dz \quad (16)$$

Where, $f(x, t)$, $g(y, t)$ and $h(z, t)$ represent the distribution functions of Fe_2Al_5 phase along X , Y and Z axes respectively, and Z axis is set as the direction normal to the interface between Al and steel. These functions are supposed to be independent to each other.

Supposing that $f(x, t)$ and $g(y, t)$ have the same formula since the growth of the IMPs is isotropic in the plane perpendicular to Z axis according to the FIB result shown in Figure 123 (c). Then, equation (16) can be transformed to:

$$V = (\int f(x, t)dx)^2 \cdot \int h(z, t)dz = \frac{(\int f(x, t)dx \cdot \int h(z, t)dz)^2}{\int h(z, t)dz} \quad (17)$$

The volume of Fe_2Al_5 phase is now derived as following:

$$V_{\text{Fe}_2\text{Al}_5} = \frac{A_{\text{Fe}_2\text{Al}_5}^2}{\int_{\text{Fe}_2\text{Al}_5} h(z, t)dz} \quad (18)$$

According to Fick's second law, the diffusion along Z axis can be treated as a classic case of one-dimensional diffusion, therefore the corresponding diffusion distance will be:

$$\sigma_z = (2D_z t)^{\frac{1}{2}} \quad (19)$$

Where, D_z is the diffusion coefficient of Al atom in solid steel in z -direction, and is supposed to be constant here.

According to equation (18),

$$V_{\text{Fe}_2\text{Al}_5} = \frac{A_{\text{Fe}_2\text{Al}_5}^2}{(2D_z t)^{\frac{1}{2}}} \quad (20)$$

Figure 126 shows the relationship between $V_{\text{Fe}_2\text{Al}_5}$ and dipping time t . As shown in Figure 126, the growth of Fe_2Al_5 volume can be divided into two distinct regions as that in Figure 125: In the first region, there is no apparent relationship between $V_{\text{Fe}_2\text{Al}_5}$ and dipping time t , which might be due to the complicate mechanisms that take effect such as the diffusion of molten Al, and chemical reactions for the formation of FeAl_3 as well as the formation of Fe_2Al_5 ; However in the second region, a steady growth of Fe_2Al_5 phase is observed and linearly fitted with dipping time at logarithm scale. The coefficient of the fitting line is 0.14945, which indicates that the volume of Fe_2Al_5 is dependent on the dipping time with the exponent ~ 0.15 . The result for the first time correlates the volumetric growth of Fe_2Al_5 phase with dipping time.

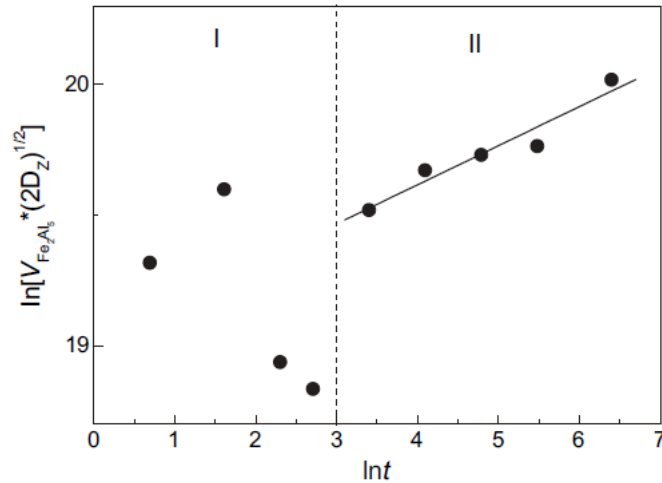


Figure 126: Volume of Fe₂Al₅ phase as a function of dipping time

Considering the model with an ideal reactants/diffusion source located at the center of a media, the volume induced by the diffusion depends on $t^{1.5}$ based on the assumption that the diffusion is isotropic in 3D space since in 1D the diffusion distance is according to $t^{0.5}$ as shown in equation (19). There might be two major factors which are responsible for this difference: One is that the reaction takes place on a 2D interface, not on a 3D one; And the other one could be that the diffusion is anisotropic in 3D space probably due to the stress effects^[94] or the heterogeneous nucleation of the IMPs at the interface which needs further theoretical modeling and analysis.

There are some advantages for introducing imaging processing to the analysis of the IMPs:

1. It's only depending on the real reaction patterns of resultants during the diffusive reaction process, and all the acquired parameters are based on the imaging analysis which is carried out automatically by software, which can minimize the subjective deviations related to different researchers.
2. This method is useful for a resultant pattern consisted of a series of intermetallic phases, such as two or three different intermetallic phases or more formed during the reaction. The area of different intermetallic phases can be acquired separately based on their difference in contrast in BSE images and analyzed then, where the previously adopted method is only focused on the 1D geometry of the intermetallic phases is not suitable for the analysis of such complicate systems, especially when the interfacial boundary between neighboring intermetallic phases is not smooth.
3. The method is based on the statistic results of the resultants, and can deal with a plenty of resulting images, which enhance its reliability, while the measurement of maximal or minimal thickness (or other parameters) of the intermetallic phases faces challenges

when the morphology of the intermetallic phase is highly irregular and when lots of results have to be processed.

Therefore, it's believed that the methodology applied here can be adopted for the analysis of other interfacial reactions, and helps the construction of a standardized and generalized method for diffusion processes or diffusive reactions.

8. Summary and Outlook

In this work the interface formation of composite casting aluminum around steel inserts has been investigated. While at first for principal understanding and calibration purposes pure aluminum was cast around mild steel inserts, the work later concentrated on the binary alloys Al-7Cu, Al-7Mg, Al-7Zn and especially Al-7Si, mainly because most commercial casting alloys lie within the Al-Si system. For investigative purposes the silicon content in the binary Al-Si alloys was varied to eutectic (12 %) and hyper-eutectic (17 %) concentrations. Additionally commercial alloys such as AlSi7Mg (A356) and AlMg5Si2Mn (Magsimal59) have been tested.

The interface formation (IF) was studied in several aspects:

- IF depending in mass ratio between aluminum and steel
- Wetting experiments in a controlled atmosphere
- Evolution with time via dipping tests considering alloy composition (see above)
- Real world IF via squeeze casting

In all these trials the steel partner of the compound casting (mild steel, material number 1.0226) and the temperature of the aluminum (700°C) during the experiments were kept constant in order to keep the results comparable.

It was shown that the interface formation with time depends strongly on the amount of phases possible. While Al-7Zn and Al-7Cu, which form none and just two intermetallic phases respectively, have a considerable growth speed, the interface formation of Al-7Si takes place at a much slower rate. This is desirable since the intermetallic phases are very brittle and the interface would even more the weakest link of the compound casting.

In terms of practical advice to the foundry industry this work can give suggestions as well. As can be seen from the results mechanical testing of the interface, the intermetallic compound can add 10 MPa and more to the strength of the final compound. Furthermore the layer will not have cracks that might form upon load compared to compound castings that solely rely on force- and shape bonding and thus may help reduce the corrosion.

For a caster this thesis can give the following recommendations:

- Interface formation can be obtained for steel inserts when compound casting with aluminum

- Complex shapes are not suited for compound casting if an intermetallic interface is desired: The formation strongly depends on the heat household of the casting, an insert with varying dimensions will have different interface thickness. The same applies to castings where the insert is symmetric but the width of the casting differs along the insert.
- The steel insert needs to be coated, typically with zinc, otherwise even a freshly etched steel insert will oxidize within seconds upon putting it into place (i.e. blue annealing), that is the die which has certainly more than 250°C, however, a zinc thickness that is too high will not lead to a proper interface. Furthermore casting speed has to be adjusted as well.
- The interface formation will not work properly if the insert has more than 10 % mass than the surrounding aluminum at the casting spot (Al-Fe mass ratio must be > 10:1)

To sum up it must me unfortunately said, that for commercial applications except the most demanding ones (concerning mechanical properties) the required conditions for a proper interface formation are demanding in such a way that most of the time it will not be feasible to design the casting just to suit these circumstances.

For modeling the ways of reaction and diffusion kinetics have been described. As can be seen, the limiting factor at the beginning of the interface formation is the reaction kinetics, which is subsequently restricted by the diffusion kinetics through the intermetallic layer. While this model works nicely with a layered interface with multiple intermetallics, it has been shown, that especially with alloys in the Al-Si system the situation is far more complex. While $\text{Fe}_2(\text{Al},\text{Si})_5$ (η) and (τ_6) form an intermetallic layer, phases like $\text{Fe}_2\text{Al}_2\text{Si}$ (τ_1) and $\text{Fe}_3\text{Al}_4\text{Si}_2$ (τ_3) form either as island shaped phase or as lamellar structure. For such complex phase formation an analytical approach is not feasible.

However, 3D growth of intermetallic phase Fe_2Al_5 formed between molten Al and solid steel is investigated with FIB technology and analyzed with an accurate imaging analysis method. The relationship between increased IMPs and the decreased steel confirms that the growth of intermetallic phase is not controlled by the chemical reaction between Al and Fe. A 3D model based on diffusion mechanism reveals that the volume of IMPs increases as a function of $t^{0.15}$ where t is dipping time. The method applied in this thesis can be expanded for the analysis of other interfacial reactions in solid-solid and solid-liquid systems with complicated resultants morphology.

9. References

- [1] European Automobile Manufacturers Association: Monitoring of ACEA's commitment on CO₂ Emission Reduction from Passenger Cars (1995-1999), (2000)
- [2] FEI: ESEM operation manual, (2000)
- [3] Carvalho I. et al: Reducing fuel consumption through modular vehicle architectures, *Applied Energy* 93, (2012), pp 556-563
- [4] Fka: Determination of Weight Elasticity of Fuel Economy for Conventional ICE Vehicles, Hybrid Vehicles and Fuel Cell Vehicles, Report 55510, (2007)
- [5] Bjelkengren C.: The Impact of Mass Decomponding on Assessing the Value of Vehicle Lightweighting, Massachusetts Institute of Technology, (2008)
- [6] Tolouei R., Titheridge H.: Vehicle mass as a determinant of fuel consumption and secondary safety performance, *Transportation Research Part D14*, (2009), pp 385-399
- [7] Fontaras G., Samars Z.: On the way to 130 g CO₂/km – Estimating the future characteristics of the average European passenger car, *Energy Policy* 38, (2010), pp 1826-1833
- [8] Jambor A., Beyer M.: New cars – new materials, *Materials & Design* 18, (1997), pp 203-209
- [9] Saur E.: L'Aluminium dans L'Automobile, *Matériaux et Techniques*, (1988), pp 57-59
- [10] SEW 310: Physikalische Eigenschaften von Stählen, *Taschenbuch der Stahl-Eisen-Werkstoffblätter*, 10. Auflage, Stahleisen, (1992)
- [11] Shahverdi H.R. et al: Microstructural analysis of interfacial reaction between molten aluminium and solid iron, *Journal of Materials Processing Technology* 124 (3), (2002), pp 345-352
- [12] Sadayappan K., Fragner W.: Effect of Processing on the Structure and Properties of Squeeze Cast Al-7Si-0.3Mg Alloy, *Shape Casting: 2nd International Symposium*, TMS (The Minerals, Metals & Materials Society), (2007), pp 151-158
- [13] Fragner W.: Herausforderungen und Lösungsmöglichkeiten bei der Herstellung von Verbundguss-Bauteilen, 5. Ranshofener Leichtmetalltage 2008, Geinberg, Österreich

-
- [14] Fragner W.: Hybrid mal anders - Verbundguss sorgt für wirtschaftliche Leichtbaulösungen, KEM, (2007), pp 94-95
- [15] Fragner W.: Improving Mechanical Properties of AlSi9Cu3(Fe) by Adjusted Heat Treatment of Squeeze and Low Pressure die Cast Parts, International Foundry Research, (2007), pp 24-35
- [16] Fragner W., Sonnleitner R.: Investigation of the Interface Formation and its Properties for Al Compound Casting, Proceedings of EMC 2009, pp 1271-1283
- [17] Fragner W.: Metallurgische Bindung von Al-Fe, Al-Al und Al-Mg Materialhybriden mittels Gussverfahren, Schlüsseltechnologie Leichtmetallguss im Automobilbau, Bad Nauheim, Deutschland, (2006), pp 41-62
- [18] Fragner W., Kaufmann H.: Legierungsgerechte Auswahl von Gießparametern, Druckguss-Praxis 1, (2005), pp 29-33
- [19] Fragner W. et al: Interface Reaction and its Kinetics of Al and Binary Al-Si Alloys to Mild Steel Substrates, 71. Jahrestagung der Deutschen Physikalischen Gesellschaft und DPG Frühjahrstagung, 29. März 2007, CD-Rom
- [20] Fragner W. et al: Interface Reactions and its Kinetics of Al and Binary Al-Alloys on Mild Steel, Light Metal Technology 2007, Saint-Sauveur, Canada, pp 152-157
- [21] Fragner W. et al: Interface Reactions and Their Kinetics of Al and Binary Al-Si Alloys to Mild Steel Substrates, TMS 2007, 136th Annual Meeting and Exhibition, Orlando, Florida, USA, CD-Rom
- [22] Fragner W. et al: Analysis of a non-symmetric Low Pressure Die Casting part via thermo-fluid dynamic simulation and experimental trials, High Tech Diecasting Conference, (2006), Vincenca, Italy, CD-Rom (ISBN 8885298575)
- [23] Fragner W., Pola A., Peterlechner C.: Low Pressure Die Casting Simulation with Procast and Casting Reality - An Evaluation, Europam 2005, Proceedings, CD-Rom
- [24] Fragner W., Sadayappan K., Limburg D.: Mitteldruckguss und Auswirkungen des Druckes auf die Bauteilqualität, 4. Ranshofener Leichtmetalltage 2006, Proceedings, Salzburg, Österreich, pp 39-50
- [25] Fragner W., Sadayappan K., Limburg D.: Reduced-pressure casting and the effect of pressure on the part quality, Casting, Plant & Technology International 2 (2007), pp 24-32

-
- [26] Fragner W. et al: Interface Reaction of Al and Binary Al-alloys on Mild Steel Substrates in a Controlled Atmosphere, ICAA10, Materials Science Forum Vols. 519-521, (2006), pp 1157-1162
- [27] Bai K., Wu P.: Assessment of the Zn-Fe-Al system for kinetic study of galvanizing, Journal of Alloys and Compounds 347 (2002), pp 156-164
- [28] Estey C.M. et al: Constitutive behavior of A356 during the quenching operation, Materials Science and Engineering A 383 (2), (2004), pp 245-251
- [29] Bitsche R.: Simulation von Stahl-Leichtmetall Verbundguss Strukturen Herstellung und mechanisches Verhalten, 5. Ranshofener Leichtmetalltage 2008, Geinberg, Österreich
- [30] Schneider D. et al: Production of titanium aluminide valves for automotive engines by reactive sintering, Structural Intermetallics, (1997), pp 453-460
- [31] Achar D., Ruge J., Sundaresan S.: Metallurgical and mechanical investigations of aluminum-steel fusion welds I, Aluminum 6, (1980), pp 391-397
- [32] Achar D., Ruge J., Sundaresan S.: Metallurgical and mechanical investigations of aluminum-steel fusion welds II, Aluminum 7, (1980), pp 465-469
- [33] Achar D., Ruge J., Sundaresan S.: Metallurgical and mechanical investigations of aluminum-steel fusion welds III, Aluminum 8, (1980), pp 533-536
- [34] Fukumoto S. et al: Formation process of reaction layer between aluminum alloys and stainless steel by friction welding, Welding international 16, (2002), pp 941-946
- [35] Watanabe T. et al: Joining of Steel to Aluminum Alloy by Interface-Activated Adhesion Welding, Materials Science Forum 426-432, (2003), pp 4129-4134
- [36] Han Q., Viswanathan S.: Analysis of the Mechanism of Die Soldering in Aluminum Die Casting, Metallurgical and Materials Transactions A 34, (2003), pp 139-146
- [37] Awan G.H., Hasan F.: The morphology of coating/substrate interface in hot-dip-aluminized steels, Materials Science and Engineering A 472 (1-2), (2008), pp 157-165
- [38] ASM Handbook of Ternary Phase Diagrams, ASM International, 10th edition, (1992)
- [39] Al-Fe Phasendiagramm, Fe₁₃Al₄ ("Al₃Fe"), Massalski T. B. (Hrsg.), Binary Alloy Phase Diagrams, (1990)

-
- [40] Jones W.R.D., Bartlett W.L.: The viscosity of aluminium and binary aluminium alloys, *Journal of the Institute of Metals* 81, (1952), pp 145-152
- [41] Heumann T., Dittrich S.: Über die Kinetik der Reaktion von festem und flüssigem Aluminium mit Eisen, *Zeitschrift für Metallkunde* 50 (10), (1959), pp 617-625
- [42] Jayaganthan R. et al: Fractal analysis of intermetallic compounds in Sn-Ag, Sn-Ag-Bi, and Sn-Ag-Cu diffusion couples, *Materials Letters* 60 (8), (2006), pp 1089-1094
- [43] Liang J. et al: Metallurgy and Kinetics of Liquid-Solid Interfacial Reaction during Lead-Free Soldering, *Materials Transactions* 47 (2), (2006), pp 317-325
- [44] Kobayashi S., Yakou T.: Control of intermetallic compound layers at interface between steel and aluminum by diffusion-treatment, *Materials Science and Engineering A* 338 (1-2), (2002), pp 44-53
- [45] Kobashi M. et al: The Effect of Surface Active Elements on the Wetting Behavior of Iron by Molten Aluminum Alloy, *ISIJ International* 35 (5), (1995), pp 488-493
- [46] Kaufman J.G., Rooy E.L.: *Aluminum Alloy Castings, Properties, Processes and Applications*, ASM International, (2005)
- [47] Kaufmann H., Fragner W., Uggowitzer P.J.: Influence of variations in alloy composition on castability and process stability. Part I: Gravity and pressure casting processes, *International Journal of Cast Metals Research* 18 (5), (2005), pp 273-278
- [48] Sereni S., Fragner W.: Rheo-Light european project story: Rheocasting process for high performance components, *2nd International Conference on Light Metals Technology, Proceedings*, (2005), pp 187-193
- [49] Kawano T. et al: Properties of aluminum alloy-stainless steel clad material produced via vacuum roll bonding, *Welding in the World* 41, (1998), pp 88-96
- [50] Schiffl A. et al: Herausforderungen bei der Präparation von metallischen Hybridwerkstoffen, *Praktische Metallografie* 6, (2009), pp 282-291
- [51] Kral M.V., Nakashima P.N.H., Mitchell D.R.G.: Electron Microscope Studies of Al-Fe-Si Intermetallics in an Al-11 Pct Si Alloy, *Metallurgical and materials Transactions A* 37, (2006), pp 1987-1997
- [52] Liang J. et al: Metallurgy and Kinetics of Liquid-Solid Interfacial Reaction during Lead-Free Soldering, *Materials Transactions* 47 (2), (2006), p 318

-
- [53] Xiang Z.D., Rose S.R., Datta P.K.: Long term oxidation resistance and thermal stability of Ni-aluminide/Fe-aluminide duplex diffusion coatings formed on ferritic steels at low temperatures, *Intermetallics* 17 (6), (2009), pp 387-393
- [54] Yao D., Shang J.K.: Effect of Cooling Rate on Interfacial Fatigue-Crack Growth in Sn-Pb Solder Joints, *IEEE Transactions on CPMT Part B* 19 (1), (1996), pp154-165
- [55] Zberg B.: Verbundguss zwischen Aluminium und Stahl, Diplomarbeit
- [56] Gupta S.P.: Intermetallic compound formation in Fe-Al-Si ternary system Part I, *Materials Characterization* 49, (2003), pp 269-291
- [57] Gupta S.P., Maitra T.: Intermetallic compound formation in Fe-Al-Si ternary system Part II, *Materials Characterization* 49, (2003), pp 293-311
- [58] Zhang L., Lück R.: Phase Diagram of the Al-Cu-Fe quasicrystal-forming alloy system, III Isothermal sections, *Zeitschrift für Metallkunde* 94, (2003), pp 108-115
- [59] Lihl F., Nachtigall E., Schwaiger A.: Viskositätsmessungen an binären Legierungen des Aluminiums mit Silizium , Zink, Kupfer und Magnesium, *Zeitschrift Metallkunde* 59, (1968), pp 213-219
- [60] Liu L. et al: Precipitation of b-Al₅FeSi Phase Platelets in Al-Si Based Casting Alloys, *Metallurgical and Materials Transactions A* 40, (2009), pp 2457-2470
- [61] Ma D., Wang W.D., Lahiri S.K.: Scallop formation and dissolution of Cu-Sn intermetallic compound during solder reflow, *Journal of Applied Physics* 91 (5), (2002), pp 3312-3317
- [62] Malakondaiah G., Kutumbaraim V.V., Rao P.R.: In-plane anisotropy in low cycle fatigue properties of an bilinearity in Coffin-Manson plots for quarternary Al-Li-Cu-Mg 8090 alloy plate, *Materials Science and Technology* 12, (1996), pp 563-577
- [63] Madhusudana C.V.: *Thermal Contact Conductance*, Springer, 1996
- [64] Matsugi K. et al: Application of electric discharge process in joining aluminum and stainless steel sheets, *Journal of Materials Processing Technology* 135, (2003), pp 75-82
- [65] Mekhrabov A.O. et al: A study of impurity effect on ordering characteristics of Fe₃Al intermetallics, *Journal of Alloys and Compounds* 205, (1994), pp 147-155

- [66] Mondolfo L.F.: Aluminum Alloys, Structure and Properties, Butterworths, 1979
- [67] Naoi D., Kajihara M.: Growth behavior of Fe₂Al₅ during reactive diffusion between Fe and Al at solid-state temperatures, *Materials Science and Engineering A* 459 (1-2), (2007), pp 375-382
- [68] Shatynski S.R., Hirth J.P., Rapp R.A.: A theory of multiphase binary diffusion, *Acta Metallurgica* 24, (1976), pp 1071-1078
- [69] Shih T.S., Tu S.H.: Interaction of steel with pure Al, Al-7Si and A356 alloys, *Materials Science and Engineering A* 454, (2007), pp 349-356
- [70] Sonnleitner R. et al: Identifikation von intermetallischen Phasen in Stahl-Aluminum Verbunden mittels Rasterelektronenmikroskopie, 4. Ranshofener Leichtmetalltage 2006, Salzburg, Österreich, pp 287-298
- [71] Neuhäuser M., Furche T., Dahms S.: Joining inorganic, non-metallic materials with different coefficients of thermal expansion using gradient tapes, *Welding and Cutting* 2, (2002), pp 108-111
- [72] Pan J. et al: Ultrasonic Insert Casting of Aluminum Alloy, *Scripta Materialia* 43, (2000), pp 155-159
- [73] Pearson T., Wake S.J.: Improvements in the Pretreatment of Aluminum as a Substrate for Electrodeposition, *Transactions of the Institute of Metal Finishing* 75 (39), (1997), pp 93-97
- [74] Parker R.H.: An Introduction to Chemical Metallurgy, 2nd Edition, (1978), Pergamon Press, Oxford
- [75] Guy A.G.: Introduction to Materials Science, McGraw-Hill, New York, (1971)
- [76] Jost W.: Diffusion in Solids, Liquids, Gases, Academic Press, New York, (1960)
- [77] Hauffe K.: Reaktionen in und an festen Stoffen, Springer, Berlin, (1955)
- [78] Wagner C.: The evaluation of data obtained with diffusion couples of binary single-phase and multiphase systems, *Acta Metallurgica* 17 (2), (1969), pp 99-107
- [79] Kidson G.V.: Some aspects of the growth of diffusion layers in binary systems, *Journal of Nuclear Materials* 3 (1), (1961), pp 21-29

-
- [80] Dybkov V.I.: Reaction diffusion in heterogeneous binary systems – Part 1: Growth of the chemical compound layers at the interface between two elementary substances: one compound layer, *Journal of Materials Science* 21 (9), (1986), pp 3078-3084
- [81] Dybkov V.I.: Reaction diffusion in heterogeneous binary systems – Part 2: Growth of the chemical compound layers at the interface between two elementary substances: two compound layer, *Journal of Materials Science* 21 (9), (1986), pp 3085-3090
- [82] Dybkov V.I.: Reaction diffusion in heterogeneous binary systems – Part 2: Multiphase growth of the chemical compound layers at the interface between two mutually insoluble substances, *Journal of Materials Science* 22 (12), (1987), pp 4233-4239
- [83] Dybkov V.I.: Interaction of iron-nickel alloys with liquid aluminum, Part II, Formation of intermetallics, *Journal of Materials Science* 35, (2000), pp 1729-1736
- [84] Dybkov V.I.: Reaction Diffusion in Binary Solid-Solid, Solid-Liquid and Solid-Gas Systems: Common and Distinctive Features, *Defect and Diffusion Forum* 194-199, (2001), pp 1503-1522
- [85] Kofstad P.: *High-Temperature Oxidation of Metals*, Wiley, New York, (1968)
- [86] Loo F.J.J., Rieck G.D.: Diffusion in the titanium-aluminium system – I. Interdiffusion between solid Al and Ti or Ti-Al alloys, *Acta Metallurgica* 21 (1), (1973), pp 61-71
- [87] Evans U.R.: *The Corrosion and Oxidation of Metals*, Edward Arnold, London, (1960)
- [88] Arkharov V.I. et al: On the mechanism of chemical diffusion in solids and its application to oxidation, *Oxidation of Metals* 3 (3), (1971), pp 251-259.
- [89] Dybkov V.I.: Solid state growth kinetics of the same chemical compound layer in various diffusion couples, *Journal of Physics and Chemistry of Solids* 47 (8), (1986), pp 735-740
- [90] Wosik J.: *Final Report for ALWS Project*, ECHEM, (2006)
- [91] Bouayad A. et al: Kinetic interactions between solid iron and molten aluminum, *Materials Science and Engineering A* 363, (2003), pp 53-61
- [92] Bouché K., Barbier F., Coulet A.: Intermetallic compound layer growth between solid iron and molten aluminum, *Materials Science and Engineering A* 249, (1998), pp 167-175

-
- [93] Dybkov V.I.: Growth kinetics of chemical compound layers, Cambridge International Science Publishing, (1998)
- [94] Handwerker C.A., Cahn J.W., Manning J.R.: Thermodynamics and kinetics of reactions at interfaces in composites, *Materials Science and Engineering A* 126 (1-2), (1990), pp 173-189
- [95] Blanke W.: *Thermophysikalische Stoffgrößen*, Springer, (1989)
- [96] Dybkov V.I.: Growth kinetics of silicide layers: A physicochemical viewpoint, *Journal of Physics and Chemistry of Solids* 53 (5), (1992), pp 703-712
- [97] Dybkov O.V., Dybkov V.I.: Analytical treatment of diffusional growth kinetics of two intermetallic-compound layers, *Journal of Materials Science* 39, (2004), pp 6615-6617
- [98] Dybkov V.I.: Growth Of Chemical Compound Layers In Composite Materials, *Materials Letters* 3 (7-8), (1985) pp 278-281
- [99] Dybkov V.I.: Interaction of 18Cr-Ni stainless steel with liquid aluminum, *Journal of Materials Science* 25, (1990), pp 3615-3633
- [100] Salomon M., Mehrer H.: Interdiffusion, Kirkendall effect, and Al self-diffusion in ironaluminum alloys, *Zeitschrift für Metallkunde B* 96, (2005), pp 4-15
- [101] Andersson J.O. et al: Thermo-Calc & Dictra, *Computational Tools For Materials Science*, *Calphad* 26 (2), (2002), pp 273-312
- [102] Barmak K., Dybkov V.I.: Interaction of iron-chromium alloys containing 10 and 25 mass% chromium with liquid aluminum – Part II: Formation of intermetallic compounds, *Journal of Materials Science* 39, (2004), pp 4219-4230
- [103] Blumm J., Henderson J.B., Hagemann L.: Measurement of the thermophysical properties of an aluminum-silicon casting alloy in the solid and molten regions, *High Temperatures – High Pressures* 30, (1998), pp 153-157
- [104] Bouché K., Barbier F., Coulet A.: Intermetallic compound layer growth between solid iron and molten aluminium, *Materials Science and Engineering A* 249 (1-2), (1998), pp 167-175
- [105] Choe et al: Study of the Interface between Steel Insert and Aluminum Casting in EPC, *Journal Of Materials Science & Technology* 24 (1), (2008), pp 60-64

-
- [106] Fischer F.D. et al: A note on calibration of ductile failure damage indicators, *International Journal of Fracture* 73, (1995), pp 345-357
- [107] Frischherz et al: *Tabellenbuch für Metalltechnik*, Bohmann, (1988)
- [108] Guzik E., Kopycinski D.: Modeling Structure Parameters of Irregular Eutectic Growth: Modification of Magnin-Kurz Theory, *Metallurgical and materials Transactions A* 37, (2006), pp 3057-3067
- [109] Kageson P.: *Reducing CO₂ Emissions from New Cars*, European Federation for Transport and Environment, (2005)
- [110] Pontevichi Z. et al: Solid-liquid phase equilibria in the Al-Fe-Si system at 727°C, *Journal of Phase Equilibria and Diffusion* 25, (2004), pp 528-537
- [111] Regulation (EU 443-2009): Setting emission performance standards for new passenger cars as part of the Community's integrated approach to reduce CO₂ emissions from light-duty vehicles, *Office Journal of the European Union*, (2009)
- [112] Regulation (EU 510-2011): Setting emission performance standards for new light commercial vehicles as part of the Union's integrated approach to reduce CO₂ emissions from light-duty vehicles, *Office Journal of the European Union*, (2009)
- [113] Saito M., Maegawa T., Homma T.: Electrochemical analysis of zincate treatments for Al and Al alloy films, *Electrochimica Acta* 51 (10), (2005), pp 1017-1020
- [114] Shankar S., Apelian D.: Die Soldering: Mechanism of the interface Reaction between molten Aluminum Alloy and Tool Steel, *Metallurgical and Materials Transactions B* 33, (2002), pp 465-476
- [115] THERPRO: Thermo-physical Properties Database provided by the International Atomic Energy Agency, URL: <http://therpro.hanyang.ac.kr>
- [116] Winkelman G.B. et al: Morphological features of interfacial intermetallics and interfacial reaction rate in Al-11Si-2.5Cu-(0.15/0.60)Fe cast alloy/die steel couples, *Journal of Materials Science* 39, (2004), pp 519- 528
- [117] Zervas E., Lazarou C.: Influence of European passenger cars weight to exhaust CO₂ emissions, *Energy Policy* 36, (2008), pp 248-257
- [118] Zhang N. et al: Three-Dimensional Analysis Of The Growth Of Intermetallics Phases Between Solid Steel And Molten Aluminum, *Intermetallics* 18 (2), (2010), pp 221-225

- [119] Zhu H., Guo J., Jia J.: Experimental study and theoretical analysis on die soldering in aluminum die casting, *Journal of Materials Processing Technology* 123, (2002), pp 229-235

10. LIST of FIGURES

Figure 1: Brembo brake disk consisting of a ceramic and precast iron inlay	5
Figure 2: Bush bearing of steel with aluminum insert.....	5
Figure 3: Example of an aluminum piston with a steel insert	6
Figure 4: VarioStruct part produced via high pressure die casting.....	6
Figure 5: Micrograph of a CMT produced welding seam of Aluminum to a steel sheet	7
Figure 6: Al-Fe phase diagram (bottom atomic-, top weight percent) ^[38]	8
Figure 7: Measurement of micro-hardness: a) Al_5Fe_2 and b) Al_3Fe	11
Figure 8: Schematic of setup for recasting of steel with aluminum at different mass ratios ...	12
Figure 9: Quarter of a sample of steel recast with aluminum	13
Figure 10: Cooling curve and cooling rates of steel cubes recast with aluminum	14
Figure 11: Experimental setup for wetting experiments	15
Figure 12: Temperature profile and experimental procedure of the wetting experiment.....	15
Figure 13: Schematic (a) and real (b) world test setup of dipping experiment with steel strips (ambient temperature) into liquid aluminum at 700 °C.....	17
Figure 14: Steel strips dipped into a binary Al-Si7 alloy with dipping times ranging from 1 s (left) to 300 s (5 min, right)	17
Figure 15: UBE HVSC 350 t squeeze casting (SCQ) machine with dosing robot.....	18
Figure 16: Dimensions of step die casting (without insert).....	19
Figure 17: Position of the steel insert at the 14 mm thick step.....	20
Figure 18: Mass ratio Fe-Al 1:50: Al-Fe phase over the whole profile, vermicular Al-Fe phase visible in the aluminum	22
Figure 19: Mass ratio Fe-Al 1:50: Boundary layer steel/aluminum, EDX analyses from the intermetallic phase agrees with the results of the standards; The phase turned towards the aluminum could be identified as Al_3Fe , the phase turned towards the steel as Al_5Fe_2 (EDX analyses at 20 kV)	23
Figure 20: Mass ratio Fe-Al 1:50: Boundary layer steel/aluminum, EDX analyses from the intermetallic phase agrees with the results of the standards (EDX analyses at 20 kV)	23
Figure 21: Mass ratio Fe-Al 1:25: Overview boundary layer Steel/Al, different thick developed intermetallic phases, in some areas are no intermetallic phases at the boundary layer (thickness of the intermetallic phase decrease from (a) to (d)).....	24
Figure 22: Mass ratio Fe-Al 1:25: Overview boundary layer Steel/Al, different thick developed intermetallic phases; In the area at the boundary layer developed intermetallic phase, the phase extend bacillary into the Al-matrix.....	25
Figure 23: Mass ratio Fe-Al 1:25: Detectable cracks in the intermetallic phase.....	25

Figure 24: Mass ratio Fe-Al 1:25: At the boundary layer steel/Al two intermetallic phases form (Al_5Fe_2 towards steel, Al_3Fe towards Al); These two phases have different contrasts in the BSE-Picture (the phase with more aluminum is a little bit darker); EDX analyses at 20 kV	26
Figure 25: Mass ratio Fe-Al 1:25: Analyses of the boundary layer	27
Figure 26: Mass ratio Fe-Al 1:15: Overview, bacillary Al-Fe intermetallics in Al-melt	28
Figure 27: Mass ratio Fe-Al 1:15: Intermetallic phases not developed over the whole profile (no phase in the right picture)	28
Figure 28: Mass ratio Fe-Al 1:15: Al-Fe-particle in Al-matrix + EDX analysis (at 5 kV) shows Al_3Fe	28
Figure 29: Mass ratio Fe-Al 1:15: In some areas at the boundary layer Steel/Al the Al_3Fe begins to develop (EDX analysis at 5 kV)	29
Figure 30: Mass ratio Fe-Al 1:15: Visible grain structure in the intermetallic phase: Fine grained structure from Al_3Fe , relative large grain from Al_5Fe_2 ; EDX analysis at 5 kV shows the existence of two phases (Al_5Fe_2 , Al_3Fe)	29
Figure 31: Mass ratio Fe-Al 1:15: Transition region of Fe to Al (intermetallic in grain)	30
Figure 32: Mass ratio Fe-Al 1:10: Overview, Development of intermetallic phases at the flanges	31
Figure 33: Mass ratio Fe-Al 1:10: Element contrast	31
Figure 34: Mass ratio Fe-Al 1:10: The phase with more aluminum (Al_3Fe) is much finer grained than the phase with less aluminum (Al_5Fe_2)	32
Figure 35: Mass ratio Fe-Al 1:5: BSE picture from the steel surface near the crack + EDX analysis of the whole in the picture displayed area: Hardly any Al detectable ..	33
Figure 36: Mass ratio Fe-Al 1:5: SE picture from the steel surface with middle (left) and high (right) magnification; Oxide can be spotted on the surface	33
Figure 37: Mass ratio Fe-Al 1:1: BSE picture from the steel surface near the crack + EDX analysis of the whole in the picture displayed area: Hardly Al detectable	34
Figure 38: Mass ratio Fe-Al 1:1: SE picture from the steel surface with middle (left) and high (right) magnification	34
Figure 39: Mass ratio Fe-Al 1:1: BSE picture from the aluminum surface near the crack + EDX analysis of the whole in the picture displayed area: No Fe detectable, just O; Grain boundaries clearly visible	35
Figure 40: Mass ratio Fe-Al 1:1: SE pictures from the aluminum surface with different magnifications	35
Figure 41: REM/BSE pictures from cast samples steel in Al99.7 show the transition zone Steel/IMPZ/Aluminum: Constant development of the IMPZ independent from	

the mass ratio steel/aluminum and the preheating temperature of the steel cubes	37
Figure 42: REM/BSE pictures of the IMPZ with a preheating temperature of 100°C (steel cube, mass ratio Fe-Al 1:15) and quantitative tabulation from the EDX analysis at the marked points: Identification of phase Al_5Fe_2 at the border to steel and phase Al_3Fe at the border	38
Figure 43: Sample Al/Fe	39
Figure 44: Sample Al-7Si/Fe	39
Figure 45: Al/Fe (12,5x)	39
Figure 46: Al-7Si/Fe (12,5x)	39
Figure 47: Interface of Al99.98/Fe couple on the edge. The different wetting angle of aluminum und the intermetallic layer on the iron substrate can be seen.....	39
Figure 48: Intermetallic layer interface of Al99.98/Fe couple	40
Figure 49: Intermetallic layer interface Al-7Si/Fe couple	40
Figure 50: Intermetallic layer interface of Al-7Cu/Fe couple	41
Figure 51: Intermetallic layer interface of Al-7Zn/Fe couple	41
Figure 52: Al 99.98/Fe interface using an electronic microscope and phase identification of Points S1 and S2	41
Figure 53: Fe/Al-7Si interface (Al-7Si Top, Fe bottom)	42
Figure 54: Fe/Al-7Si interface (500x) and approximate areas from where EDX spectrums were taken	42
Figure 55: Sample 1, Area A: EDX points	44
Figure 56: Sample 1, Area B: EDX points	44
Figure 57: Sample 2, Area A: EDX points	44
Figure 58: Sample 2, Area B: EDX points	44
Figure 59: Score of the area ratio IMPZ/Steel by setting color levels: Red for IMPZ and green for Steel	46
Figure 60: Dip experiments Al-7Cu: Sequence of SEM pictures from the ion beam etched profile of Steel/Al-7Cu with different dipping times: Decrease of steel profile and growth of IMPZ with increasing dipping time	47
Figure 61: Dip experiments Al-7Cu: Growth of the IMPZ with increasing dipping time and decreasing steel profile, the overall thickness (Steel + IMPZ) persist constant from 60 seconds dipping time	48
Figure 62: Dip experiments Al-7Cu: REM picture of an ion beam etched profile from a compound sample Steel/Al-7Cu after 120 seconds dipping time: The different phases in the IMPZ are well specifiable	48

Figure 63: Dip experiments Al-7Cu: SEM picture (left: Secondary electrons (SEM-SE), right: Backscattered electrons (SEM-BE)) of an ion beam etched profile from a compound sample Steel-Al-7Cu after 120 seconds dipping time: Finger-shaped growth of the IMPZ into the steel and detail picture of an dispersion in Al	49
Figure 64: Dip experiments Al-7Mg: Sequence of SEM pictures from the ion beam etched profile of Steel/Al-7Mg with different dipping times: Decrease of steel profile and growth of IMPZ with increasing dipping time	50
Figure 65: Dip experiments Al-7Mg: Growth of the IMPZ with increasing dipping time and decreasing steel profile, intense growth of the overall thickness (Steel + IMPZ).....	51
Figure 66: Dip experiments Al-7Mg: SEM picture (left: Secondary electrons (SEM-SE), right: Backscattered electrons (SEM-BE)) of an ion beam etched profile from a compound sample Steel/Al-7Mg after 15 seconds dipping time.....	51
Figure 67: Dip experiments Al-7Zn: Sequence of SEM pictures from the ion beam etched profile of Steel/Al-7Zn with different dipping times: Decrease of steel profile and growth of IMPZ with increasing dipping time	53
Figure 68: Dip experiments Al-7Zn: Growth of the IMPZ with increasing dipping time and highly decreasing steel profile	53
Figure 69: Dip experiments Al-7Zn: SEM picture of an ion beam etched profile from a compound sample Steel/Al-7Zn after 5 seconds dipping time (left) and 30 seconds dipping time (right): Unbalanced dissolution of the steel.....	54
Figure 70: Dip experiments Al-7Zn: SEM picture (left: Secondary electrons (SEM-SE), right: Backscattered electrons (SEM-BE)) of an ion beam etched profile from a compound sample Steel/Al-7Zn after 5 seconds dipping time: Finger-shaped growth of the IMPZ into the steel, no correlation between grain structure of steel and the IMPZ	54
Figure 71: Dip experiments Al99.7 + 2 μm Zinc: Sequence of SEM pictures from the ion beam etched profile of Steel/Al99.7 with different dipping times: Decrease of steel profile and growth of IMPZ with increasing dipping time.....	55
Figure 72: Dip experiments Al99.7 + 2 μm Zinc: Growth of the IMPZ with increasing dipping time and decreasing steel profile, the overall thickness (Steel + IMPZ) is constant after about 60 seconds dipping time.....	56
Figure 73: Dip experiments Al99.7: SEM picture (left: Secondary electrons (SEM-SE), right: Backscattered electrons (SEM-BE)) of an ion beam etched profile from a compound sample Steel-Al99.7 after 120 seconds dipping time: No correlation between grain structure of steel and the IMPZ.....	56

-
- Figure 74: Dip experiments Al-7Si + 2 μm Zinc: Sequence of SEM pictures from the ion beam etched profile of zinc coated steel and Al-7Si with different dipping times 58
- Figure 75: Dip experiments Al-7Si + 2 μm Zinc: Little decrease of the steel profile with increasing dipping time; Growing of the IMPZ stops after 10 seconds, thus results in a decreasing of the overall thickness Steel + IMPZ 58
- Figure 76: S Dip experiments Al-7Si: EM picture (secondary electrons (SEM-SE)) of an ion beam etched profile from Steel-Al-7Si after 5 seconds (left) and 120 seconds (right) dipping time: τ_5 and Al_5Fe_2 could already be identified after 5 seconds dipping time 59
- Figure 77: Dip experiments Al-7Si: Sequence of SEM pictures from the ion beam etched profile of pickled steel and Al-7Si with different dipping times: Light decrease of steel profile; Continuous formation of IMPZ on both sides after 1 seconds dipping time; No growth of the IMPZ after 5 seconds 60
- Figure 78: Dip experiments Al-7Si + pickled: Both steel profile as well as overall thickness (steel + IMPZ) decreases during the 120 seconds dipping time. The width of the IMPZ does not change after the first 5 seconds 60
- Figure 79: Dip experiments Al-12Si + 2 μm Zinc: Sequence of SEM pictures from the ion beam etched profile of steel and Al-12Si with different dipping times: Decrease of steel profile with increasing dipping time and double sided growing of IMPZ not before 5-10 seconds; Very long, bar-shaped dispersion into the Al-Matrix, which grow with increasing dipping time 61
- Figure 80: Dip experiments Al-12Si + 2 μm Zinc: Growing of the IMPZ until 5 seconds dipping time, following the width of IMPZ is constant; The steel profile and the overall thickness (steel + IMPZ) decrease with increasing dipping time 62
- Figure 81: Dip experiments Al-12Si + pickled: Sequence of SEM pictures from the ion beam etched profile of pickled steel and Al-12Si with different dipping times: Smooth growing of the IMPZ already after 1 second dipping time; Good connection to the Al-Matrix 63
- Figure 82: Dip experiments Al-12Si + pickled: Trend of the thickness of IMPZ and steel profile: The very thin IMPZ is constant after 5 seconds dipping time. Slow decrease of steel profile with increasing dipping time 63
- Figure 83: Dip experiments Al-17Si: Sequence of SEM pictures from the ion beam etched profile of steel and Al-17Si with different dipping times: Both-sided growing of the IMPZ and connection to the Al-Matrix not before 5-10 seconds. Primary Si dispersions (bright gray areas) at the border to steel 64

Figure 84: Dip experiments Al-17Si + 2 μm Zinc: Trend of the thickness of IMPZ and steel profile: The IMPZ is constant after 5 seconds dipping time. Slow decrease of steel profile with increasing dipping time	65
Figure 85: Dip experiments Al-17Si + pickled: Sequence of SEM pictures from the ion beam etched profile of pickled steel and Al-17Si with different dipping times: Decrease of the steel profile; Connection to the Al-17Si Matrix already after 1 second dipping time.....	65
Figure 86: Dip experiments Al-17Si + pickled: Trend of the thickness of IMPZ and steel profile: The IMPZ is constant after 5 seconds dipping time. Slow decrease of steel profile with increasing dipping time	66
Figure 87: Decrease of the steel profile area during dipping into Al-7Cu, Al-7Mg, Al-7Si, Al-7Zn and Al99.7.....	67
Figure 88: Increase of the IMPZ area during dipping into Al-7Cu, Al-7Mg, Al-7Si, Al-7Zn and Al99.7	68
Figure 89: Comparison of steel profile transformation while dipping in Al-7Si, Al-12Si and Al-17Si (steel profile each zinc coated/not coated)	69
Figure 90: Trend of the steel profile and the dispersion and transformation of the IMPZ with different preprocessed steel surfaces and different Al-Si alloys	70
Figure 91: Dip experiments AlSi7Mg0.3: Sequence of SEM pictures from the ion beam etched profile of steel and AlSi7Mg0.3 with different dipping times: Decrease of the steel profile and constant thickness of IMPZ with increasing dipping time	71
Figure 92: Dip experiments AlSi7Mg0.3: Constant thickness of IMPZ and decreasing thickness of steel profile with increasing dipping time. The overall thickness (steel + IMPZ) decreases. The steel profile decreases linearly.....	71
Figure 93: Dip experiments AlMg5Si2Mn: Sequence of SEM pictures from the ion beam etched profile of steel and Magsimal59 with different dipping times: Light respectively no growing of the IMPZ and decrease of the steel profile with increasing dipping time.....	72
Figure 94: Dipping results of AlMg5Si2Mn (Magsimal59): Light respectively no growing of the IMPZ and decrease of the steel profile with increasing dipping time. The overall thickness (Stahl + IMPZ) decreases during the dipping time.....	73
Figure 95: Thickness changing of the steel strip during the dipping tests. The profile decreases faster while dipping in AlSi7Mg0.3 than in Magsimal59.....	73
Figure 96: SEM pictures of the ion beam etched profile of steel and AlSi7Mg0.3 after 150 seconds (left) and 180 seconds (right) dipping time.....	74

Figure 97: SEM pictures of the ion beam etched profile of steel and AlSi7Mg0.3 after 10 seconds dipping time and related EDX spectrum.....	75
Figure 98: SEM/BSE pictures from the 15 µm zinc coated steel profile in Al-7Si up to 10 seconds dipping time: Unbalanced growing of IMPZ; Zn accelerate the fast dissolution in the steel profile	77
Figure 99: SEM/BSE pictures + EDX-Mappings of the elements Al, Zn and Si from the 15 µm Zinc coated steel profile in Al-7Si with 1 second dipping time: Especially in areas with heavy dissumption of steel there is no Zn at the boundary layer between steel and IMPZ (picture right bottom).....	78
Figure 100: SEM/BSE pictures + EDX-Mappings of the elements Fe, Al, Zn and Si from the 15 µm Zinc coated steel profile in Al-7Si with 1 second dipping time: High concentration of Zn in the Al-Si alloy near the IMPZ. No Zn at the boundary layer steel/IMPZ is detectable	79
Figure 101: SEM/BSE pictures + EDX-Mappings of the elements Fe, Al, Zn and Si from the 15 µm Zinc coated steel profile in Al-7Si with 10 second dipping time: As seen in the 1 second dipped steel part also after 10 seconds dipping time Zn is detectable on the boundary layer steel/IMPZ where the steel profile dissipate very fast.....	80
Figure 102: Sequence of SEM pictures from the ion beam etched profile of steel and Al-7Si with different dipping times: Steel with 5µm zinc coat; Formation of IMPZ and decrease of the steel profile depending on the dipping time	81
Figure 103: Sequence of SEM pictures from the ion beam etched profile of steel and Al-7Si with different dipping times: Steel with 15µm zinc coat; Formation of IMPZ and decrease of the steel profile depending on the dipping time.....	82
Figure 104: IMPZ, between steel and Al-7Si after 1 second dipping time. Chemical analysis were made on the marked points	82
Figure 105: IMPZ, between steel and Al-7Si after 10 second dipping time. Chemical analysis were made on the marked points	83
Figure 106: Schematic view of sampling after „Squeeze Cast“ experiments: Metallic continuity only in the boundary area of the casting part (area 2).....	85
Figure 107: SEM/BSE pictures of the boundary layer steel/aluminum and EDX analysis on the marked points: No connection, very thin IMPZ at the steel surface, Zn goes into the aluminum melt.....	86
Figure 108: SEM/BSE pictures at the boundary layer steel/aluminum: Construction of Al-Fe-Zn-Si-particles in boundary area, no bonding in this area.....	87
Figure 109: SEM/BSE pictures: Porous structure in the zone between steel and aluminum .	88

Figure 110: SEM/BSE pictures from the transition zone steel/aluminum and EDX analysis at the marked areas: At the border to steel an accumulation of Si, Zn, and O was detected	89
Figure 111: Aluminum/Steel compound castings after mechanical trench: Connection Al-alloy/steel is very bad	90
Figure 112: Profile pure aluminum/steel in the middle and bottom area from the cast composite; The raw structures at the boundary layer arise from different etching behavior. The graphics below shows the elements dispersal along the red line drawn in the SEM picture.....	91
Figure 113: Assembly for evaluating interface strength in cast compound structures with tensile test specimen.....	93
Figure 114: Schematic and image of Al-Fe compound cast specimen from Monalite die.....	93
Figure 115: Results of tensile tests for strength of formed interface	94
Figure 116: Schematic diagram to illustrate the growth of the $ApBq$ layer between the elements A and B according to Dybkov ^[80]	97
Figure 117: Growth of the $ApBq$ layer under conditions of its simultaneous dissolution into the liquid at a constant rate ^[80]	102
Figure 118: Schematic phase diagram of a binary system with three chemical compounds ^[83]	103
Figure 119: Schematic diagram to illustrate the growth of the $ArBs$ layer between the mutually insoluble elements A and B ^[89]	104
Figure 120: Schematic diagram to illustrate the growth of the $ArBs$ layer between the $ApBq$ and B phases ^[93]	105
Figure 121: Schematic diagram to illustrate the growth of the $ArBs$ layer between the $ApBq$ and $AlBn$ compounds ^[93]	106
Figure 122: Representation of a duplex structure of the $ArBs$ layer in the $ApBq - ArBs - B$ system ^[93]	107
Figure 123: (a) Microstructures of the IMPs dipping time 10 s; (b) Collection of BSE maps, the geometry of each strip is 445.90 μm x 60.53 μm ; (c) FIB cross-section (dipping time: 10 s).....	110
Figure 124: Image analysis via phase coding method, (a) original image; (b) phase coded image.....	112
Figure 125: Relationship between AIMP and steel.....	114
Figure 126: Volume of Fe_2Al_5 phase as a function of dipping time	116

11. LIST of TABLES

Table 1: Averages and Standard deviations of EDX analysis of 71Al 29Fe (Fe_5Al_2) and 75,5Al 24,5Fe ($\text{Fe}_{13}\text{Al}_4$ or more commonly named Fe_3Al)	10
Table 2: Mass ratio of steel to aluminum.....	13
Table 3: Cube experiments: the metallographic comparison of Fe-Al ratios 1:50 and 1:15 show that with increasing steel mass compared to aluminum melt the chemical bonding of the interface decreases (Trial 1), whereas with high mass ratios there is a continuous intermetallic layer	21
Table 4: Wetting angles of Al and Al-alloys on Fe as an average of 12 measurements each with standard deviation as well as the maximum width of the intermetallic layer.....	40
Table 5: Expected/possible IMP's formed at the Fe/Al interface	42
Table 6: EDX measurements from Figure 55 to Figure 58, the intermetallic compounds detected and their phase names	45
Table 7: Dip experiments Al-7Cu: EDX analysis from the in Figure 62 marked points: The composition conforms the phases Al_5Fe_2 and Al_3Fe with little percentage of Cu.....	49
Table 8: Dip experiments Al-7Cu: EDX analysis from the in Figure 63 marked points at the dispersions in the Al-Matrix	49
Table 9: Dip experiments Al-7Mg: EDX analysis from the in Figure 66 marked points: The composition conforms the phases Al_5Fe_2 and Al_3Fe , compared to Al-7Cu the concentration of Mg in the IMPZ is higher	52
Table 10: Dip experiments Al-7Zn: EDX analysis from the in Figure 70 marked points: the composition conforms the phases Al_5Fe_2 and Al_3Fe , the concentration of Zn inside the IMPZ is marginal (ca 1 at %)	54
Table 11: Dip experiments Al99.7: EDX analysis from the in Figure 73 marked points: The composition of 1, 2, and 3 conforms the phase Al_5Fe_2 with little decrease of the Fe concentration towards aluminum The composition of 4 conforms to Al_3Fe phase ...	56
Table 12: Dip experiments Al-7Si: EDX analysis from the six in Figure 76 marked points conform to the phases $(\text{Al}_{1-x}\text{Si}_x)_5\text{Fe}_2$, $\text{Fe}_{25}\text{Al}_{60}\text{Si}_{15}$, $(\text{Al}_{1-x}\text{Si}_x)_3\text{Fe}$ and $\text{Fe}_2\text{Al}_7\text{Si}$ (τ_5) ...	59
Table 13: EDX analysis of the marked points in Figure 97	75
Table 14: Chemical composition of IMPZ at the points shown in Figure 104.....	83
Table 15: Chemical composition of IMPZ at the points shown in Figure 105.....	84
Table 16: EDAX results from Figure 123 (a)	110
Table 17: Area of IMPs and steel.....	112

12. APPENDIX

Publications in the course of this Thesis

In the course of this work several publications and conference contributions have been published. For lucidity purposes they are listed here.

Zhang N., Wosik J., Fragner W., Sonnleitner R., Nauer G.E.: Three-Dimensional Analysis Of The Growth Of Intermetallics Phases Between Solid Steel And Molten Aluminum, *Intermetallics* 18 (2), (2010), pp 221-225

Fragner W., Sonnleitner R.: Investigation of the Interface Formation and its Properties for Al Compound Casting, *Proceedings of EMC 2009*, pp 1271-1283

Schiffel A., Fragner W., Kainhofer C., Papis K.: Herausforderungen bei der Präparation von metallischen Hybridwerkstoffen, *Praktische Metallografie* 6, (2009), pp 282-291

Fragner W., Sadayappan K., Limburg D.: Reduced-pressure casting and the effect of pressure on the part quality, *Casting, Plant & Technology International* 2, (2007), pp 24-32

Fragner W.: Hybrid mal anders - Verbundguss sorgt für wirtschaftliche Leichtbaulösungen, *KEM*, (2007), pp 94-95

Fragner W.: Improving Mechanical Properties of AlSi9Cu3(Fe) by Adjusted Heat Treatment of Squeeze and Low Pressure die Cast Parts, *International Foundry Research*, (2007), pp 24-35

Fragner W., Zberg B., Sonnleitner R., Uggowitz P.J., Löffler F.: Interface Reaction of Al and Binary Al-alloys on Mild Steel Substrates in a Controlled Atmosphere, *ICAA10, Materials Science Forum Vols. 519-521*, (2006), pp 1157-1162

Kaufmann H., Fragner W., Uggowitz P.J.: Influence of variations in alloy composition on castability and process stability. Part I: Gravity and pressure casting processes, *International Journal of Cast Metals Research* 18 (5), (2005), pp 273-278

Fragner W., Kaufmann H.: Legierungsgerechte Auswahl von Gießparametern, *Druckguss-Praxis* 1, (2005), pp 29-33

Fragner W.: Herausforderungen und Lösungsmöglichkeiten bei der Herstellung von Verbundguss-Bauteilen, *5. Ranshofener Leichtmetalltage 2008*, Geinberg, Österreich

Fragner W., Papis K., Wosik J., Uggowitz P., Löffler J.: Interface Reactions and its Kinetics of Al and Binary Al-Alloys on Mild Steel, *Light Metal Technology 2007*, Saint-Sauveur, Canada, pp 152-157

Sadayappan K., Fragner W.: Effect of Processing on the Structure and Properties of Squeeze Cast Al-7Si-0.3Mg Alloy, Shape Casting: 2nd International Symposium, TMS (The Minerals, Metals & Materials Society), (2007), pp 151-158

Fragner W., Papis K., Sonnleitner R., Uggowitz P., Löffler J.: Interface Reactions and Their Kinetics of Al and Binary Al-Si Alloys to Mild Steel Substrates, TMS 2007, 136th Annual Meeting and Exhibition, Orlando, Florida, USA, CD-Rom

Fragner W., Papis K., Sonnleitner R., Uggowitz P., Löffler J.: Interface Reaction and its Kinetics of Al and Binary Al-Si Alloys to Mild Steel Substrates, 71. Jahrestagung der Deutschen Physikalischen Gesellschaft und DPG Frühjahrstagung, (2007) CD-Rom

Sonnleitner R., Fragner W., Nauer G.E., Kaufmann H., Uggowitz P.J.: Identifikation von intermetallischen Phasen in Stahl-Aluminum Verbunden mittels Rasterelektronenmikroskopie, 4. Ranshofener Leichtmetalltage 2006, Salzburg, Österreich, pp 287-298

Fragner W., Sadayappan K., Limburg D.: Mitteldruckguss und Auswirkungen des Druckes auf die Bauteilqualität, 4. Ranshofener Leichtmetalltage 2006, Proceedings, Salzburg, Österreich, pp 39-50

Fragner W., Pola A., Kaufmann H., Roberti R.: Analysis of a non-symmetric Low Pressure Die Casting part via thermo-fluid dynamic simulation and experimental trials, High Tech Diecasting Conference, (2006), Vincenza, Italy, CD-Rom (ISBN 8885298575)

Fragner W.: Metallurgische Bindung von Al-Fe, Al-Al und Al-Mg Materialhybriden mittels Gussverfahren, Schlüsseltechnologie Leichtmetallguss im Automobilbau, Bad Nauheim, Deutschland, (2006), pp 41-62

Fragner W., Pola A., Peterlechner C.: Low Pressure Die Casting Simulation with Procast and Casting Reality - An Evaluation, Europam 2005, Proceedings, CD-Rom

Sereni S., Fragner W.: Rheo-Light european project story: Rheocasting process for high performance components, 2nd International Conference on Light Metals Technology, Proceedings, (2005), pp 187-193